

NASA CR-54909  
GA-6890



TUNGSTEN NUCLEAR ROCKET  
PHASE I  
FINAL REPORT

GPO PRICE \$ \_\_\_\_\_  
CFSTI PRICE(S) \$ \_\_\_\_\_  
Hard copy (HC) \$ 7.06  
Microfiche (MF) 2.00

Part 1

FACILITY FORM 808  
N 66 25573  
(ACCESSION NUMBER)  
406  
(PAGES)  
CR-54909  
(NASA CR OR TMX OR AD NUMBER)  
(THRU)  
22  
(CATEGORY)

ff 653 July 65

prepared for  
NATIONAL AERONAUTICS AND SPACE ADMINISTRATION  
Contract SNPC-27  
by

**GENERAL ATOMIC**  
DIVISION OF  
**GENERAL DYNAMICS**

JOHN JAY HOPKINS LABORATORY FOR PURE AND APPLIED SCIENCE  
P.O. BOX 608. SAN DIEGO 12. CALIFORNIA

### NOTICE

This report was prepared as an account of Government sponsored work. Neither the United States, nor the National Aeronautics and Space Administration (NASA), nor any person acting on behalf of NASA:

- A.) Makes any warranty or representation, expressed or implied, with respect to the accuracy, completeness, or usefulness of the information contained in this report, or that the use of any information, apparatus, method, or process disclosed in this report may not infringe privately owned rights; or
- B.) Assumes any liabilities with respect to the use of, or for damages resulting from the use of any information, apparatus, method or process disclosed in this report.

As used above, "person acting on behalf of NASA" includes any employee or contractor of NASA, or employee of such contractor, to the extent that such employee or contractor of NASA, or employee of such contractor prepares, disseminates, or provides access to, any information pursuant to his employment or contract with NASA, or his employment with such contractor.

Requests for copies of this report should be referred to

National Aeronautics and Space Administration  
Office of Scientific and Technical Information  
Attention: AFSS-A  
Washington, D. C. 20546

NASA CR-54909

GA-6890

TUNGSTEN NUCLEAR ROCKET  
PHASE I  
FINAL REPORT

Part 1

April 22, 1966

Work done by:

R. G. Bardes  
C. F. Bohren  
W. K. Brunot  
S. C. Cohen  
M. K. Drake  
S. J. Friesenhahn  
F. H. Fröhner  
E. M. Gillette  
E. Haddad  
G. F. Hoover

G. K. Houghton  
G. D. Joanou  
C. Jupiter  
L. O. Lavigne  
W. M. Lopez  
J. M. Lovallo  
B. McGehee  
M. H. Merrill  
R. A. Moore  
D. Naliboff

J. D. O'Neill  
J. C. Peak  
T. B. Sanderson  
C. B. Smith  
N. Smith  
C. A. Stevens  
L. Stewart  
G. D. Trimble

Report written by:

R. G. Bardes  
S. C. Cohen  
S. J. Friesenhahn  
E. M. Gillette  
E. Haddad  
G. D. Joanou  
C. Jupiter  
R. A. Moore  
J. C. Peak  
G. D. Trimble

prepared for

NATIONAL AERONAUTICS AND SPACE ADMINISTRATION

Contract SNPC-27

**GENERAL ATOMIC**

DIVISION OF

**GENERAL DYNAMICS**

JOHN JAY HOPKINS LABORATORY FOR PURE AND APPLIED SCIENCE

P.O. BOX 608, SAN DIEGO, CALIFORNIA 92112

## TABLE OF CONTENTS

	<u>Page</u>
I. INTRODUCTION. . . . .	1-1
II. NUCLEAR ROCKET CRITICAL FACILITY . . . . .	2-1
2.1 INTRODUCTION. . . . .	2-1
2.2 GENERAL DESCRIPTION OF THE CRITICAL ASSEMBLY . . . . .	2-1
2.2.1 Structure . . . . .	2-1
2.2.2 Water System . . . . .	2-9
2.2.3 Control Console . . . . .	2-12
2.2.4 Control Rods . . . . .	2-12
2.2.5 Regulating Rods . . . . .	2-16
2.2.6 Instrumentation . . . . .	2-16
2.2.7 Neutron Source . . . . .	2-19
2.2.8 Poison Tubes . . . . .	2-19
2.2.9 Fuel Elements . . . . .	2-24
2.3 COMPARISON OF CORE CONFIGURATIONS . . . . .	2-35
2.3.1 Core I . . . . .	2-35
2.3.2 Core II . . . . .	2-36
2.3.3 Core III . . . . .	2-36
III. EXPERIMENTAL METHODS AND RESULTS . . . . .	3-1
3.1 CORE LOADING. . . . .	3-1
3.2 REACTIVITY MEASUREMENT TECHNIQUE . . . . .	3-3
3.2.1 Regulating Rod Worth . . . . .	3-4
3.2.2 Safety Rod Worth . . . . .	3-5
3.2.3 Measurement of the Excess Reactivity Held Down by Cadmium Solutions . . . . .	3-6
3.2.4 Poison Tube Worths at Different Radial Locations . . . . .	3-8
3.2.5 Worth of Poison Tubes Having Different Cadmium Concentrations . . . . .	3-8
3.2.6 Worth of Individual Fuel Element Components	3-10
3.2.7 Neutronic Simulation Experiment . . . . .	3-13
3.2.8 Worth of the Upper End Reflector in Core I .	3-16
3.2.9 Worth of Various Boron Concentrations in Core I . . . . .	3-16
3.2.10 Substitution of Boron-Stainless Steel for Tungsten in the Central Fuel Element of Core II . . . . .	3-19

	<u>Page</u>
3.3 FOIL MEASUREMENTS . . . . .	3-20
3.3.1 General Methods . . . . .	3-20
3.3.2 Radial Power Density in Element G-7 . . . . .	3-21
3.3.3 Azimuthal Flux and Power Distribution in One Fuel Element . . . . .	3-22
3.3.4 Interstitial Flux Measurements . . . . .	3-24
3.3.5 Flux and Power Distributions Throughout Core . . . . .	3-27
3.3.6 Cadmium Ratio Measurements . . . . .	3-32
3.3.7 Relative Power Calibration, Core III . . . . .	3-37
3.3.8 Absolute Power Measurements . . . . .	3-44
3.4 TEMPERATURE COEFFICIENT MEASUREMENTS . . . . .	3-45
3.4.1 Method . . . . .	3-45
3.4.2 Results . . . . .	3-47
3.5 PULSED NEUTRON MEASUREMENTS . . . . .	3-47
3.5.1 Method . . . . .	3-47
3.5.2 Results . . . . .	3-51
3.6 GAMMA HEATING EXPERIMENTS . . . . .	3-53
3.6.1 Introduction. . . . .	3-53
3.6.2 Thimble Ionization Chambers . . . . .	3-53
3.6.3 Absolute Calibration of the Energy Deposition in the Graphite Chambers . . . . .	3-60
3.6.4 Absolute Calibration of the Energy Deposition in the Polyethylene Chambers. . . . .	3-63
3.6.5 Thimble Ionization Chamber Measurements in Core III of the Tungsten Nuclear Rocket Reactor . . . . .	3-75
3.6.6 Time History of the Gamma Intensity in Core III of the Tungsten Nuclear Rocket Reactor . . . . .	3-75
3.6.7 Results and Discussions of Sources of Error in the Absorbed Dose Measurements in Core III of the Tungsten Nuclear Rocket Reactor . . . . .	3-82
IV. ANALYTICAL METHODS. . . . .	4-1
4.1 COMPUTING THE SPATIAL FINE STRUCTURE IN A CELL . . . . .	4-1
4.2 HIGH ENERGY DISADVANTAGE FACTORS. . . . .	4-2
4.3 COMPUTATION OF $k_{\infty}$ . . . . .	4-7

	<u>Page</u>
4.4 TRANSPORT CROSS SECTION . . . . .	4-8
4.4.1 Transport Cross Section in the P-1 Approximation . . . . .	4-8
4.4.2 Transport Approximation of the Multigroup Boltzmann Equation . . . . .	4-12
4.5 NUMERICAL EXAMPLE . . . . .	4-16
4.6 COMPUTATION OF $k_{\text{eff}}$ . . . . .	4-18
4.7 MONTE CARLO ANALYSIS OF HIGH ENERGY LEAKAGE. . . . .	4-18
4.7.1 Purpose of Monte Carlo Calculations . . . . .	4-18
4.7.2 Description of the Monte Carlo Code . . . . .	4-18
4.7.3 Results of Analysis . . . . .	4-26
4.7.4 Conclusions . . . . .	4-29
4.8 ONE-DIMENSIONAL CALCULATIONS . . . . .	4-30
4.9 TWO-DIMENSIONAL CALCULATIONS . . . . .	4-30
4.10 CALCULATION OF THE CADMIUM THERMAL DISADVANTAGE FACTORS . . . . .	4-32
4.10.1 One-Dimensional Tube-Centered Calculation. . . . .	4-32
4.10.2 Two-Dimensional Transport Calculation . . . . .	4-35
4.11 TREATMENT OF RESONANCE ABSORPTION. . . . .	4-39
4.11.1 Conventional Treatment Using GAM-II. . . . .	4-39
4.11.2 Treatment of the Interstitial Cellular Material. . . . .	4-42
4.11.3 Resonance Interference. . . . .	4-51
4.11.4 $U^{235}$ Resonance Calculation . . . . .	4-52
4.11.5 Two-Region Resonance Calculation . . . . .	4-52
4.11.6 Special Collision Probability Tables . . . . .	4-55
4.12 TREATMENT OF THE BORON PLATE BOUNDARY IN THE BERYLLIUM-REFLECTED CORE . . . . .	4-55
4.13 CALCULATION OF THE EFFECTIVE DELAYED NEUTRON FRACTION. . . . .	4-59

	<u>Page</u>
V. MEASUREMENT AND EVALUATION OF NEUTRON CROSS SECTIONS . . . . .	5-1
5.1 INTRODUCTION. . . . .	5-1
5.2 EPITHERMAL U <sup>235</sup> CROSS SECTIONS . . . . .	5-2
5.3 THE ENERGY DEPENDENCE OF NEUTRON CAPTURE CROSS SECTION OF TUNGSTEN ISOTOPES FROM 0.01 TO 10.0 eV . . . . .	5-5
5.3.1 Introduction. . . . .	5-5
5.3.2 Experimental Techniques . . . . .	5-7
5.3.3 Method of Analysis . . . . .	5-29
5.3.4 Experimental Results . . . . .	5-39
5.3.5 Conclusions. . . . .	5-41
VI. ANALYTICAL RESULTS AND COMPARISON WITH EXPERIMENT . . . . .	6-1
6.1 CRITICALITY . . . . .	6-1
6.1.1 Variation of the Multiplication Factor with Lattice Pitch . . . . .	6-1
6.1.2 Criticality Results for the 3.0-in. Pitch, Water-Reflected Core . . . . .	6-4
6.1.3 Criticality Results for the 2.9-in. Pitch, Water-Reflected Core . . . . .	6-9
6.1.4 Criticality Results for the 3.0-in. Pitch, Beryllium-Reflected Core . . . . .	6-12
6.1.5 Summary of Criticality Results . . . . .	6-12
6.2 REACTIVITY. . . . .	6-16
6.2.1 Prompt Neutron Lifetime . . . . .	6-16
6.2.2 Effective Delayed Neutron Fraction. . . . .	6-17
6.2.3 Reactivity and the Asymptotic Period . . . . .	6-18
6.2.4 Control Rod Worths . . . . .	6-20
6.2.5 Calculation of the Excess Reactivity . . . . .	6-25
6.2.6 Radial Worth of the Cadmium Poison Tubes . . . . .	6-29
6.2.7 Cadmium Worth as a Function of Concentration . . . . .	6-31
6.2.8 Worth of Fuel Assembly Components . . . . .	6-31
6.2.9 Worth of Upper Reflector . . . . .	6-34
6.2.10 Neutronic Simulation Experiment . . . . .	6-34
6.3 FLUX AND POWER DISTRIBUTIONS. . . . .	6-35

	<u>Page</u>
6.3.1 Power Density in the Fuel Rings . . . . .	6-35
6.3.2 Gold Cadmium Ratios . . . . .	6-38
6.3.3 Flux and Power Distributions in the Core. . . . .	6-40
6.3.4 Analysis in Support of the Gamma Heating Experiment. . . . .	6-43
6.4 TEMPERATURE COEFFICIENTS . . . . .	6-46
6.5 CALCULATION OF THE PROMPT NEUTRON DECAY CONSTANT . . . . .	6-57
VII. CRITICAL EXPERIMENTS PERFORMED BY NASA LEWIS RESEARCH CENTER . . . . .	7-1
7.1 DESCRIPTION OF EXPERIMENTS . . . . .	7-1
7.2 METHOD OF ANALYSIS . . . . .	7-5
7.3 RESULTS . . . . .	7-7
7.3.1 Experiment 1 . . . . .	7-7
7.3.2 Experiment 2 . . . . .	7-8
7.3.3 Experiment 3 . . . . .	7-8
7.3.4 Experiment 4 . . . . .	7-9
7.3.5 Experiment 5 . . . . .	7-13
7.3.6 Experiment 6 . . . . .	7-14
7.3.7 Experiment 7 . . . . .	7-14
7.3.8 Experiment 8 . . . . .	7-15
7.3.9 Experiment 9 . . . . .	7-16
7.3.10 Experiment 10. . . . .	7-16
7.4 SUMMARY OF RESULTS. . . . .	7-17
7.5 RECALCULATION OF EXPERIMENTS 5 AND 10. . . . .	7-22
7.6 DISCUSSION AND CONCLUSIONS . . . . .	7-25
VIII. DISCUSSION OF RESULTS . . . . .	8-1
8.1 REFINED CALCULATION OF CRITICALITY . . . . .	8-1
8.1.1 Two-Dimensional Calculation of the Unit Cell Thermal Disadvantage Factors . . . . .	8-1
8.1.2 Two-Dimensional Calculation of the Cadmium Thermal Disadvantage Factors . . . . .	8-4
8.1.3 Treatment of the Interstitial Material in Resonance Absorption Calculations . . . . .	8-5
8.1.4 Resonance Interference. . . . .	8-6
8.1.5 $U^{235}$ Resonance Calculation . . . . .	8-7
8.1.6 Two-Region Resonance Calculation . . . . .	8-9



	<u>Page</u>
8.1.7 Two-Dimensional Diffusion Calculation . . .	8-12
8.1.8 Estimation of the Effect of Approximations in the Refined Calculation . . . . .	8-13
8.2 REACTIVITY MEASUREMENTS AND ANALYSIS . .	8-18
8.2.1 Areas of Agreement Between Experiment and Analysis . . . . .	8-18
8.2.2 Prompt Neutron Lifetime . . . . .	8-19
8.2.3 Excess Reactivity. . . . .	8-19
8.2.4 Fuel Element Component Worths. . . . .	8-20
8.2.5 Simulation Experiment . . . . .	8-20
8.3 FLUX AND POWER DISTRIBUTIONS. . . . .	8-21
8.4 TEMPERATURE COEFFICIENTS . . . . .	8-22
8.5 MEASUREMENT OF THE ASYMPTOTIC DECAY CONSTANT . . . . .	8-25
IX. CONCLUSIONS AND SUGGESTIONS FOR FUTURE WORK .	9-1
9.1 REVIEW AND MEASUREMENT OF CROSS SECTIONS	9-1
9.2 ANALYSIS OF CRITICAL EXPERIMENTS AT THE LEWIS RESEARCH CENTER . . . . .	9-2
9.3 CRITICALITY MEASUREMENTS AND ANALYSIS. .	9-2
9.4 REACTIVITY MEASUREMENTS AND ANALYSIS . .	9-3
9.5 FLUX AND POWER DISTRIBUTIONS. . . . .	9-3
9.6 TEMPERATURE COEFFICIENTS . . . . .	9-4
9.7 ASYMPTOTIC DECAY CONSTANT . . . . .	9-4
9.8 CALCULATION OF ZONED CORES . . . . .	9-4
REFERENCES . . . . .	R-1

LIST OF ILLUSTRATIONS

	<u>Page</u>
2.1 Nuclear rocket critical facility area . . . . .	2-2
2.2 Photograph of critical assembly building . . . . .	2-3
2.3 Photograph showing water circulation system . . . . .	2-4
2.4 Top view of the reactor tank . . . . .	2-5
2.5 Reactor tank assembly . . . . .	2-6
2.6 Grid plate layout . . . . .	2-8
2.7 Grid plate installation. . . . .	2-10
2.8 Critical assembly water flow schematic. . . . .	2-11
2.9 Control console . . . . .	2-13
2.10 Control rod blade . . . . .	2-14
2.11 Safety rod assembly . . . . .	2-15
2.12 Regulating rod . . . . .	2-17
2.13 Nuclear instrumentation . . . . .	2-18
2.14 Nuclear instrumentation scram amplifier . . . . .	2-20
2.15 Critical assembly scram system . . . . .	2-21
2.16 Poison tube . . . . .	2-22
2.17 Fuel element. . . . .	2-25
2.18 Fuel element subassembly . . . . .	2-26
2.19 Fuel forming press. . . . .	2-28
2.20 Fuel forming die . . . . .	2-29
2.21 Fuel and tungsten distribution among fuel elements . . . . .	2-30
2.22 Cross section of reactor tank and core support structure . . . . .	2-37
2.23 Side reflector, 3.0-in. pitch, Be reflected core . . . . .	2-38
2.24 Bottom reflector, 3.0-in. pitch, Be reflected core . . . . .	2-40
3.1 Cadmium worth at various radii . . . . .	3-9
3.2 Worth of various cadmium concentrations in Cores I and II . . . . .	3-11
3.3 Worth of various cadmium concentrations in Cores I and III . . . . .	3-12
3.4 Top reflector worth in Core I . . . . .	3-17
3.5 Worth of boron poison in Core I . . . . .	3-18
3.6 Azimuthal activation of manganese foils, Core I . . . . .	3-23
3.7 Azimuthal relative power in fuel element G-7. (Core III) . . . . .	3-25
3.8 Manganese foil activations around fuel element A-4 (Azimuthal Plot) . . . . .	3-26
3.9 Flux traverse with Cu wire, Core I . . . . .	3-28
3.10 Axial flux traverse, Core I . . . . .	3-29
3.11 Radial power traverse through G-row, Core I. . . . .	3-30
3.12 Radial power traverse at 90° to G-row, Core I . . . . .	3-31
3.13 Axial power traverse, Core III. . . . .	3-33
3.14 Radial power traverse at Stage 3 level, Core III . . . . .	3-34

	<u>Page</u>
3.15	Radial power traverse at Stage 11 level, Core III. . . . . 3-35
3.16	E-ring activations at Stages 6, 16, 21, Core III . . . . . 3-36
3.17	Radial power profile, Core III . . . . . 3-41
3.18	Axial power profiles, E-ring . . . . . 3-42
3.19	Axial power profiles, E-ring (normalized) . . . . . 3-43
3.20	Change of reactivity with temperature . . . . . 3-48
3.21	Change of reactivity with reflector temperature . . . . . 3-49
3.22	Landsverk 2500 rad carbon dosimeter details . . . . . 3-54
3.23	Landsverk 5000 rad polyethylene dosimeter details . . . . . 3-55
3.24	Disassembly view of carbon dosimeter . . . . . 3-56
3.25	Landsverk dosimeters and charger-reader . . . . . 3-57
3.26	Dosimeter calibration apparatus . . . . . 3-61
3.27	Typical carbon dosimeter response curve . . . . . 3-65
3.28	Typical polyethylene dosimeter response curve . . . . . 3-66
3.29	Calorimeter electronics block diagram . . . . . 3-69
3.30	Cross section of calorimeter . . . . . 3-70
3.31	Calorimeter control and readout circuits . . . . . 3-71
3.32	Placement of dosimeters in Core III of the tungsten nuclear rocket reactor . . . . . 3-76
3.33	Gamma intensity time history for dosimeter run one . . . . . 3-78
3.34	Gamma intensity time history for dosimeter run two . . . . . 3-79
3.35	Gamma intensity time history for dosimeter run three . . . . . 3-80
3.36	Gamma intensity time history for dosimeter run four . . . . . 3-81
3.37	Absorbed dose in graphite dosimeters in nuclear rocket core poison tubes . . . . . 3-83
3.38	Absorbed dose in graphite dosimeters in nuclear rocket core poison tubes . . . . . 3-84
3.39	Absorbed dose in polyethylene dosimeters in nuclear rocket core poison tubes . . . . . 3-85
3.40	Absorbed dose in graphite dosimeters in nuclear rocket core fuel elements . . . . . 3-86
4.1	Group 1 flux vs cell radius . . . . . 4-1
4.2	Mockup fuel element and hexagonal cell used in Monte Carlo analysis . . . . . 4-20
4.3	Cumulative probability radial source distribution mockup 5-ring cell . . . . . 4-21
4.4	Local/average fission rates vs axial distances . . . . . 4-22
4.5a	Actual geometry of poison tube in lattice . . . . . 4-33
4.5b	One-dimensional approximation for disadvantage factor calculation . . . . . 4-33
4.6	Geometry of GAMBLE XY cell calculation . . . . . 4-34
4.7	Average thermal group disadvantage factor of cadmium as a function of cadmium atom density . . . . . 4-36
4.8	Two dimensional cell description . . . . . 4-38
4.9	Configuration for mean-chord length derivation . . . . . 4-41

	<u>Page</u>
4. 10	Multiple body annular ring configuration. . . . . 4-46
4. 11	Flux in tungsten rings and interstitial material . . . . 4-48
4. 12	Radial flux plot for fuel element with interstitial material, from 40GP GAPLSN . . . . . 4-49
4. 13	Neutron flux in energy region of 500 to 67 keV. . . . . 4-57
4. 14	Neutron flux in energy region of 0.05 to 0.09 eV . . . . 4-58
5. 1	View of large liquid scintillator showing the associated shielding and collimation. . . . . 5-8
5. 2	Calculated first interaction probability for a single gamma to interact before escaping the large liquid scintillator. . 5-9
5. 3	Pulse height distributions due to captures in W <sup>182</sup> and W <sup>183</sup> . . . . . 5-10
5. 4	Pulse height distributions due to captures in W <sup>184</sup> and W <sup>186</sup> . . . . . 5-11
5. 5	Comparison of capture gamma ray pulse height distribu- tions obtained from the 4.15 and 21.2 eV levels in W <sup>182</sup> . 5-13
5. 6	Cross sectional view of electron target and moderator assembly . . . . . 5-14
5. 7	Schematic of electronic configuration used in time-of- flight and pulse height data acquisition . . . . . 5-16
5. 8	Flux shape comparisons using thick boron slab and cadmium samples and a thin BF <sub>3</sub> tube with a 1/v reson- ance. . . . . 5-20
5. 9	Comparison of flux shapes measured with thick indium and boron slab samples . . . . . 5-22
5. 10	Low energy gold cross sections obtained from various sources . . . . . 5-23
5. 11	Flux calibration data using the 4.15 eV resonance in W <sup>182</sup> . The sample is .01 inch natural tungsten. . . . . 5-25
5. 12	Absolute neutron flux as a function of time . . . . . 5-27
5. 13	Tungsten 182 cross section . . . . . 5-32
5. 14	Tungsten 183 cross section . . . . . 5-33
5. 15	Tungsten 184 cross section . . . . . 5-34
5. 16	Tungsten 186 cross section . . . . . 5-35
5. 17	Natural tungsten cross section . . . . . 5-36
5. 18	Gold cross section . . . . . 5-37
6. 1	Variation of eigenvalue with fuel element pitch . . . . . 6-3
6. 2	Two-dimensional core configuration . . . . . 6-6
6. 3	Solution of the inhour equation for the 3.0-in. pitch, water- reflected core . . . . . 6-19
6. 4	XY GAMBLE representation. . . . . 6-21
6. 5	Group 5 flux along X axis. . . . . 6-23
6. 6	Group 5 flux along Y axis. . . . . 6-24

	<u>Page</u>
6.7	Removal worth of 1 cm thick annulus of homogenized Cd <sup>113</sup> . . . . . 6-27
6.8	Removal worth of homogenized Cd <sup>113</sup> per sq. cm of core area. . . . . 6-28
6.9	Measured versus calculated activation for Cu foils, 3.0-in. pitch, water-reflected core . . . . . 6-41
6.10	Radial power distribution, 3.0-in. pitch, water-reflected core. . . . . 6-42
6.11	Axial power traverse, 3.0-in. pitch, Be-reflected core . 6-44
6.12	Radial power distribution, 3-in. pitch, Be-reflected core . 6-45
6.13	Comparison of experimental and calculated values of the effect of temperature on reactivity . . . . . 6-53
7.1	Fast neutron spectra at inner regions of ZPR cores 3, 5, and 3 (Normalized to one source neutron) . . . . . 7-10
7.2	Thermal neutron spectra at inner regions of ZPR cores 3, 5, and 8 (Normalized to one neutron slowing down below 2.38 eV) . . . . . 7-11
7.3	Thermal radial flux profiles. . . . . 7-12
7.4	Fission source vs radius. Lewis experiment No. 10 (normalized to: absorptions plus leakage = 1.0) . . . . 7-28
8.1	Effect of Cd concentration on U <sup>235</sup> disadvantage factors (2 DXY P <sub>0</sub> cell calculation) . . . . . 8-3
8.2	Flux in moderator region; 17.6 to 22.6 eV . . . . . 8-10
8.3	Flux in absorber region; 17.6 to 22.6 eV . . . . . 8-11

LIST OF TABLES

	<u>Page</u>
2.1	Grid plate tolerances . . . . . 2-7
2.2	Poison concentrations and codings. . . . . 2-23
2.3	Fuel ring specifications . . . . . 2-33
2.4	Tungsten ring specification . . . . . 2-33
2.5	Additional fuel element components . . . . . 2-34
2.6	Side reflector material specifications . . . . . 2-39
2.7	Bottom reflector material specifications . . . . . 2-39
3.1	Excess reactivity of standard core . . . . . 3-2
3.2	Regulating rod worths. . . . . 3-5
3.3	Safety rod worth. . . . . 3-5
3.4	Typical pattern used in determining the total excess reactivity . . . . . 3-6
3.5	Excess reactivity of standard cores without cadmium in poison tubes . . . . . 3-7
3.6	Excess reactivity of standard cores with increased cadmium loadings . . . . . 3-7
3.7	Radial worth of poison tubes. . . . . 3-8
3.8	Poison tube worth vs cadmium concentration . . . . . 3-10
3.9	Fuel element components worth (location G-7). . . . . 3-10
3.10	Additional fuel element components worths, Core I . . . . . 3-13
3.11	Specification for simulation section . . . . . 3-13
3.12	Physical specifications of the five-stage enriched tungsten section. . . . . 3-14
3.13	Worth of top reflector . . . . . 3-16
3.14	Measured worth of various boron concentrations . . . . . 3-16
3.15	Weight of boron stainless steel foils . . . . . 3-19
3.16	Chemical analysis of boron stainless steel . . . . . 3-19
3.17	Relative power density - Stage 12 of element G-7. . . . . 3-22
3.18	Cadmium ratio measurements . . . . . 3-32
3.19	Relative radial power distribution data . . . . . 3-37
3.20	Relative power per fuel ring in the 12th stage of G-7 . . . . . 3-38
3.21	Radial power, Stage 12 . . . . . 3-40
3.22	Axial power profile E-ring . . . . . 3-44
3.23	Absolute power calibration . . . . . 3-45
3.24	Location of temperature measuring sensors . . . . . 3-46
3.25	Results of the pulsed neutron source measurements . . . . . 3-52
3.26	Dosimeter calibration using 7.0 MeV bremsstrahlung radiation . . . . . 3-64

	<u>Page</u>	
3. 27	The Landsverk Electrometer Company calibration certificate. . . . .	3-67
3. 28	Calibration of the ion chambers in the TRIGA reactor . . .	3-74
3. 29	Results of ionization chamber measurements in Core III of the tungsten nuclear rocket reactor . . . . .	3-87
4. 1	Disadvantage factors, $\phi_{\text{fuel}}/\sqrt{\phi}$ mod . . . . .	4-5
4. 2	Age, leakage fraction, and effective multiplication factor of the mockup reference core . . . . .	4-5
4. 3	Unit cell disadvantage factors . . . . .	4-17
4. 4	Energy bounds for input data group structure . . . . .	4-23
4. 5	Monte Carlo estimate of leakage from mockup core (14.9 MeV-87.5 keV) . . . . .	4-27
4. 6	Comparison between results from GAZE and FMC-N . . . . .	4-27
4. 7	Comparison of volume averaged flux in various cell regions (14.9 MeV-87.5 keV) . . . . .	4-28
4. 8	Comparison of disadvantage factors . . . . .	4-29
4. 9	Dimensions of the mockup unit cell . . . . .	4-31
4. 10	Effective absorption cross section of $W^{182}$ from 2.38 to 8.32 eV . . . . .	4-47
4. 11	Uranium <sup>235</sup> fission spectrum and delayed neutron spectrum . . . . .	4-63
5. 1	Measured values of the $U^{235}$ fission integral and $\alpha$ . . . . .	5-3
5. 2	Results of the examination of various epithermal $U^{235}$ cross section sets . . . . .	5-4
5. 3	Abundances . . . . .	5-28
5. 4	Capture cross section at .0253 eV. . . . .	5-40
5. 5	Relative contribution of various isotopes to natural tungsten thermal cross section . . . . .	5-40
5. 6	Class(1) errors in normalization . . . . .	5-42
6. 1	Ten-group structure for eigenvalue calculations . . . . .	6-2
6. 2	Variation of eigenvalue with fuel element pitch (121-element core) . . . . .	6-2
6. 3	Homogenized atom densities for the 3.0-in. pitch core. . . . .	6-5
6. 4	Results of the refined calculation of the 3.0-in. pitch, water-reflected core . . . . .	6-7
6. 5	Neutron balances for 3.0-in. pitch, water-reflected core from one-dimensional radial diffusion calculation . . . . .	6-8
6. 6	Homogenized atom densities for the 2.9-in. pitch, water-reflected core . . . . .	6-10
6. 7	Neutron balance for the 2.9-in. pitch, water-reflected core from radial diffusion calculation . . . . .	6-11
6. 8	Homogenized atom densities for the 3.0-in. pitch Be-reflected core . . . . .	6-13
6. 9	Neutron balance for the 3.0-in. pitch, Be-reflected core from radial diffusion calculation . . . . .	6-14

	<u>Page</u>
6.10	Summary of criticality results . . . . . 6-15
6.11	Comparison of measured and calculated values of the prompt neutron lifetime . . . . . 6-16
6.12	Calculated values for the effective delayed neutron fraction . . . . . 6-17
6.13	Effective delayed neutron fractions and decay constants for $U^{235}$ in 3.0-in. pitch core . . . . . 6-18
6.14	Five-group structure for control rod calculations . . . . . 6-22
6.15	Rod worth results . . . . . 6-22
6.16	Comparison of predicted and measured excess reactivity . . . . . 6-29
6.17	Comparison of experimental and analytical poison rod worths (0.1255 molar $(Cd(NO_3)_2)$ ) . . . . . 6-31
6.18	Comparison of experimental and calculated worths for various cadmium concentrations . . . . . 6-32
6.19	Comparison of experimental and analytical fuel element component worths (3.0-in. pitch, Water-Reflected Core) . . . . . 6-33
6.20	Comparison of experimental and analytical fuel element component worths (Center Cell in the 2.9-in. Pitch Core) . . . . . 6-33
6.21	Comparison of measured and calculated top reflector worths . . . . . 6-34
6.22	Comparison of neutron balance for mockup and pseudo-reference fuel stages . . . . . 6-36
6.23	Removal worth of nuclides in mockup and pseudo-reference element . . . . . 6-37
6.24	Comparison of calculated and measured power density . . . . . 6-38
6.25	Comparison of experimental and calculated cadmium ratios for gold . . . . . 6-40
6.26	Comparison of measured and calculated relative powers in Stage 12 . . . . . 6-47
6.27	Foil activation calculation . . . . . 6-47
6.28	Water and cadmium density reduction factors . . . . . 6-48
6.29	Group structure for temperature coefficient calculations . . . . . 6-50
6.30	Thermal utilization calculated by GATHER with 5- and 18-group disadvantage factors . . . . . 6-50
6.31	Temperature coefficient results for the 3.0-in. pitch, water-reflected core . . . . . 6-51
6.32	Temperature coefficient results for the 3.0-in. pitch, beryllium-reflected core . . . . . 6-51
6.33	Overall temperature coefficient (water-reflected core) . . . . . 6-52
6.34	Components of the temperature coefficient for the 3.0-in. pitch, water-reflected core . . . . . 6-55
6.35	Components of the temperature coefficient for the 3.0-in. pitch, beryllium-reflected core . . . . . 6-56



	<u>Page</u>	
6.36	Comparison of calculated and measured values of $\alpha$ (3.0-in. pitch, water-reflected core). . . . .	6-59
7.1	Experiments selected for analysis. . . . .	7-1
7.2	Dimensions of critical assemblies. . . . .	7-2
7.3	Dimensions of tungsten tube inserts . . . . .	7-3
7.4	Volume fractions . . . . .	7-3
7.5	Homogenized atom densities. . . . .	7-4
7.6	Sixteen-group structure used for Lewis experiment eigen- value calculations . . . . .	7-5
7.7	Axial leakages/source neutron . . . . .	7-7
7.8	Results for ZPR 1 . . . . .	7-8
7.9	Results for ZPR 2 . . . . .	7-8
7.10	Results for ZPR 3 . . . . .	7-9
7.11	Results for ZPR 4 . . . . .	7-9
7.12	Results for ZPR 5 . . . . .	7-13
7.13	Results for ZPR 6 . . . . .	7-14
7.14	Results for ZPR 7 . . . . .	7-15
7.15	Results for ZPR 8 . . . . .	7-15
7.16	Comparison of GAZE and GAMBLE, experiment 8 . . . . .	7-16
7.17	Results for ZPR 9 . . . . .	7-16
7.18	Results for ZPR 10. . . . .	7-16
7.19	Summary of results . . . . .	7-17
7.20	Neutron balance. . . . .	7-18
7.21	Neutron balance. . . . .	7-19
7.22	Neutron balance. . . . .	7-20
7.23	Neutron balance. . . . .	7-21
7.24	Maximum estimated effect on eigenvalue of using a tung- sten density of 0.0635 atom/b-cm. . . . .	7-22
7.25	Revised homogenized atom densities for Lewis critical experiments Nos. 5 and 10 (atoms/b-cm multiplied by $10^4$ )	7-23
7.26	Buckling used in spectrum calculations for Lewis experi- ments Nos. 5 and 10 ( $B^2$ in $\text{cm}^{-2}$ ). . . . .	7-24
7.27	Results of recalculation of experiments Nos. 5 and 10 . . . . .	7-25
7.28	Neutron balance from recalculation . . . . .	7-26
8.1	Comparison of one- and two-dimensional disadvantage factor calculations (cadmium omitted) . . . . .	8-2
8.2	$U^{235}$ thermal disadvantage factors from three GAPLSN cell representations . . . . .	8-4
8.3	Comparison of one- and two-dimensional cadmium disad- vantage factor results. . . . .	8-5
8.4	Effective absorption cross sections in the 3.0-in. pitch core from 2.38 to 61.4 eV . . . . .	8-5
8.5	Effective absorption cross sections of the tungsten isotopes with and without resonance overlap; $1/E$ spectrum . . . . .	8-6

	<u>Page</u>
8.6	Effective absorption cross sections of the tungsten isotopes with and without overlap from $U^{238}$ ; $1/E$ spectrum . . . . . 8-7
8.7	Comparison of $U^{235}$ infinite dilution cross sections with resonance self-shielded cross sections 2.38 eV to 14.9 MeV. . . . . 8-8
8.8	Effective absorption cross sections of the tungsten isotopes from 2.38 to 61.4 eV obtained from one- and two-region calculations; 3.0-in. pitch core spectrum. . . . . 8-9
8.9	Epithermal advantage factors from tungsten two-region calculation . . . . . 8-12
8.10	Effective absorption cross sections of the tungsten isotopes with $U^{238}$ overlap; $1/E$ spectrum . . . . . 8-15
8.11	Comparison of disadvantage factors obtained for isolated cell and repeating array . . . . . 8-17

ABSTRACT

25573

This report describes the critical experiments and nuclear analysis performed at General Atomic in support of the Tungsten Water-Moderated Nuclear Rocket Reactor being developed by NASA-Lewis Research Center.

Descriptions of the critical facility and the critical assemblies are given. Experimental measurements are presented and compared with analytical results. Analytical methods are reviewed and some critical experiments previously performed at the NASA-Lewis Research Center are analyzed.

Three different core configurations of 121 fuel elements were assembled; two different pitches and both water and beryllium reflectors were used. Excess reactivity was held down by a cadmium nitrate solution contained in 204 poison tubes throughout the core. The fuel element consisted of an assembly of enriched uranium-aluminum alloy, depleted uranium, tungsten foil, and structural aluminum.

Experimental results include the excess reactivity available in the cores, the worth of poison tubes and fuel element components at various locations, the temperature coefficient of the cores, flux and power distributions in a cell and throughout the core, neutron and gamma ray dose rate distributions throughout the core, pulsed neutron measurements, and reactivity comparisons using a special fuel section of enriched tungsten.

Nuclear analysis of the assemblies required careful treatment of the extreme heterogeneities of the core. A detailed analysis which accounts for the two-dimensional cell structure, resonance overlap, and two-region resonance effects gave good agreement between calculations and the experimental results.

## I. INTRODUCTION

This Phase I final report describes the critical experiments and the analytical work performed under Contract SNPC-27 in support of the Tungsten Water-Moderated Nuclear Rocket Reactor under development by NASA - Lewis Research Center. This reactor concept utilizes tungsten metal enriched in the low-capture cross section isotope W-184 to attain high temperature performance capabilities with a reasonable fissile material inventory.

The report is published in two parts, each under separate cover, to facilitate handling of the unclassified portion of the document which is contained in this Part I. It has been organized as follows: Section II contains a description of the Critical Facility. Section III gives the results of the critical experiment program and Section IV describes the analytical methods and presents the results of some numerical experiments related to these methods. Section V describes the evaluation of neutron cross sections performed in support of this program and presents the results of measurements on the capture cross sections of the W isotopes in the energy range 0.01 to 10 eV. Section VI contains the comparison between the analytical results and those of the experimental program. Section VII gives the comparison between theory and experiment for the Lewis Laboratory Critical experiments, Section VIII contains a discussion of the results, and finally Section IX discusses conclusions and suggestions for future work.

In addition to this final report the following reports and papers were issued during the course of the contract:

1. "Tungsten Nuclear Rocket Critical Facility, Description and Hazards Analysis," Tungsten Nuclear Rocket Staff, General Atomic report, GA-5846 Rev. (1965).
2. "Technical Specification for the General Atomic Tungsten Nuclear Rocket Critical Facility," R. G. Bardes and J. C. Peak, General Atomic report, GA-6315 (1965).
3. "Neutronic Simulation of the Tungsten Water-Moderated Nuclear Rocket Reactor," S. C. Cohen, G. D. Joanou, R. A. Moore, and J. C. Peak, General Atomic report, GA-6141 (1965).
4. "Neutron Cross Sections for Aluminum," G. D. Joanou and C. A. Stevens, General Atomic report GA-5884 (1965).
5. "Neutron Cross Sections for the Tungsten Isotopes," G. D. Joanou and C. A. Stevens, General Atomic report GA-5885 (1965).
6. "Neutron Cross Sections for Beryllium," G. D. Joanou and C. A. Stevens, General Atomic report GA-5905 (1965).
7. "Neutron Cross Sections for U-235," G. D. Joanou and C. A. Stevens, General Atomic report GA-5944 (1965).
8. "Neutron Cross Sections for U-238," G. D. Joanou and C. A. Stevens, General Atomic report, GA-6087 Rev. (1965).
9. "Neutron Cross Sections for the Cd Isotopes," M. K. Drake General Atomic report (unpublished).
10. "The Neutron Capture Cross Section of the Tungsten Isotopes from 0.01 to 10.0 eV," S. J. Friesenhahn, E. Haddad, F. H. Fröhner, and W. M. Lopez, General Atomic report GA-6832 (1965).
11. "Criticality Calculations for the Three-Inch Pitch As-Built Core," J. C. Peak, S. C. Cohen, M. H. Merrill, and J. M. Lovallo, General Atomic report, GA-6484 (1965).
12. "Precritical Calculations for the 2.9-in. Pitch, TWMR Critical Assembly," J. C. Peak and J. M. Lovallo, General Atomic report, GA-6633 (1965).

13. "Precritical Calculations for the 3.0-in. Pitch, Beryllium-Reflected TWMR Critical Facility," J. C. Peak and J. M. Lovallo, General Atomic report GA-6807 (1965).
14. "GAROL, A Computer Program for Evaluating Resonance Absorption Including Resonance Overlap," C. A. Stevens, and C. V. Smith, General Atomic report GA-6637 (1965).
15. "High Energy Disadvantage Factors for Cylindrical Cells," S. C. Cohen, General Atomic report GA-6141 (1965).
16. "Final Report - Gamma and Neutron Dose Measurements for a Thermal Tungsten Nuclear Rocket Experiment," C. P. Jupiter and G. D. Trimble, General Atomic report GA-6942 (1965).
17. "Tungsten Water-Moderated Rocket Critical Assembly, Analytical Methods and Experimental Results," J. C. Peak and R. G. Bardes, Trans. Am. Nuc. Soc. 8, 2 (1965).
18. "Investigation of the Flux Recovery Assumption in Resonance Computations," C. A. Stevens and G. D. Joanou, Trans. Am. Nuc. Soc. 8, 1 (1965).
19. "Calculation of the Fast-Flux Fine Structure in the Cylindrical Cell Approximation," S. C. Cohen, Trans. Am. Nuc. Soc. 8, 2, (1956).
20. "Tungsten Nuclear Rocket Monthly Progress Report," Nuclear Rocket Staff, General Atomic reports, GACD-5787, GACD-5872, GACD-5975, GACD-6066, GACD-6166 (1 to 11-65).
21. "On the Transport Approximation of the Multigroup Boltzmann Equation," S. C. Cohen, General Atomic report GAMD-5922 (1964).
22. "Preparation of Cumulative Probability Tables for the Flexible Monte Carlo Code," J. C. Peak, General Atomic report GAMD-6250 (1965).
23. "FLUX, A Code for Collapsing and Punching Output Fluxes from GAPLSN and GAZE," S. C. Cohen, General Atomic report GAMD-6615 (1965).

## II. NUCLEAR ROCKET CRITICAL FACILITY

### 2.1 INTRODUCTION

The critical facility at General Atomic consists of three buildings. They are: (1) Critical Assembly Building, (2) Fuel Assembly Building where the fuel elements were fabricated and assembled and later modified and (3) Control Building (see Fig. 2.1). The Critical Assembly Building (Fig. 2.2) is a steel-reinforced concrete building having walls and roof two feet thick for shielding and containment. The temperature in the Critical Assembly Building is maintained constant by use of a heat pump. The Critical Assembly Building and the Fuel Assembly Building are located within a fenced exclusion area, while the Control Building, which also houses office space, is outside the fenced area and is shielded from the Critical Building by an earthen embankment.

### 2.2 GENERAL DESCRIPTION OF THE CRITICAL ASSEMBLY

#### 2.2.1 STRUCTURE

The Critical Assembly consists of a reactor, water dump tank, associated plumbing, safety and control rods, control and research instrumentation, and control circuitry. Some of this equipment is shown in Figs. 2.3 and 2.4.

Fig. 2.5 shows design details of the reactor tank assembly. The basic structure element of the critical assembly is the reactor tank base plate, which is a 1-1/4-in. thick aluminum plate seven feet in diameter mounted on four braced support legs. The 10-in. diameter water dump line, the two overflow lines, and the reactor tank recirculation line connections are welded to the bottom of this plate.

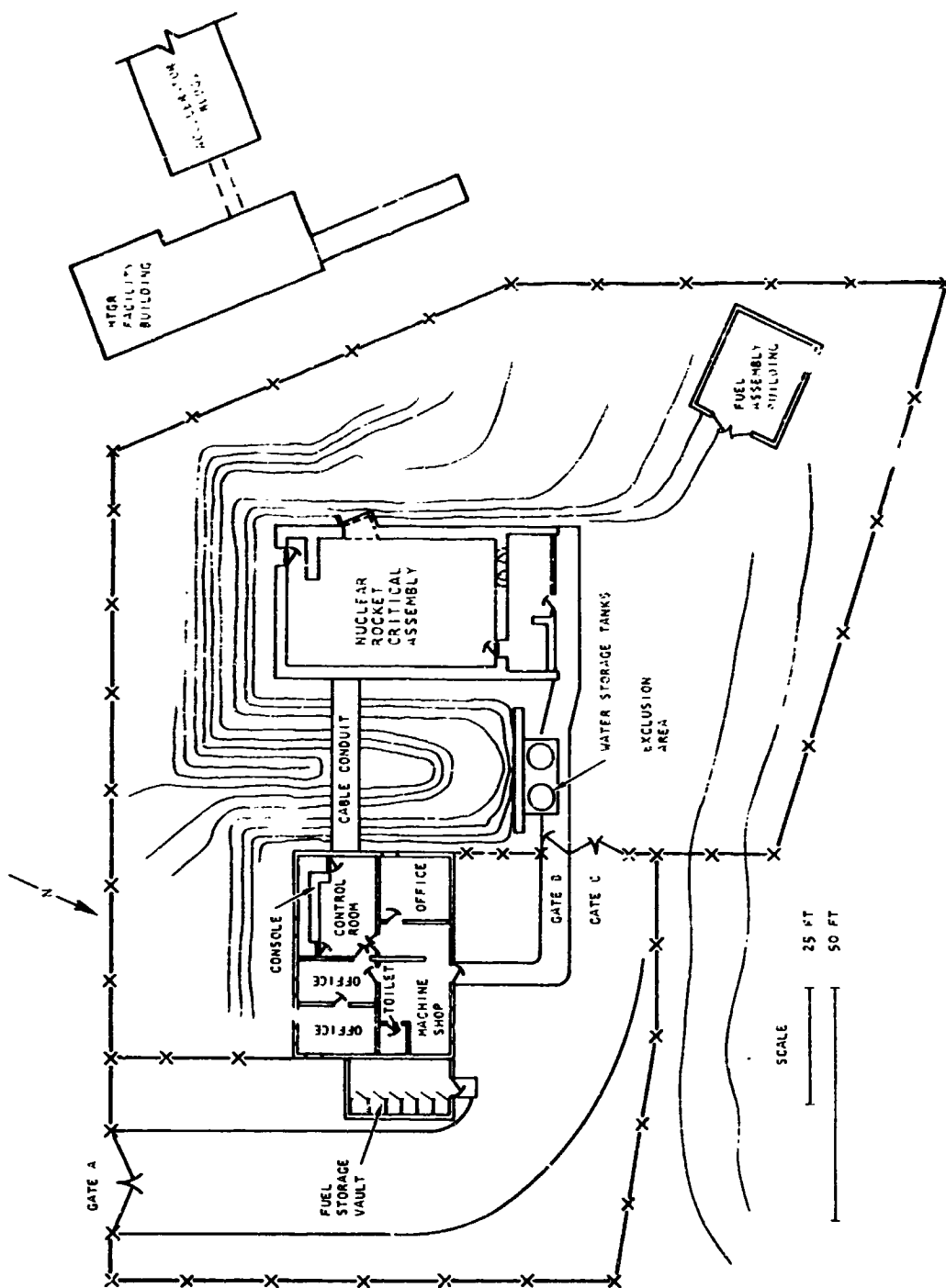


Fig. 2.1--Nuclear rocket critical facility area



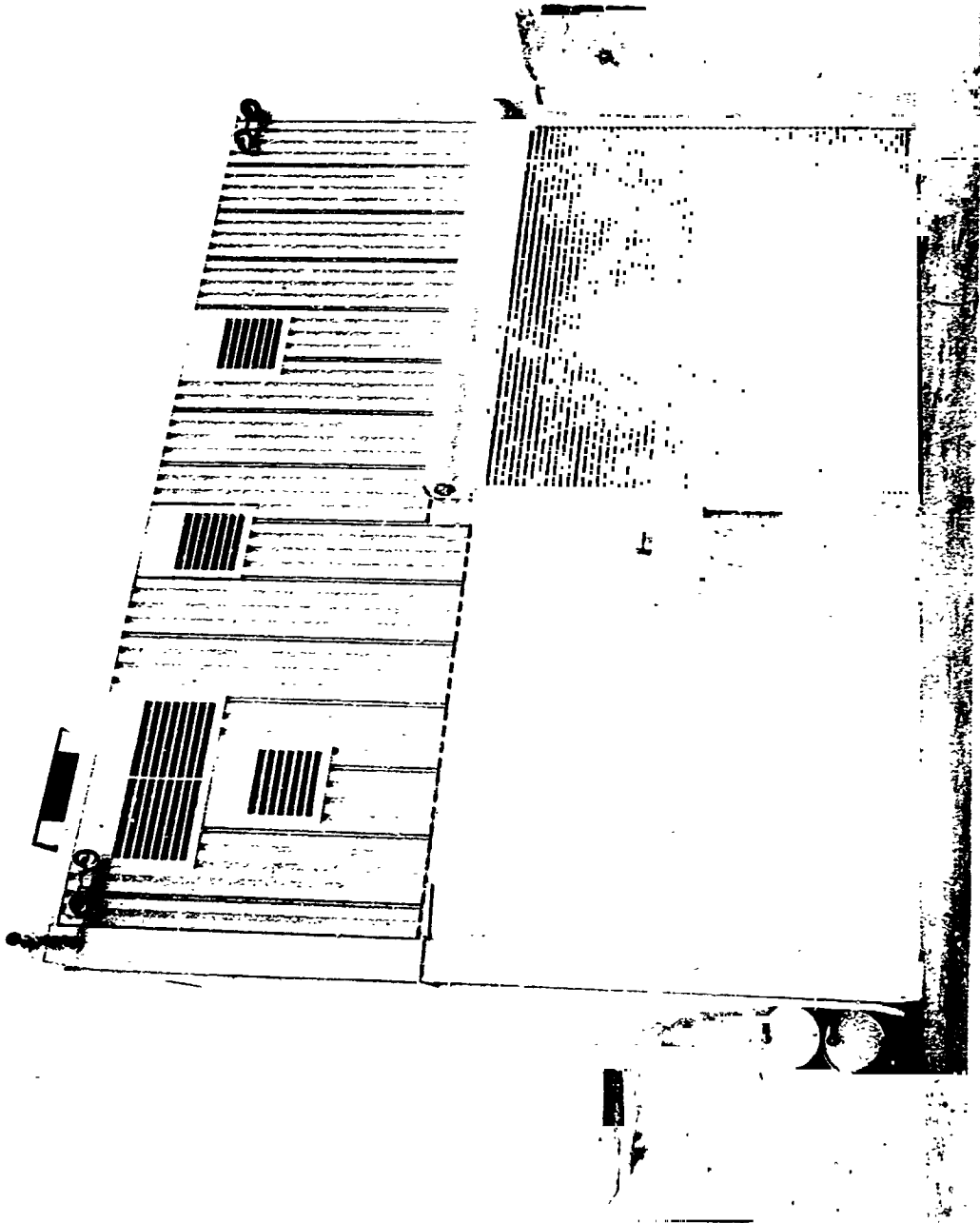


Fig. 2.2--Photograph of critical assembly building



Fig. 2.3--Photograph showing water circulation system

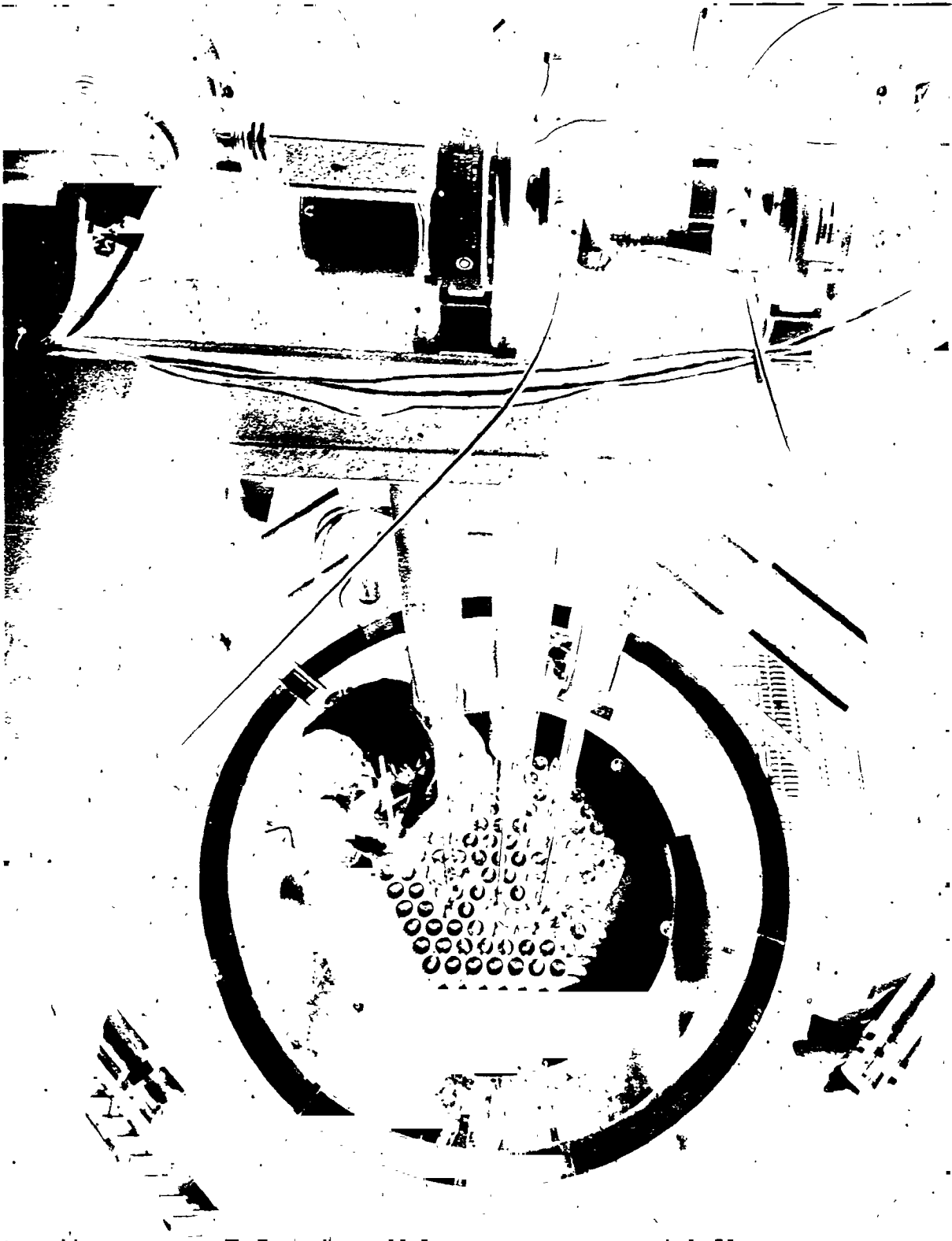


Fig. 2.4--Top view of the reactor tank

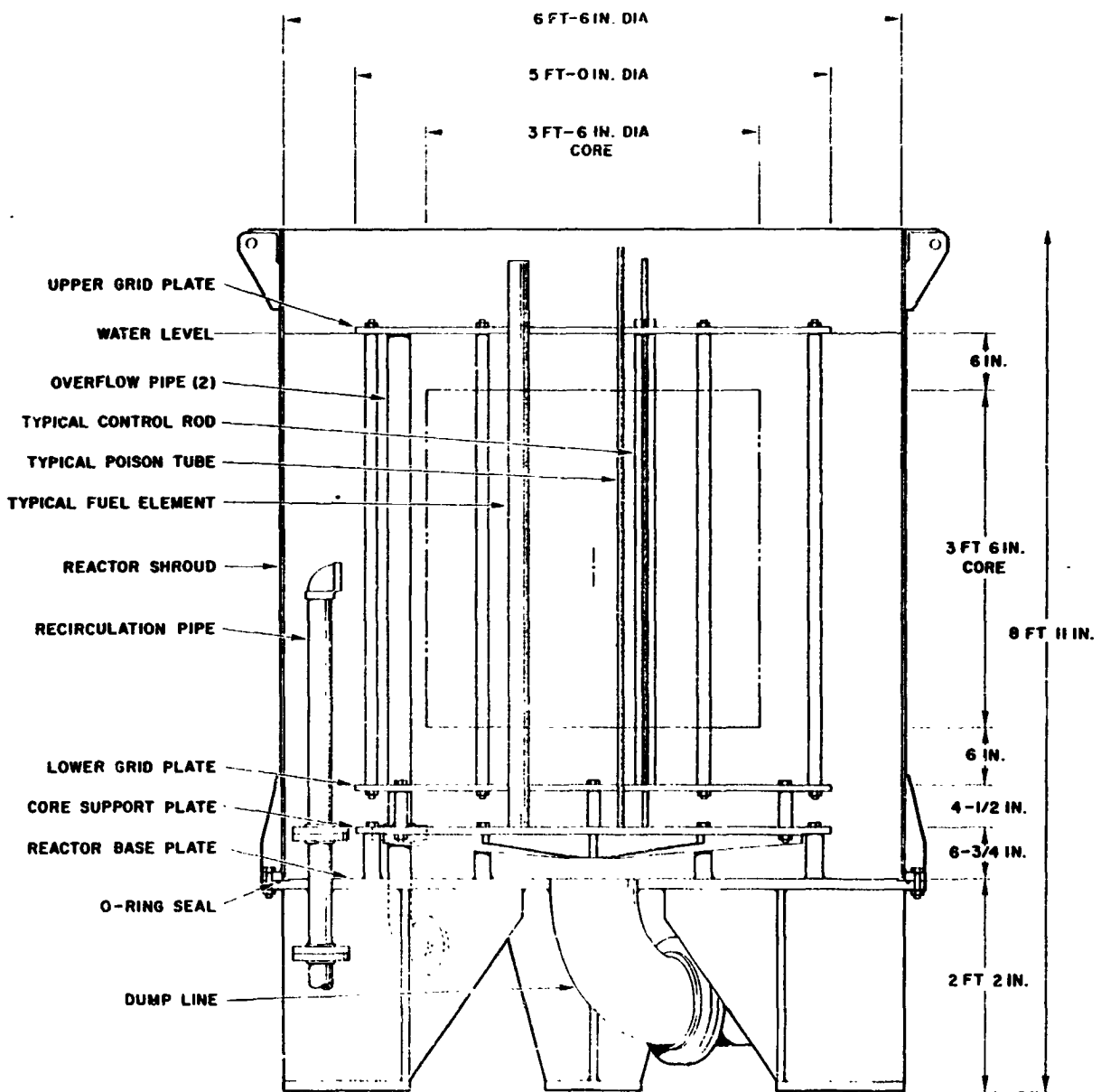


Fig. 2.5--Reactor tank assembly

The cylindrical reactor shroud is bolted to the base plate to form a reactor tank 78-in. in diameter and 82-in. deep. Six standoffs on the base plate are used to mount the aluminum core support plate, which is 3/4-in. thick and five feet in diameter. The top surface is machined to provide a flat surface, to a tolerance of 0.010-in., upon which the fuel elements and poison tubes rest. This is the basic reference plane for the core components.

Fuel element and poison tube positioning is accomplished by using two aluminum grid plates. Figure 2.6 shows the general grid plate layout and the identification system in which upper case letters refer to fuel element positions and lower case letters to poison tube positions. There are 127 fuel element positions and 216 poison tube positions.

The grid plates were made of 1-in. thick stress-relieved aluminum plates (6061T651) five feet in diameter. The plates were precision bored on a horizontal boring mill controlled by a programmed magnetic tape. Table 2.1 gives the hole size tolerances on the grid plates.

Table 2.1

GRID PLATE TOLERANCES

<u>Fuel Element</u>	<u>Poison Tube</u>
2:574 + 0.003 - 0.000	0:572 + 0.003 - 0.000

Hole positions were held to within a 0.002-in. radius of true position.

In assembling the grid plate structure, the core support plate was leveled to within .010-in. The lower grid plate was mounted to the core support plate by use of six 2-in. diameter stainless steel standoffs. The upper grid plate was then mounted on six stainless steel stanchions and positioned axially and azimuthally directly over the lower grid plate

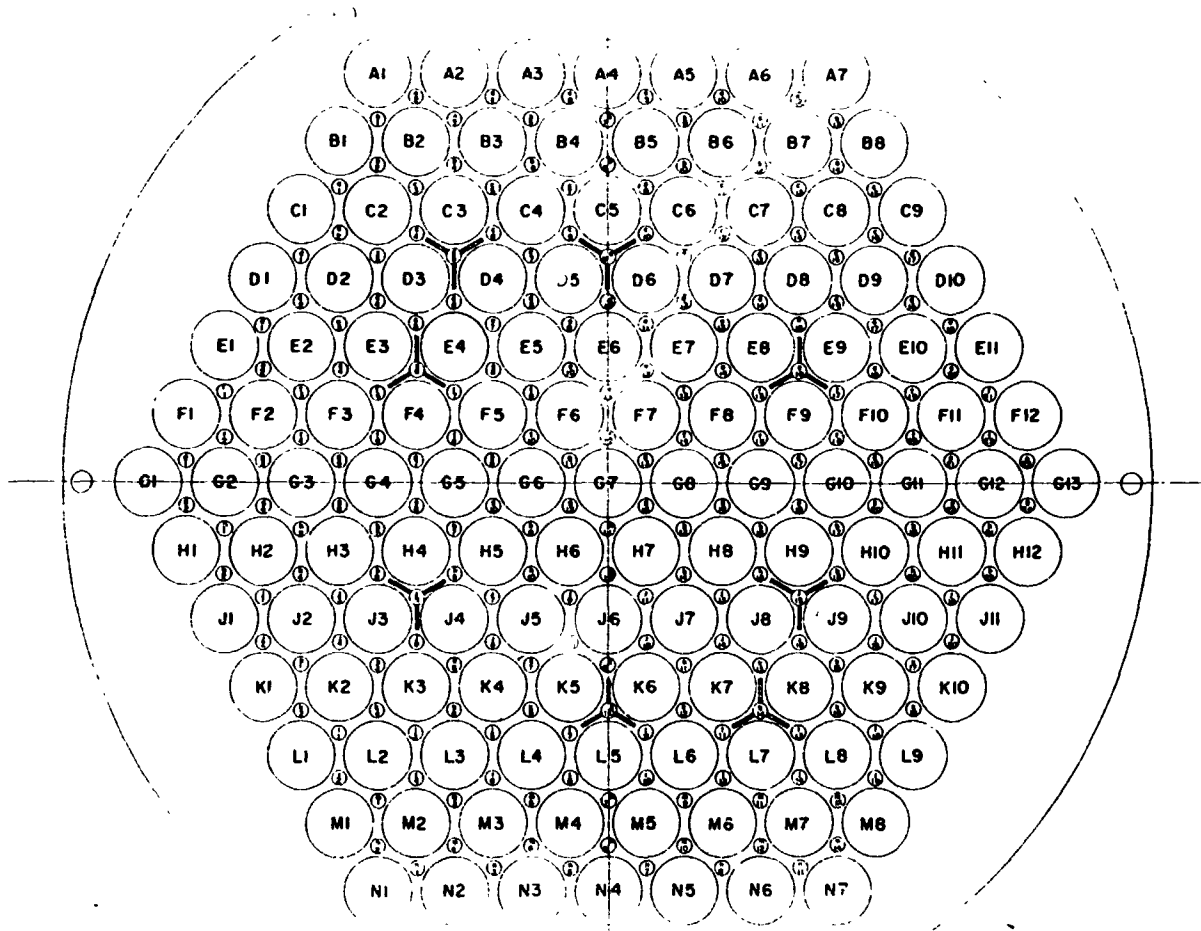


Fig. 2.6--Grid plate layout

by use of optical equipment. The standoffs and the stanchions were heat treated for high strength and were machined to a length tolerance of  $\pm 0.002$  inch. A view of the grid plates is provided in Fig. 2.7.

The core thus consists of an array of fuel elements and poison tubes held vertically at the proper spacing by the grid plates with all removable elements resting on the core support plates.

### 2.2.2 WATER SYSTEM

The critical assembly water system (Fig. 2.8) has the capability of pumping, heating, chilling, filtering, and demineralizing the water in either the dump tank or the reactor tank. A centrifugal pump rated at approximately 150 gallons per minute circulates water in one of several modes. The modes are; (1) Dump Tank Recirculation Mode, in which water is circulated from the dump tank through the heater-chiller and demineralizer system and back to the dump tank, (2) Reactor Tank Recirculation Mode, in which water is pumped from the reactor tank through the heater-chiller and demineralizer system and back into the reactor tank and, (3) Fill Mode, in which water is pumped from the dump tank into the reactor tank at either the 150 gpm rate or at a reduced rate of approximately 10 gpm. The various modes of operation are controlled by spring-loaded pneumatically-operated ball valves which are actuated electrically from the interlock system. The system was designed for fail-safe operation in the event of loss of power.

The height of the water in the reactor tank was recorded with a servo-manometer which is a water manometer with a servo-follower directly coupled to a Veeder-Root counter. The Veeder-Root counter reads out to 0.001-in. The manometer is capable of reproducing to an accuracy of  $\pm 0.001$  inch.

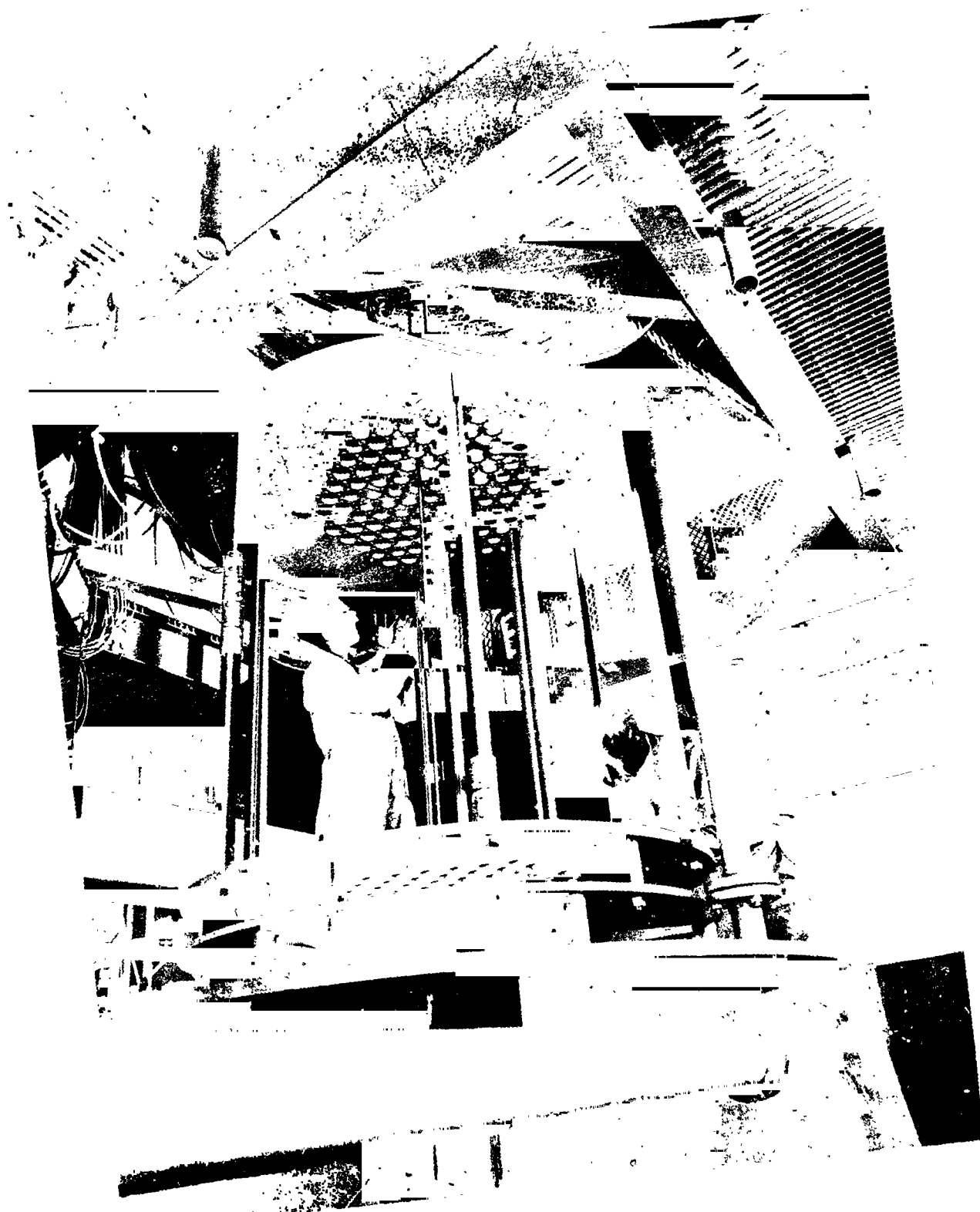


Fig. 2.7--Grid plate installation



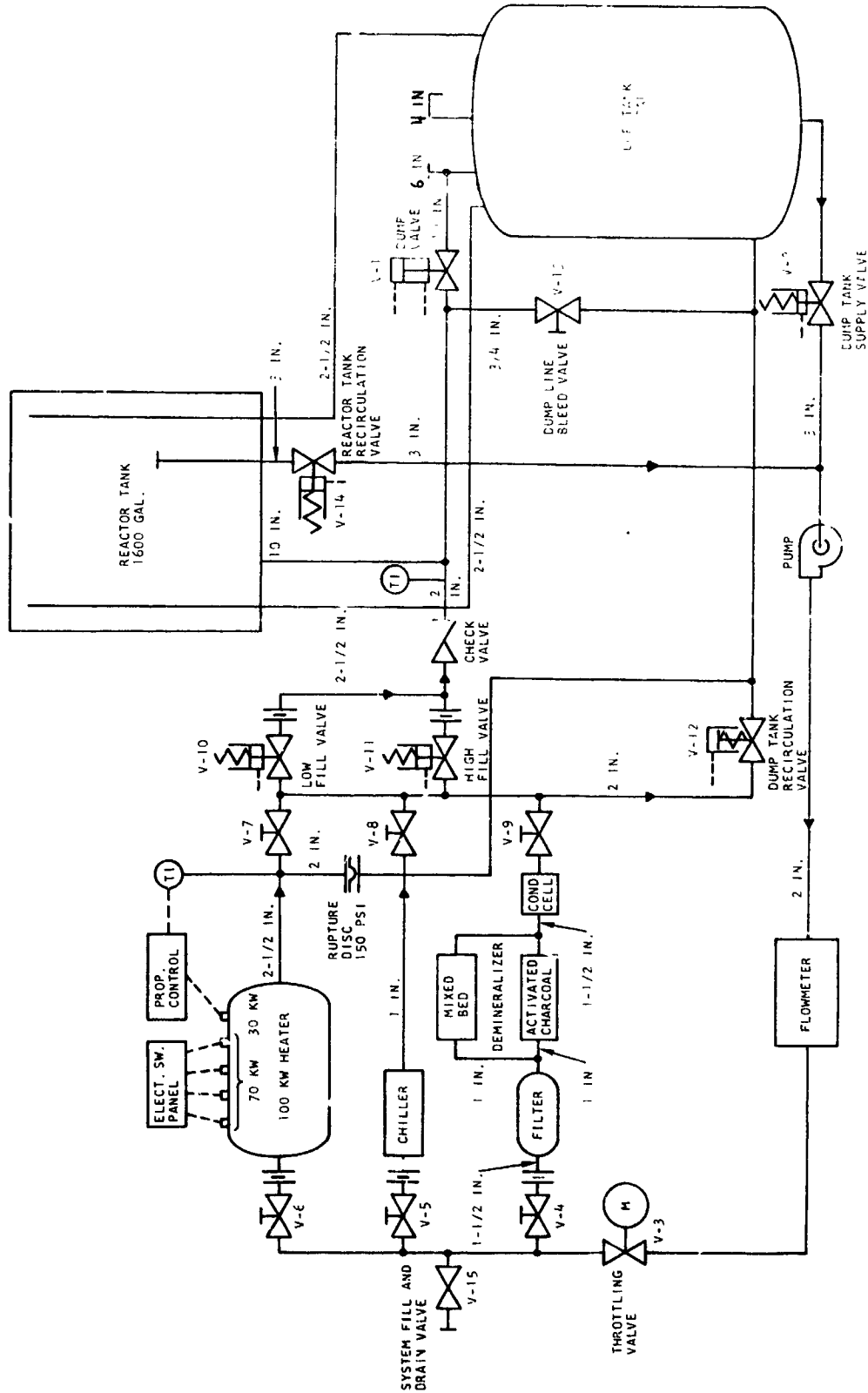


Fig. 2.8--Critical assembly water flow schematic

The water heater is a 100 kVA circulation heater fabricated from stainless steel. It is capable of heating 1800 gallons of water at a rate of approximately  $10^{\circ}\text{C}$  per hour. As the temperature of the water approaches the desired operating temperature about two-thirds of the heating elements are cut out from the circuit and the remaining third are operated from a saturable reactor type proportional control system. This system maintains the water temperature constant to within  $\pm 0.10^{\circ}\text{C}$  over a range from room temperature to  $80^{\circ}\text{C}$ .

### 2.2.3 CONTROL CONSOLE

The Critical Assembly is remotely operated from the control console shown in Fig. 2.9. This control system displays the nuclear instrumentation readings, the control rod positions, water height and fill rates, and the condition of the interlock logic.

### 2.2.4 CONTROL RODS

There are eight vertically-acting control rods, of which six are scrammable, gravity-fall safety rods. The shape of the blade (Fig. 2.10) permits its insertion in the tricuspid space formed by three adjacent fuel elements. The rods are guided by a stainless-steel rod tensioned between the core support plate and the overhead steel framework.

The upper end of the safety rod is fitted with a piston and magnet armature (Fig. 2.11). The piston arrests the fall of the rod at the end of the cylinder. The safety rods are withdrawn and held cocked by means of cylindrical electromagnets riding with ball bushings on the tensioned guide rod. Each electromagnet is raised and lowered by a two-phase, positive reversing motor and teleflex drive unit illustrated in Fig. 2.11. "Teleflex" is the trade name used for a commercially produced stainless steel cable that is helically wound such that it can be driven with a precision machined drive gear. The system thus acts as a flexible rack and pinion.

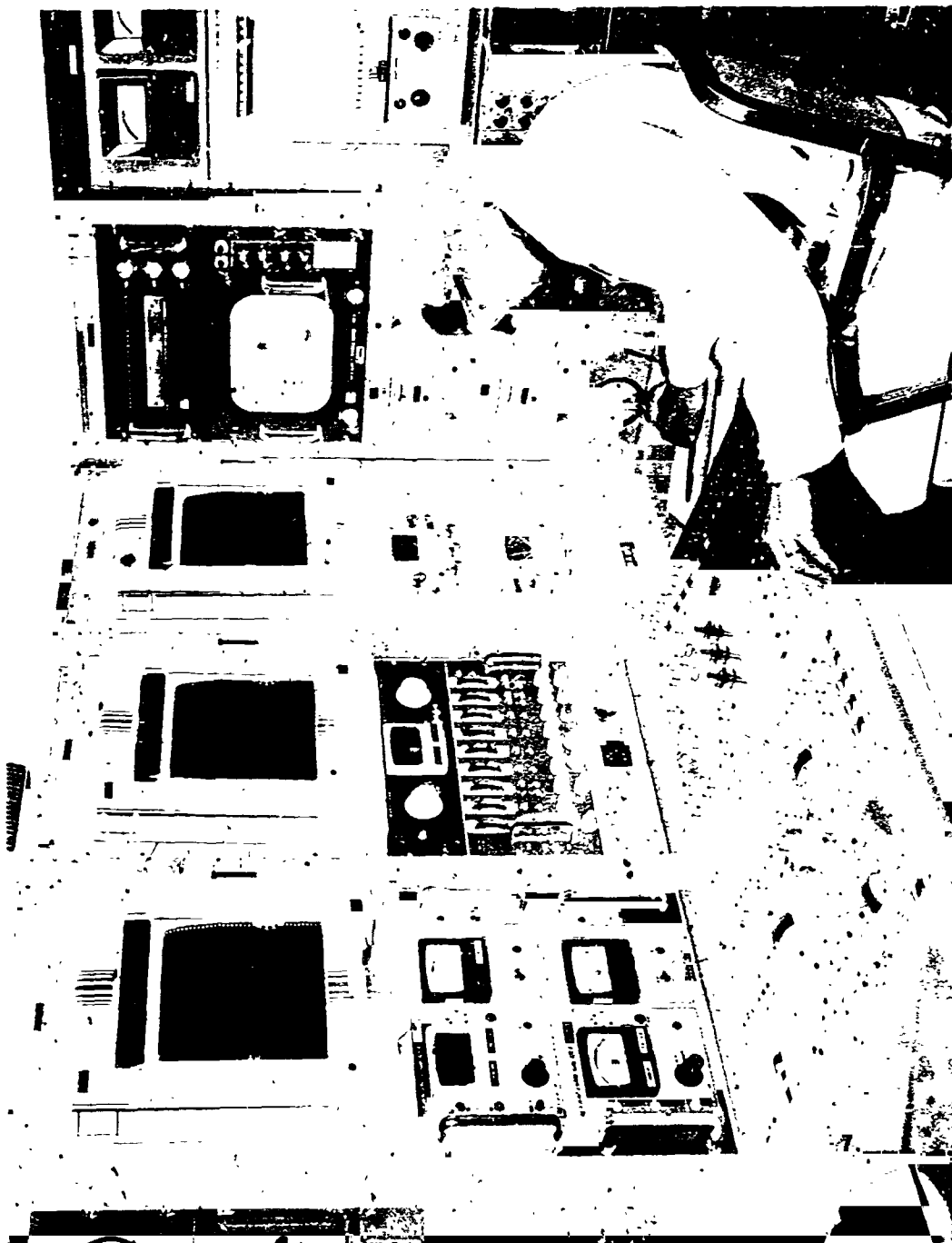


Fig. 2.9--Control console

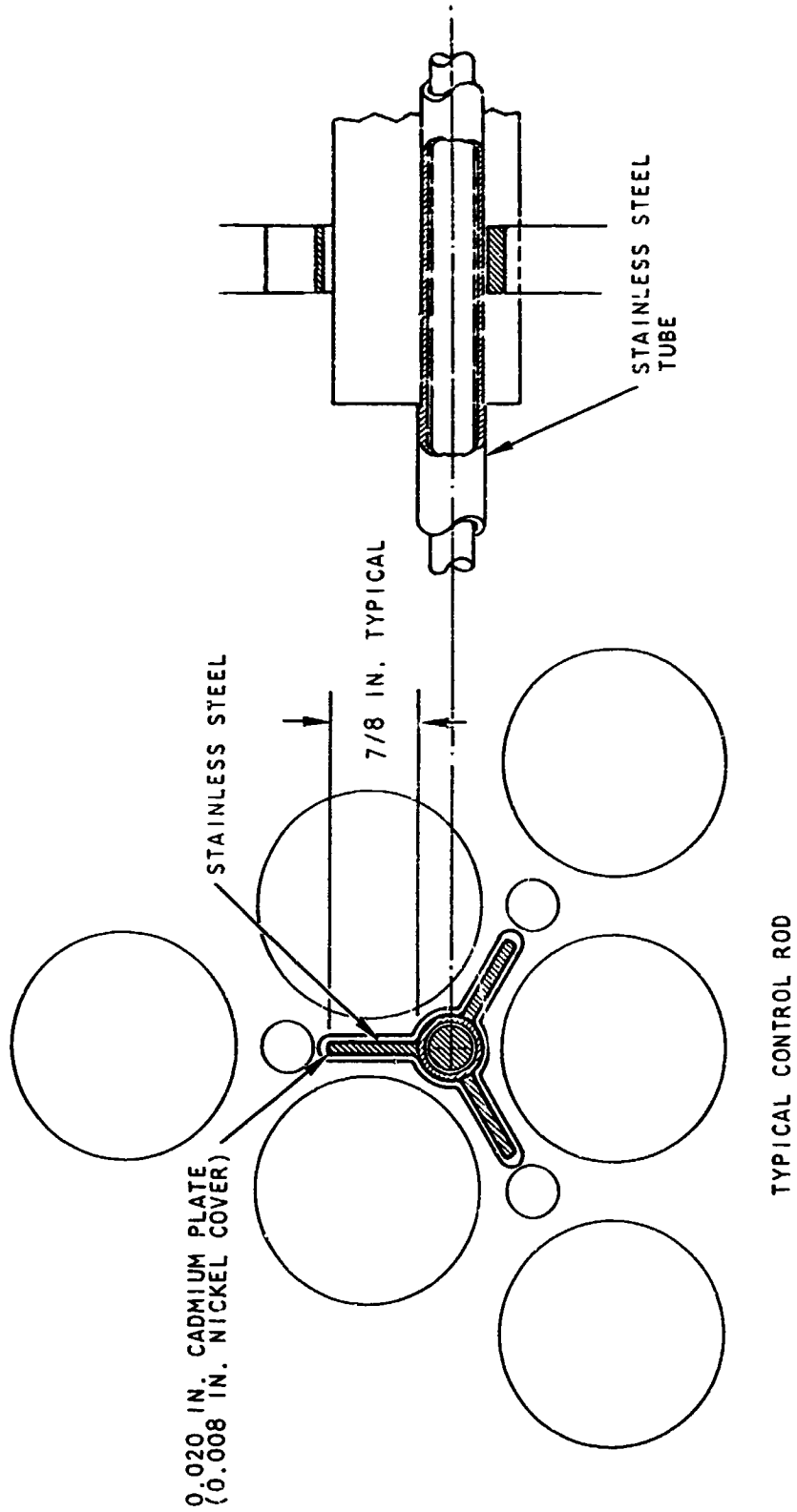


Fig. 2.10--Control rod blade

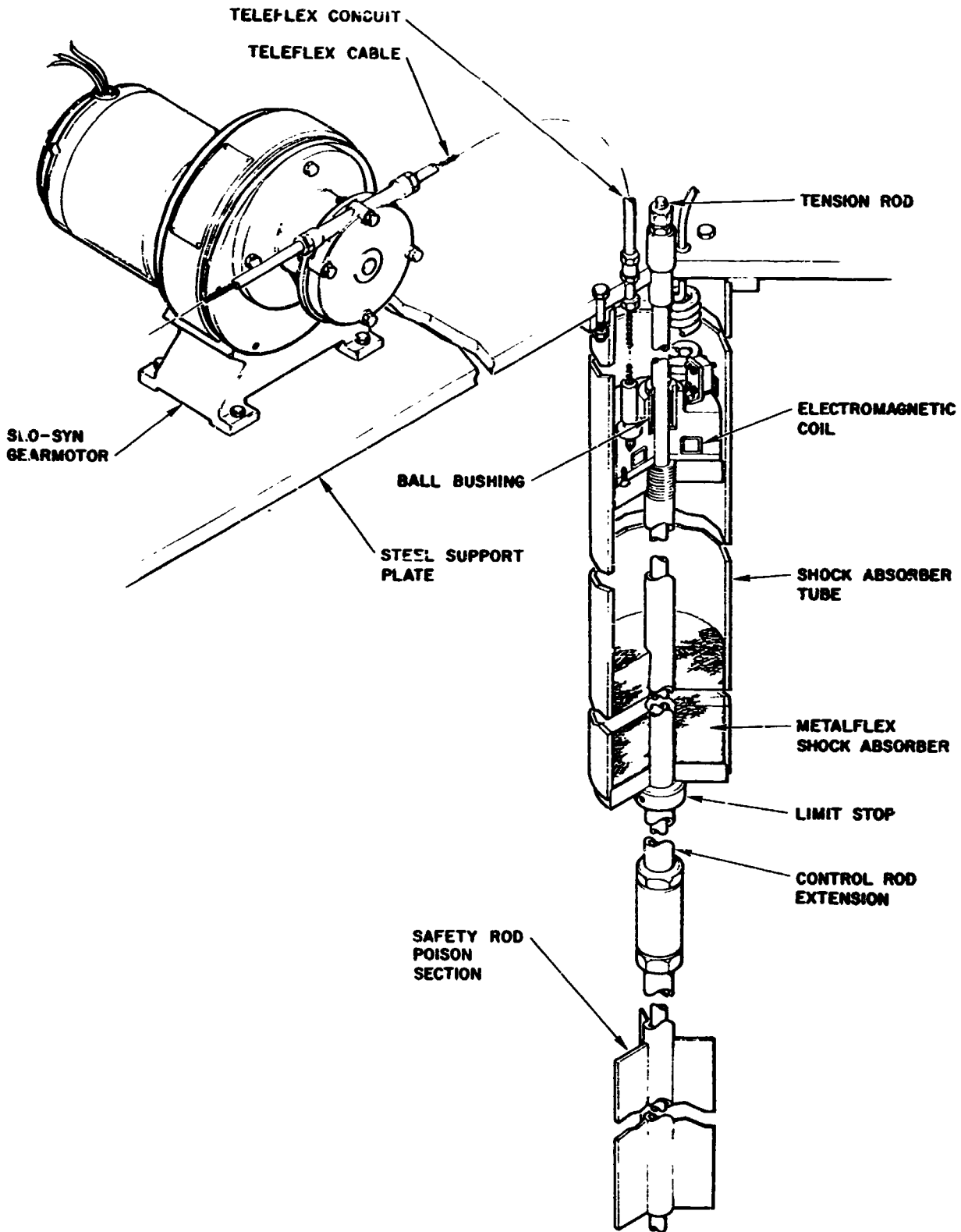


Fig. 2.11--Safety rod assembly

The instant starting and positive reversing motors used to drive the safety rods are 100-pole synchronous type with the speed determined by the line frequency (60 cycles). This ensures that the motors will not operate beyond their inherent speed of 72 RPM. The speed is reduced from 72 to 6 RPM using a 12 to 1 gear reducer. The gear reducer is coupled to the teleflex drive unit which gives a rod withdrawal rate of approximately 0.8-in. per second.

#### 2.2.5 REGULATING RODS

Two of the eight control rods are used as regulating rods (Fig. 2.12). They have synchro-motor transmitters connected directly to the rod drive units. These transmitters are connected to synchro-motor receivers in the control room and drive Veeder Root counters which monitor the regulating rod position. These rods are also provided with rod-full-in and rod-full-out limit switches. The regulating rod drive motors can be operated from a dc stepping circuit to be "stepped" from pole to pole. By using the stepping switch, the regulating rods can be raised or lowered in increments of 0.013-in. per step.

#### 2.2.6 INSTRUMENTATION

The nuclear instrumentation (Fig. 2.13) consists of two log N-Period ion chamber channels, two linear photomultiplier channels, one linear ion chamber channel, two  $\text{BF}_3$  proportional count rate meter channels, and three fission counter channels. The three fission counters are connected to linear pulse amplifiers and the discriminated outputs of these amplifiers are counted with three automatically programmed scalers and printers. These channels were used for core multiplication and period measurements.

The remaining nuclear instrumentation channels were used as safety circuits. The output signals from each channel (7-level and 2-period) were

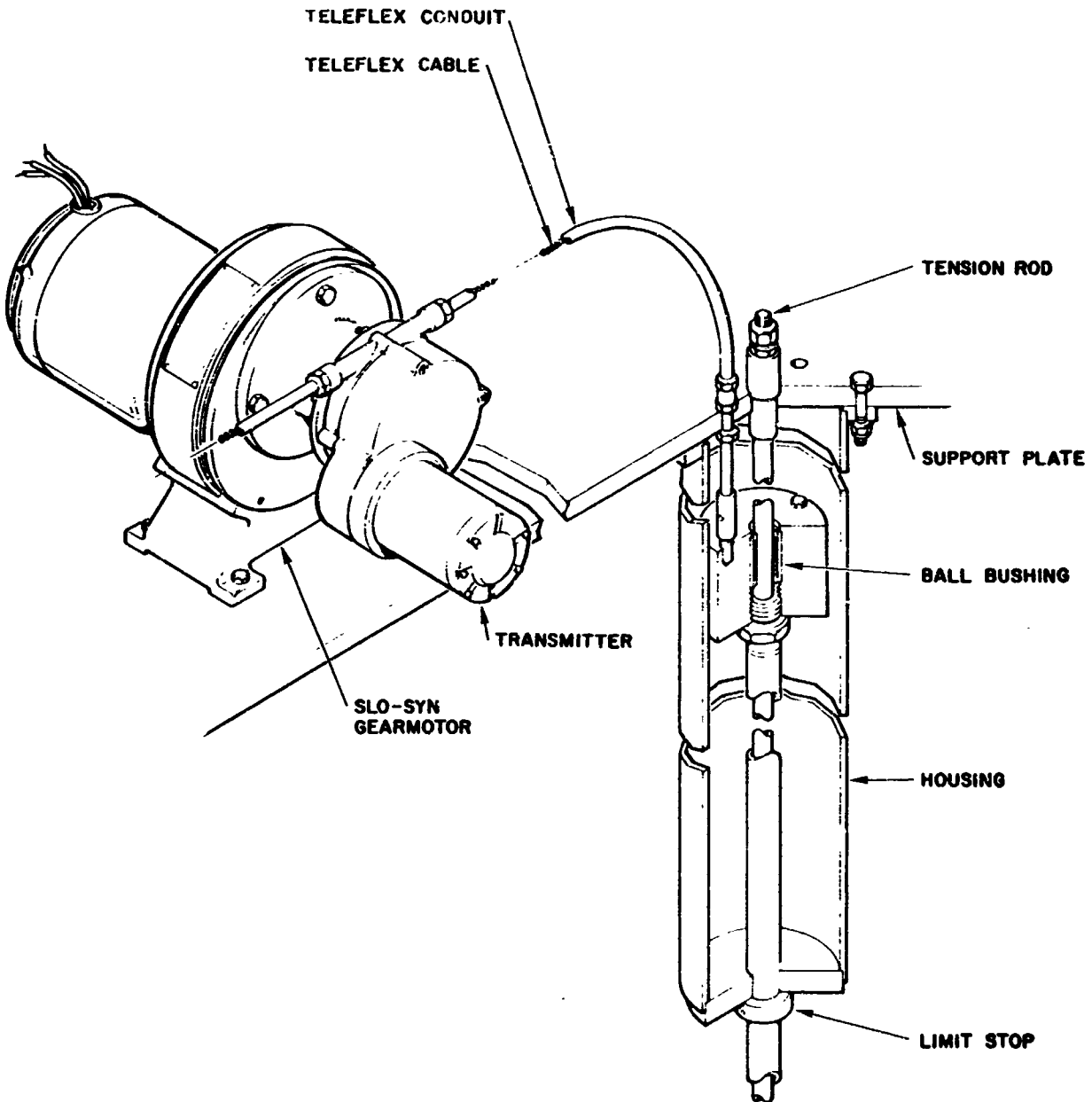


Fig. 2.12--Regulating rod

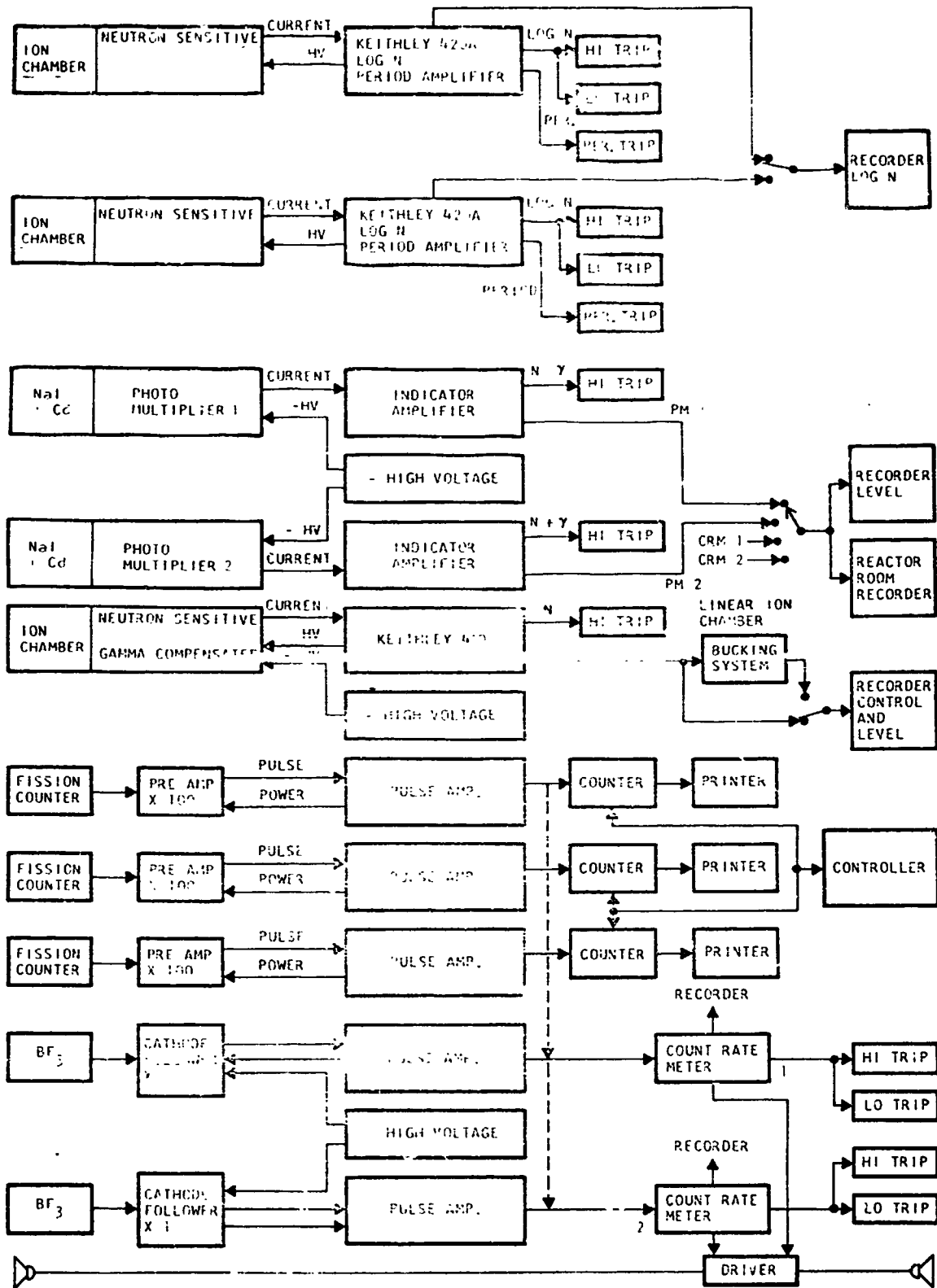


Fig. 2.13--Nuclear instrumentation



used to drive a fast solid state comparator (Fig. 2.14). The comparator circuitry was designed and built at General Atomic and proved to be highly reliable with respect to speed, stability, sensitivity, and ease of adjustment. A scram signal on any one of the channels (Fig. 2.15) drops the safety rods and opens the dump valve. Special provisions for by-passing channels and for other safety features are discussed in the Hazards Report<sup>(1)</sup> and the Technical Specifications for the facility.<sup>(2)</sup>

### 2.2.7 NEUTRON SOURCE

A polonium-beryllium source is used for startup. Its position is logically interlocked with the enabling power for control rods so that no rod withdrawal or water fill may be initiated unless the source is in the reactor assembly. After achieving criticality the source is withdrawn from the core by a synchronous motor-teleflex drive system and stored in a stainless steel drum filled with borated water.

### 2.2.8 POISON TUBES

The core excess reactivity was adjusted to the desired level with cadmium nitrate solution contained in nickel-plated aluminum tubes. The tubes were sealed at the ends with a double seal. One seal was a standard O-ring and the other a tight mechanical seal formed by magnetically swaging the tube over the end plug. Fig. 2.16 shows the poison tube dimensions. The primary purpose of the nickel plating was to prevent the formation of aluminum hydroxide which could cause some of the cadmium nitrate to precipitate. Filling of all of the poison tubes to the same level was accomplished by first filling to slightly beyond the desired level and then drawing off the excess.

Various concentrations of cadmium nitrate were used during the experimental program ranging from 0.0 to 0.5 mole/liter. Table 2.2 is a summary of the concentrations used.



Fig. 2.14.--Fast solid state comparator

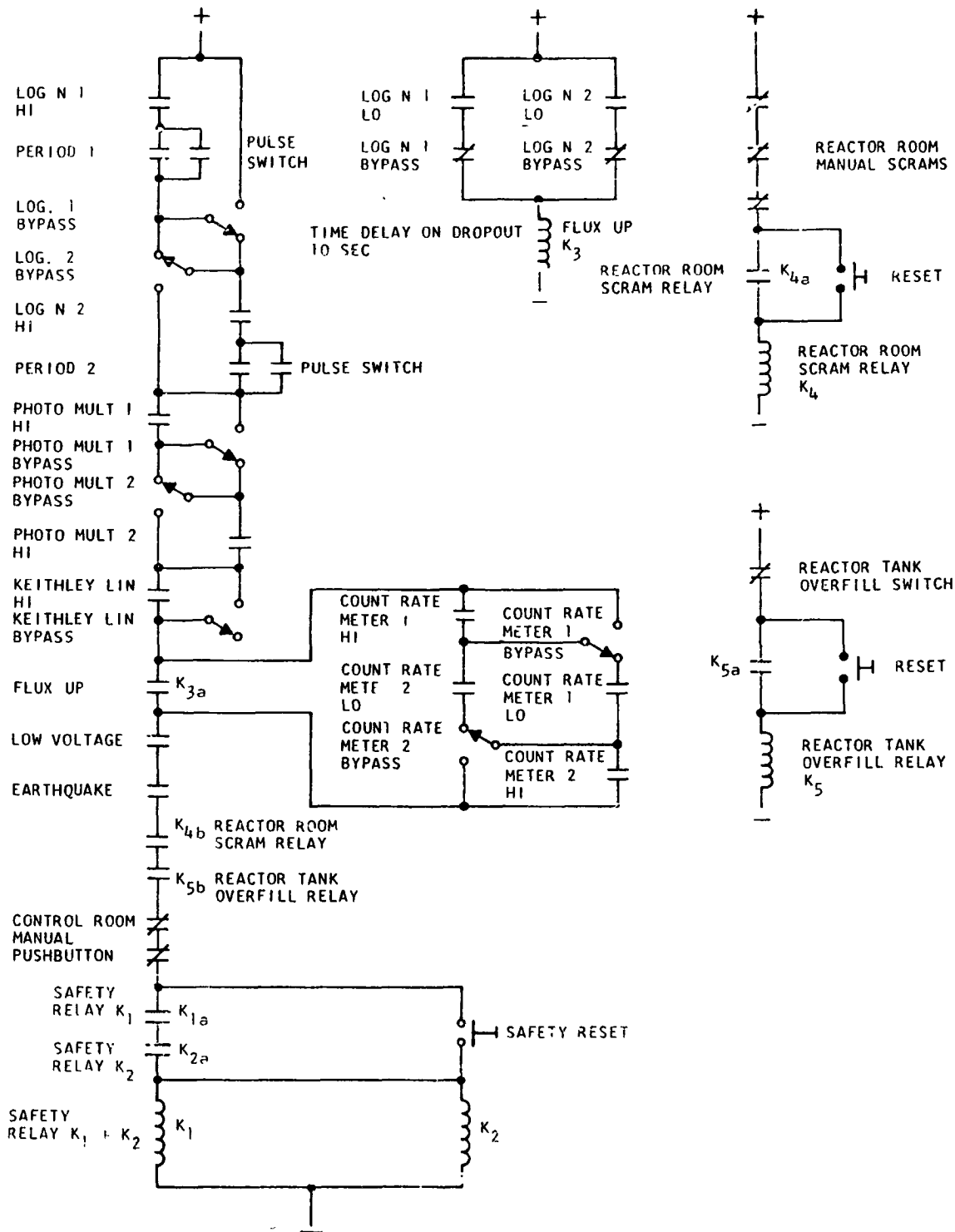


Fig. 2. 15--Critical assembly scram system

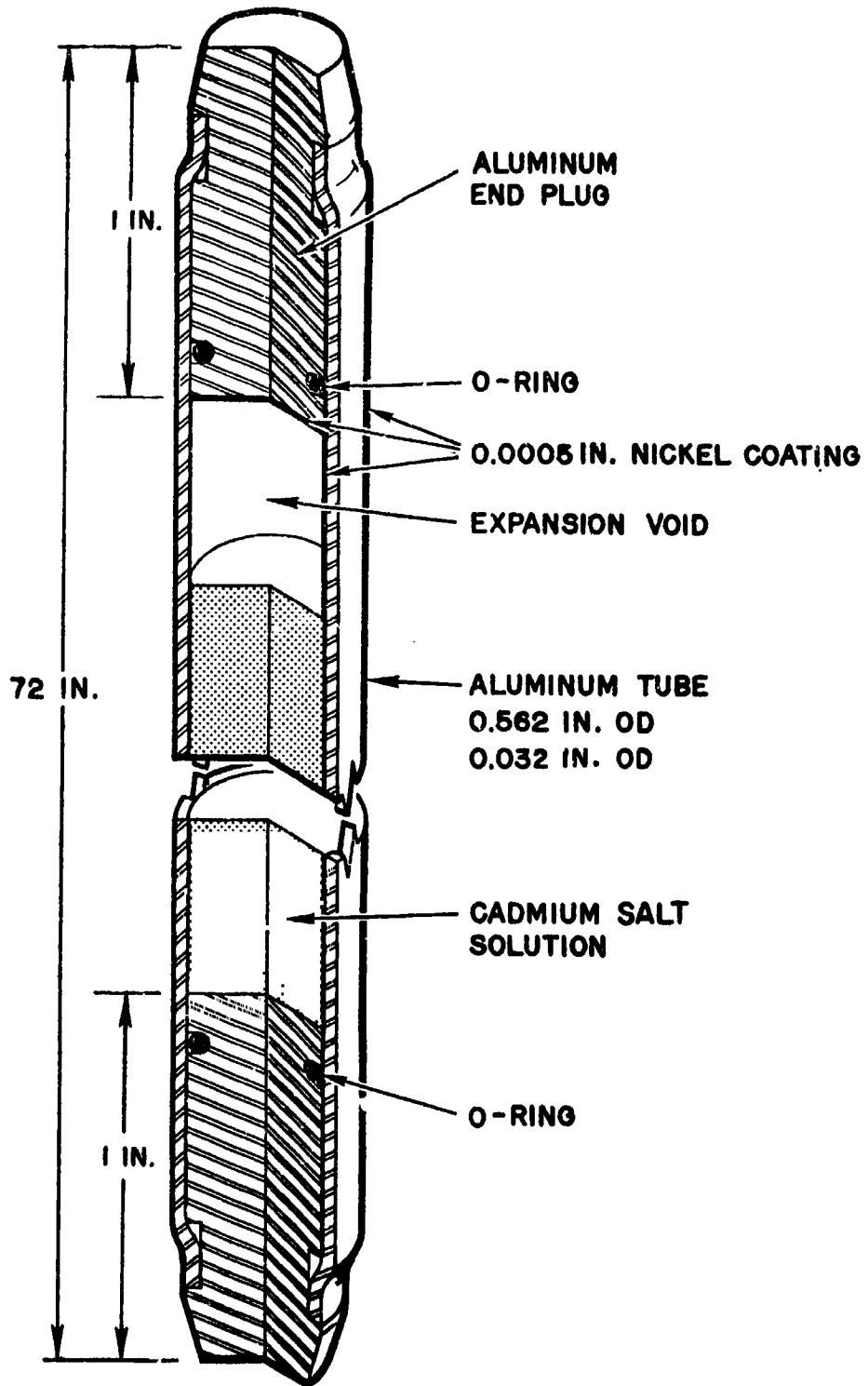


Fig. 2. 16--Poison tube

Table 2.2  
POISON CONCENTRATIONS AND CODINGS

<u>Type</u>	<u>Color Code</u>	<u>(Moles Cd/liter)</u>	<u>Remarks</u>
A	Red	0.09557	
B	Green	0.1108	
C	Blue	0.1255	Core I Final Concentration
D	Black	0.1677	
E	Yellow	0.2899	
F	*	0.0312	
G	*	0.0623	
H	Orange	0.04309	Core II Final Concentration
---	*	0.2500	
---	*	0.5000	
---	Black Band	0.0000	Water Tubes
J	White	0.2120	
K	Copper	0.2202	Core III Final Concentration
L	Gray	0.4045	

\*Marked on individual poison tubes

A precise knowledge of the concentration of the cadmium nitrate solution is important, and preparation and analysis of the solutions were done with great care. Each solution was prepared by appropriate dilution of a prescribed quantity of 1.00 molar cadmium nitrate stock solution. After preparing the required amount of solution in a 50-liter polyethylene container, samples were drawn off and analyzed using the following two methods: (1) electrodeposition as cadmium metal and (2) gravimetrically as cadmium sulfate.

The electrodeposition method is based on the electroplating of the cadmium from a small known amount of the solution on a platinum electrode of known weight. The amount of cadmium deposited is then determined by reweighing the electrode. This method can determine the concentration to within about  $\pm 0.1\%$ .

Using the gravimetric procedure, 10 to 20 ml of the cadmium nitrate solution was put in each of four porcelain crucibles that had previously been ignited and weighed. Concentrated sulfuric acid was added to each crucible and the solutions were evaporated to dryness. The samples were then ignited at  $700-800^{\circ}\text{C}$  for several hours, cooled, and weighed. This method is capable of determining the cadmium concentration to about  $\pm 0.1\%$ . If the results of the two techniques did not agree to within  $0.2\%$ , the entire procedure was repeated.

#### 2.2.9 FUEL ELEMENTS

The fuel element assembly and subassembly are shown in Figs. 2.17 and 2.18. The subassembly consists of 24 stages each containing five concentric rings of uranium-aluminum alloy and one ring of depleted uranium. These rings are lined with natural tungsten and are positioned on thin-wall aluminum tubing. The fuel rings contain approximately 35 wt % metallic uranium, which is 93.15% enriched. The rings are

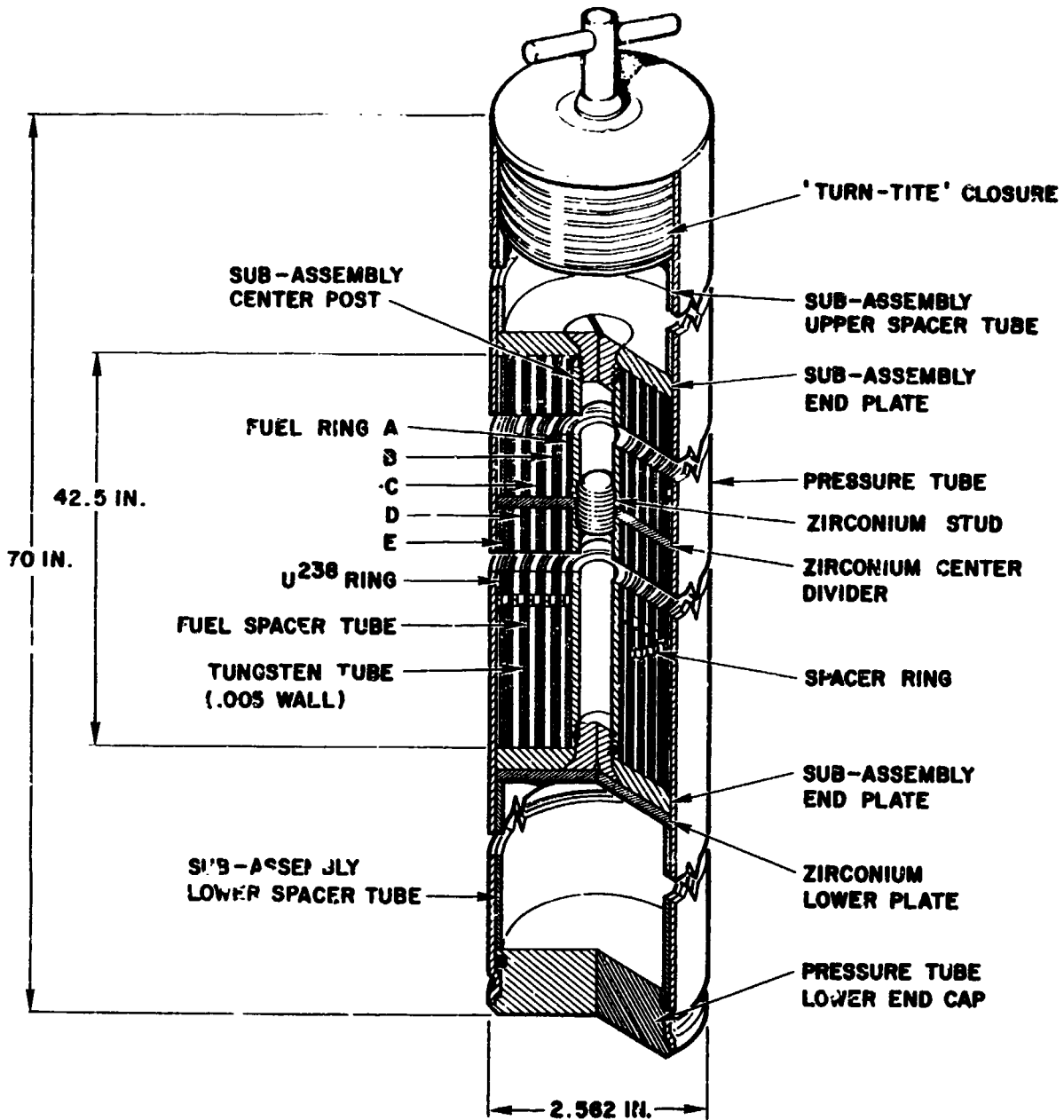


Fig. 2. 17--Fuel element



Fig. 2.18--Fuel element subassembly



0.042-in. thick and 1-5/8-in. high. The stages are separated axially by 1/8-in. corrugated aluminum spacer rings. These spacer rings also position the fuel radially.

A total of 15,000 fuel rings were fabricated at General Atomic by shearing an existing supply of uranium aluminum alloy fuel foils into proper lengths and then forming them into right circular cylinders with a precision die in a crank press (Figs. 2.19 and 2.20).

Each fuel ring is lined on the inside with 0.005-in. of natural tungsten. The outermost ring of the subassembly is 0.040-in. thick depleted uranium and is lined on the inside with an 0.003-in. ring of natural tungsten.

A zirconium divider and a stud between the 12th and 13th stages are required for safety. They prevent the accumulation at the bottom of the core of melted fuel from the upper stages in the event of the Maximum Credible Accident.

Since the fuel and tungsten rings were not of uniform thickness they were weighed and grouped by weights. The fuel elements were assembled by selecting components from the weight groups in an order that tended to preserve the average value in a given fuel element. Figure 2.21 shows the weight distributions among elements. All of the tungsten is within  $\pm 1\%$  of the average element and approximately 95% of the  $U^{235}$  is within  $\pm 1\%$  of the average element weight.

The depleted uranium rings have an i.d. of  $2.137 \pm 0.005$ -in. and a wall thickness of 0.040-in. They contain  $0.22 \pm 0.02$  wt % of  $U^{235}$  and are plated with 0.0003-in. of nickel to prevent oxidation. Each ring has an average weight of 137.26 grams, comprised of 135.98 grams of  $U^{238}$ , 0.30 grams of  $U^{235}$  and 0.98 grams of nickel.

A 121-element core contains 95.82 kg. of  $U^{235}$  and 191.31 kg. of tungsten.

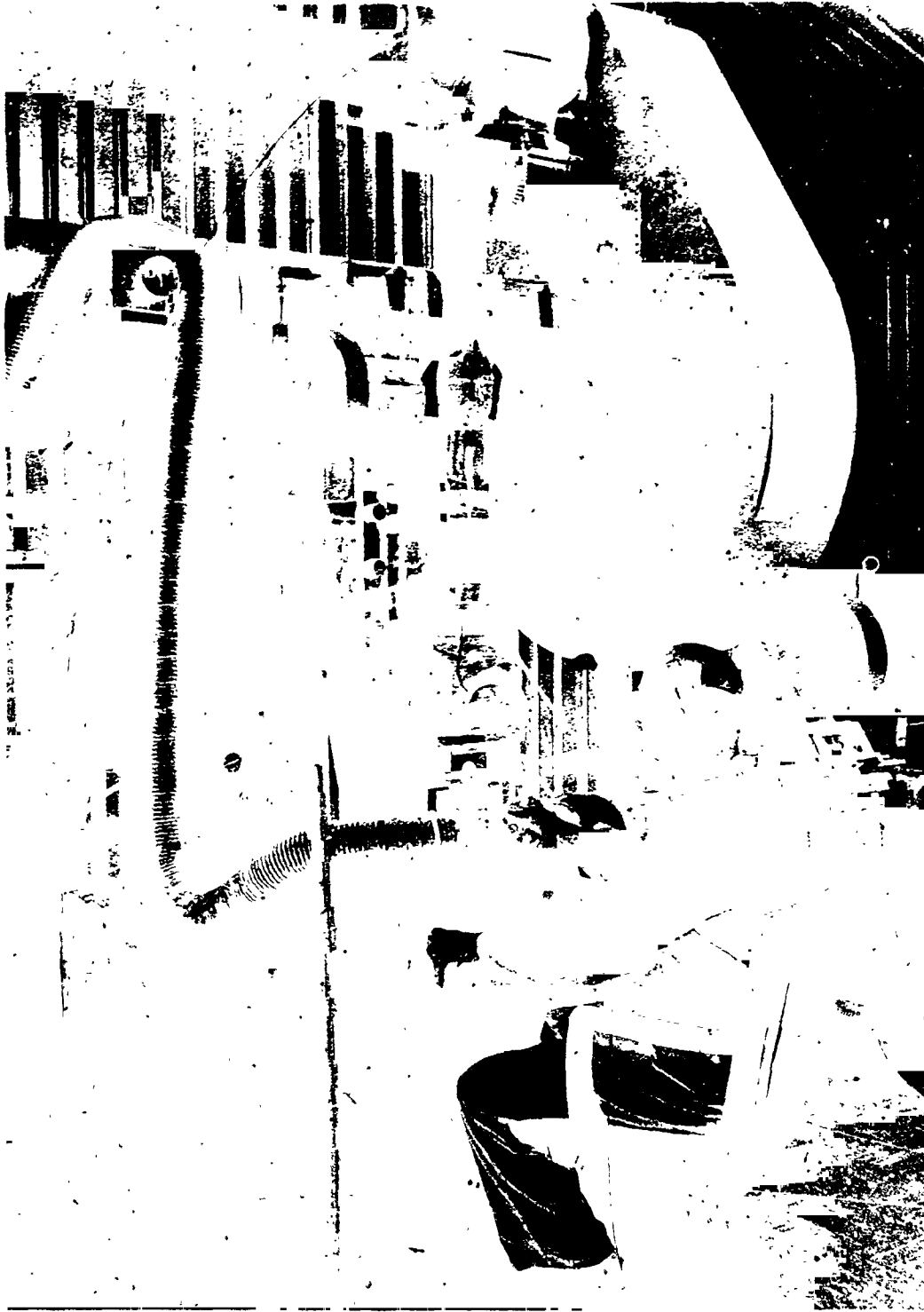


Fig. 2. 19--Fuel forming press



Fig. 2.20--Fuel forming lie

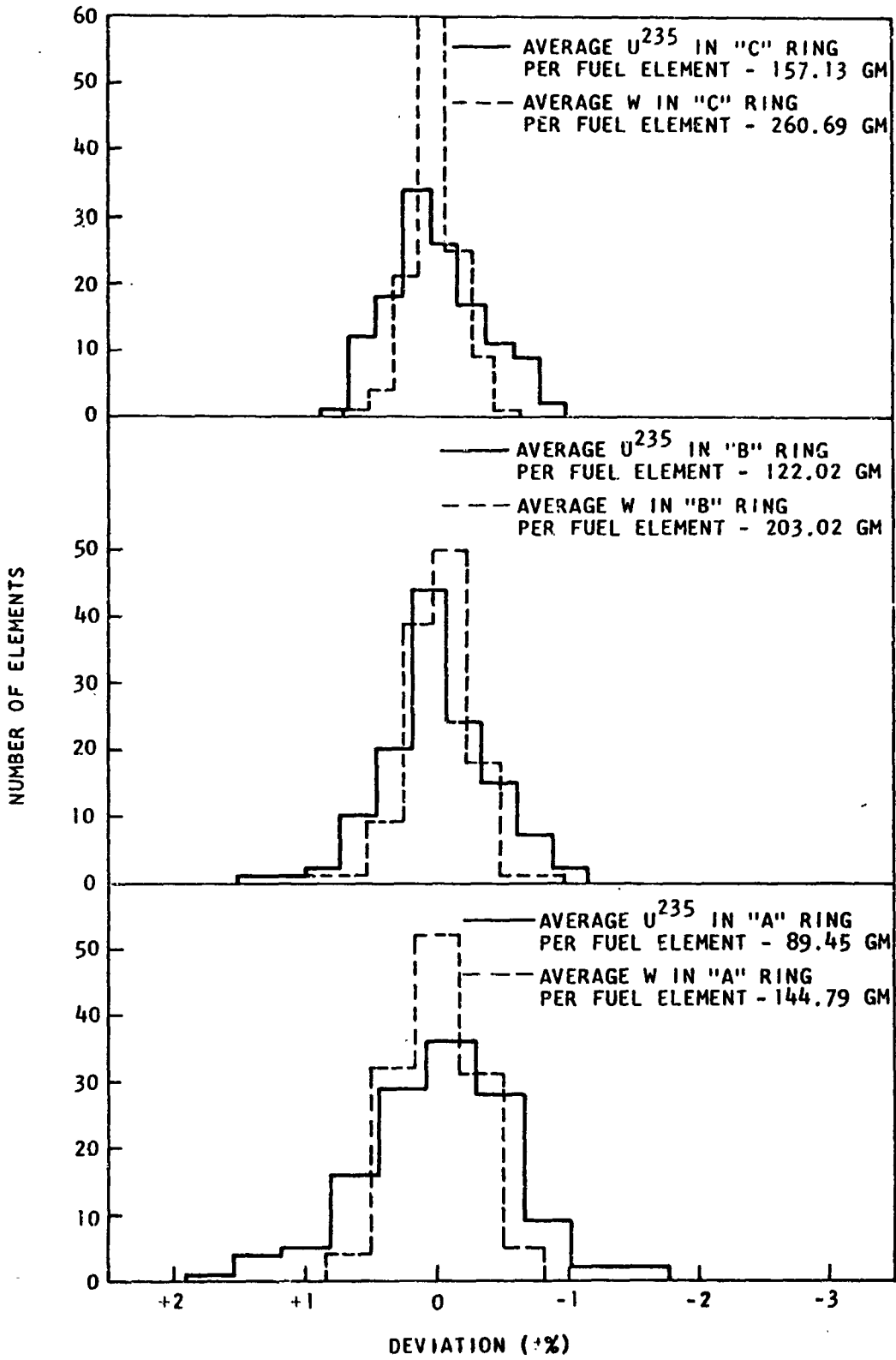


Fig. 2.21--Fuel and tungsten distribution among fuel elements  
(Sheet 1 of 3)

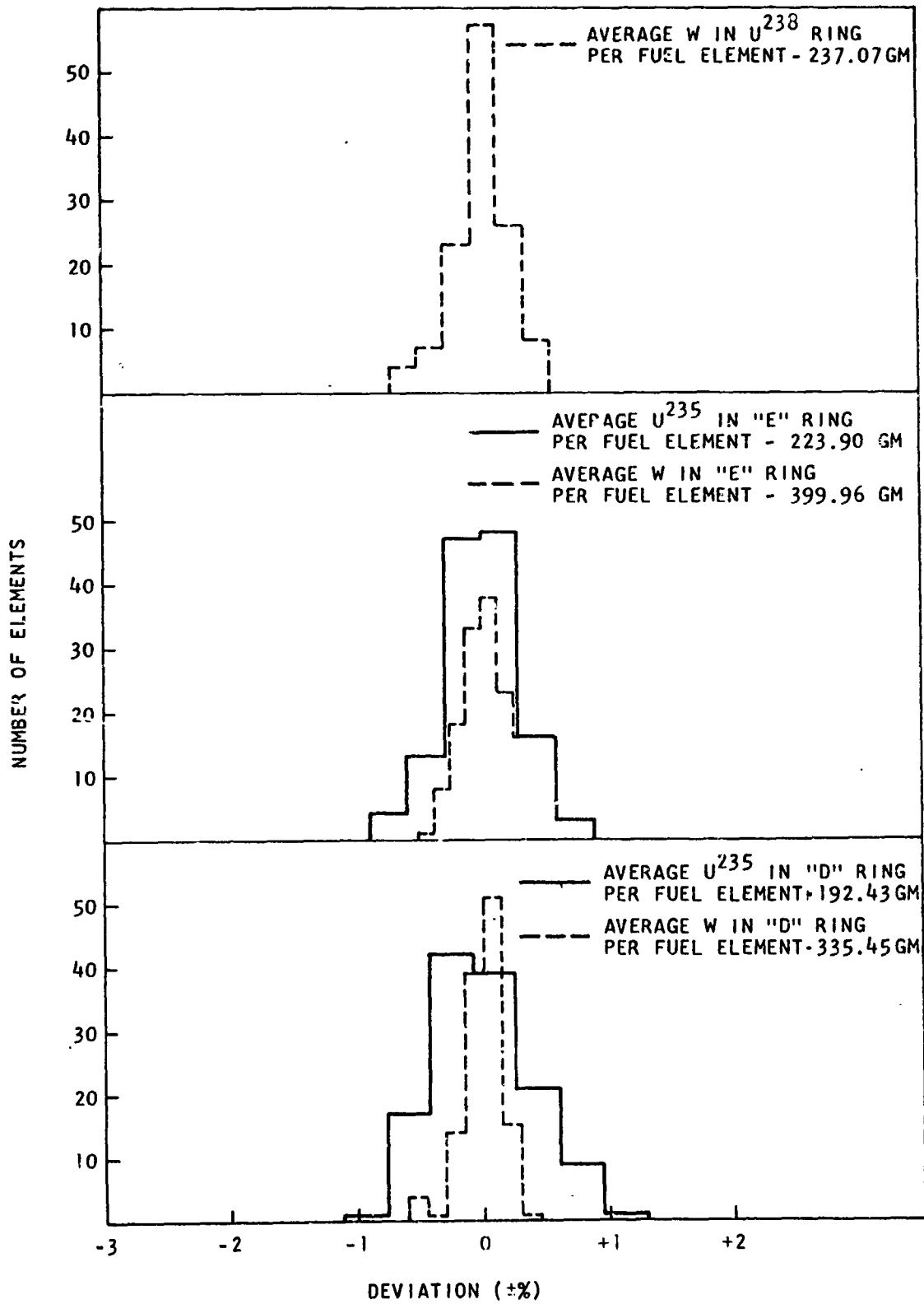


Fig. 2.21--Fuel and tungsten distribution among fuel elements  
(Sheet 2 of 3)

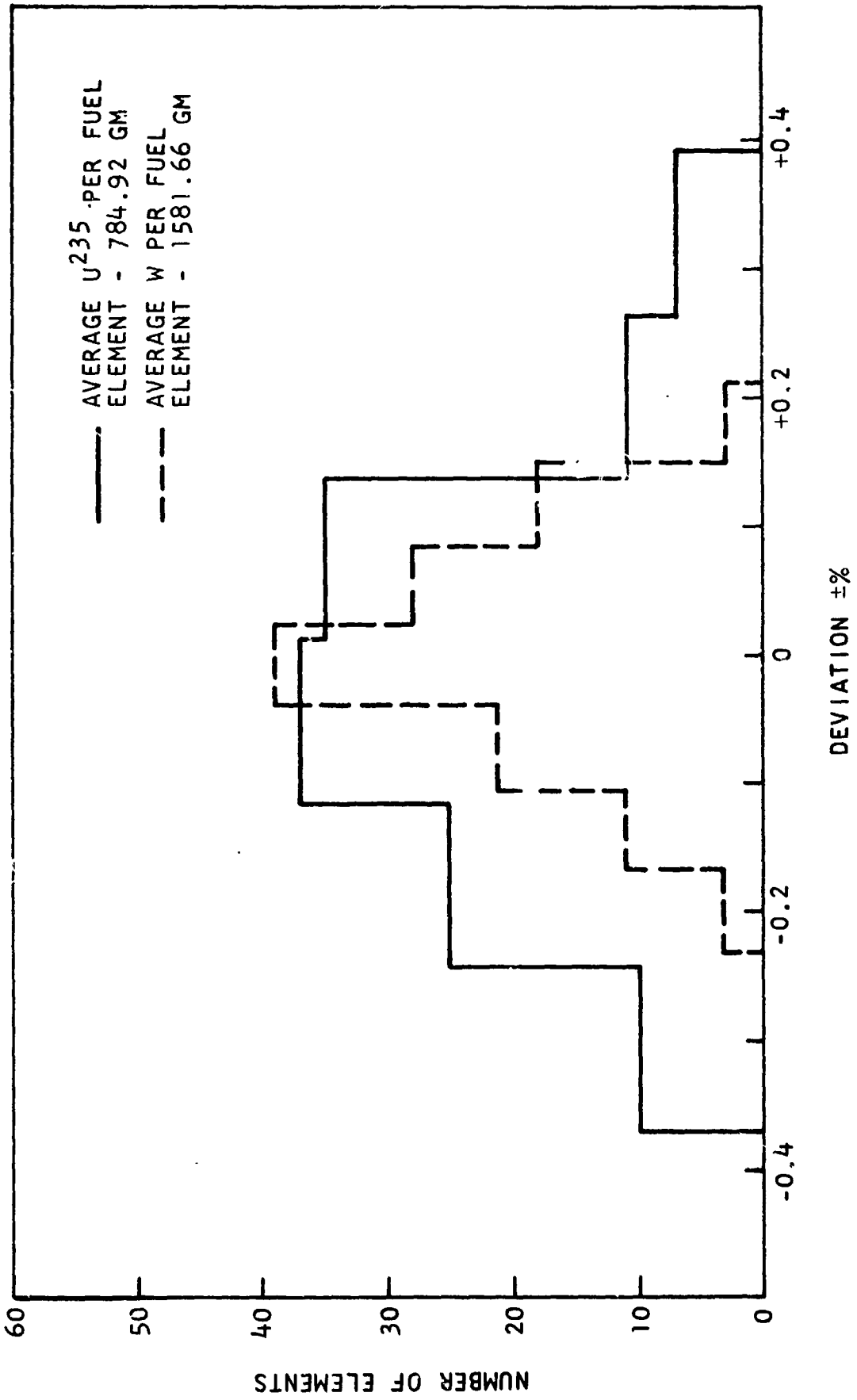


Fig. 2.21--Fuel and tungsten distribution among fuel elements  
(Sheet 3 of 3)

Table 2.3 shows the average weights and dimensions of the fuel rings.

Table 2.3  
FUEL RING SPECIFICATIONS

Ring	i. d. (in.)	Wall Thickness (in.)	Average U-Al Wt (g)	Average U <sup>235</sup> Wt (g)	Average U <sup>238</sup> Wt (g)	Average Al Wt (g)
A	0.785	0.042	11.347	3.727	0.274	7.346
B	1.097	0.042	15.476	5.084	0.374	10.018
C	1.409	0.042	19.931	6.547	0.481	12.903
D	1.721	0.042	24.408	8.018	0.590	15.800
E	2.033	0.042	28.400	9.329	0.686	18.385

Table 2.4 shows the average weights and dimensions of the tungsten rings.

Table 2.4  
TUNGSTEN RING SPECIFICATIONS

Liner for Ring	i. d. (in.)	Wall Thickness (in.)	Average Wt (g)
A	0.775	0.005	6.033
B	1.087	0.005	8.459
C	1.399	0.005	10.862
D	1.711	0.005	13.977
E	2.023	0.005	16.665
U <sup>238</sup>	2.131	0.003	9.878

Table 2.5 shows the weights of the remaining fuel element components.

Table 2.5

## ADDITIONAL FUEL ELEMENT COMPONENTS

ALUMINUM

<u>Component</u>	<u>Grams Per Unit</u>	<u>Units Per Subassembly</u>	<u>Total Grams Per Subassembly</u>
Center Post	228 ± 2	2	456 ± 4
Radial Spacer Tube A	101 ± 1	2	202 ± 2
Radial Spacer Tube B	137 ± 1	2	274 ± 2
Radial Spacer Tube C	167 ± 1	2	334 ± 2
Radial Spacer Tube D	194 ± 2	2	388 ± 4
Corrugated Spacer Ring A		24	5 ± 1
Corrugated Spacer Ring B		24	7 ± 1
Corrugated Spacer Ring C		24	9 ± 1
Corrugated Spacer Ring D		24	11 ± 1
Corrugated Spacer Ring E		24	13 ± 1
Subassembly Lower Screw	15 ± 1	1	15 ± 1
Subassembly Upper Screw	22 ± 1	1	22 ± 1
Subassembly End Plate	43 ± 1	2	86 ± 2

---



---

1,822 ± 23 Grams

ZIRCONIUM

<u>Component</u>	<u>Grams Per Unit</u>	<u>Units Per Subassembly</u>	<u>Total Grams Per Subassembly</u>
Center Plate	58 ± .4	1	58 ± .4
Stud	23 ± .2	1	23 ± .2
End Plate	61 ± .5	1	61 ± .5

---



---

142 ± 1.1



The pressure tubes were made from 6061-T3 and have an average o. d. of 2.562-in. and a wall thickness of 0.065-in. They were hard anodized to prevent galling during insertion of the tubes in the grid plates. The lower end cap was sealed to the pressure tube by a combination O-ring and mechanical seal, the latter being accomplished on a General Atomic "Magneform" magnetic forming machine.

The upper end of each pressure tube was sealed using "turn-tite" adjustable seals that were modified for this purpose.

### 2.3 COMPARISON OF CORE CONFIGURATIONS

Three separate and distinct core configurations were used throughout the experimental program. They have been sequentially numbered, in the order in which they were built, as Core I, Core II, and Core III for ease of reference throughout the remainder of this report. Each of the three cores used the identical reactor structure, control rods, and fuel element subassemblies. They differed only in the reflector configurations and grid plate lattice spacings (pitch).

#### 2.3.1 CORE I

The first core built used a 3.00-in. triangular pitch between fuel elements. The side reflectors were full density water (neutronically infinite in extent). The top and bottom reflectors were 6.0-in. thick and were composed of water in the same volume fraction as in the core, since both the pressure and poison tubes extended above and below the fueled region of the core. The aluminum axial spacer tubes shown in Fig. 2.17 were considered to be part of the end reflectors. Figure 2.5 shows the positioning of the core within the reactor tank. Water levels were determined by measuring up six inches from the top of the fuel rings in Stage 24. The servo-manometer readings were checked and the overflow levels set in this way before loading fuel into the assembly.

The Core I configuration had 121 fuel elements. The six "corner" locations A-1, A-7, G-13, N-7, N-1 and G-1 were empty to make the core a better approximation of a right circular cylinder. The final cadmium nitrate concentration used in Core I was 0.1255 moles/liter (type C). A maximum of 207 poison tubes could be used, because nine poison tube locations were taken up by the eight control rods and one source tube. The actual number of poison tubes in the core at any one time was varied in order to shim the excess reactivity of the core to desired values for experimental purposes. Locations b-1, a-2, a-12, b-13, g-23, g-24, m-14, n-11, n-1, m-2, g-2, and g-1 were used for this purpose.

### 2.3.2 CORE II

The only difference between Core I and Core II was the lattice pitch and the cadmium concentration. Core II had a 2.90-in. pitch and a final cadmium concentration of 0.0431 moles/liter (type H).

### 2.3.3 CORE III

The third core built used the original 3.00-in. pitch grid plates. However, the side and bottom reflectors were made primarily from beryllium metal and the top reflector was water (with voids) 2.0-in. thick. In addition, the subassembly axial spacers were removed from the fuel elements so that the subassembly rested on the bottom of the pressure tube. Water levels were determined by measuring up two inches from the top of the fuel rings in Stage 24. The servo-manometer readings were checked and the overflow levels set in this way before loading fuel into the assembly.

Figures 2.22 and 2.23 show the mounting of the side beryllium reflectors. The scalloped aluminum faceplates on the beryllium boxes were designed so that the amount of water around the edge cells would be the same as the remaining core cells. Polyethylene was used to give a better

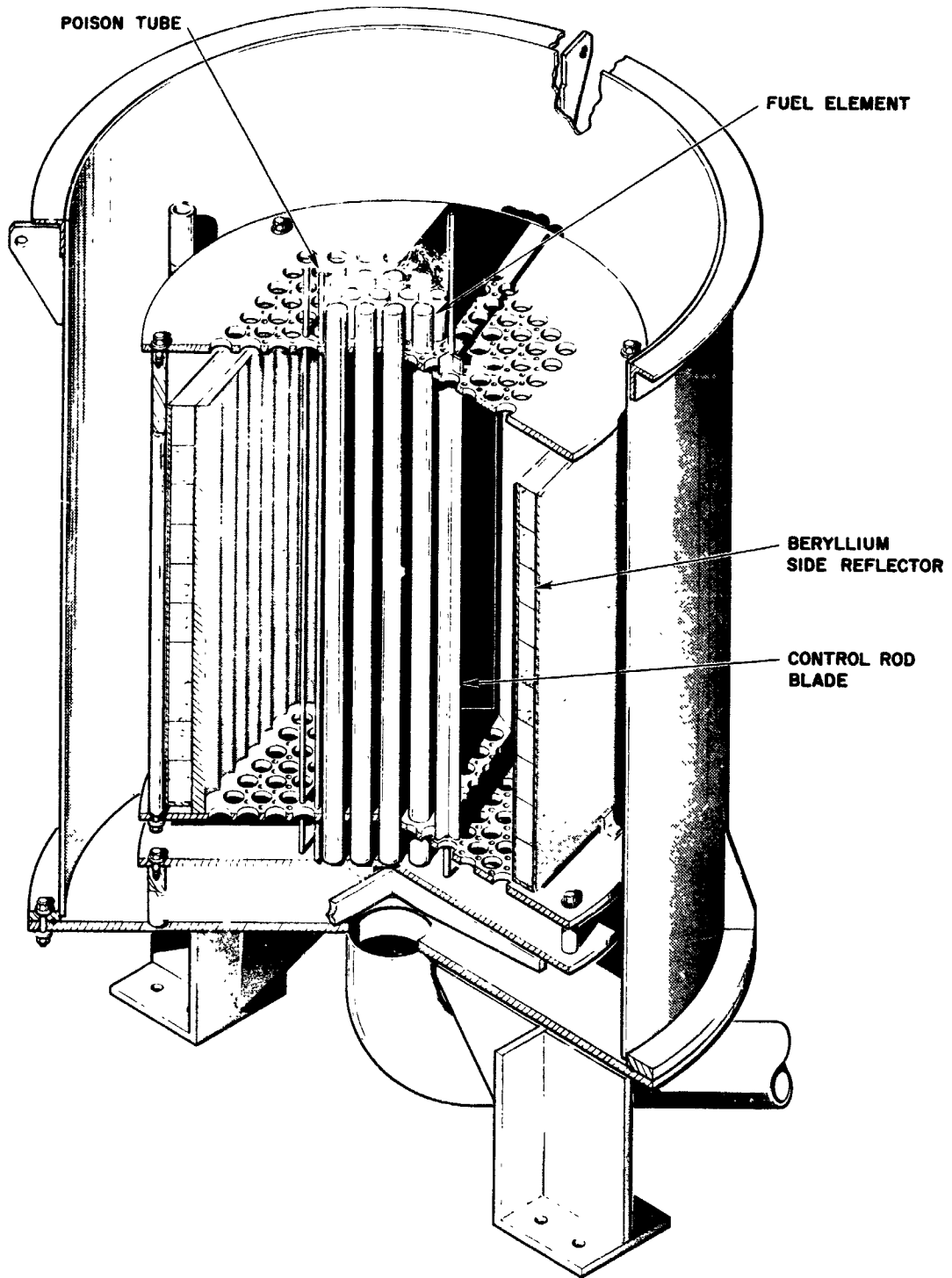


Fig. 2.22--Cross section of reactor tank and core support structure

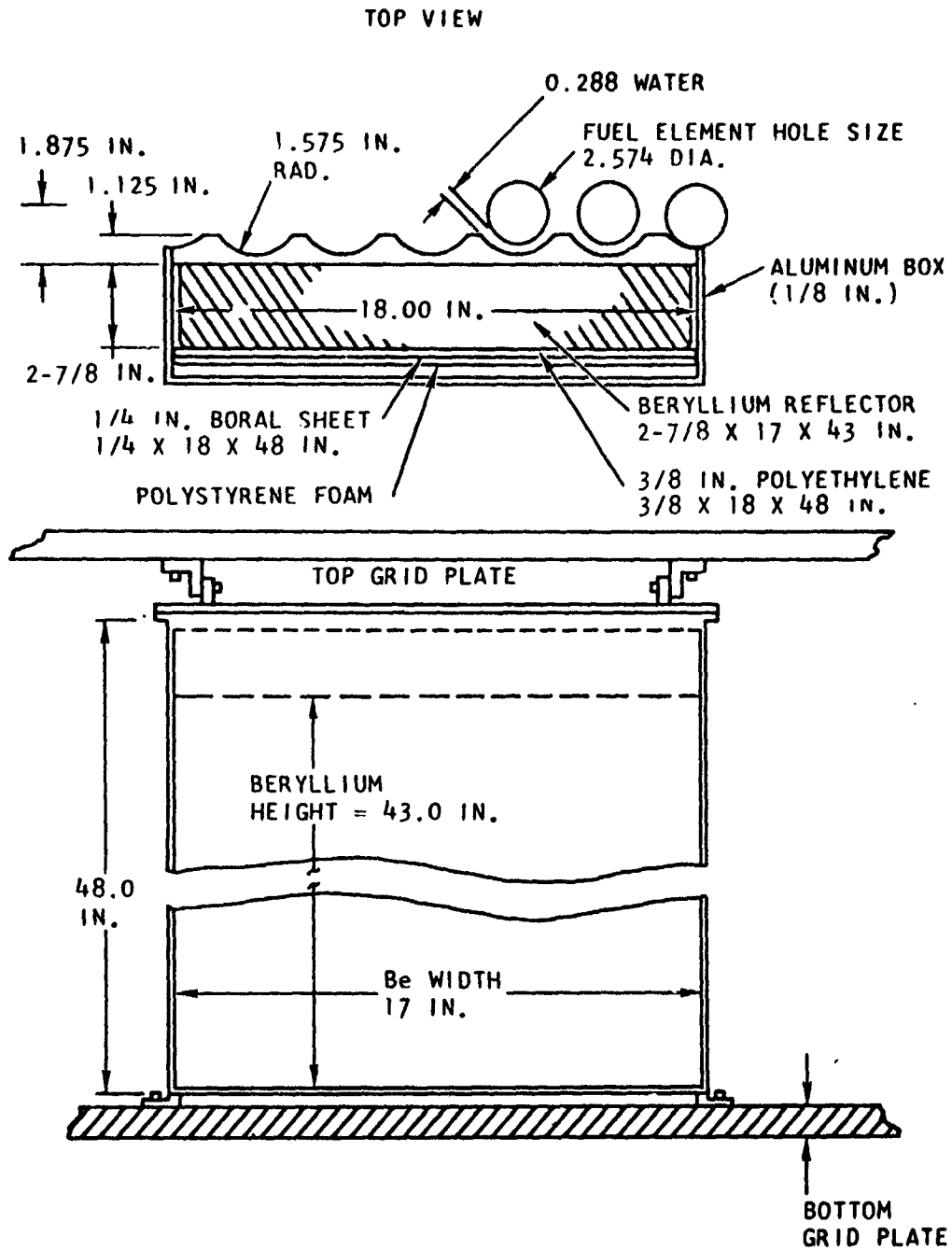


Fig. 2.23--Side reflector, 3.0-in. pitch, Be reflected core

simulation of the reference design which has cooling water in the reflector. Boral sheets approximated a vacuum boundary for thermal neutrons which exists in the reference design. Grid plate locations A-1, A-7, G-13, N-7, N-1, and G-1 were filled with voided pressure tubes for the same reason.

The bottom beryllium reflector (Fig. 2.24) is contained in a leak-proof aluminum container that fits between the core support plate and the bottom grid plate.

Specifications for the composition of the side and bottom reflectors are shown in Tables 2.6 and 2.7.

Table 2.6

## SIDE REFLECTOR MATERIAL SPECIFICATIONS

<u>Material</u>	<u>Thickness</u>	<u>Density</u>
Be Metal Blocks	2-7/8 in.	1.846 gm/cm <sup>3</sup>
Polyethylene Sheet	3/8 in.	1.0 gm/cm <sup>3</sup>
Aluminum	See Fig. 2.23	2.7 gm/cm <sup>3</sup>
Al Clad Boral Sheet		
Al Clad	0.041 in. each side	2.7 gm/cm <sup>3</sup>
Core, 35 wt % B <sub>4</sub> C		
65 wt % Al	.168 in.	2.626 gm/cm <sup>3</sup>

Table 2.7

## BOTTOM REFLECTOR MATERIAL SPECIFICATIONS

<u>Material</u>	<u>Thickness</u>	<u>Density</u>
Be Metal Blocks	4.0 in.	1.846 gm/cm <sup>3</sup>
Aluminum	See Fig. 2.24	2.7 gm/cm <sup>3</sup>

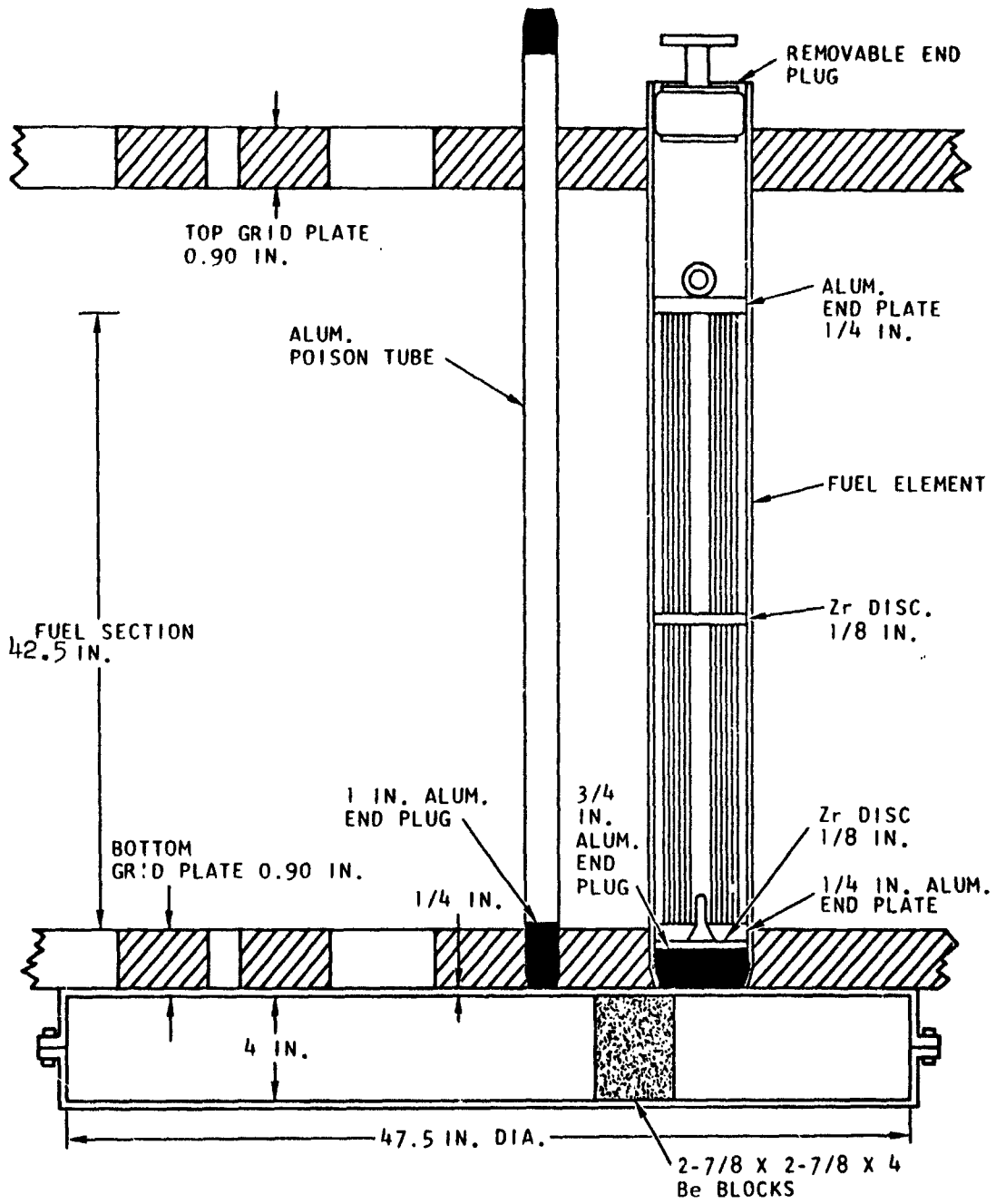


Fig. 2.24--Bottom reflector, 3.0-in. pitch, Be reflected core

### III. EXPERIMENTAL METHODS AND RESULTS

#### 3.1 CORE LOADING

The initial critical loading of all three cores was accomplished using the inverse source multiplication technique. The increase in source multiplication following each loading step was monitored on three fission counter channels and one linear ion chamber channel. Before loading fuel, Cores I and III were loaded with 121 empty pressure tubes and a complete inventory of poison tubes. Core II was first loaded to a critical configuration starting with the empty pressure tubes but without poison tubes. In all cases fuel was loaded starting with the center elements and working outward. Loading in this manner resulted in inverse multiplication curves which are concave upward, a desirable situation from the standpoint of safety.

In all three cases criticality was achieved before the full complement of 121 fuel elements was loaded. This necessitated increasing the cadmium concentration in the poison tubes. This was accomplished by first increasing the concentration in five of the poison tubes and then measuring the reactivity decrease. If the change was close to the anticipated value, the complete inventory of poison tubes was changed to the new concentration which made the core subcritical. Fuel element loadings based on the source multiplication were then resumed until criticality was attained with the 121-fuel element pattern.

A "standard core" has been defined for comparison of results. This core contains 121 fuel elements, 204 poison tubes, no rod guides, and no source tube. Poison locations a-2, b-1, a-12, b-13, g-23, g-24,

m-14, n-11, n-1, m-2, g-2 and g-1 (used to shim the core to the desired excess reactivity) were defined to contain water filled tubes in the standard core. Locations d-9, e-16, j-15, k-10, j-5, and e-6 which contain the safety rod guides, and location h-10 which contains the source tube were defined to be filled with poison tubes in the standard core. Experimental corrections were made in the following results to account for the missing poison tubes at these locations. This was done by measuring the reactivity difference between a stainless steel rod or tube and a poison tube at equivalent locations. Experimental corrections have also been made to account for the shim poison tubes and for fuel elements if less than 121 were loaded.

Table 3.1 shows the corrected excess reactivities for the three standard cores that were investigated.

Table 3.1  
EXCESS REACTIVITY OF STANDARD CORE

	<u>Core</u>	<u>Poison Tube Type</u>	<u>Excess Reactivity (\$)</u>
I	3.0-in. pitch water reflected	C	0.10
II	2.9-in. pitch water reflected	H	1.11
III	3.0-in. pitch beryllium reflected	K	0.34

The reactivity of a core containing 85 fuel elements on a 2.9-in. pitch and no poison tubes was found to be \$0.47. Applying estimated corrections to account for the control rod guides and source tube the symmetric loading of 85 fuel elements (no fuel elements in the outer "ring" or in B2, B7, G2, G12, M2, and M7) had an excess reactivity of \$0.80.



### 3.2 REACTIVITY MEASUREMENT TECHNIQUE

Reactivity measurements on the above cores were made using three standard techniques. These are: (1) measurement of positive periods, (2) subcritical source multiplication measurements, and (3) pulsed neutron source measurements.

The measurement of positive periods involved two separate techniques. For relatively fast periods three fission counter channels using signals from probes located just beyond the side reflectors, were automatically programmed to count for 29 seconds, printout for 1 second, and repeat. The ratio of successive counts obtained in this manner is a constant for a given asymptotic period. An average of about five ratios from each of the three counters was used to measure the period. The reactivity was then derived from solutions of the inhour equation.

The second method for measuring positive periods was the drift technique. This technique is useful only over the narrow range of reactivities where the increase in neutron population with time is essentially linear. Experimentally, these measurements were made using a compensated ion chamber driving a micro-microammeter. The output signal from the latter was used to drive a recorder through a bridge circuit which contained a bucking voltage. After nulling the output signal the positive deviation could be measured with a hundredfold amplification. By drawing a straight line through the recorder trace the reactivity can be computed directly using the relationship that, for long periods,

$$\rho = \frac{\text{constant}}{\tau} \quad (3.1)$$

The accuracy of the reactivity measurements was affected by several factors. These include the positioning accuracy of the calibrated regulating rod; the accuracy of the regulating rod calibration curve; minor variations in moderator water temperature between one measurement and the next; and the accuracy of calculating the effective delayed neutron fraction which is used in relating reactivity to positive period. An additional

uncertainty peculiar to Core III was the thickness of the upper water reflector, which was not neutronically infinite. Since the upper reflector was worth approximately \$0.10 per inch in Core III, very minor changes in the reflector thickness were quite noticeable.

As a conservative estimate, individual measurements of reactivity made on Cores I and II are believed accurate to within  $\pm$  \$0.001 while measurements on Core III are believed accurate to within  $\pm$  \$0.002.

The subcritical source multiplication technique was used to obtain rough results when the experimental conditions necessitated that the core be subcritical. The technique was to first generate a curve showing the relation between the source multiplication and the amount that the reactor was subcritical. Regulating rods and poison tubes that had been previously calibrated by the positive period technique were used to determine the latter. The curves generated in this manner were used in measuring safety rod worths and in calibrating the regulating rods over that part of their range that exceeded the \$0.50 core excess reactivity limit. This method of measurement is subject to error because of geometry effects and was used only when limited accuracy was required.

The third method of measuring reactivity is the technique of observing the prompt decay following the introduction of a short burst of fast neutrons. This technique is discussed in Section 3.5.

### 3.2.1 REGULATING ROD WORTH

The regulating rods were calibrated in the following way. First, the core excess reactivity was adjusted to a value just under the maximum allowable value of \$0.50 by removing several of the peripheral poison tubes. With one regulating rod fully withdrawn, the second regulating rod was adjusted so that the core was a fraction of a cent supercritical. The drift technique was used to determine the amount. The second rod was then partially withdrawn and the period corresponding to a five to ten cent

reactivity insertion measured. The first rod was then inserted to bring the reactor back to a long enough period for a drift type measurement. This procedure was repeated until enough data were obtained to draw an accurate integral rod worth curve. Because of the maximum excess reactivity limit of \$0.50, the first few inches of the regulating rod calibration were obtained using the subcritical source multiplication technique. Table 3.2 shows the total integral worth of regulating rod number 2 in each of the three cores.

Table 3.2  
REGULATING ROD WORTHS

<u>Core</u>	<u>Worth (\$)</u>
I	0.525
II	0.500
III	0.475

### 3.2.2 SAFETY ROD WORTH

Since the interlock system precludes the withdrawal of a safety rod after the regulating rods have been withdrawn, the safety rod worths were determined using the subcritical source multiplication technique. This was accomplished using the calibrated regulating rods to adjust the core multiplication to several known subcritical values; in this way curves showing the inverse source multiplication vs dollars subcritical could be drawn. The results obtained are shown in Table 3.3.

Table 3.3  
SAFETY ROD WORTH

<u>Core</u>	<u>Single Rod Worth (\$)</u>
I	0.64
II	0.61
III	0.56

### 3.2.3 MEASUREMENT OF THE EXCESS REACTIVITY HELD DOWN BY CADMIUM SOLUTIONS

The grid plate contains 216 locations for poison tubes, rod guides, and the source. A total of 207 locations are available for cadmium poison tubes, nine locations being taken up by the eight stainless steel rod guides and the stainless steel source tube.

These 216 locations can be grouped into symmetric groups containing either six, twelve, or eighteen poison tubes at twenty distinct radii from the center of the core. Thus it is possible to measure the worth of representative groups of poison tubes, weight them by their occurrence, and add the results. This procedure will be referred to as the reactivity mapping technique.

Table 3.4 shows the groupings and occurrence of a typical pattern. The poison tubes in each group were replaced with similar tubes containing pure water. The resultant reactivity change was then measured on the calibrated regulating rods.

Table 3.4  
TYPICAL PATTERN USED IN DETERMINING  
THE TOTAL EXCESS REACTIVITY

<u>Group</u>	<u>Poison Tubes</u>	<u>Weight Factor</u>
1	f-11, f-7, j-18, k-1, h-11	6
2	c-14, e-8, g-15, k-5, l-16	12
3	j-14, k-6, c-3, f-2, g-23	12
4	j-16, e-18, d-3, j-1, a-8	12

A similar procedure was followed for mapping the worth of poison tubes having a higher cadmium concentration than the standard loading for a given core.

Table 3.5 shows the results obtained by mapping the worth of the standard poison tubes for each of the three primary cores. These results indicate what the total excess reactivity of a standard core would be if the cadmium nitrate solution in the poison tubes was replaced with pure water.

Table 3.5  
EXCESS REACTIVITY OF STANDARD CORES  
WITHOUT CADMIUM IN POISON TUBES

<u>Core</u>	<u>Poison Tube Type</u>	<u>Excess Reactivity (\$)</u>
I	C	+ 14.39
II	H	+ 6.61
III	K	+ 20.55

Table 3.6 shows the results obtained by mapping the poison tube worths for higher cadmium concentrations in each of the three primary cores. These results indicate what the excess reactivity would be for a standard core using the higher cadmium concentration.

Table 3.6  
EXCESS REACTIVITY OF STANDARD CORES  
WITH INCREASED CADMIUM LOADINGS

<u>Core</u>	<u>Poison Tube Type</u>	<u>Excess Reactivity (\$)</u>
I	D	- 3.24
	E	- 9.37
II	C	- 6.32
	D	- 9.09
III	E	- 2.89
	L	- 7.04

### 3.2.4 POISON TUBE WORTHS AT DIFFERENT RADIAL LOCATIONS

The reactivity change associated with the replacement of a tube filled with cadmium nitrate by a similar tube containing water was measured at various locations in Cores I and III. The change in position of the calibrated regulating rods, with the reactor on a slight positive reactivity drift, was used to determine the worth of the change. Table 3.7 presents the results obtained in tabular form and Fig. 3.1 shows the results graphically.

Table 3.7  
RADIAL WORTH OF POISON TUBES

<u>Location</u>	<u>Radius (cm)</u>	<u>Worth of Type "C" in Core I (\$)</u>	<u>Worth of Type "K" in Core III (\$)</u>
f-12	4.40	- 0.132	- 0.167
f-11	8.80	- 0.125	---
e-12	11.64	- 0.119	- 0.154
e-11	15.86	- 0.110	---
d-12	19.18	- 0.099	- 0.129
d-11	23.28	- 0.083	---
c-12	26.76	- 0.073	- 0.105
c-11	30.80	- 0.055	---
b-12	34.36	- 0.041	- 0.071
b-11	38.35	- 0.030	- 0.064
a-12	41.97	- 0.037	---

### 3.2.5 WORTH OF POISON TUBES HAVING DIFFERENT CADMIUM CONCENTRATIONS

The worth of the cadmium nitrate in a single poison tube as a function of the concentration was measured in all three cores at location f-12.

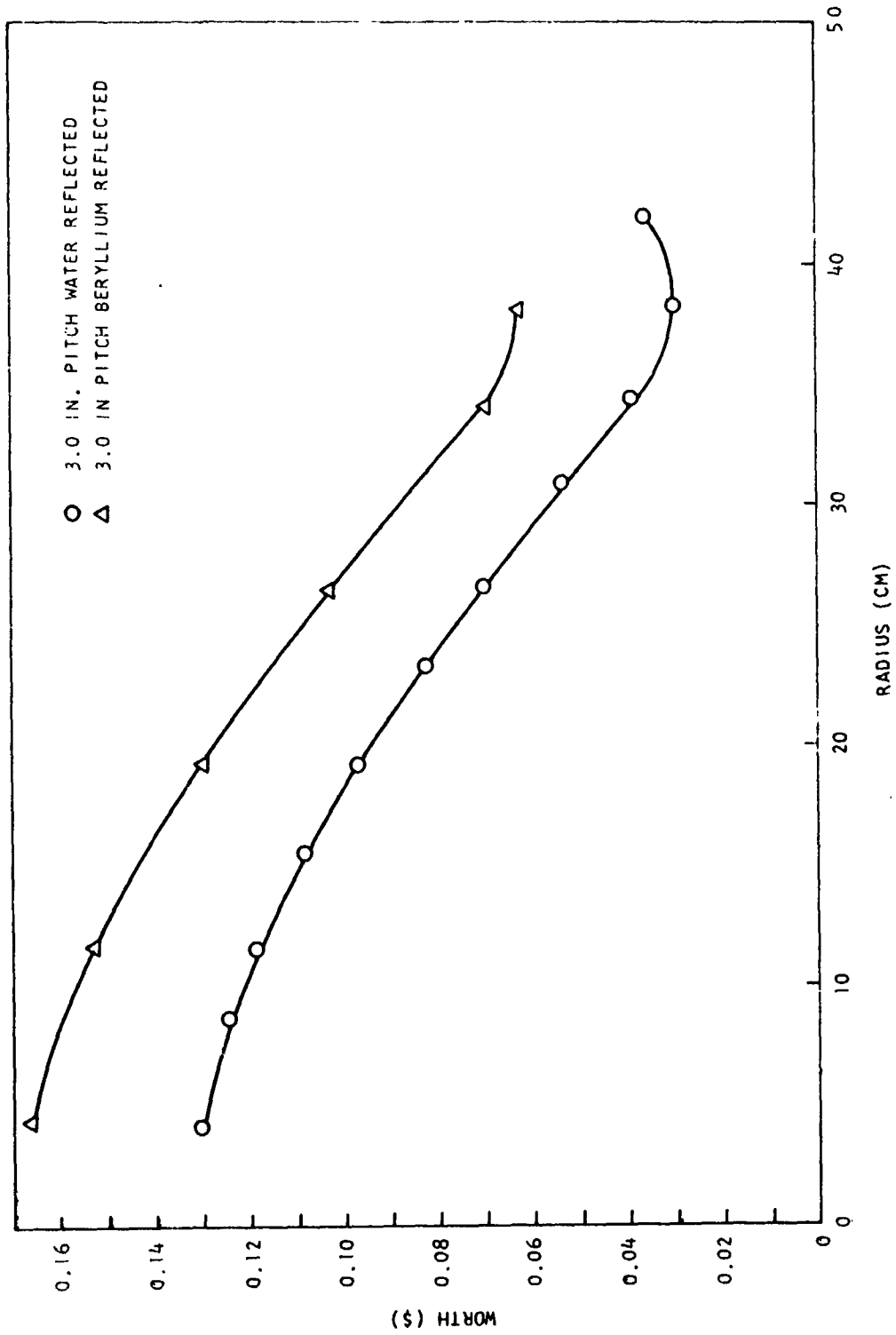


Fig. 3.1--Cadmium worth at various radii

The results are shown in Table 3.8 and in Figs. 3.2 and 3.3.

Table 3.8

POISON TUBE WORTH VS CADMIUM CONCENTRATION

Cadmium Concentration (moles/liter)	Worth, Core I (\$)	Worth, Core II (\$)	Worth, Core III (\$)
0.0431	- 0.039	- 0.048	- 0.050
0.06275	- 0.074		
0.0956	- 0.106	- 0.093	- 0.090
0.1108	- 0.121		
0.1255	- 0.132	- 0.116	
0.1677	- 0.161	- 0.143	- 0.143
0.2202	---	---	- 0.167
0.250	- 0.201	- 0.185	---
0.290	---	---	- 0.189
0.500	- 0.275	- 0.252	- 0.250

### 3.2.6 WORTH OF INDIVIDUAL FUEL ELEMENT COMPONENTS

Fuel element component worths were determined by measuring the change in core reactivity when the component under study was removed from all 24 stages of the fuel element. Table 3.9 shows the results obtained in location G-7 for all three cores.

Table 3.9

FUEL ELEMENT COMPONENTS WORTH  
(LOCATION G-7)

Components	Worth, Core I (\$)	Worth, Core II (\$)	Worth, Core III (\$)
Uranium-Aluminum	+ 1.08	+ 0.16 (E-Ring only) + 0.11 (D-Ring only)	+ 0.96
Tungsten	- 0.35	- 0.33	- 0.28
U <sup>238</sup> Ring	- 0.11	- 0.11	- 0.10



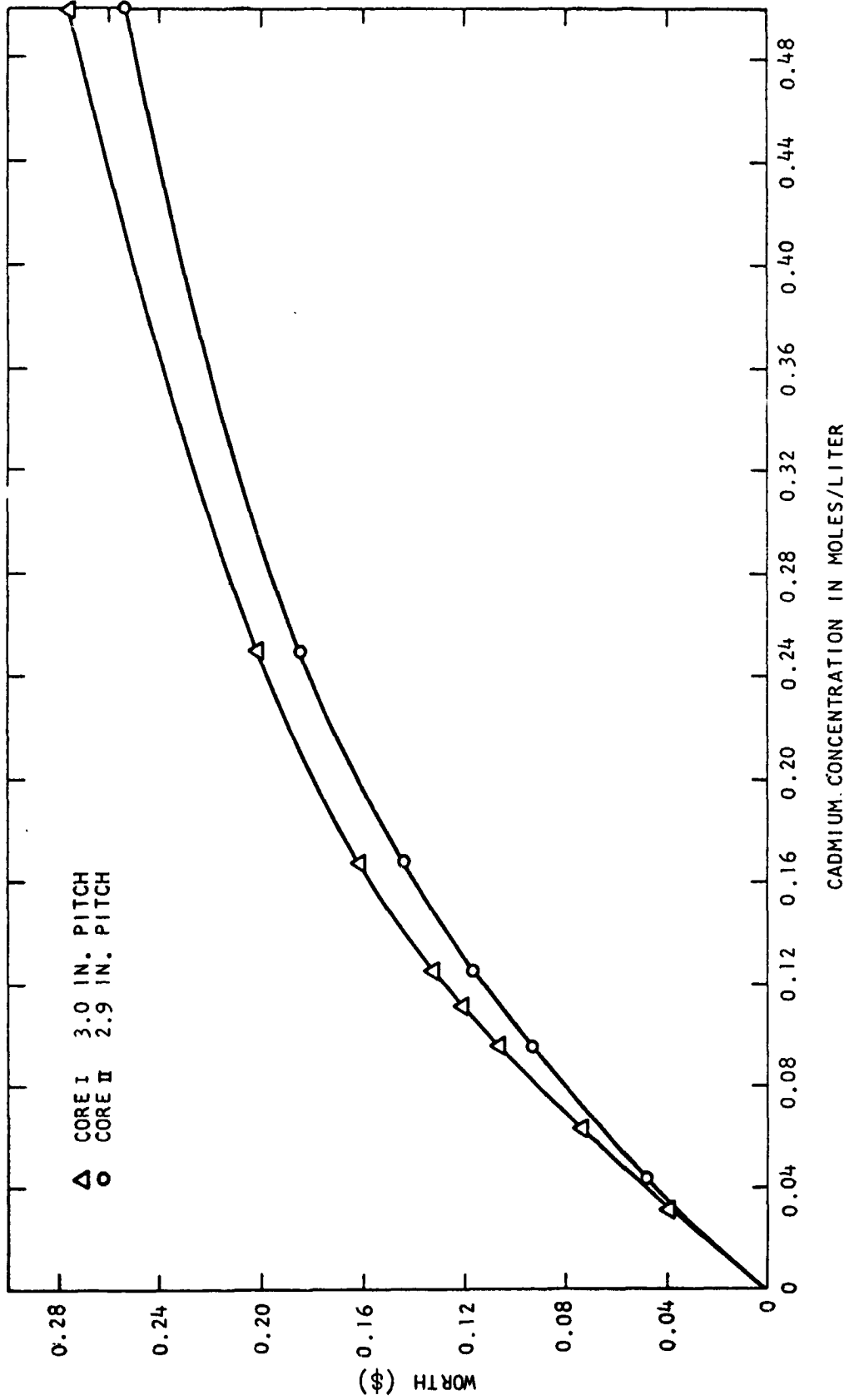


Fig. 3.2--Worth of various cadmium concentrations in Cores I and II

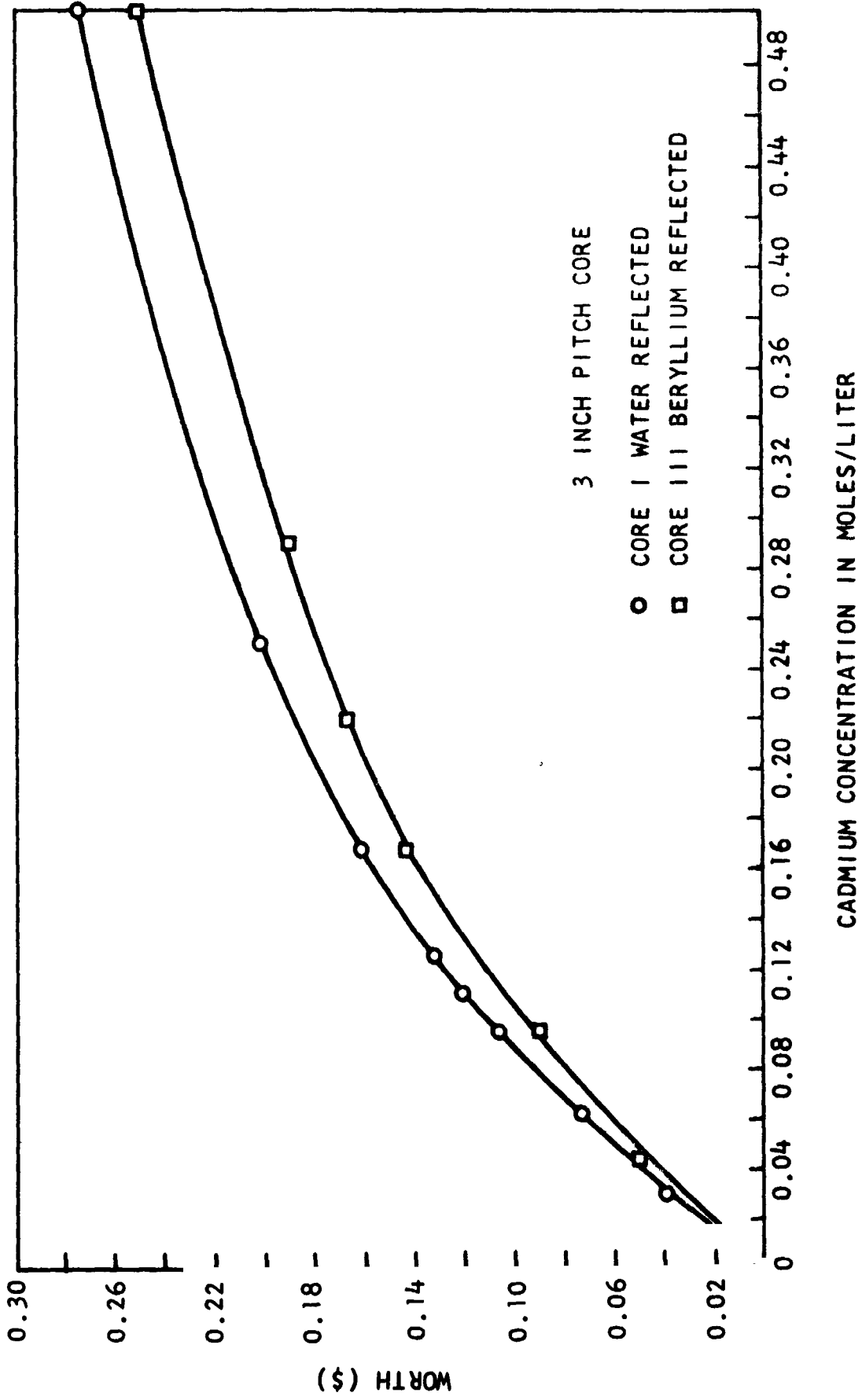


Fig. 3.3--Worth of various cadmium concentrations in Cores I and III

Table 3.10 shows some additional results obtained in Core I.

Table 3.10  
ADDITIONAL FUEL ELEMENT COMPONENTS WORTHS,  
CORE I

<u>Material</u>	<u>Location G-7 Worth (\$)</u>	<u>Location B-6 Worth (\$)</u>	<u>Location A-5 Worth (\$)</u>
Uranium Aluminum + Aluminum	1.082	0.366	0.358
Tungsten	- 0.352	- 0.101	- 0.071
U <sup>238</sup> Ring	<u>- 0.113</u>	<u>- 0.027</u>	<u>- 0.019</u>
Fuel Element vs Void (Algebraic Sum)	<u>0.617</u>	<u>0.238</u>	<u>0.268</u>
Fuel Element vs Void (Measured Directly)	<u>0.619</u>	<u>0.240</u>	<u>0.270</u>

### 3.2.7 NEUTRONIC SIMULATION EXPERIMENT

As a check on the validity of the neutronic simulation a five-stage enriched tungsten fuel element section was fabricated at the Oak Ridge National Laboratory and supplied to General Atomic by the National Aeronautics and Space Administration. Tables 3.11 and 3.12 give the physical specifications of this element.

Table 3.11  
SPECIFICATION FOR SIMULATION SECTION

<u>Tungsten Isotope</u>	<u>Percent in Rings 1-10</u>	<u>Percent in Ring 11</u>
180	< 0.006	< 0.010
182	2.019	6.202
183	1.581	81.822
184	93.889	8.742
186	2.505	3.224

Table 3. 12  
 PHYSICAL SPECIFICATIONS OF THE FIVE-STAGE ENRICHED TUNGSTEN SECTION

Cylinder No.	i. d.	o. d.	Stage 1 Weight (g)	Stage 2 Weight (g)	Stage 3 Weight (g)	Stage 4 Weight (g)	Stage 5 Weight (g)	Total (g)	Average (g)
1	0.492	0.543	13.77	14.00	16.87	14.51	16.95	76.100	15.220
2	0.651	0.691	11.89	16.30	15.97	15.65	16.71	76.520	15.304
3	0.820	0.863	21.195	23.14	20.19	22.038	25.14	111.703	22.340
4	0.991	1.039	32.86	34.55	33.10	33.64	30.66	164.810	32.962
5	1.155	1.187	27.12	26.12	24.11	29.70	27.87	134.920	26.984
6	1.323	1.355	31.87	31.22	27.72	28.27	32.83	151.910	30.382
7	1.493	1.544	47.31	50.46	49.46	52.42	55.36	255.010	51.002
8	1.653	1.687	47.80	45.11	50.63	43.90	33.14	220.580	44.116
9	1.823	1.854	40.75	39.01	42.18	41.44	45.23	208.610	41.722
10	1.992	2.034	74.83	69.59	69.19	67.83	65.47	346.910	69.382
11	2.148	2.170	44.460	44.700	44.120	44.720	43.550	221.550	44.310

<u>U<sup>235</sup> Cylinders</u>									
Cylinder No.	i. d.	Wall Thickness	Stage 1 Weight (g)	Stage 2 Weight (g)	Stage 3 Weight (g)	Stage 4 Weight (g)	Stage 5 Weight (g)	Total (g)	Average (g)
1A	0.482	0.0042	3.121	3.176	3.183	2.884	2.876	15.240	3.048
4A	0.973	0.0042	5.702	5.862	6.159	6.030	6.228	29.981	5.996
4AA	0.982	0.0043	5.5535	5.3230	5.3475	5.5050	5.2989	27.0279	5.4055
7A	1.484	0.0042	9.235	9.054	9.154	9.089	9.307	45.839	9.168
10A	1.983	0.0042	12.770	12.976	12.577	12.880	12.692	63.895	12.779

The stages are each 1.625-in. in height and are separated by 0.125-in. aluminum spacers. The five-stage enriched tungsten fuel element section was used to replace stages eight through twelve of the central fuel element G-7 in Core III.

There were two goals in the simulation experiment. The first goal was to compare the worth of the mockup fuel element section to that of the enriched tungsten fuel element section with five rings and then with eleven rings of tungsten in place. These two enriched tungsten fuel element configurations bracketed the reference case; the five-ring configuration contained reference amounts of W-182, W-183, and W-186, but was deficient in W-184, and the eleven-ring case contained the reference amount of W-184 but an excess of W-182, W-183, and W-186. The worth of the mockup fuel element was found to be between the worth of the five-ring and eleven-ring configurations, as required if the mockup design was indeed a good representation of the reference fuel element.

The second goal of the experiment was to adjust the number of tungsten rings so that there would be no reactivity difference between the five enriched stages and five stages of the standard fuel element. This was accomplished with tungsten rings 1, 4, 7, 10 and 11 in place. However, when checking the separate worth of the fuel used in the enriched stages with the worth of the fuel in five of the stages fabricated at General Atomic, a difference of approximately two cents was found. Further, the worth of the fuel in both assemblies was found to depend on the amount of tungsten present in the five stages. To eliminate these differences new spacers were fabricated that enabled the uranium-aluminum alloy mockup fuel to be used in the five enriched tungsten stages. In this configuration a reactivity match was achieved with enriched tungsten rings 1, 2, 4, 6, 7, 9, 10 and 11 present. The five enriched stages were actually \$ 0.0008 more reactive; however, under the conditions of these measurements the results are believed to be accurate only to  $\pm$  \$ 0.001.

## 3.2.8 WORTH OF THE UPPER END REFLECTOR IN CORE I

Measurements were made of the worth of the upper end reflector in Core I. Figure 3.4 shows the measured integrated worth to approximately 12.0 in. The offset in the curve at 6 in. represents the 7/8-in. thick aluminum grid plate. The total worth of an infinite upper reflector is approximately \$ 0.75 from extrapolation of Fig. 3.4. Table 3.13 is a tabulation of the results shown in Fig. 3.4.

Table 3.13

## WORTH OF TOP REFLECTOR

<u>Reflector Height</u>	<u>Integrated Worth</u>
1.015-in.	\$ 0.182
1.945-in.	\$ 0.310
4.390-in.	\$ 0.544
6.035-in.	\$ 0.611
8.035-in.	\$ 0.657
10.035-in.	\$ 0.693
12.035-in.	\$ 0.714

## 3.2.9 WORTH OF VARIOUS BORON CONCENTRATIONS IN CORE I

The reactivity worth, relative to water, of a single poison tube containing various concentrations of boric acid was measured in location f-12. The results are given in Table 3.14 and graphed in Fig. 3.5.

Table 3.14

MEASURED WORTH OF VARIOUS  
BORON CONCENTRATIONS

<u>Boron Concentration (moles/liter)</u>	<u>Worth of One Tube in f-12 (\$)</u>
0.2856	- 0.069
0.4236	- 0.096
0.5614	- 0.121
0.6993	- 0.142

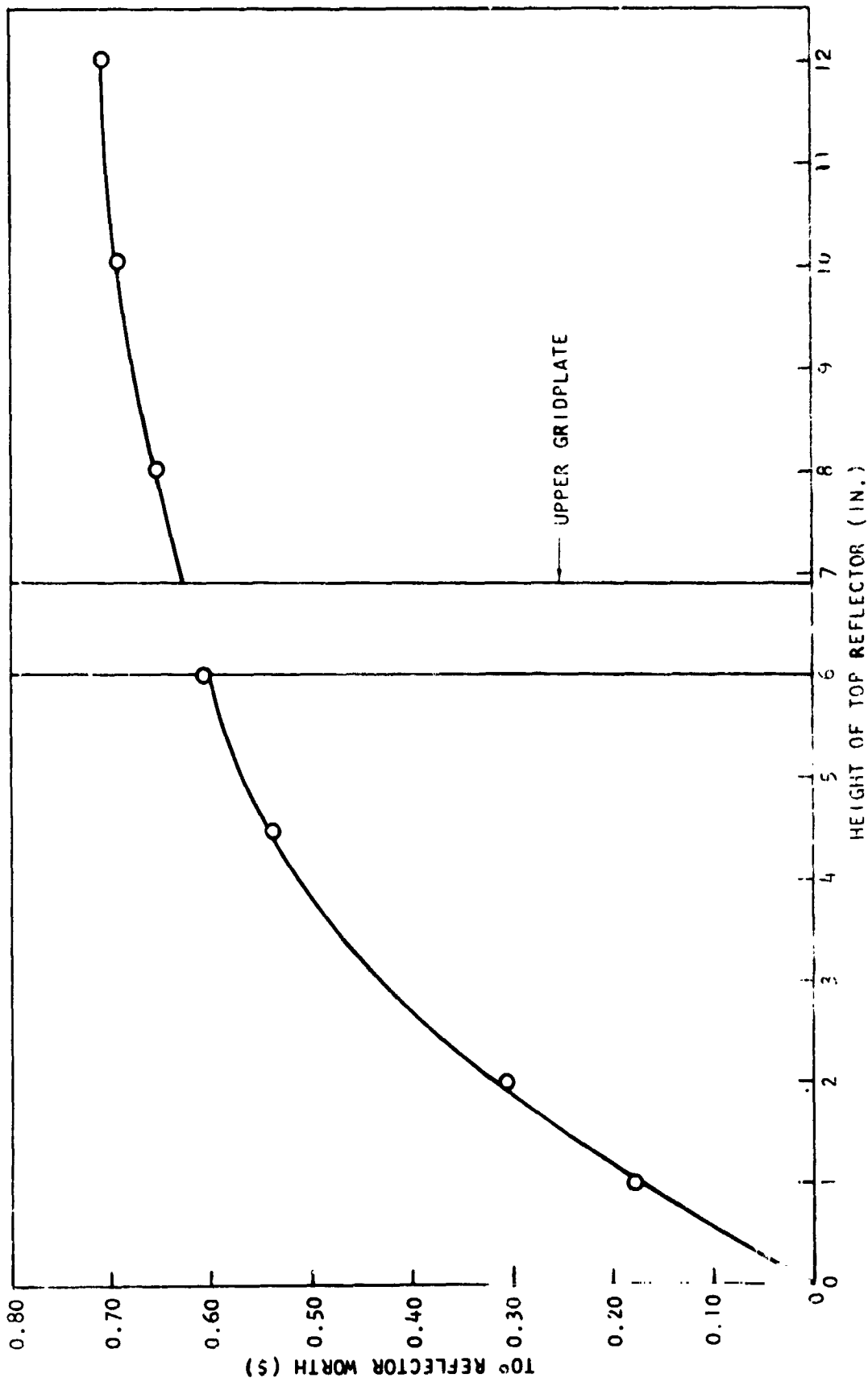


Fig. 3.4--Top reflector worth in Core I

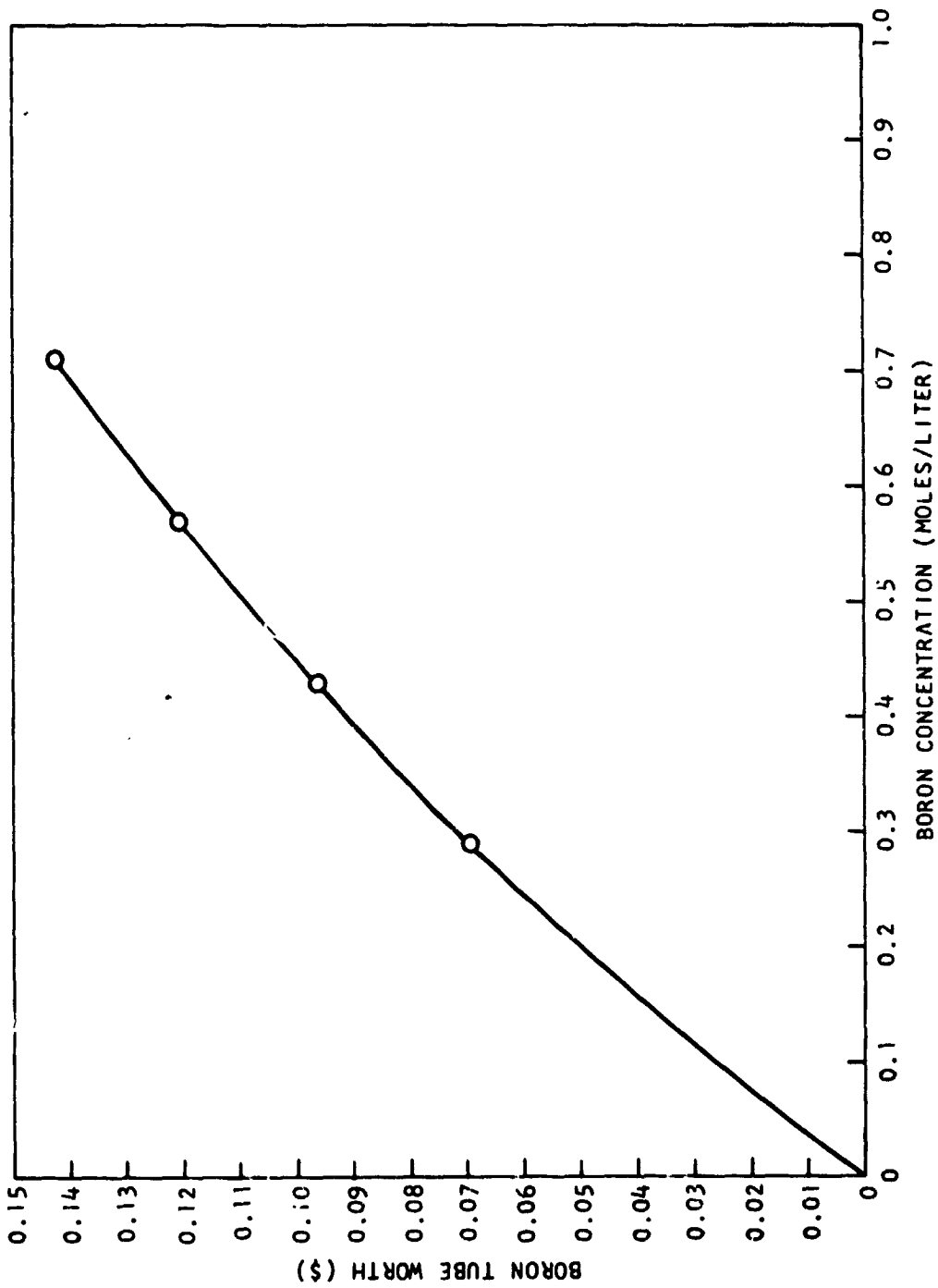


Fig. 3.5--Worth of boron poison in Core I



### 3.2.10 SUBSTITUTION OF BORON-STAINLESS STEEL FOR TUNGSTEN IN THE CENTRAL FUEL ELEMENT OF CORE II

Boron stainless steel foils were substituted for tungsten foils in the central fuel element (G-7) to provide experimental worth data that would be virtually independent of resonance absorption. One nonover-lapping wrap of the boron stainless steel foil was inserted in place of each of the tungsten foil wraps inside the element. The thickness of the borated foil was 0.0025 in. Weights of the foils for the 24 stages of one element are given in Table 3.15.

Table 3.15

#### WEIGHT OF BORON STAINLESS STEEL FOILS

<u>Foil Position</u>	<u>Weight of 24 foils (g)</u>
Liner, Ring A	24.77
Liner, Ring B	34.00
Liner, Ring C	44.99
Liner, Ring D	54.52
Liner, Ring E	64.81
Liner, Ring F	68.08

The reactivity worth of the boron stainless steel foil was - \$0.257 when compared to a fuel element containing neither tungsten nor boron stainless steel foil. The worth of the tungsten wrap under the same conditions was \$0.331.

A chemical analysis of the major additives to the steel was made in duplicate for each of two samples. Table 3.16 lists the results. The duplicate analyses for boron are both listed to provide an indication of the precision of the results.

Table 3.16

#### CHEMICAL ANALYSIS OF BORON STAINLESS STEEL

<u>Sample</u>	<u>%B</u>	<u>%Ni</u>	<u>%Cr</u>	<u>%Mn</u>
1	(1.43, 1.44)	10.2	15.3	1.65
2	(1.44, 1.42)	10.4	14.7	1.65

### 3.3 FOIL MEASUREMENTS

#### 3.3.1 GENERAL METHODS

A sodium-iodide (thallium-activated) well-crystal coupled to a photomultiplier tube and shielded by lead bricks was set up in the control building to count activated specimens. Automatic counting equipment allowed repetitive sample counting on an accurately controlled time basis. Thus, whenever it was necessary to follow the time decay of irradiated foils, a sequence of counting time followed by a sample-changing time could be cycled without difficulty.

Most specimens counted were enclosed in 2-dram polyethylene vials for handling. Such vials readily fitted the well of the 1-3/4-in. by 2-in. crystal and permitted rapid handling along with high counting sensitivity.

Conventional foil materials were used in most measurements. Copper, manganese, and gold foils were irradiated to obtain relative flux distributions either in the cell or throughout the core. Uranium-aluminum foils were also used to make direct relative power distribution measurements.

An extensive mapping of the Core III relative power distribution was required for use in conjunction with the gamma heating experiments discussed in Section 3.6. This was accomplished by counting the relative gamma activity of the fuel rings in an extensive region of the core. The gamma radiation from each fuel ring was counted above 400 keV gamma energy while being rotated about its axis. A small 120 rpm electric motor equipped with a series of aluminum mandrels was located above a scintillation crystal for this purpose. By this means it was possible to average the variations in fuel density and also the azimuthal variations of fission product activity in fuel rings near the core-reflector interface.

Absolute power calibrations of Core III were accomplished using both gold and manganese alloy foils. One-fourth in. diameter discs of 0.002-in. gold and 0.005-in. manganese alloy (80 wt % Mn - 20 wt % Cu) were activated in the TRIGA reactor and counted, as foils, on a 3-in. by 3-in. scintillation crystal. The foils were then dissolved and a known portion of the solutions evaporated on a thin film for  $4\pi$  beta counting to determine the absolute disintegration rate. This technique absolutely calibrated the scintillation crystal for gamma counting in the exact geometry that was used for foils activated in the critical assembly.  $4\pi$  beta counting of foils activated in the critical assembly is unsatisfactory because of their low specific activity. Gold and manganese are well suited to this method, as the decay schemes are simple and well known; the isotopes occur in 100% abundance; and the half-lives are convenient. Copper was tried but it is not as suitable, since the branching ratio of the beta decay of  $\text{Cu}^{64}$  is not too well known and because of positron emission which causes difficulty in determining the absolute beta counting rate.

Corrections for irradiation time, decay time, and counting time were then applied to the experimentally determined disintegration rate to find the saturated activity of the foil in disintegrations/minute/gram of material. The difference in bare and cadmium-covered activities, or the subcadmium activation, was then related to power through calculational techniques and a knowledge of the activation cross section of the foil material.

### 3.3.2 RADIAL POWER DENSITY IN ELEMENT G-7

Circular foils of 1/4-in. diameter were punched from the uranium-aluminum fuel rings of Stage 12 of fuel element G-7. Before irradiating these foils, their gamma spectra were displayed on a multi-channel analyzer and examined for evidence of fission product activity from any previous use. No significant high-energy background was noted.

The relative amount of  $U^{235}$  in each foil was measured by counting the 165-185 keV gamma rays which accompany the natural decay of the  $U^{235}$ . The foils were irradiated in place in all three cores. The fission product activity of the foils was measured by integral counting above a gamma ray energy of 600 keV, using the activity of one foil, repetitively counted, to obtain a decay correction curve. Two foils were exposed at positions  $180^\circ$  apart in each fuel ring. Table 3.17 shows the average of the two measurements, normalized to 1.000 at the E-ring, for each core studied.

Table 3.17  
RELATIVE POWER DENSITY - STAGE 12 OF ELEMENT G-7

Ring	Average Radius (Cm)	Power Density		
		Core I	Core II	Core III
E	2.634	1.000	1.000	1.000
D	2.238	0.824	0.797	0.812
C	1.842	0.723	0.705	0.703
B	1.445	0.670	0.658	0.654
A	1.049	0.653	0.621	0.622

### 3.3.3 AZIMUTHAL FLUX AND POWER DISTRIBUTION IN ONE FUEL ELEMENT

Azimuthal mapping of the thermal flux around fuel elements G-7 and A-4 was accomplished in Core I using strips of manganese-copper alloy foils. Three-eighth in. wide strips of 0.005-in. foil were taped to the outside of the  $U^{238}$  ring on the 14th fuel stage. Following irradiation, the strips were cut into squares and the integral manganese activity was gamma-counted above 1.60 MeV. Background subtraction (nearly negligible at this bias) and weight corrections were made. The results are shown in the azimuthal flux map of Fig. 3.6. It is apparent that the

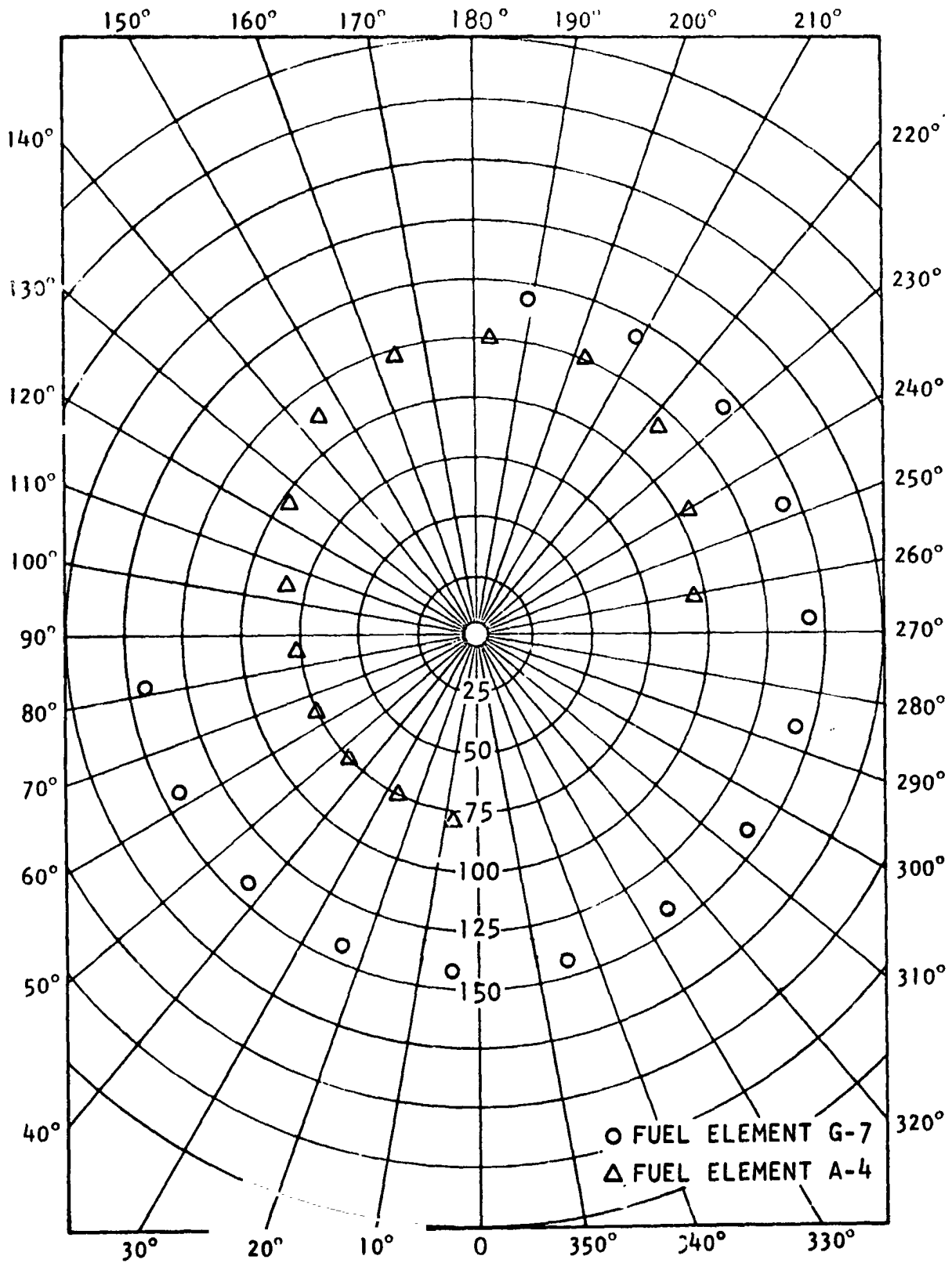


Fig. 3.6--Azimuthal activation of manganese foils, Core I

thermal flux is closely symmetrical about the center element G-7, and that scalloping of the flux is not present. The mapping of element A-4 shows the thermal flux peaking at the core-reflector interface (the 180° position).

A check was made of the azimuthal power distribution in the central element G-7 of Core III. Five adjacent foils were punched from a 60° sector of Stage 11 and were irradiated during an axial power mapping run (the central one of these foils simultaneously served in the axial power mapping). Results of this mapping are exhibited in Fig. 3.7, where it can be seen that no azimuthal power asymmetry exists.

#### 3.3.3.1 Measurement of the Worth and Effect of Water at the Core-Reflector Interface

To determine the worth of water at the core-reflector interface and its effect on local flux and power distributions, the core-reflector interface water gap was reduced from 0.288 in. to 0.163 in. on one of the six side reflectors.

Reactivity measurements made before and after the five aluminum inserts were installed showed that a reduction in water gap of 0.125 in. at the interface resulted in a reactivity loss of \$0.031.

Manganese foils were placed around the U<sup>238</sup> ring on Stage 12 of fuel element A-4. The relative activities obtained are shown in Fig. 3.8.

#### 3.3.4 INTERSTITIAL FLUX MEASUREMENTS

The thermal flux variation in the trifluted area between adjacent fuel elements was mapped in Core I using the following technique. A plexiglass holder was fabricated to hold copper wire segments, vertically oriented, in the interstitial spaces between adjacent fuel elements and between a fuel element and a cadmium poison tube. Twenty-one 1/4-in. segments of wire, 0.025-in. in diameter, were exposed for 30 minutes at a power of 10 watts. Following irradiation, the copper activities were

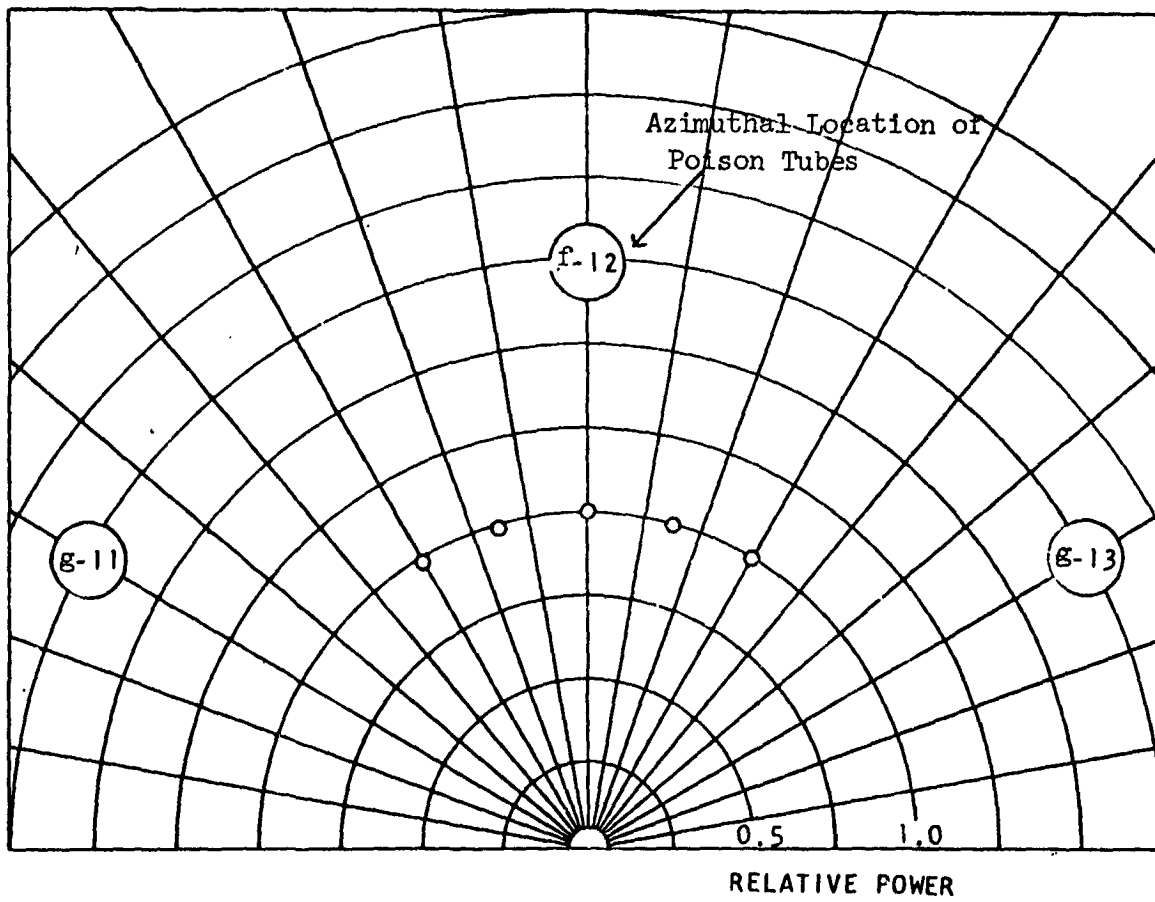


Fig. 3.7--Azimuthal relative power in fuel element G-7 (Core III)

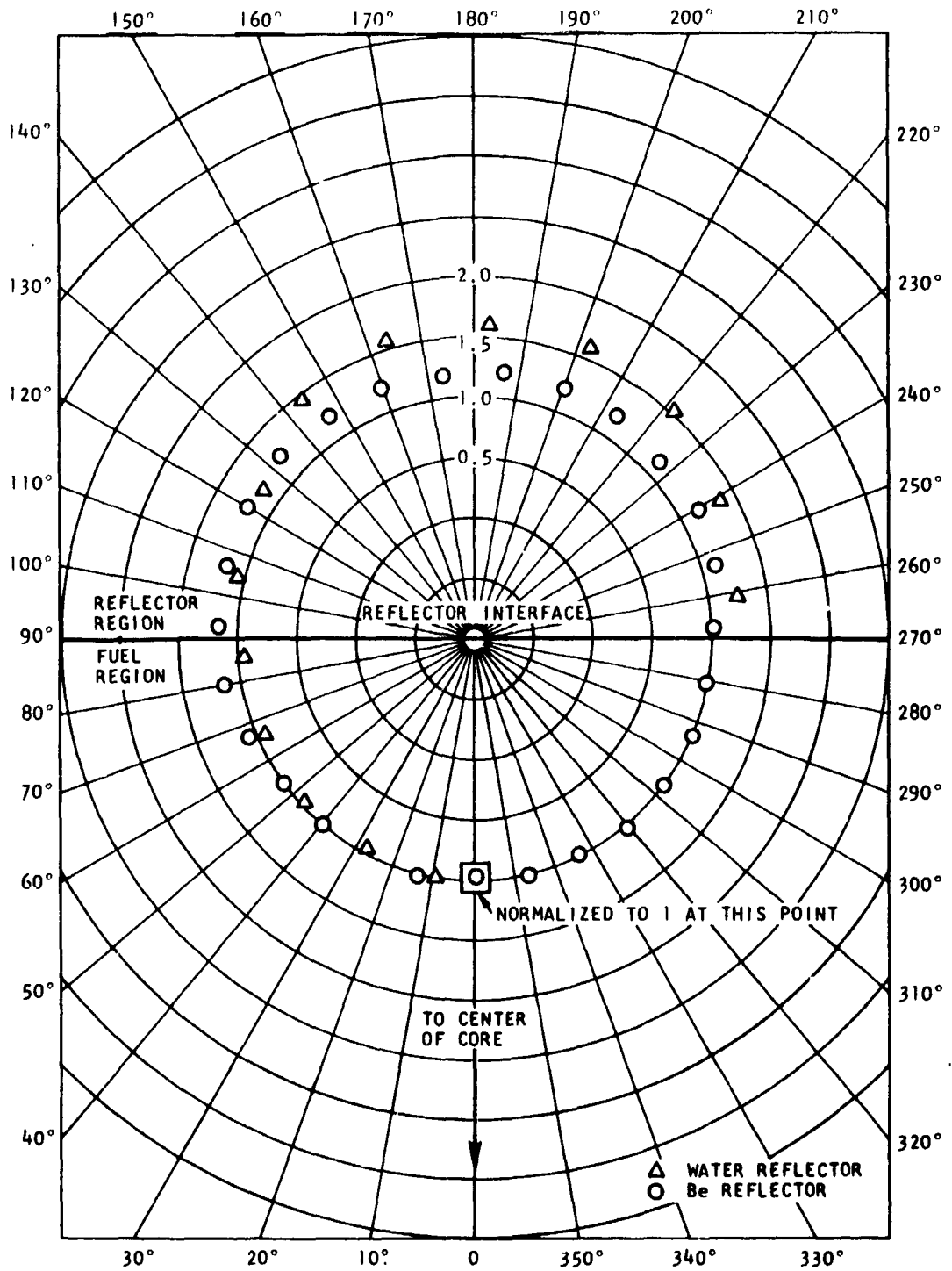


Fig. 3.8--Manganese foil activations around fuel element A-4 (Azimuthal Plot)



analyzed using a 3-in. diameter well-crystal system to display the gamma-ray spectrum on a 256-channel analyzer. Results are shown in Fig. 3.9.

### 3.3.5 FLUX AND POWER DISTRIBUTIONS THROUGHOUT CORE

An axial flux map was made in Core I using copper and manganese foils. These foils were taped to the outside of the  $U^{238}$  ring in element G-7 and to the aluminum top and bottom spacer tubes. They were irradiated for approximately 20 minutes at ten watts. The gamma radiation from the decay of the 2.58 hour half-life Mn-56 and that of the 12.9 hour Cu-64 were counted in the scintillation well-crystal counter. The manganese activation was sufficient to enable counting of the 1.80-MeV and 2.12-MeV photopeaks. The copper foils were counted above a bias of 400 keV to detect the .510-MeV annihilation radiation.

The foils used were weighed and the usual corrections were made for weight deviations, counter background, and decay. Results of the axial mapping are shown in Fig. 3.10.

A radial power map for Core I was made at the Stage 12 level of the reactor core using circular foils punched from the "E" rings of the uranium-aluminum fuel alloy and gamma-counting the fission product activity.

Results of the radial power mapping along the "G" element row are shown in Fig. 3.11. The variation in power among individual fuel rings is clearly shown in those elements where all five rings of the elements were punched and counted. Furthermore, the thermal flux return from the reflector shows up in the power spike at the outer edge of the core.

Mapping of the radial traverse at  $90^\circ$  to the "G" element row (through elements G-7, E-6, C-5, and A-4) is shown in Fig. 3.12. Here

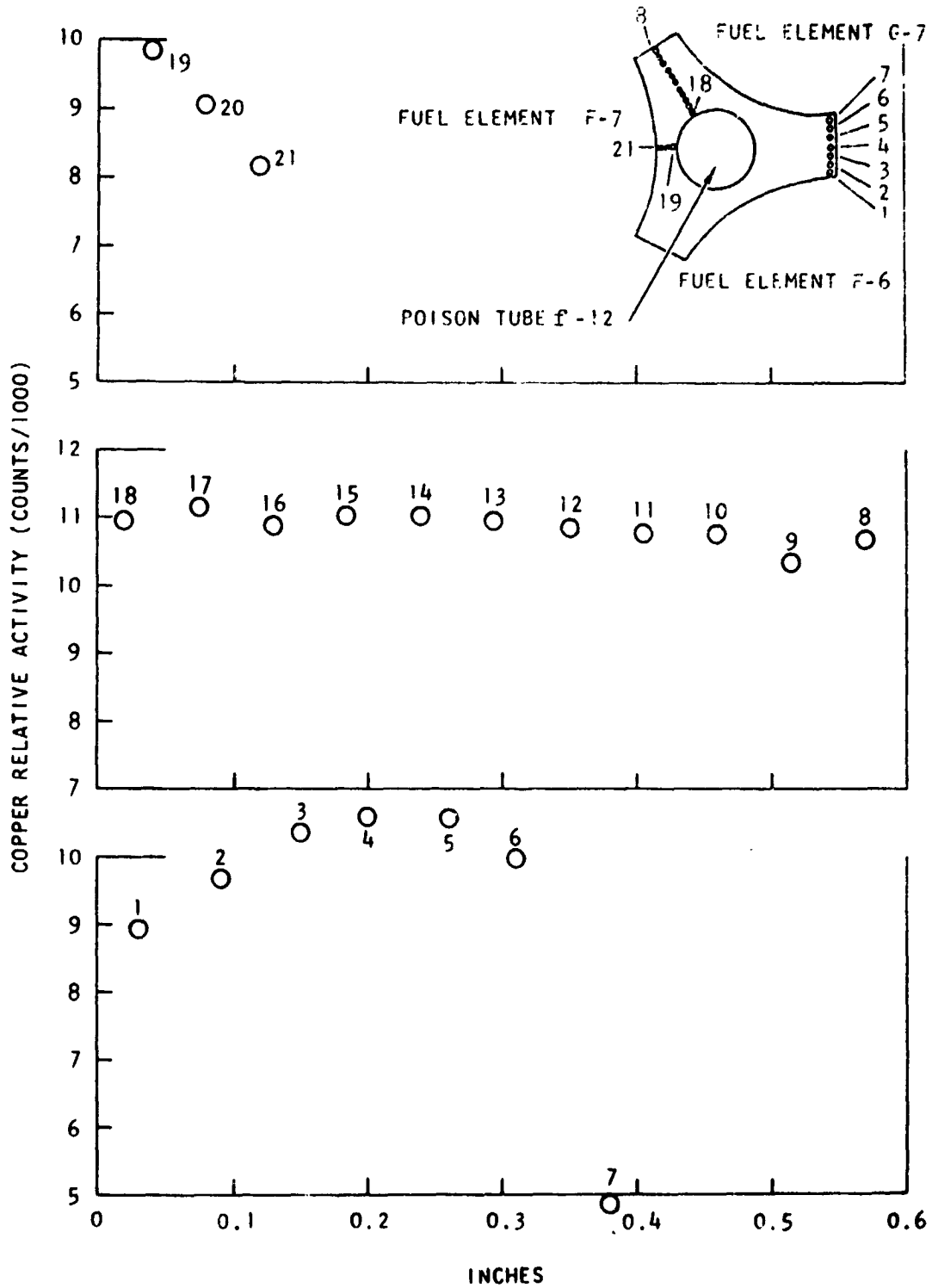


Fig. 3. 9--Flux traverse with Cu wire, Core I

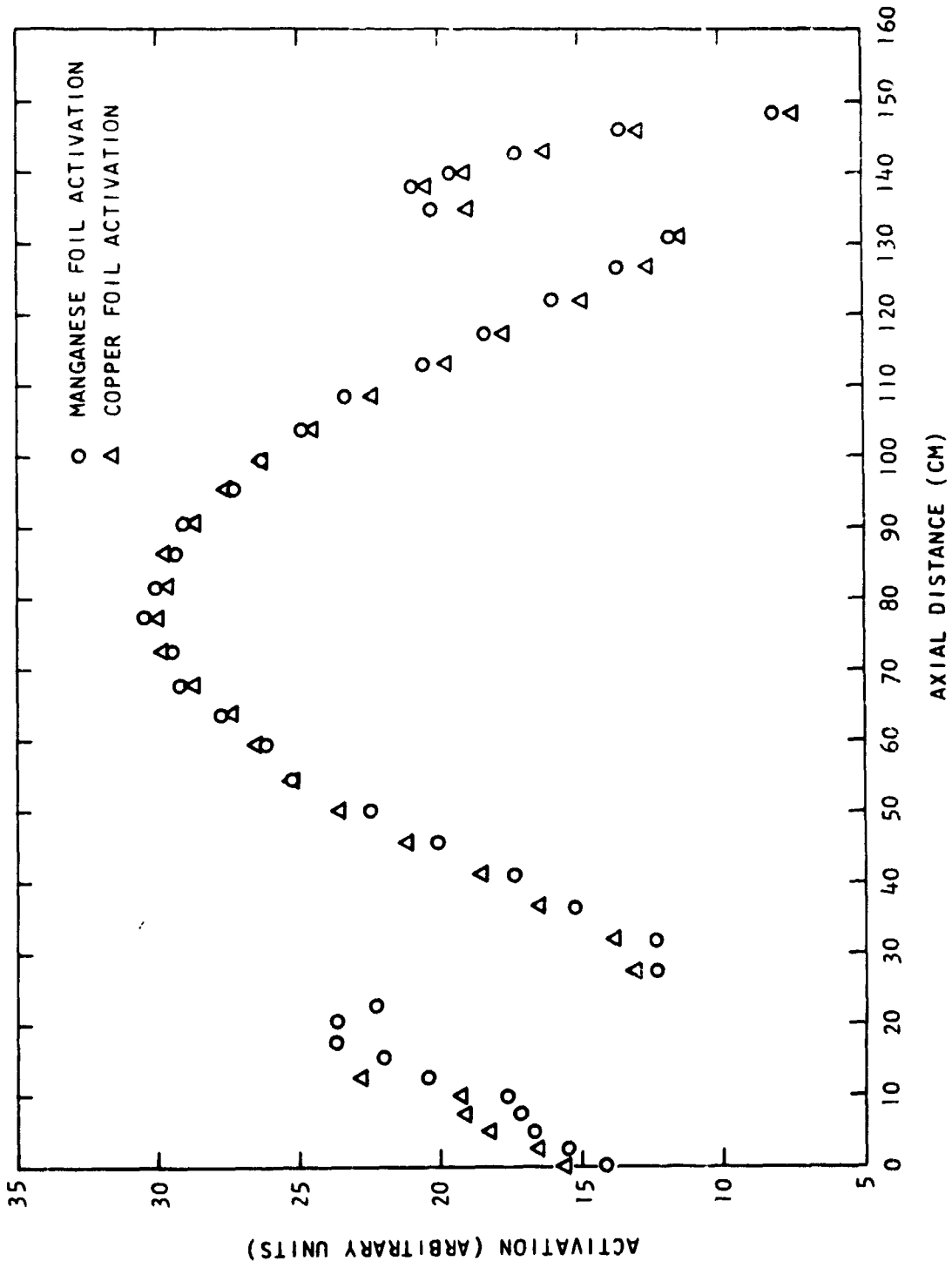


Fig. .3.10--Axial flux traverse, Core I

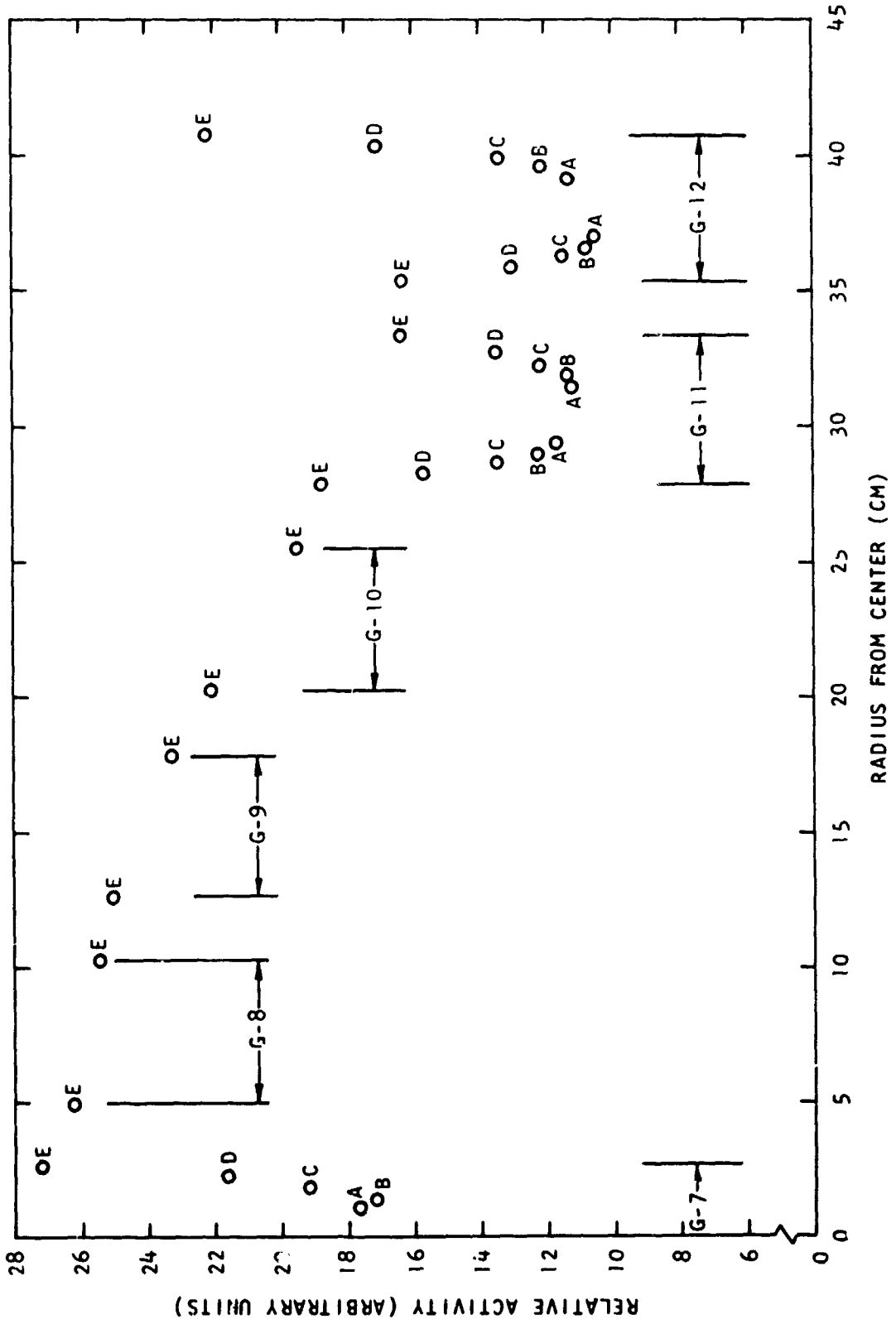


Fig. 3.11--Radial power traverse through G-row, Core I

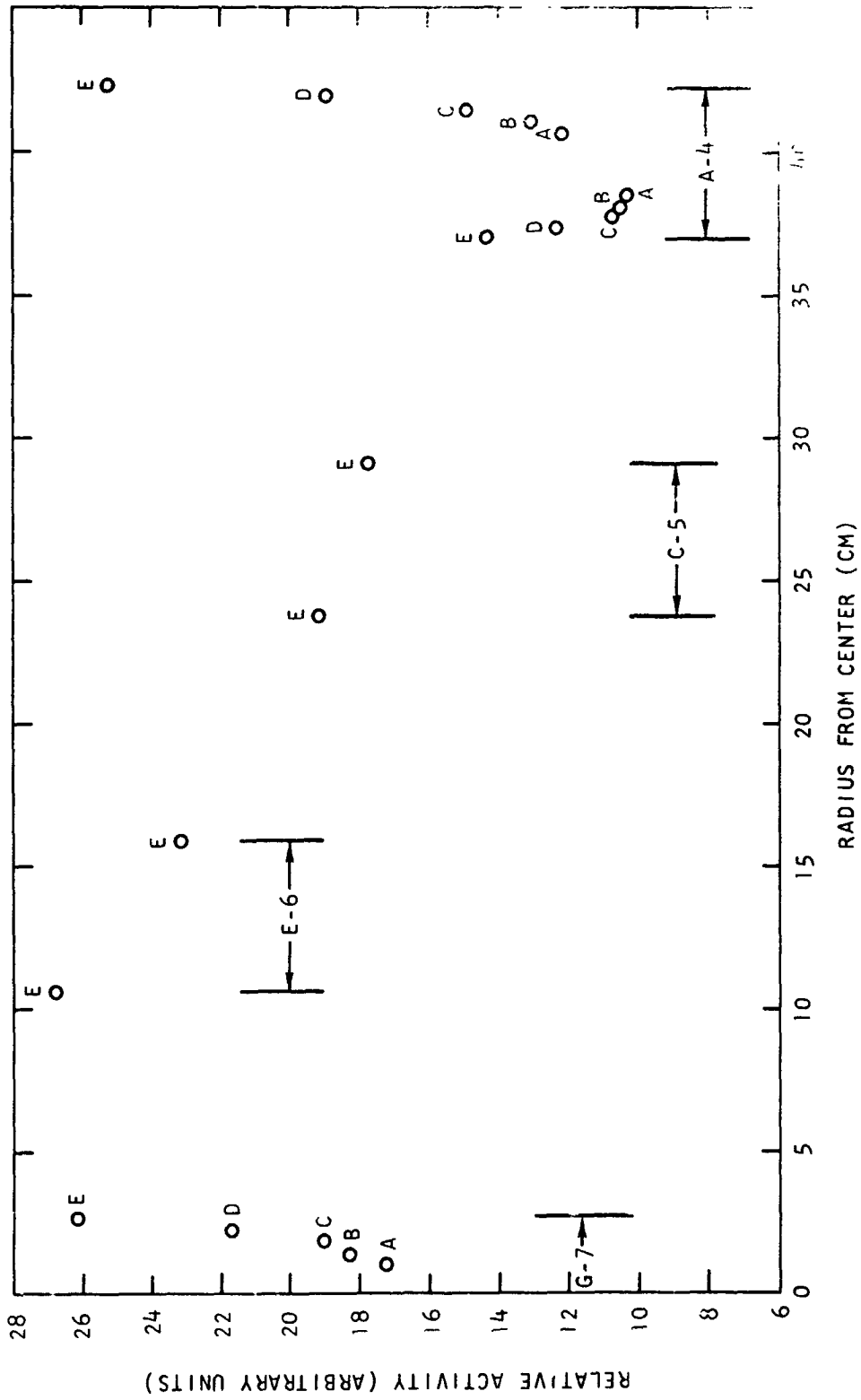


Fig. 3.12--Radial power traverse at 90° to G-row, Core I

the skewing of the power distribution through the element at the core-reflector interface (which is more clearly defined at element A-4 than at element G-12), is quite noticeable.

An axial power map for Core III was made in element G-7 with U-AL foils from fuel ring E of each stage. At each stage height, two foils which were 180 degrees apart were activated. The average activation of the two foils at each stage is plotted in Fig. 3.13, where the influence of the bottom beryllium reflector can clearly be seen.

Radial power traverses for Core III were made in the four fuel elements G-7, E-6, C-5 and A-4. Stages 3, 6, 11, 16, and 21 were chosen for mapping and foils from the "E" rings of each element at these axial stage heights were counted. Additional mappings through the inner rings of elements G-7 and A-4 were made in Stages 3 and 11. Results of the radial power mapping are displayed in Figs. 3.14 through 3.16, where the relative activation is shown.

### 3.3.6 CADMIUM RATIO MEASUREMENTS

The cadmium ratio of several common foil materials was measured in all three cores. The foils were 1/4-in. diameter and were covered with 3/8-in. diameter cadmium covers, 0.022 in. thick. The foils, both bare and covered, were taped to the outside of the U<sup>238</sup> ring on the twelfth fuel element stage. Table 3.18 gives the results.

Table 3.18

#### CADMIUM RATIO MEASUREMENTS

Core	Fuel Element	Material	Thickness (in.)	Cadmium Ratio
I	G-7	Au	0.002	1.51
I	G-7	Mn	0.005 (80 wt % Mn)	3.12
I	A-4 <sup>a</sup>	Au	0.002	2.54
I	A-4 <sup>a</sup>	Mn	0.005 (80 wt % Mn)	7.16
II	G-7	Au	0.002	1.45
III	G-7	Au	0.002	1.48
III	G-7	Mn	0.005 (80 wt % Mn)	2.52
III	G-7	Cu	0.005	4.32

<sup>a</sup>At core-reflector interface

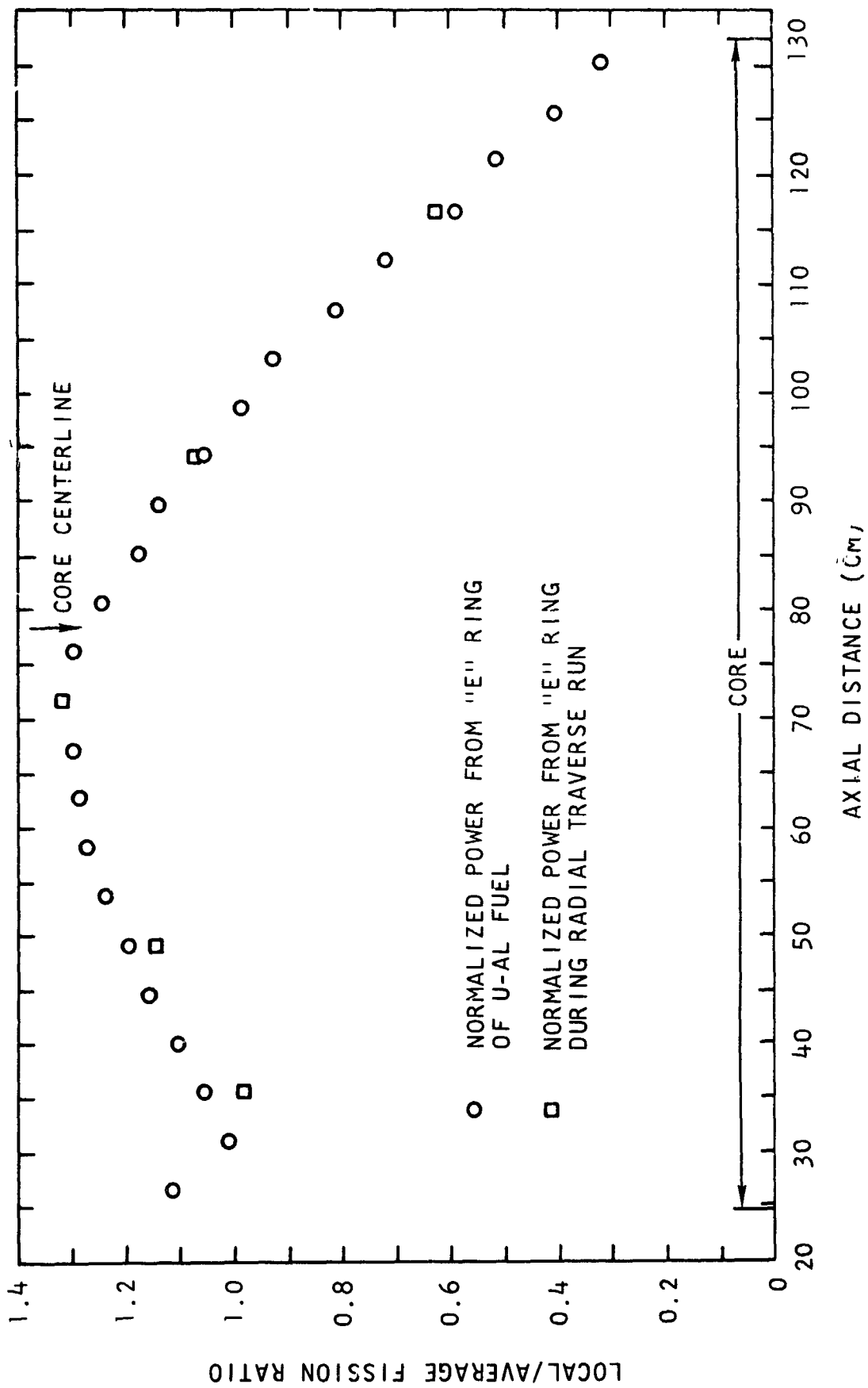


Fig. 3.13--Axial power traverse, Core III

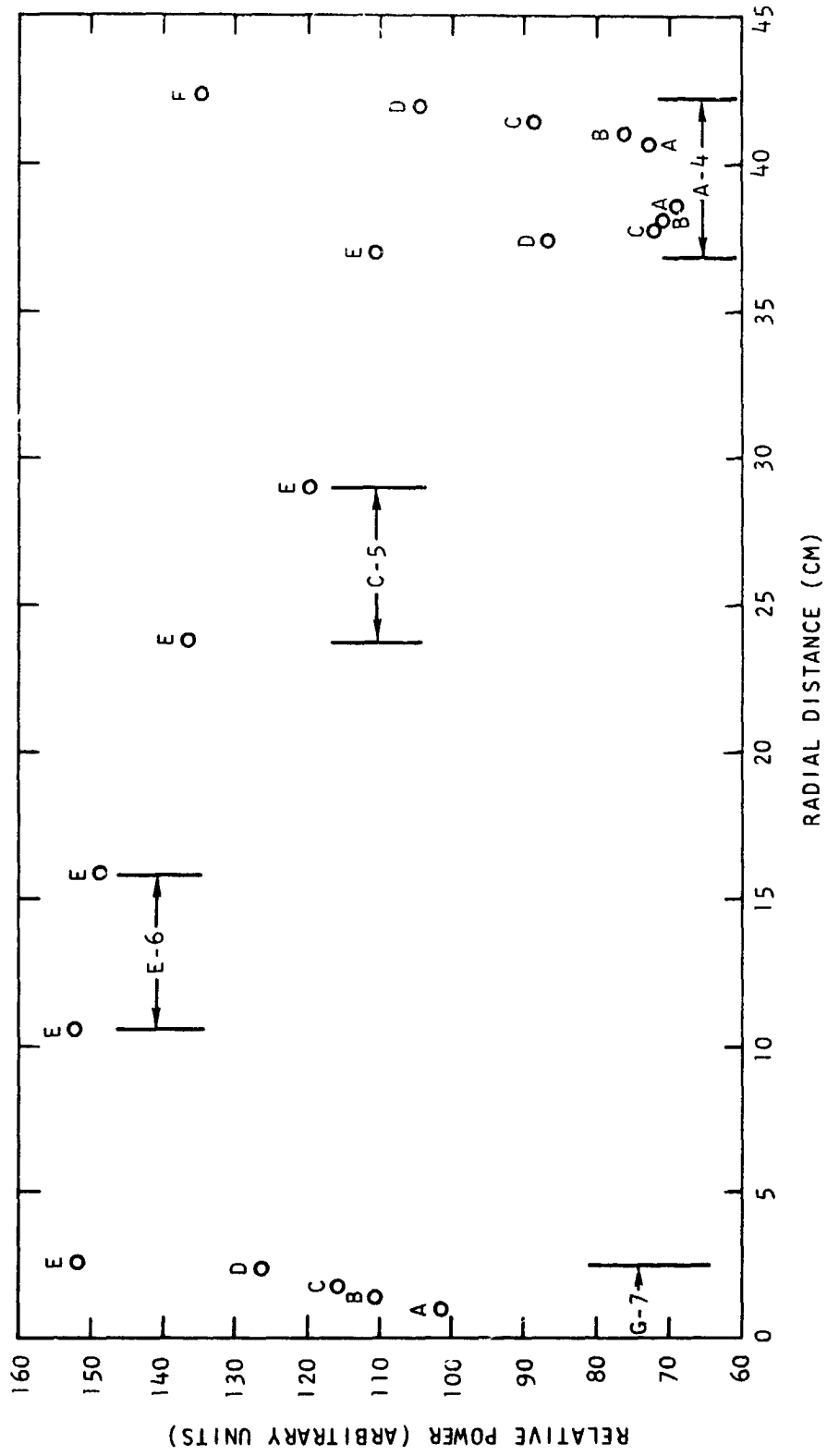


Fig. 3. 14--Radial power traverse at Stage 3 level, Core III



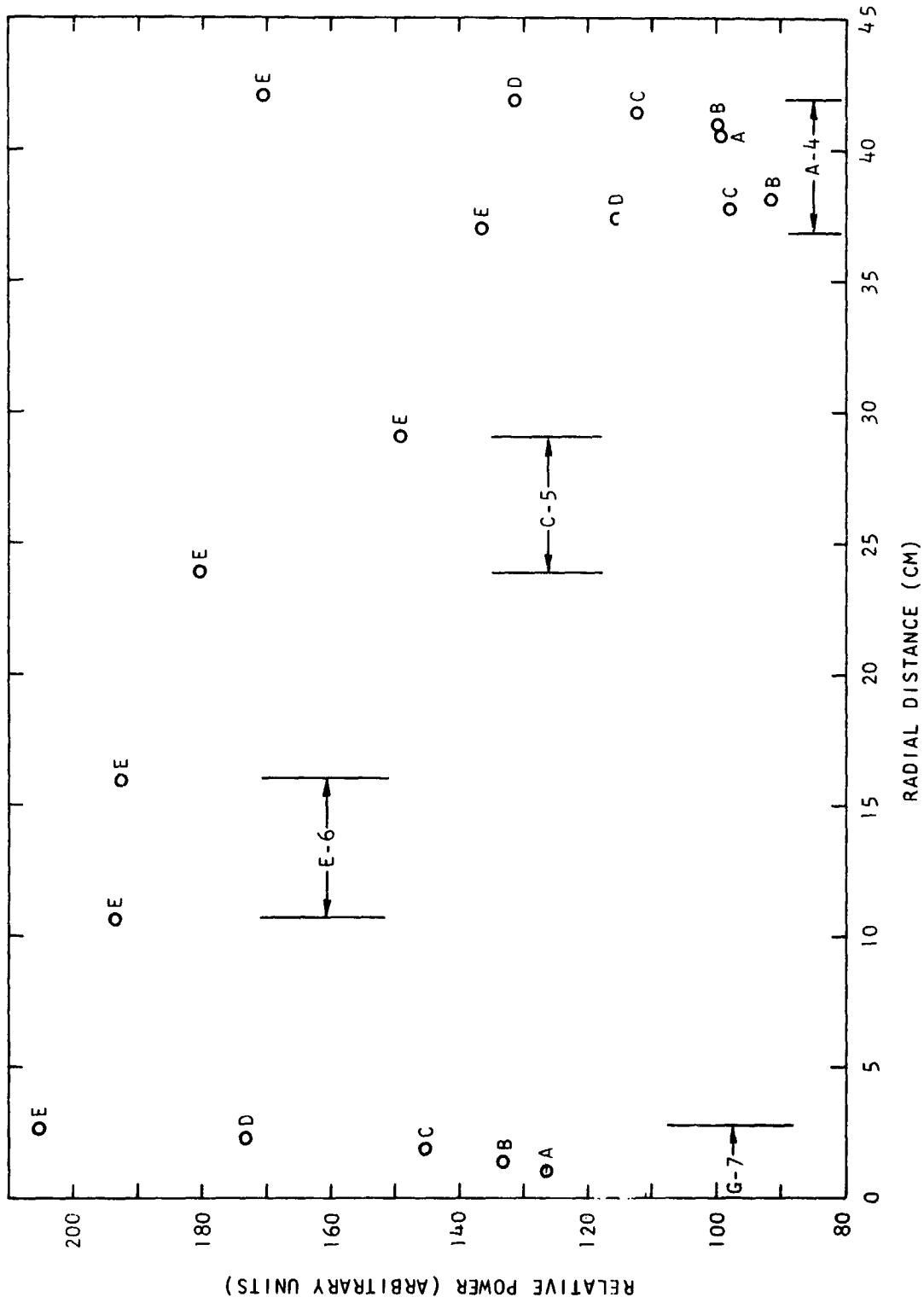


Fig. 3.15--Radial power traverse at Stage 11 level, Core III

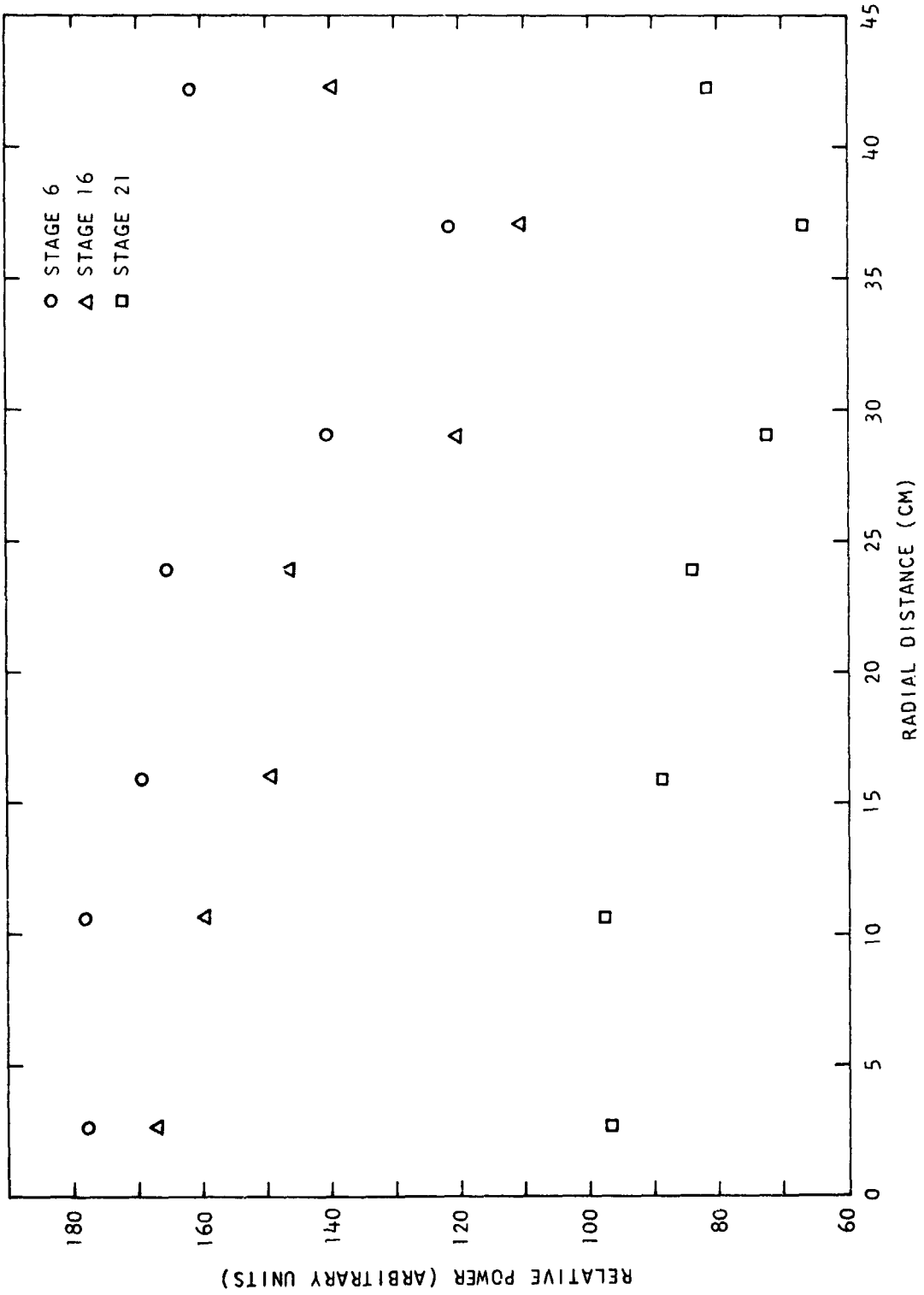


Fig. 3.16--E-ring activations at Stages 6, 16, 21, Core III

## 3.3.7 RELATIVE POWER CALIBRATION, CORE III

3.3.7.1 Radial

The irradiated fuel rings from the twelfth stages of the elements within the triangle G-1, G-7, and K-1 were gamma counted while rotating on a mandrel as previously described. One fuel ring (the A-ring of element G-7) was chosen for use as a standard to be repetitively counted. The decay curve generated was then used to normalize all counts to the same counting time. Normalization of the  $U^{235}$  content of the fuel rings was accomplished by weighing the rings. A constant weight percent of  $U^{235}$  was assumed.

Following the reduction of the counting data, all rings of a given diameter were normalized to the corresponding ring in element G-7, which was arbitrarily set equal to 1.000. Results are shown in Table 3.19.

Table 3.19

## RELATIVE RADIAL POWER DISTRIBUTION DATA

<u>Fuel Element</u>	<u>Stage-12 Fuel Ring</u>				
	<u>A</u>	<u>B</u>	<u>C</u>	<u>D</u>	<u>E</u>
K-1	0.740	0.725	0.717	0.739	0.772
J-1	0.730	0.691	0.702	0.713	0.754
J-2	0.717	0.695	0.727	0.703	0.713
J-3	0.808	0.787	0.781	0.794	0.818
H-1	0.739	0.752	0.762	0.766	0.796
H-2	0.688	0.665	0.647	0.663	0.687
H-3	0.794	0.770	0.755	0.771	0.804
H-4	0.885	0.887	0.882	0.851	0.904
H-5	0.958	0.938	0.971	0.933	0.949
G-2	0.719	0.685	0.691	0.697	0.734
G-3	0.749	0.698	0.718	0.715	0.762
G-4	0.855	0.820	0.866	0.848	0.854
G-5	0.936	0.909	0.963	0.938	0.937
G-6	0.984	0.988	0.980	0.960	0.999
G-7	1.000	1.000	1.000	1.000	1.000

Due to differences in counting geometry from one size fuel ring to another, it is not possible to use the above data to relate the power in the five sizes of fuel rings. In order to obtain this relation, the five fuel rings from the 12th stage of fuel element G-7 were flattened and cut to equal areas. They were then gamma counted in the same geometry. The results thus obtained are proportional to the power density in each ring, which is shown in the second column of Table 3.20. Multiplying the power density by the average weight of  $U^{235}$  per ring and renormalizing to 1.000 for the E-ring, gives the relative power among fuel rings, as shown in the fourth column of Table 3.20.

Table 3.20  
RELATIVE POWER PER FUEL RING IN THE  
12th STAGE OF G-7

<u>Ring</u>	<u>Power Density</u>	<u>Avg. Wt. <math>U^{235}</math> Per Ring (gm)</u>	<u>Relative Power</u>
A	0.672	3.727	0.2685
B	0.704	5.084	0.3836
C	0.756	6.547	0.5305
D	0.835	8.018	0.7176
E	1.000	9.329	1.000

The last column forms the basis for normalization of the entire map of the 12th stage in the triangular sector of the core. Renormalization of Table 3.19 gives the results shown in Table 3.21, where the fuel rings of G-7 now have the proper relative power.

A useful number to be used in comparing the preceding results with calculations is the peak-to-average value. This has been computed by dividing the sum of Column 5 of Table 3.21 by the total number of fuel elements (121 to obtain the average relative Stage 12 power-per-fuel element. The peak-to-average value is then found to be 1.264.

A plot of the radial power distribution based on the results of Table 3.21 is shown in Fig. 3.17. A renormalization of the data, assigning the value of 1.634 to fuel element G-7, was made to facilitate comparison with calculations.

#### 3.3.7.2 Axial

The "E" and "A" fuel rings from all 24 stages of fuel elements G-7, G-4 and K-1 were irradiated and then gamma counted using the rotating mandrel procedure. The E-ring results are given in Table 3.22. They are normalized to the value 1.634 at the 12th stage of fuel element G-7 to facilitate comparison with calculation. The relative normalization between the three fuel elements is based on the Stage 12 radial data given in Table 3.21. Figure 3.18 is a plot of these data.

The curves of Fig. 3.18 are redrawn normalized to the local/average fuel element power for each element in Fig. 3.19. The similarity of the three curves is an indication of the separability of the axial and radial flux profiles.

The A-ring axial data had essentially the same relative shape as the E-ring data.

#### 3.3.7.3 Total Relative Power

If the relative radial power distribution shown in Table 3.21 is combined with the axial distribution for fuel element G-4 (G-4 is taken to represent the average axial shape for the core) and the resultant total power normalized to 1.00, the power in Stage 12 of fuel element G-7 will be 1.59. This number may be compared with the calculated value of 1.645.

Table 3.21  
RADIAL POWER, STAGE 12

Fuel Element	Relative Power Per Ring					Relative Power Per Stage	No. of Similar Elements	Relative Power in Core	Percent Core Power
	A	B	C	D	E				
K-1	.199	.278	.380	.530	.772	.744	6	4.464	4.66
J-1	.196	.265	.372	.512	.754	.724	12	8.688	9.07
J-2	.193	.267	.386	.505	.713	.712	12	8.544	8.92
J-3	.217	.302	.414	.570	.818	.800	6	4.800	5.01
H-1	.158	.288	.404	.550	.796	.771	12	9.252	9.67
H-2	.185	.255	.343	.476	.687	.671	12	8.052	8.41
H-3	.213	.295	.401	.553	.804	.781	12	9.372	9.79
H-4	.238	.340	.468	.611	.904	.883	12	10.596	11.08
H-5	.257	.360	.515	.670	.949	.949	6	5.694	5.95
G-2	.193	.263	.367	.500	.734	.709	6	4.254	4.44
G-3	.201	.268	.381	.513	.762	.733	6	4.398	4.59
G-4	.230	.315	.459	.609	.854	.851	6	5.106	5.33
G-5	.251	.349	.511	.673	.937	.938	6	5.628	5.88
G-6	.264	.379	.520	.689	.999	.983	6	5.898	6.16
G-7	.2685	.3936	.5305	.7176	1.000	1.000	1	1.000	1.04
							121	95.746	100.00

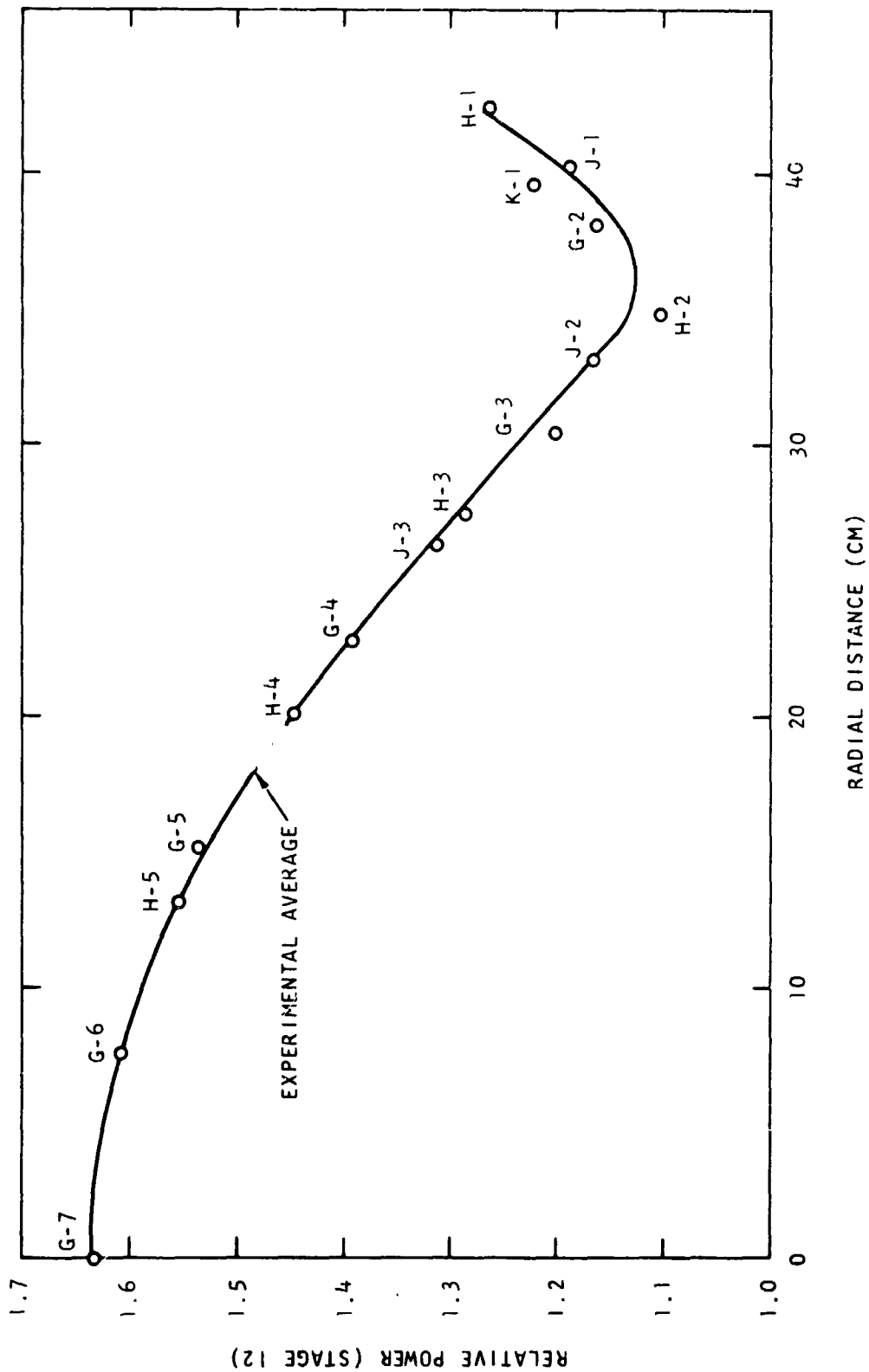


Fig. 3.17--Radial power profile, Core III

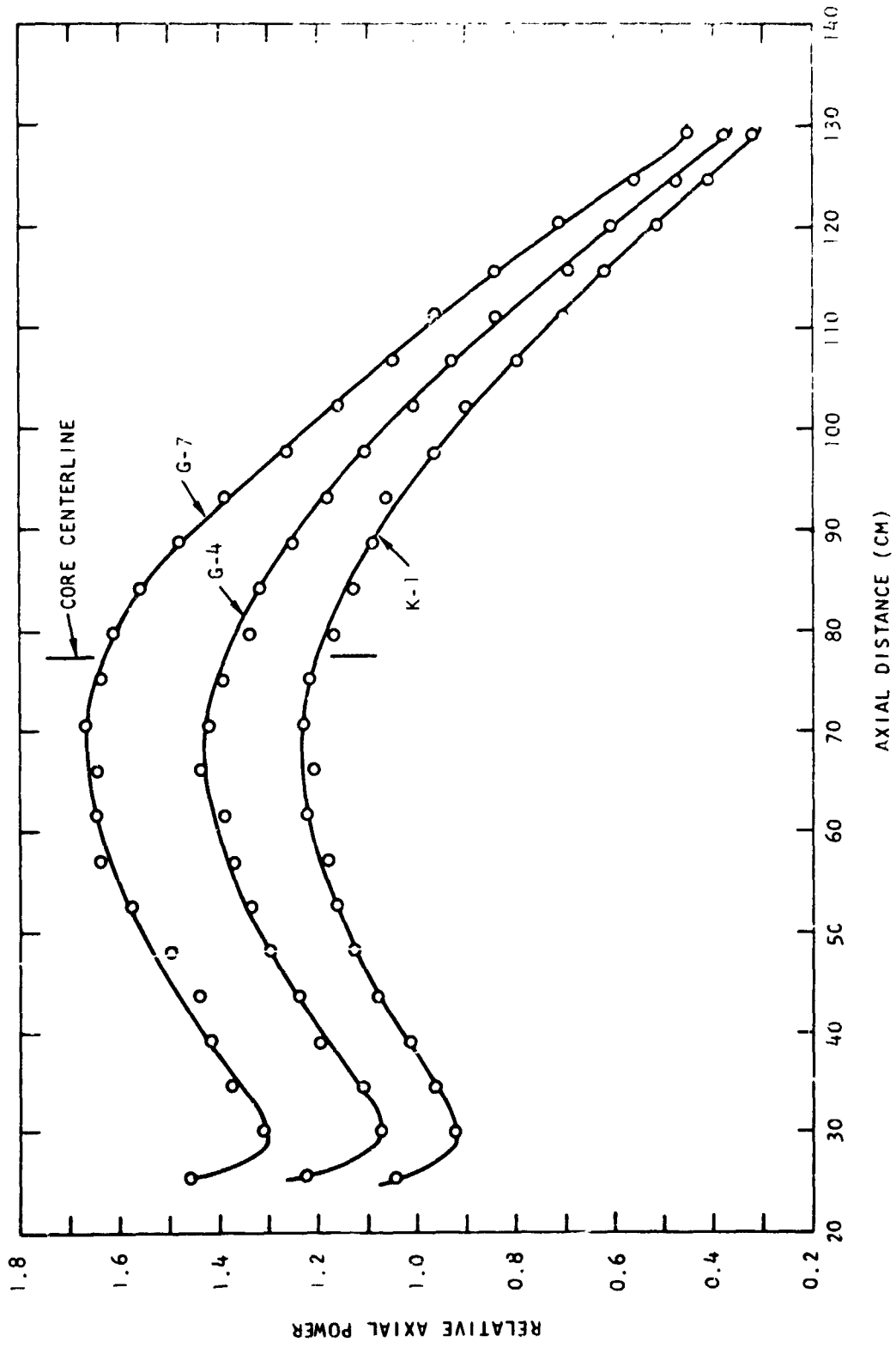


Fig. 3.18--Axial power profiles, E-ring



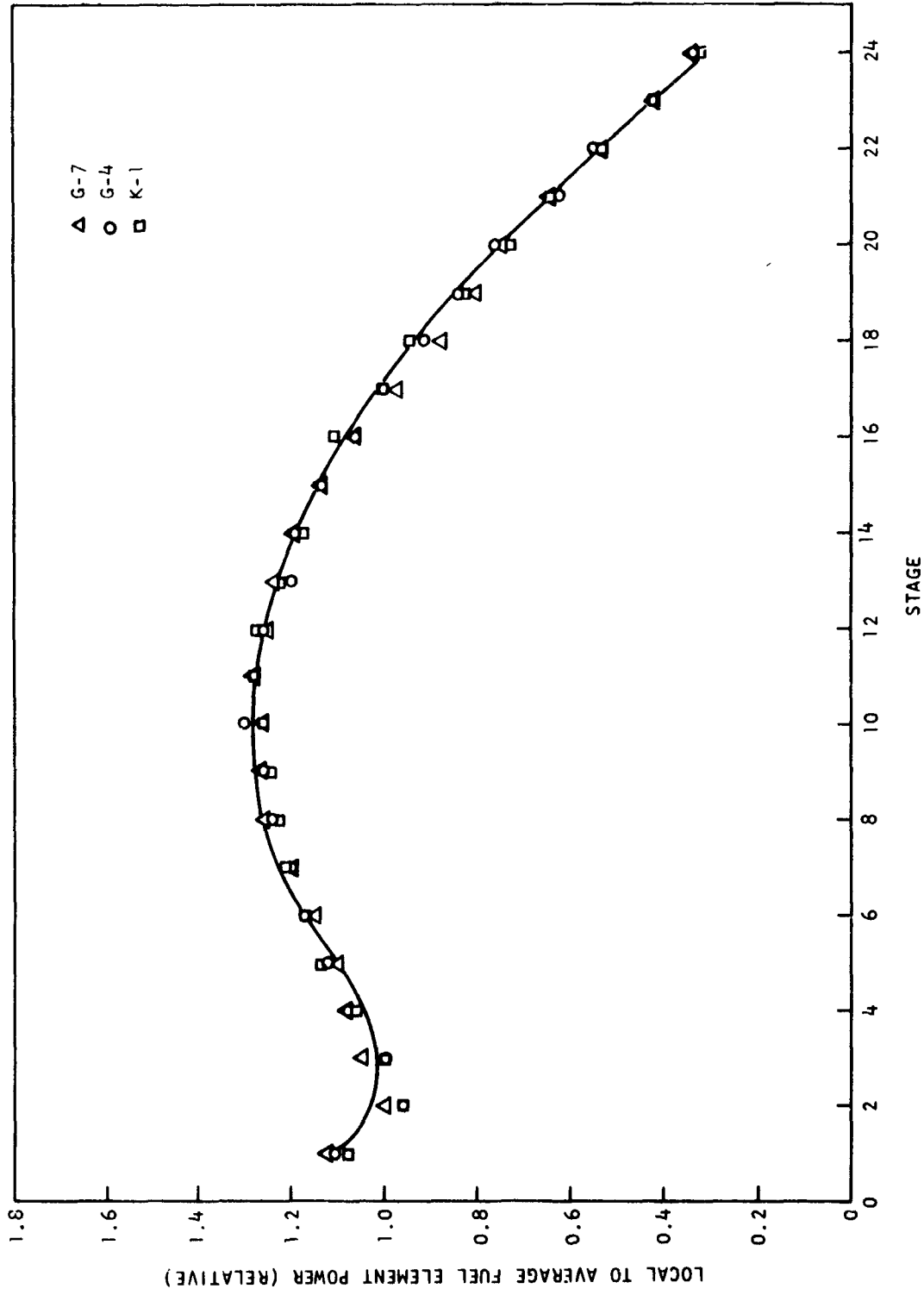


Fig. 3.19--Axial power profiles, E-ring (normalized)

Table 3.22  
AXIAL POWER PROFILE  
E-RING

<u>Stage No.</u>	<u>Axial Position of Center of Ring (cm)</u>	<u>Fuel Element</u>		
		<u>G-7</u>	<u>G-4</u>	<u>K-1</u>
1	25.75	1.460	1.223	1.034
2	30.25	1.309	1.075	0.922
3	34.75	1.368	1.104	0.960
4	39.25	1.414	1.191	1.010
5	43.75	1.433	1.240	1.077
6	48.25	1.494	1.296	1.121
7	52.75	1.575	1.332	1.159
8	57.25	1.639	1.368	1.174
9	61.75	1.646	1.387	1.218
10	66.25	1.643	1.434	1.205
11	70.75	1.668	1.419	1.228
12	75.25	1.634	1.390	1.216
13	79.75	1.609	1.332	1.164
14	84.25	1.557	1.319	1.123
15	88.75	1.475	1.247	1.084
16	93.25	1.386	1.172	1.059
17	97.75	1.261	1.102	0.961
18	102.25	1.153	1.004	0.895
19	106.75	1.045	0.927	0.794
20	111.25	0.960	0.836	0.701
21	115.75	0.840	0.690	0.617
22	120.25	0.705	0.605	0.515
23	124.75	0.553	0.469	0.406
24	129.25	0.448	0.375	0.312

### 3.3.8 ABSOLUTE POWER MEASUREMENTS

Bare and cadmium-covered gold and manganese-copper alloy foils were exposed on the exterior of the  $U^{238}$  ring at Stage 12 of fuel element G-7 in Core III. Following irradiation, they were counted in the manner previously described in Section 3.3.1.

The conversion factors relating the absolute disintegration rates to the fluxes and hence the core power were obtained by calculation as discussed in Section 6.3.4.

Results of several measurements, all of which were made with the core at a constant power for over one half-hour are shown in Table 3.23.

Table 3.23  
ABSOLUTE POWER CALIBRATION

Foil Material	Thickness (in.)	Power (watt)		
		Run 1	Run 2	Run 3
Au	.002	82.6	85.2	84.7
Mn	.002	80.7	--	--
Mn	.005	--	72.8	70.4

The manganese-copper alloy exhibits a wider spread than expected. This may be due in part to uncertainty in the chemical analysis of the alloy or in part to nonhomogeneity of the alloy. Since the gold was in pure form the average of the gold results is considered to be the more reliable measurement. Thus an absolute power of 84.2 watts, the average of the gold measurements, is recommended for use in the analysis of the gamma heating experiments discussed in Section 3.6.

### 3.4 TEMPERATURE COEFFICIENT MEASUREMENTS

#### 3.4.1 METHOD

The change in reactivity associated with heating of the water in all three cores was measured by the following procedure. First, since a predominantly negative temperature coefficient was anticipated, the core excess reactivity was adjusted to a value slightly in excess of \$0.40.

With the reactor just at delayed critical, the reactor tank water was circulated through the heater loop and its temperature raised. The change in reactivity with increasing water temperature was compensated for by movement of the regulating rods. After reaching the desired higher temperature the heater was put under proportional control and the system allowed to come to temperature equilibrium. The poison tube in position g-14 contained water with no cadmium and three iron-constantan thermocouples. Four thermocouples and one thermohm were positioned as shown in Table 3.24.

Table 3.24

## LOCATION OF TEMPERATURE MEASURING SENSORS

<u>Thermocouple</u>	<u>Radial Position</u>	<u>Axial Position</u>
1	g-14	Lower reflector interface
2	g-14	Center of core
3	g-14	Upper reflector interface
4	10 in. beyond the reflector interface at midcore height	
(thermohm)	10 in. beyond the reflector interface at midcore height	

There were also several iron-constantan thermocouples in the beryllium side reflector of Core III. Typically, a ten-degree centigrade increase in water temperature could be made in about one hour with another half-hour being required to attain sufficient equilibrium to enable a reliable positive drift measurement to be made at a fixed regulating rod setting. The water temperature measurements were generally uniform to within  $\pm 0.25^{\circ}\text{C}$  after about 1/2 hour although a slightly longer time was required in the beryllium-reflected core. The thermohm bridge measurement of the absolute temperature is accurate to about  $\pm 0.02^{\circ}\text{C}$ .

In all cases the calibration of the regulating rods was checked at the higher temperature and found to be essentially identical with the room temperature calibration.

### 3.4.2 RESULTS

Figure 3.20 shows the relative change in core excess reactivity resulting from the increase in water temperature.

In addition, in Core III a rough measurement was made to determine the size and magnitude of the beryllium reflector temperature coefficient. This was accomplished in the following manner. The water in the dump tank was preheated to approximately 70°C. (The reflector and core components were slightly above room temperature.) The hot water was then pumped into the reactor tank. The temperature sensors at the locations indicated in Table 3.24 were used to determine when the poison tube temperature was the same as the bulk water temperature. This occurred quite rapidly. The beryllium reflector temperature increase was much slower. The change in reactivity was measured as the reflector temperature increased from 47°C to 65°C. With water temperature held constant at 66.8°C the results shown in Fig. 3.21 were obtained. There is considerable uncertainty in their interpretation because of effects arising from the nonuniformity of the beryllium temperature and possible changes in the fuel element subassembly temperature.

## 3.5 PULSED NEUTRON MEASUREMENTS

### 3.5.1 METHOD

The technique of pulsing was identical in all three cores and utilized a Kaman A-801 neutron generator. The generator controls were mounted in the control room and the neutron generating head, which consists of a pulse transformer and deuterium-tritium source tube, was

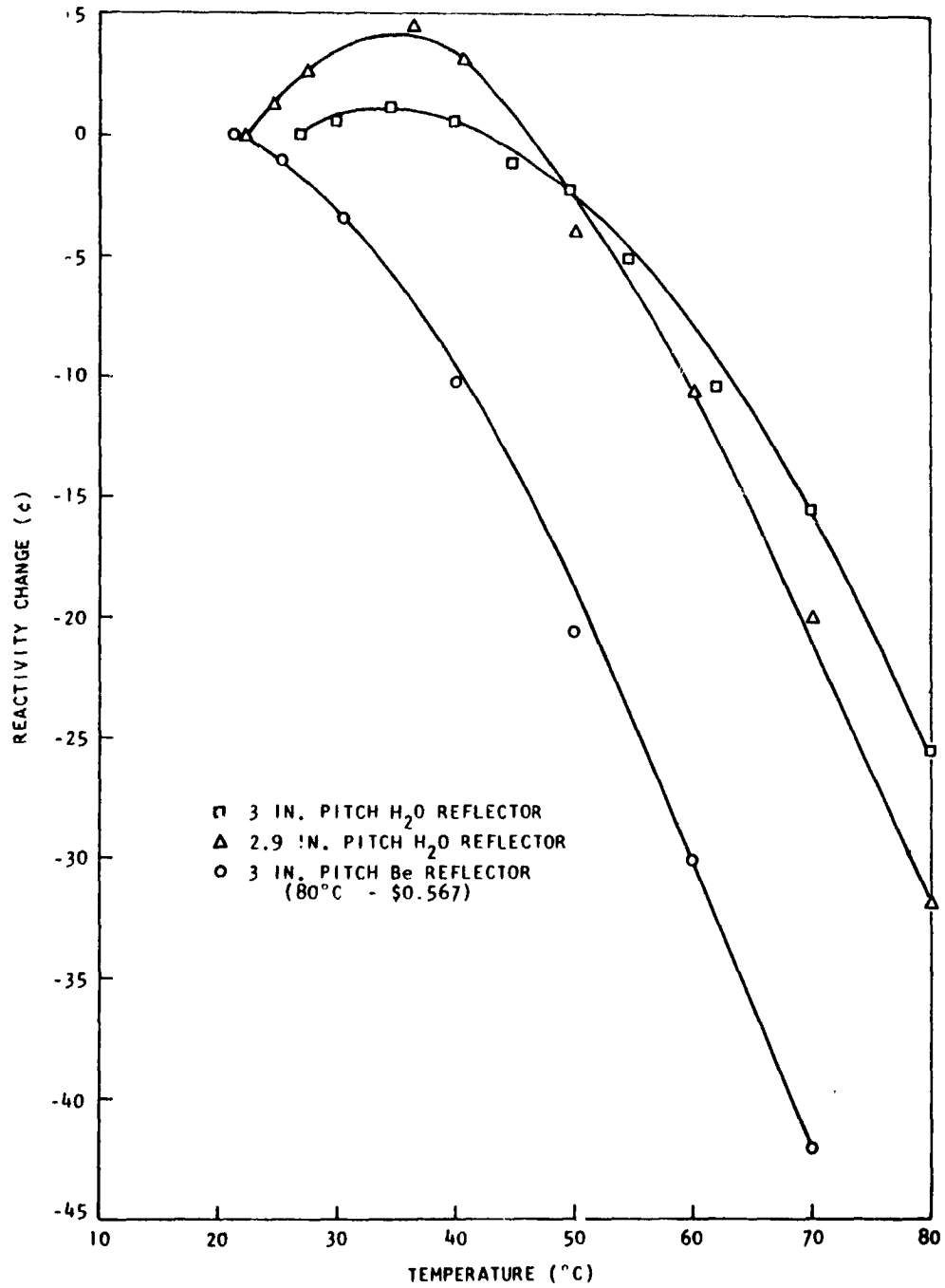


Fig. 3.20--Change of reactivity with temperature

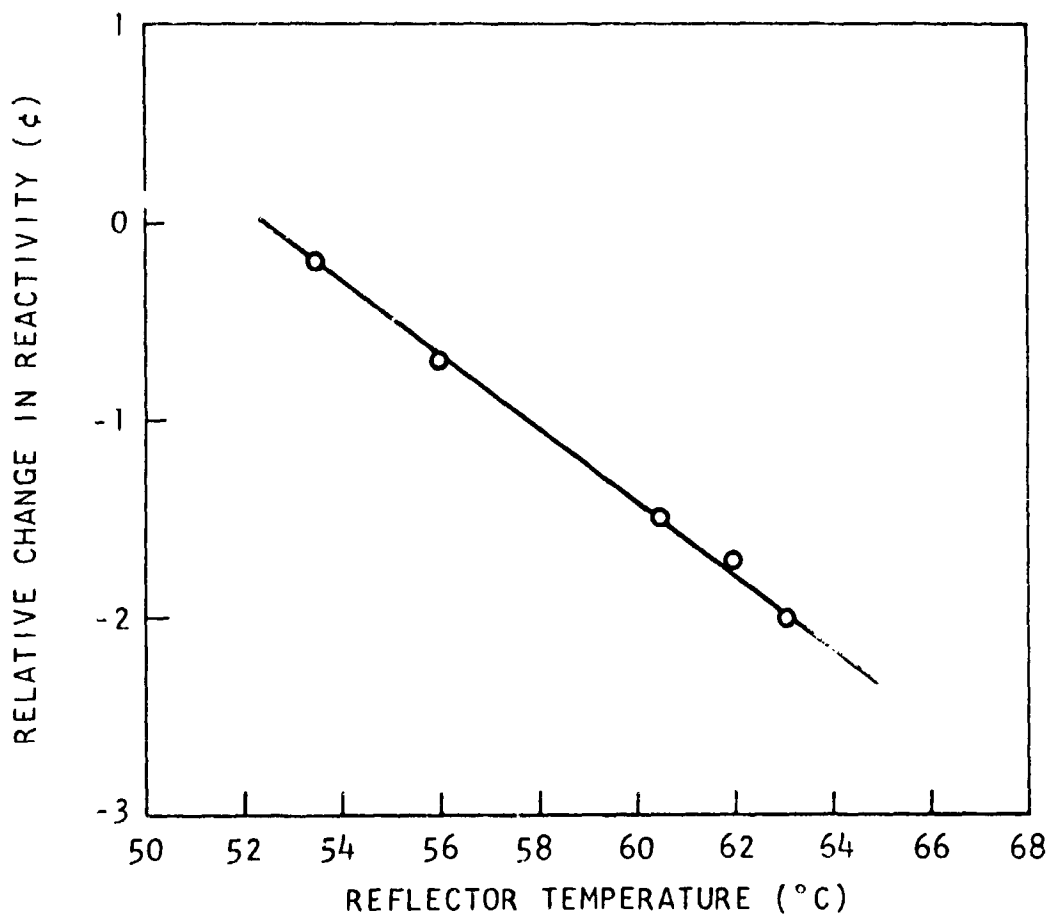


Fig. 3. 21--Change of reactivity with reflector temperature

mounted in a water-tight container just outside of the side reflector region at about midcore height. The neutrons are generated in this type of unit by applying a short high-current electrical pulse to the pulse transformer. This results in a high potential being developed between the deuterium source and the tritium bearing target. Deuterium ions are accelerated into the tritium-bearing target, producing 14-MeV neutrons. The manufacturer's specifications claim that the generator can produce bursts of up to  $10^8$  neutrons at a maximum pulse rate of 10 per second.

The detection and time analysis of the resultant neutron burst were accomplished in the following manner. A small  $\text{BF}_3$  probe was placed in a voided poison tube in core location f-12. The output pulses from the probe were integrated in a fast solid-state preamplifier attached to the probe. These pulses were shaped and delay line clipped in a fast solid-state amplifier in the control room. The amplified pulses were then fed into a fast solid-state integral discriminator. The output from the latter, which is a very short duration square wave, was used to drive the time analyzer. The analyzer was gated on by a timing pulse from the pulse generator control unit. Discriminator output pulses following the neutron burst were counted in various time interval channels in the analyzer, the minimum channel width being 16 microseconds.

Data obtained in this way were reduced by first subtracting the background, i. e., the essentially constant number of counts in each channel following the prompt decay. During this time the delayed neutrons act as a source and the total neutron population depends on the core multiplication. The data were then plotted on semilogarithmic graph paper. By neglecting the first few channels where transient effects and counting rate losses cause distortion, the prompt decay constant  $\alpha$  was determined by fitting the data with a straight line and determining the time required for the neutron population to fall off by a factor of  $e$ .



To determine the ratio of  $\bar{l}/\beta_{\text{eff}}$  (the prompt mean lifetime divided by the effective delayed neutron fraction) experimentally, all three of the cores were pulsed at very near delayed critical, the amount subcritical being determined from a calibrated control rod.

### 3.5.2 RESULTS

All of the following data have been reduced using the following expressions to relate reactivity and the experimentally determined values of  $\alpha$ .

$$\rho_p = \rho - 1 = \frac{\Lambda\alpha}{\beta_{\text{eff}}} \quad (3.2)$$

$$\Lambda = \bar{l}/k_{\text{eff}} \quad (3.3)$$

$$\rho = \frac{k-1}{k\beta_{\text{eff}}} \quad (3.4)$$

$\rho_p$  is the prompt reactivity in dollars,  $\rho$  is the delayed reactivity in dollars.  $\Lambda$  is the mean generation time, and  $\bar{l}$  is the prompt mean lifetime. Using the value of  $\alpha$  measured for the just subcritical core, expressions (3.2) through (3.4) were solved for  $\bar{l}/\beta_{\text{eff}}$ . Since this ratio is rather insensitive to changes in the cadmium concentrations, the value obtained in the just subcritical core was used in relating the value of  $\alpha$  to reactivity for the cores with the same pitch and reflectors but with increased cadmium loadings. An iterative procedure was followed until the value for the generation time  $\Lambda$ , as determined from expressions (3.2) through (3.4), converged.

Corrections have been applied to account for the absence of poison tubes at the control rod, source tube, and detector locations; thus the following results represent the standard core configuration of 121 fuel

elements and 204 poison tubes. The results shown in Table 3.25 are analyzed in Section 6.5.

Table 3.25

## RESULTS OF THE PULSED NEUTRON SOURCE MEASUREMENTS

Core	Poison Tubes	$\alpha$ (sec <sup>-1</sup> )	$\bar{\lambda}/\beta_{\text{eff}}$ (sec)	Iterated Reactivity (\$)	"Standard Core" Reactivity (\$)
I	C	- 340.0	$4.06 \times 10^{-3}$	- 0.28	
	D	- 940.0		- 2.88	- 2.91
	E	- 2280.0		- 8.80	- 9.01
II	H	- 317.0	$4.12 \times 10^{-3}$	- 0.305	
	C	- 1578.0		- 5.79	- 5.73
III	K	- 306.0	$4.51 \times 10^{-3}$	- 0.38	
	E	- 674.0		- 2.08	- 2.77
	L	- 1316.0		- 5.14	- 6.06

The 2.9-in. pitch core was initially loaded without cadmium poison tubes to obtain data on an unpoisoned core. A pulsed neutron measurement of  $\alpha$ , the prompt neutron decay constant, was made on the symmetric loading of 61 fuel elements. (This loading filled the center location plus the next four "rings" shown in Fig. 2.6.) The value of  $\alpha$  obtained for the 61-element array was  $1701. \text{ sec}^{-1}$ .

The loading was continued until criticality was achieved with the 84th element. The symmetric loading of 85 fuel elements with no poison tubes was found to have an excess reactivity of \$0.47 without applying corrections. This loading filled the inner five rings with the exception of locations B2, B7, G2, G12, M2, and M7. After obtaining several calibration points on the regulating rods, this core was pulsed while \$0.14 subcritical. A value of  $\alpha = 285. \text{ sec}^{-1}$  was obtained. This gives a value of  $\bar{\lambda}/\beta_{\text{eff}} = 4.00 \times 10^{-3}$  seconds.

Type H poison tubes were added to the 85-element core at all points interior to the loaded elements (128 poison tubes). The core was pulsed and found to have a value of  $\alpha = -1502 \text{ sec}^{-1}$ .

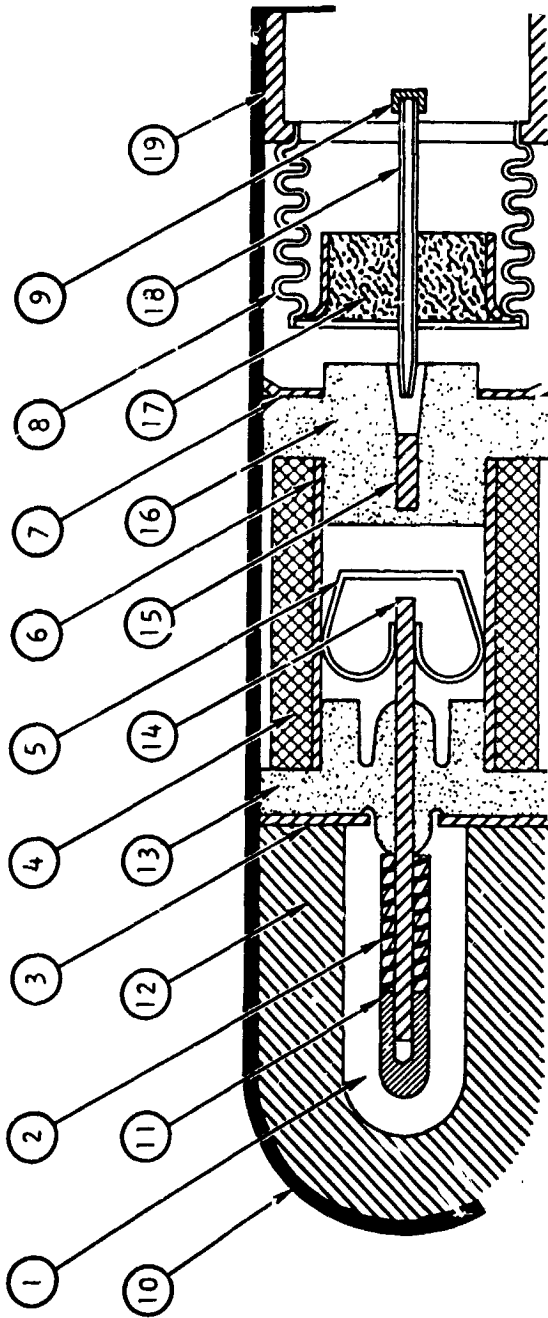
### 3.6 GAMMA HEATING EXPERIMENTS

#### 3.6.1 INTRODUCTION

The measurement of the gamma and neutron dose distribution in both the radial and axial dimensions of Core III were made using thimble ionization chambers of two types: one sensitive mainly to energy deposition from gamma rays and the other sensitive to the energy deposition from both gamma rays and fast neutrons. The absolute gamma sensitivity of the ionization chambers was determined using an X-ray machine,  $\text{Co}^{60}$  radiation, and 7 MeV electron bremsstrahlung. The radiative energy deposition in the neutron dosimeters was determined by comparing their response with that of a water calorimeter in the TRIGA Mark I reactor. A time history of the gamma intensity in the critical assembly core was also made showing the contribution of delayed gammas to the total gamma radiation.

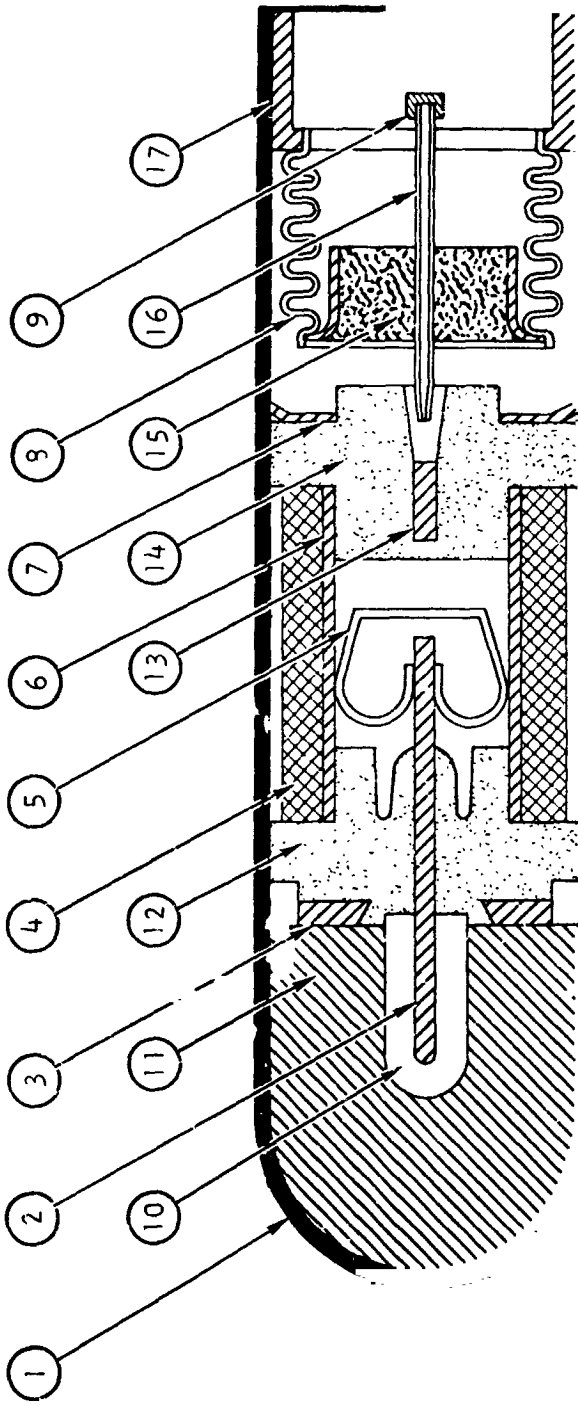
#### 3.6.2 THIMBLE IONIZATION CHAMBERS

The two types of thimble ionization chambers used for these measurements were fabricated by the Landsverk Electrometer Company, and are shown diagrammatically in Figs. 3.22 and 3.23. An exploded view of one of these is shown in Fig. 3.24, and a photograph of the dosimeters is shown in Fig. 3.25. The chambers were hermetically sealed so that they could be immersed in water without discharging them. They were charged and read by exerting pressure on the contact pin; this stretches the bellows until the pin makes contact with the electrode (see Fig. 3.22).



- |  |                                     |
|--|-------------------------------------|
| 1. IONIZABLE VOLUME - 0.176 CU. CM.<br>(CARBON DIOXIDE GAS)          | 11. ALUMINUM ELECTRODE CAP          |
| 2. CARBON ELECTRODE SHEATH (0.064 IN. DIA.)                          | 12. CARBON CHAMBER (0.134 IN. WALL) |
| 3. ALUMINUM SHIELD (0.015 IN. THICK)                                 | 13. ELECTRODE INSULATOR             |
| 4. CONDENSER (6000 MMFD.)  | 14. ALUMINUM ELECTRODE              |
| 5. ELECTRODE CLIP  | 15. ELECTRODE CONTACT BAR           |
| 6. ALUMINUM CONDENSER CORE   | 16. CONDENSER INSULATOR             |
| 7. RETAINER RING   | 17. GLASS SEAL                      |
| 8. BELLOWS ASSEMBLY  | 18. CONTACT PIN                     |
| 9. END CAP   | 19. END SLEEVE                      |
| 10. ALUMINUM SHELL<br>1.900 IN. LONG - 490 IN. DIA. - 0.015 IN. WALL |                                     |

Fig. 3.22--Landsverk 2500 rad carbon dosimeter details



- |    |   |     |  |
|----|---|-----|--|
| 1. | ALUMINUM SHELL<br>1.850 IN. LONG - 0.490 IN. DIA.<br>- 0.015 IN. WALL | 10. | IONIZABLE VOLUME 0.040 CU. CM.<br>(ETHYLENE GAS) |
| 2. | ALUMINUM ELECTRODE (0.025 IN. DIA.)                                   | 11. | POLYETHYLENE CHAMBER<br>(0.165 IN. WALL)         |
| 3. | BAKELITE SHIELD   | 12. | ELECTRODE INSULATOR                              |
| 4. | CONDENSER (3000 MMFD.)  | 13. | ELECTRODE CONTACT BAR                            |
| 5. | ELECTRODE CLIP  | 14. | CONDENSER INSULATOR                              |
| 6. | ALUMINUM CONDENSER CORE   | 15. | GLASS SEAL                                       |
| 7. | RETAINER RING   | 16. | CONTACT PIN                                      |
| 8. | BELLOWS ASSEMBLY  | 17. | END SLEEVE                                       |
| 9. | END CAP   |     |  |

Fig. 3.23--Landsverk 5000 rad polyethylene dosimeter details

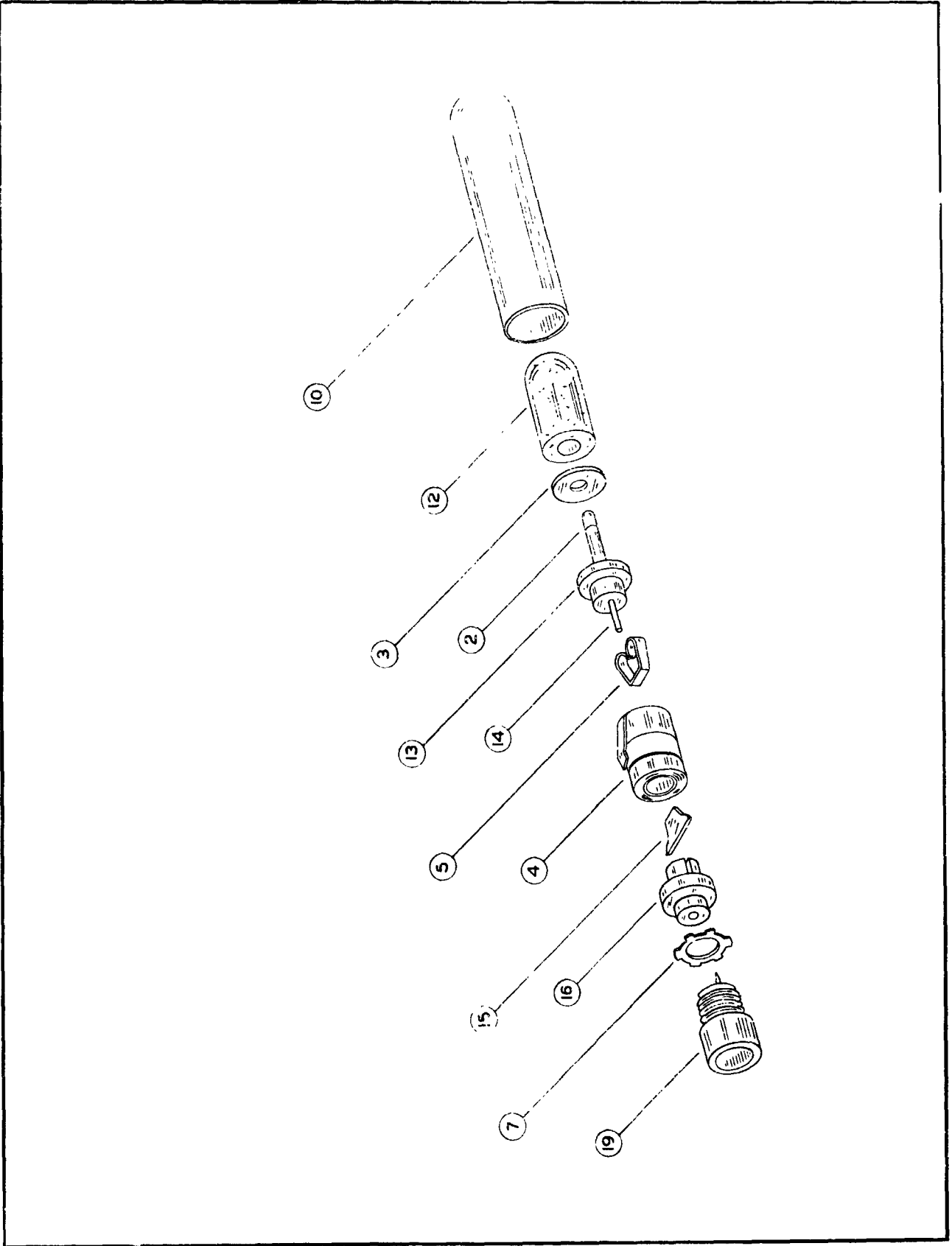


Fig. 3.24--Disassembly view of carbon dosimeter

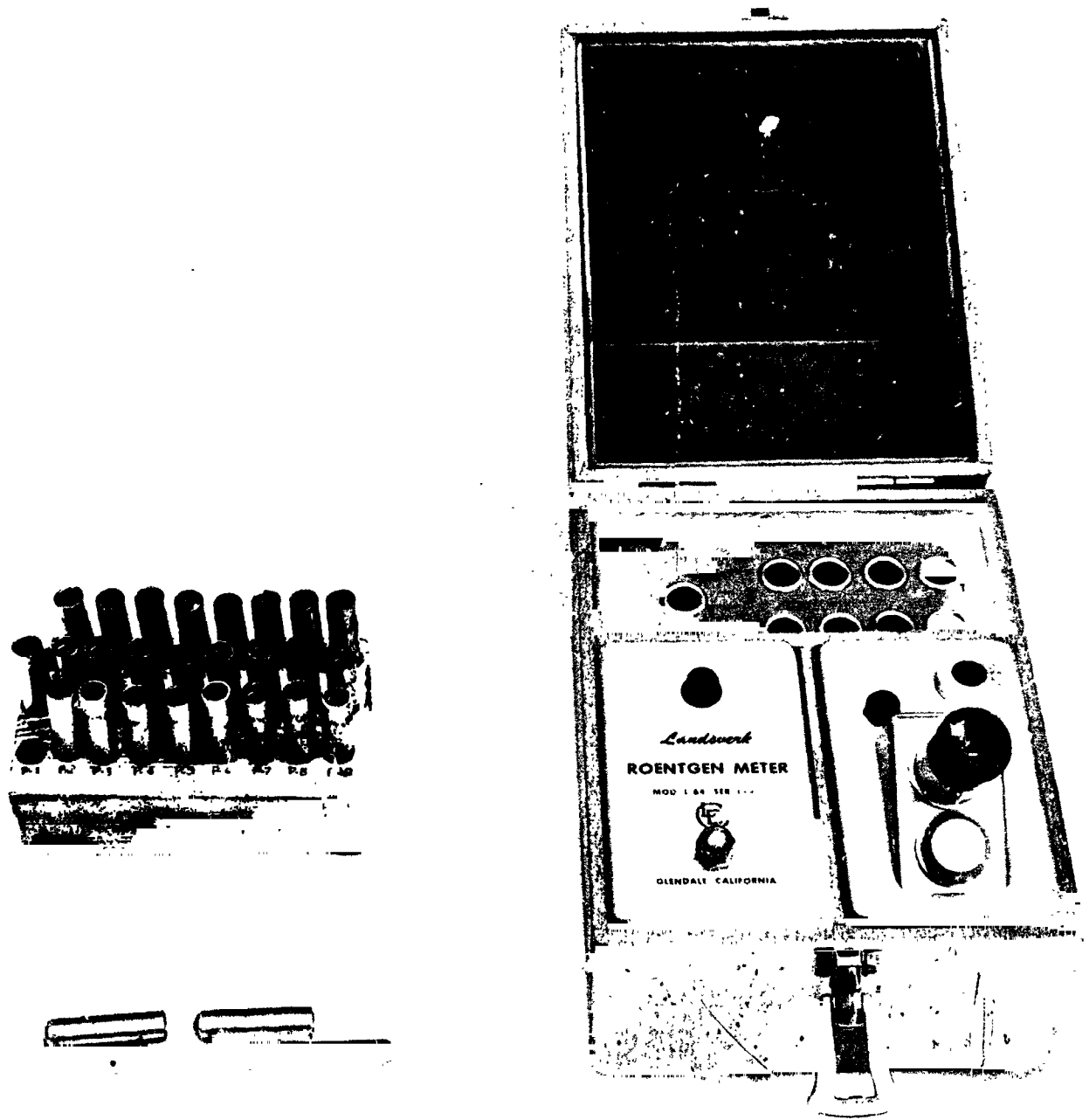


Fig. 3. 25--Landsverk dosimeters and charger-reader

The charger reader was a Landsverk Model L-64. This unit has a small capacitance compared to that of the ionization chambers and therefore can be ignored. The electrical leakage rate of the dosimeters was about 2% full scale per day.

The design of the thimble ionization chambers is discussed in the following two sections.

### 3.6.2.1 Graphite-Carbon Dioxide Thimble Ionization Chambers

Sixteen chambers having graphite walls, filled with carbon dioxide, and sensitive primarily to energy deposition from gamma rays were used. These devices have a small inherent neutron sensitivity due to carbon recoils. However, because of the short range of the recoils, virtually all of the response results from ionization created by particles originating in the gas. In order to reduce the response to ionization produced in the cavity by proton recoils from the polystyrene insulator the chambers were designed so that only a small solid angle was subtended by the effective cavity volume at the insulator. This is the purpose of the 0.015-in. thick aluminum shield shown in Figs. 3.22 and 3.23. The effectiveness of this design is aided by the poor collection efficiency near the insulator. The outside diameter of the chambers was limited to 0.490 in. so that they would fit into the center of the fuel element support post and the poison tubes. This limited the thickness of the graphite walls to 0.544 gm/cm<sup>2</sup> which exceeds the range of a 1.25 MeV electron and corresponds to charged particle equilibrium<sup>(3, 4)</sup> for a 1.5 MeV photon. During the measurements the ionization chambers were surrounded by aluminum in the fuel elements and both aluminum and water in the poison tubes; this in effect increased the thickness of wall material surrounding the ionizable volume of the chambers. Generally, equilibrium ionization is reached at thicknesses much less than the range of the highest energy secondary electron. Assuming that only aluminum surrounded the ionizable volume, then for the Compton region the absorbed dose would be 4% less than for



carbon. Under the same assumptions, the absorbed dose in water would be 11% more.<sup>(5)</sup> Since the carbon walls are an equilibrium thickness for 1.50 MeV gammas, only those gammas above this range are in question. However, in the worst case, i. e., assuming water around the carbon wall dosimeter, and also since only about 0.4 of the fission energy is above this value, the error caused by the walls not being in equilibrium should be not more than 4%. The graphite-carbon dioxide dosimeters are 1.9 in. long and have an ionizable volume of 0.176 cm<sup>3</sup>. The 0.064-in. diameter aluminum-graphite electrode structure shown in Fig. 3.22 gives the electrode stability and helps tailor the energy response while limiting the amount of aluminum in the ionizable volume.

#### 3.6.2.2 Polyethylene-ethylene Thimble Ionization Chambers

Nine polyethylene wall ethylene-filled chambers were used. They are sensitive to energy deposition from both gamma rays and fast neutrons. Physically they were 1.85 in. long with an ionizable volume of 0.040 cm<sup>3</sup> as shown in Fig. 3.23. The aluminum electrode is 0.025 in. in diameter. The diameter of these chambers was also limited to 0.490 in. for the same reasons as the graphite wall dosimeters, resulting in a wall thickness of the polyethylene of 0.385 gm/cm<sup>2</sup>. This thickness exceeds the range of the 1.0 MeV electrons, providing an equilibrium thickness for 1.25 MeV gamma rays. The polyethylene-walled ionization chambers were placed mainly in poison tubes and therefore, for most of the measurements, were surrounded by water. Since the absorbed dose in water and polyethylene varies by only about 3% in the Compton region, this increases the effective thickness of the wall material surrounding the ionizable volume, reducing the maximum error caused by the walls not being infinite to 3%.

### 3.6.3 ABSOLUTE CALIBRATION OF THE ENERGY DEPOSITION IN THE GRAPHITE CHAMBERS

The graphite-walled carbon dioxide-filled thimble ionization chambers were absolutely calibrated by comparison with a Victoreen Model 70-5 thimble chamber.

A 7 MeV beam of electrons from the General Atomic linear accelerator impinged upon a thick fansteel (89% tungsten, 7% nickel, 4% copper) target, producing a bremsstrahlung spectrum with nearly a fission source distribution. Since the electron beam was 7 MeV, which is below the threshold for  $(\gamma, n)$  reactions, no neutrons were produced. A 4-in. thick, 12-in. diameter graphite disc, shown in Fig. 3.26, was placed 74 in. from and on the center line with the bremsstrahlung target. Eighteen 1/2-in. diameter holes 2-3/4 in. deep were drilled into the disc on a 9-in. diameter circle. One of these holes was enlarged to accommodate the Victoreen chamber. The thickness of graphite between the ionization chamber and the front surface of the disc was 3.2 cm, being slightly greater than the range of a 7 MeV electron. During the measurements, the disc was rotated at 2 rpm to insure a uniform dose to each of the dosimeters. All of the graphite dosimeters were placed in the graphite disc at the same time, eliminating any intercalibration errors among the dosimeters.

Since the range of the Victoreen dosimeter was limited to 25 roentgens and the Landsverk dosimeters have a range of several thousand roentgens, a photodiode-plastic fluor detector<sup>(6)</sup> was used to monitor the measurements and perform an intercalibration. All of the Landsverk carbon-walled dosimeters were intercalibrated on a relative basis during a single measurement. The instantaneous dose rate was  $1 \times 10^3$  r/sec, using a pulse length of 4.5  $\mu$ sec and a pulse repetition rate of 180 per sec from the Linac, yielding a total dose of approximately half scale or about 1400 roentgens for a running time of 30 minutes. The Victoreen chamber



Fig. 3. 26--Dosimeter calibration apparatus

has a linear response at dose rates below  $5 \times 10^4$  r/sec;<sup>(6)</sup> it is expected that the Landsverk dosimeters are linear up to at least  $3 \times 10^3$  r/sec.

The exposure level of the Victoreen thimble chamber versus the monitor reading was measured several times to obtain an average value; the maximum deviation was less than 1%. The same geometry used for the Landsverk dosimeters was used for this measurement. For each measurement the Victoreen dosimeter was irradiated for a length of time sufficient to obtain a midscale reading.

The Victoreen ionization chamber reading was corrected by the ratio of the monitor readings for the two measurements and converted to rads by the conversion factor 1 roentgen equals 0.87 rad. The percent of full scale for the Landsverk carbon wall dosimeters was multiplied by 2500 rads, which was the expected full scale reading, and divided by the corrected value of the Victoreen ionization chamber reading in rads to give the sensitivity of the Landsverk dosimeters. The Landsverk chamber reading divided by the sensitivity was used to give the true absorbed dose. It is estimated that this absolute calibration procedure gives the true absorbed dose within  $\pm 5\%$ . The possible individual errors in this calibration are summarized below:

- $\pm 2\%$  in the average energy to produce an ion pair in air for the roentgen-to-rad conversion.
- $\pm 2\%$  in the reading of the Landsverk dosimeters
- $\pm 2\%$  in the reading of the Victoreen dosimeter
- $\pm 1\%$  in the value used to convert the Victoreen ionization chamber reading to the intercalibration run for the Landsverk ionization chambers.
- $\pm 2\%$  in the monitor readings
- $\pm 2\%$  in the true roentgen value of the Victoreen dosimeter.

In this calibration, the Victoreen ionization chamber behaves as a thin-walled ionization chamber filled with air and surrounded by an air equivalent material, in this case carbon. The mass energy absorption

coefficient for carbon and air is the same for electron energies from 7 MeV to about 150 keV. The Victoreen dosimeter has a nylon wall with a nominal thickness of  $67 \text{ mg/cm}^2$  which is infinite to a 270 keV electron. It is intended for use over an effective energy range of 30-400 keV. In the energy range of 30 to 400 keV the chamber had an efficiency of 1.00. However, even at 20 keV its efficiency drops only to 0.90 and at 10 keV it is about 0.65. Therefore, the Victoreen ionization chamber behaves as an air-equivalent dosimeter under the conditions discussed above from about 7 MeV to about 20 keV.

The results of the absolute calibration of the graphite wall carbon dioxide-filled Landsverk dosimeter are tabulated in Table 3.26. A typical energy response curve for the carbon chamber is shown in Fig. 3.27 and for a polyethylene chamber in Fig. 3.28. The energy response for each dosimeter is listed in Table 3.27 as measured by the Landsverk Electrometer Company.

The polyethylene chambers were also placed in the graphite disc as a means of intercalibration. Since the walls of these chambers are polyethylene the absorbed dose is characteristic of polyethylene and therefore roughly 1.14 larger than the dose in carbon. On this basis an estimate of the rad value of the polyethylene chambers can be made; it is shown in Table 3.26.

#### 3.6.4 ABSOLUTE CALIBRATION OF THE ENERGY DEPOSITION IN THE POLYETHYLENE CHAMBERS

##### 3.6.4.1 Design Considerations of the Calorimeter

A calorimeter was designed and built to provide a means of calibration for the polyethylene dosimeters. Water was used for the neutron energy absorbing medium of the calorimeter. Because fluxes produced in the NUROC core when it is operated around 100 watts are insufficient to produce an appreciable temperature rise rate in water ( $\sim 10^{-4} \text{ }^\circ\text{C/min}$ )

Table 3.26  
 DOSIMETER CALIBRATION USING 7.0 MeV BREMSSTRAHLUNG  
 RADIATION

Landsverk Dosimeter Number	Dosimeter Reading in % of Full Scale			Rad Value Obtained from Victoreen R Meter	Corrected Dosimeter Full Scale Rad Value	
	Uncorrected Reading	Drift Correction	Corrected Reading		Indiv. Run	Average
C-1	56.4	0	56.4	2300	4078	4039
C-1	51.0	0	51.0	2030	3980	
C-2	63.5	0	63.5	2300	3622	3622
C-3	63.5	0	63.5	2300	3622	3573
C-3	57.6	0	57.6	2030	3524	
C-1A	63.2	0	63.2	2300	3639	3639
C-5	57.9	0	57.9	2300	3972	3941
C-5	51.9	0	51.9	2030	3911	
C-6	56.0	0	56.0	2300	4107	4107
C-7	58.0	0	58.0	2300	3966	3928
C-7	52.2	0	52.2	2030	3889	
C-8	63.2	0	63.2	2300	3639	3639
C-9	56.8	0	56.8	2300	4049	4038
C-9	50.4	0	50.4	2030	4028	
C-10	61.4	0	61.4	2300	3746	3746
C-11	56.2	0	56.2	2300	4093	4089
C-11	49.7	0	49.7	2030	4085	
C-12	60.9	0	60.9	2300	3777	3777
C-13	71.5	0	71.5	2300	3217	3194
C-13	64.0	0	64.0	2030	3171	
C-14	58.9	0	58.9	2300	3905	3886
C-14	52.5	0	52.5	2030	3866	
C-15	61.8	3.7	58.1	2300	3959	3959
C-16	65.2	.6	64.6	2300	3560	3560
P-1	26.9	0	26.9	2630	9780	9530
P-1	25.0	0	25.0	2320	9280	
P-2	22.2	0	22.2	2320	10440	10440
P-3	22.3	0	22.3	2320	10400	10400
P-4	23.6	0	23.6	2320	9840	9840
P-5	22.0	0	22.0	2320	19530	10530
P-6	25.5	0	25.5	2320	9100	9100
P-7	26.8	0	26.8	2320	8650	8650
P-8	28.0	0	28.0	2320	8280	8280
P-9	22.0	0	22.0	2320	10530	10530

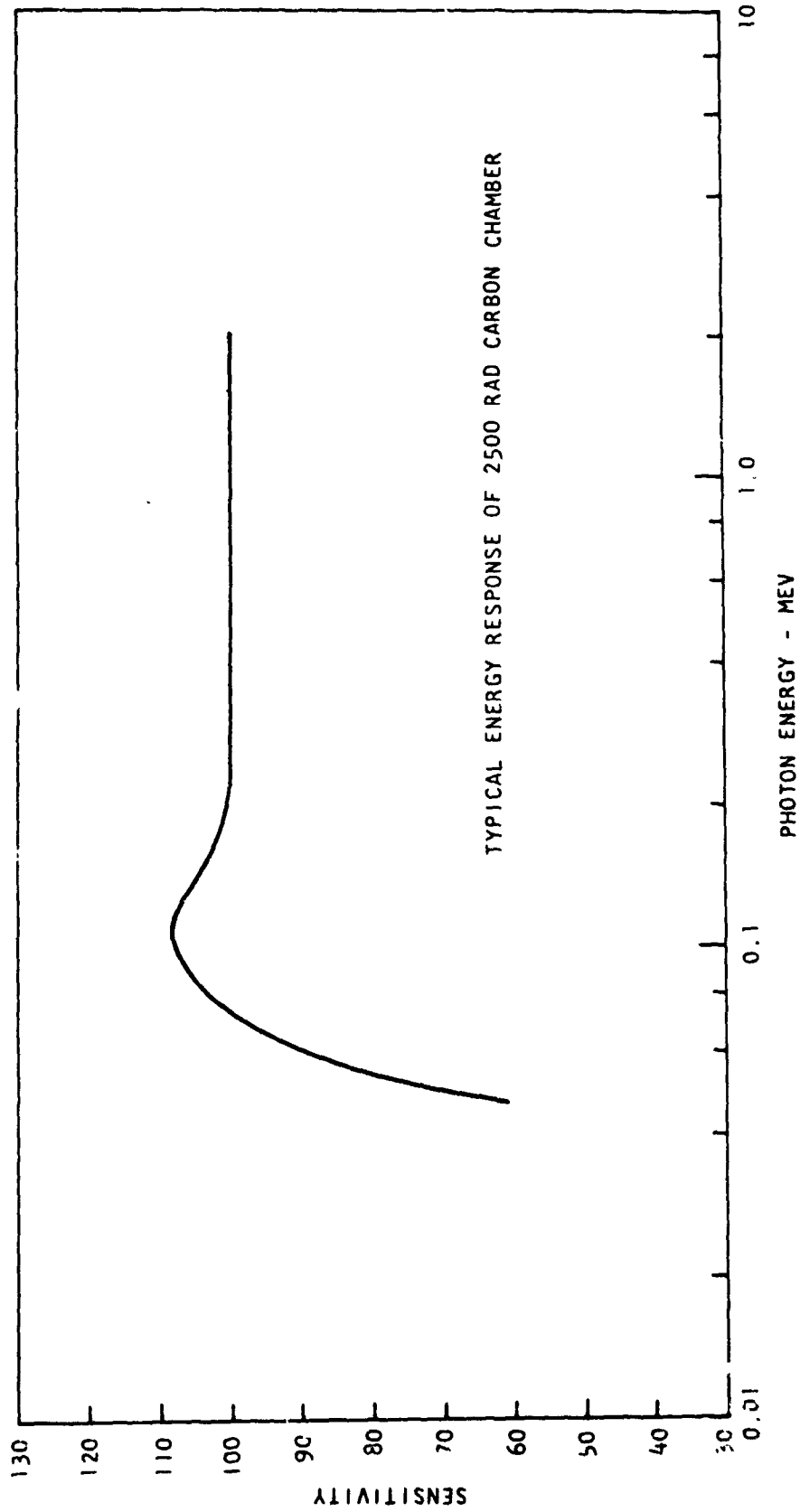


Fig. 3.27--Typical carbon dosimeter response curve

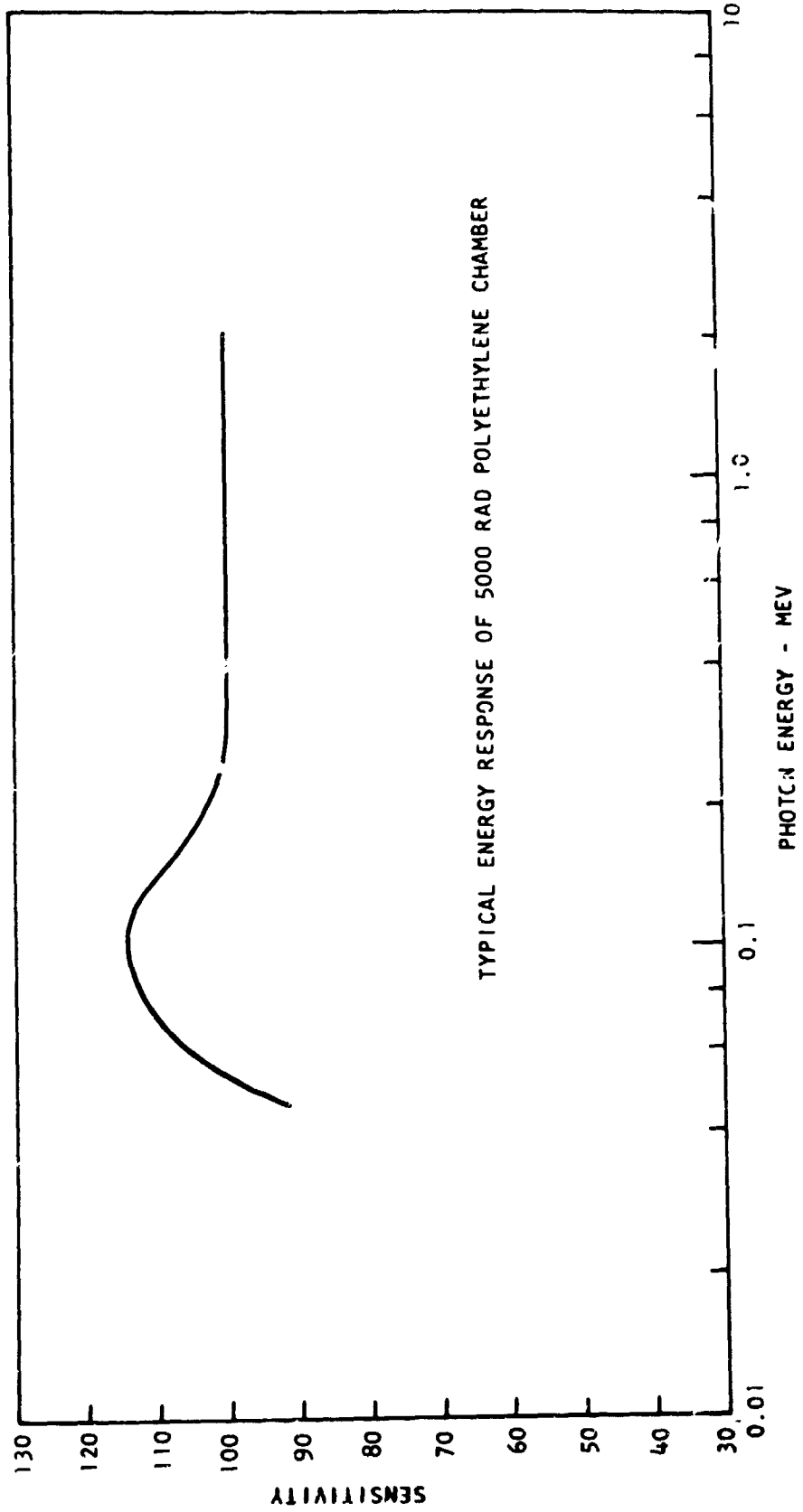


Fig. 3.28--Typical polyethylene dosimeter response curve



Table 3.27  
 THE LANDSVERK ELECTROMETER COMPANY  
 CALIBRATION CERTIFICATE\*

<u>Serial No.</u>	<u>Range</u>	<u>CO<sup>60</sup></u>	<u>120 keV</u>	<u>80 keV</u>	<u>46 keV</u>
C1	2500 RAD (Carbon)	76.2	81.1	89.6	46.6
C2	"	78.4	82.5	90.3	44.3
C3	"	94.4	93.5	88.8	51.2
C4	"	74.0	73.3	66.9	35.9
C5	"	86.0	84.8	89.6	43.7
C6	"	84.4	83.6	77.7	42.9
C7	"	87.0	86.0	81.6	46.0
C8	"	84.8	84.2	76.8	42.0
C9	"	80.0	79.4	82.7	40.0
C10	"	90.2	89.3	81.9	43.5
C11	"	85.6	84.8	80.3	41.7
C12	"	85.2	84.4	77.3	41.7
C13	"	107.2	106.2	96.0	49.2
C14	"	85.8	85.0	81.4	43.2
C15	"	84.4	83.4	75.5	42.4
C16	"	94.0	93.1	85.4	44.3
P1	5000 RAD (Polyethylene)	88.6	93.9	90.6	51.8
P2	"	78.0	83.2	81.5	46.8
P3	"	81.2	82.3	78.6	45.4
P4	"	94.4	192.9	103.8	60.9
P5	"	80.0	85.3	84.4	49.4
P6	"	75.2	72.9	69.2	36.1
P7	"	89.8	102.9	86.9	47.9
P8	"	84.6	86.5	85.2	43.2
P9	"	80.9	85.3	86.6	46.5

\*Dated November, 1965

at 100 watts could be expected), the calorimeter was designed to be used in the Torrey Pines TRIGA Mark I reactor which may be operated at a much higher power and hence produce a much greater temperature rise rate. The outer jacket of the calorimeter was held to a maximum diameter of 1.250 in. to allow it to fit into a tube in the TRIGA core. Since the size was restricted, an adiabatic jacket was used to reduce heat transfer between the water absorbing mass and its environment. This adiabatic jacket was placed half-way between the outer jacket and the water mass and was made of aluminum and epoxy with a nichrome heating coil potted into the epoxy; adjustment of the power dissipated in the coil almost completely eliminated heat transfer between the water mass and its environment. Heat transfer was further reduced by using fine (.006 in. diameter) copper connection wires to lead into the water mass, keeping all heat paths between the water mass and the adiabatic jacket long and of small cross sectional area. All interior surfaces were painted white and the area around the jacket was evacuated. Since the neutron and gamma energy would be absorbed by the vessel walls as well as by the water, the vessel was designed to have a small mass compared to the water mass. Sheet polyvinyl chloride (PVC) was thermoformed into a two-piece bottle with approximately .004 in. thick walls. A thin (~ .002 in.) coating of epoxy was painted on the outside of the vessel to eliminate vapor pumping since the PVC is not impervious to water vapor. Details of the calorimeter are shown in Figs. 3.29, 3.30, and 3.31.

Fine control of the temperature difference between the water mass and the adiabatic jacket and the ability to accurately sense small incremental temperature changes in the water mass dictated the use of thermistors as temperature sensing elements. The thermistors selected were Fenwall bead, type GA 45J1, with a nominal resistance at 25°C of 50,000 ohms, a spherical diameter of .043 in. and a temperature coefficient of resistance of 4.6%/°C. A pair of these thermistors, matched to within 0.2% of each

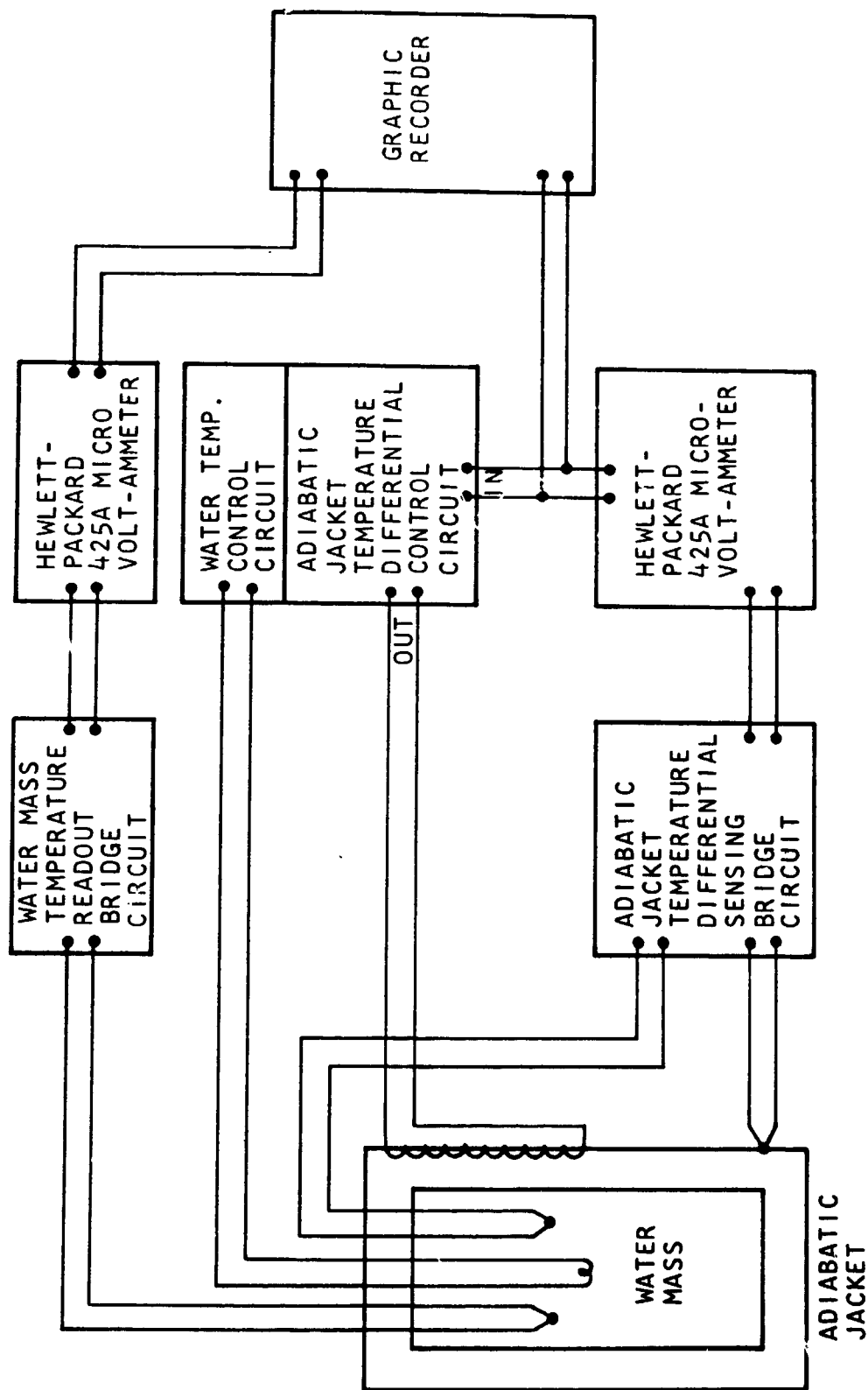


Fig. 3.29 -- Calorimeter electronics block diagram

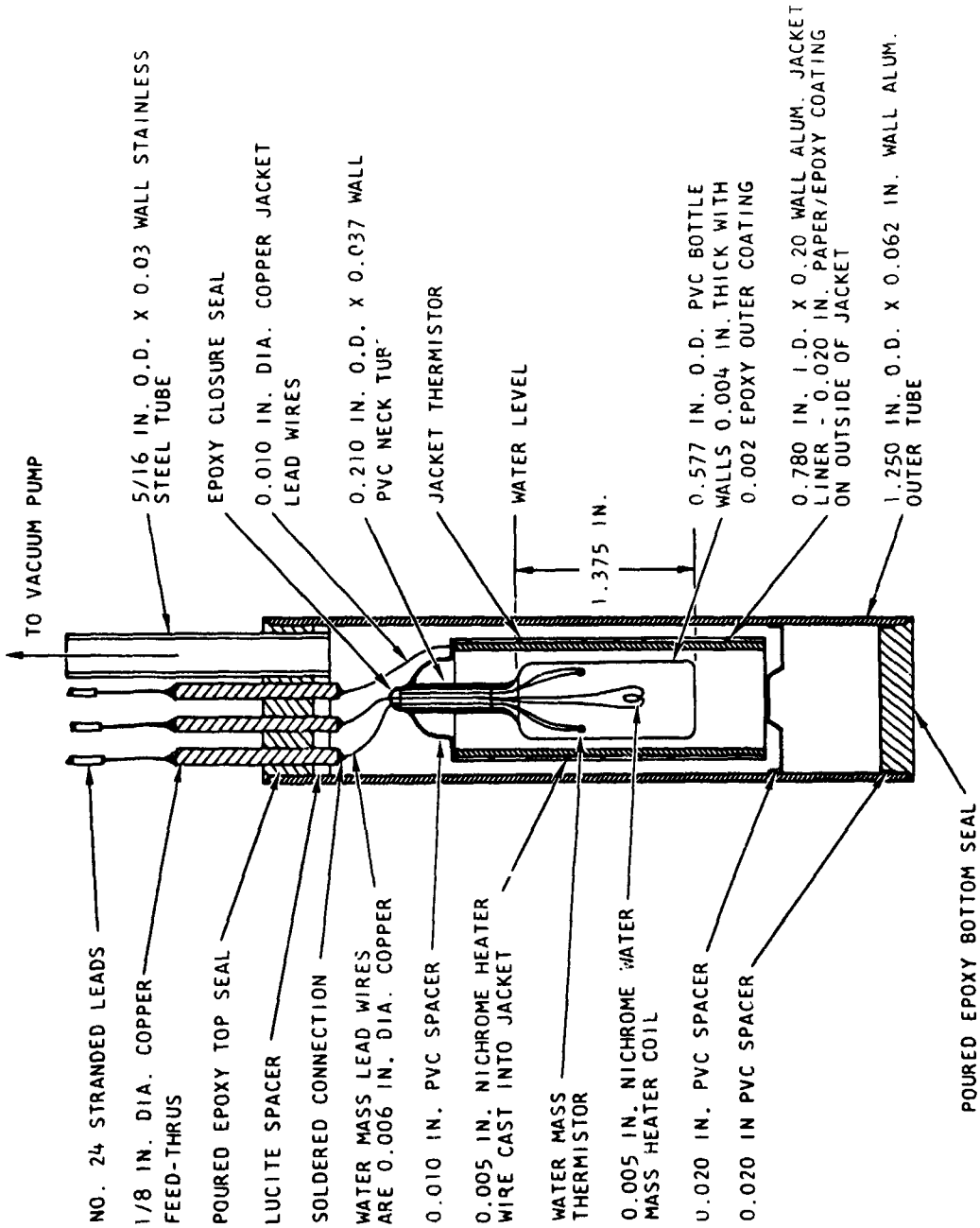


Fig. 3.30--Cross section of calorimeter

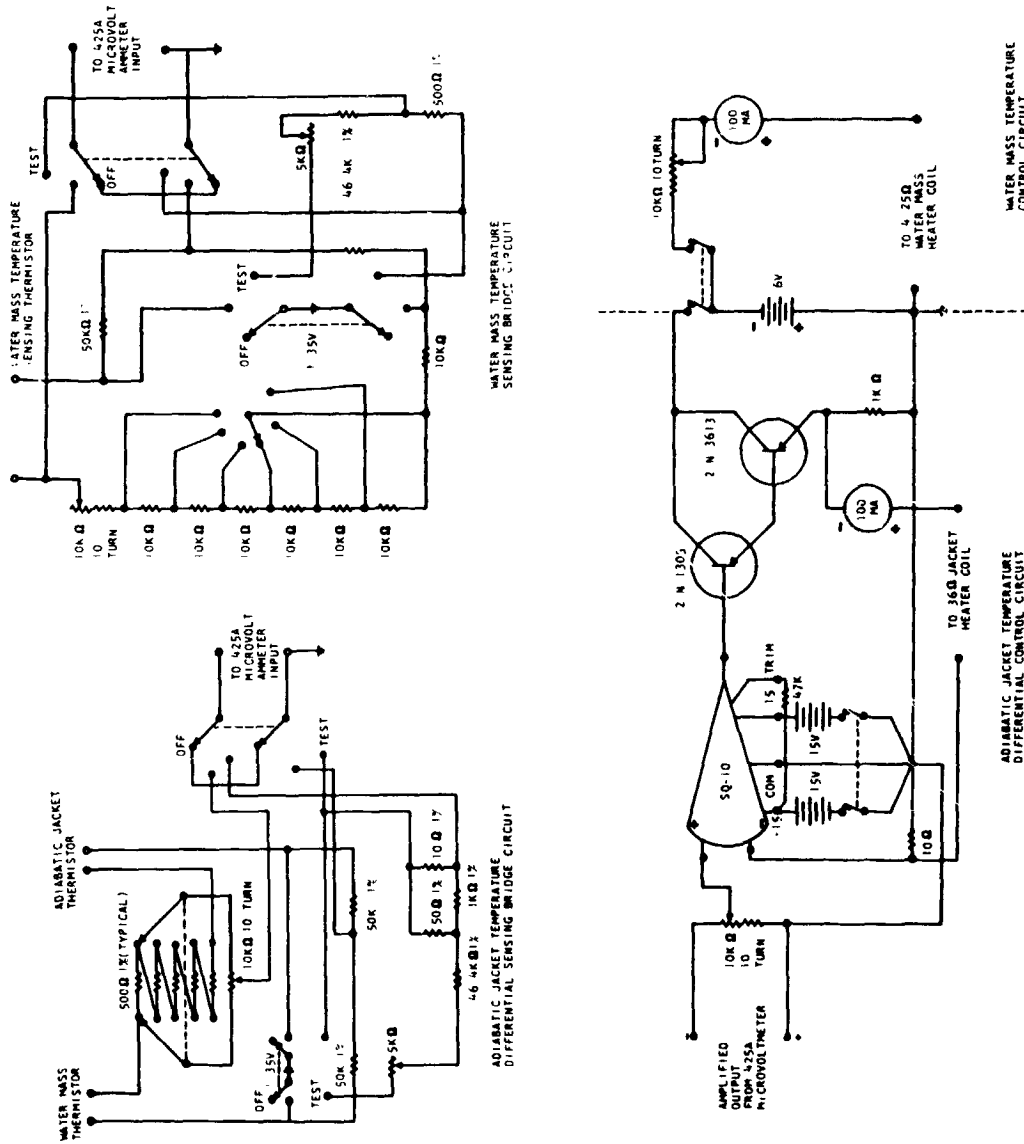


Fig. 3.31--Calorimeter control and readout circuits

other, were imbedded, one in the adiabatic jacket and one in the water mass; they form two legs of a bridge circuit as shown in Fig. 3.31 and are used to control the temperature of the adiabatic jacket with respect to the water mass to eliminate heat transfer. An additional thermistor in the water mass forms one leg of the other bridge circuit of Fig. 3.31 and is carefully calibrated to allow accurate monitoring of the rate of temperature rise in the water mass. The calibration procedure for the thermistor was as follows: The entire water mass assembly was placed in a large volume of water contained by a vacuum-jacketed glass-walled flask. A copper-constantan thermocouple was located on the surface of the calorimeter water mass and, using an ice bath cold junction, connected to a Rubicon precision potentiometer which allowed accurate determination of the temperature of the water bath. A battery-driven resistance heater was used to raise slowly the temperature of the water bath and the calorimeter water mass assembly suspended within it. The output of the bridge circuit as a function of temperature change was monitored by the Hewlett-Packard 425A microvoltmeter and a Varian strip chart recorder, and was found to be 14.85 millivolts per degree centigrade which agreed very well with calculations based on the manufacturer's rated temperature coefficient of resistance. This constant was used in the analysis of subsequent measurements. A 4.25-ohm nichrome heater coil was included in the water absorbing mass to control the temperature and provide a check on the operation of the system.

#### 3.6.4.2 Calorimeter Operation

Once the jacket controls were correctly adjusted, the calorimeter was tested by applying power to the water mass coil and observing the rate of temperature rise of the water mass on the strip-chart recorder. The slope of the temperature rise curve (in millivolts per minute) gives the heating rate since the thermistor constant is known to be 14.85 millivolts per degree centigrade.

When the calorimeter was operated in the reactor, a temperature rise rate of  $0.0829^{\circ}$  centigrade per minute was observed at a steady state reactor power level of 10 kilowatts; this rate was obtained from the recorder trace which showed a voltage change rate (due to the change in resistance in the calibrated thermistor in the water mass) of 1.23 millivolts per minute. Since  $0.0829^{\circ}\text{C}/\text{minute}$  corresponds to 0.0829 gram-calories per gram per minute for pure water at  $13^{\circ}\text{C}$  (the temperature of the reactor water during the calibration runs) the heat input rate to the calorimeter water mass is given by

$$\begin{aligned} 0.0829 \text{ gram-calories/gram-minute} \times 4.19 \times 10^7 \text{ ergs/gram-calorie} \\ = 3.47 \times 10^6 \text{ ergs/gram-minute} \end{aligned}$$

and the dose rate in water is

$$\frac{3.47 \times 10^6 \text{ ergs/gram-minute}}{10^2 \text{ ergs/gram-rad}} = 3.47 \times 10^4 \text{ rads/minute at 10 KW}$$

The reactor power level during the irradiation of the dosimeters was 1.8 kilowatts; therefore the dose rate in water corresponding to the readings of the dosimeters is 6250 rads/minute.

As a check on the calorimeter operation, the reactor was operated at 20 kilowatts with a heating rate of  $.167^{\circ}\text{C}/\text{min}$  being obtained in the calorimeter water mass. Doubling the power doubles the heating rate which indicates that the relative power rates of the reactor are well known and that the calorimeter is able to accurately follow the reactor power level changes.

The results of the absolute calibration of the polyethylene in chambers against a water calorimeter is shown in Table 3.28. Also shown in the calibrated rad reading of several carbon ion chambers which were placed in the same reactor core position as the polyethylene chambers.

Table 3.28a  
 CALIBRATION OF THE ION CHAMBERS IN THE  
 TRIGA REACTOR

Landsverk Dosimeter Number	Dosimeter Reading in Percent of Full Scale			Rad Value Obtained from Calorimeter	Corrected Dosimeter Full Scale Rad Value	
	Uncorrected Reading	Position Correction	Corrected Reading		Individual Run	Average
P-1	9.5	.982	48.6	6250	12860	12860
P-2	41.1	1.02	41.9	6250	14920	14920
P-3	43.4	1.02	44.3	6250	14090	14090
P-4	45.0	.982	44.1	6250	14190	14190
P-5	43.1	1.02	43.9	6250	14220	14220
P-6	55.4	.982	54.4	6250	11480	11400
P-6	56.3	.982	55.3	6250	11310	
P-7	50.4	1.02	51.4	6250	12150	12150
P-8	51.5	.982	50.6	6250	12360	12360
P-9	43.5	.982	42.7	6250	14620	14620
P-9	41.3	1.02	42.2	6250	14810	
P-9	42.4	1.02	43.3	6250	14420	

Table 3.28b

Landsverk Dosimeter Number	Dosimeter Reading in Percent of Full Scale			Rad Value for Dosimeter Reading Corresponding to Percent Full Scale
	Uncorrected Reading	Position Correction	Corrected Reading	
C-2	60.8	1.02	62.0	2246
C-5	57.4	1.02	58.6	2309
C-9	53.3	1.02	54.3	2152
C-14	56.5	.982	55.5	2196



### 3.6.5 THIMBLE IONIZATION CHAMBER MEASUREMENTS IN CORE III OF THE TUNGSTEN NUCLEAR ROCKET REACTOR

The Tungsten Nuclear Rocket Reactor core exhibited a twelve-fold symmetry as shown in Fig. 2.6, Section 2.2.1. All of the thimble ionization chamber measurements were made in one sector of symmetry. The placement of these chambers is shown in Fig. 3.32. A total of 25 ionization chambers was used for each measurement: 16 graphite and 9 polyethylene wall chambers. A total of four runs was required; the power level for each run was 84.2 watts.

The ionization chambers were placed above and below the zirconium stud in the fuel elements using 3/8-in. diameter by 0.060-in. wall thickness aluminum tube spacers. In the poison tubes, 5/16-in. diameter, 0.06-in. wall thickness aluminum tube spacers were used and the void between chambers was filled with cadmium nitrate. For each run the same graphite-walled chamber was placed in the G-7 fuel element and the same polyethylene chamber in the G-16 poison tube to monitor the relative power level between runs. The relative variation in the power level from run to run as indicated by the ionization chambers was about 3%. Each run lasted 40 minutes as the reactor was being brought to power, and the period of the reactor was 30 seconds, making a total of about 139 seconds to reach full power. This is about 6% of the total running time. It took approximately 8 minutes to remove the chambers from the poison tubes and about 10 minutes from the fuel elements after the reactor was shut down.

### 3.6.6 TIME HISTORY OF THE GAMMA INTENSITY IN CORE III OF THE TUNGSTEN NUCLEAR ROCKET REACTOR

A determination of the gamma intensity time history was made for each of the four reactor operating runs in which dosimetry measurements were made. A gamma scintillation detector capable of discriminating

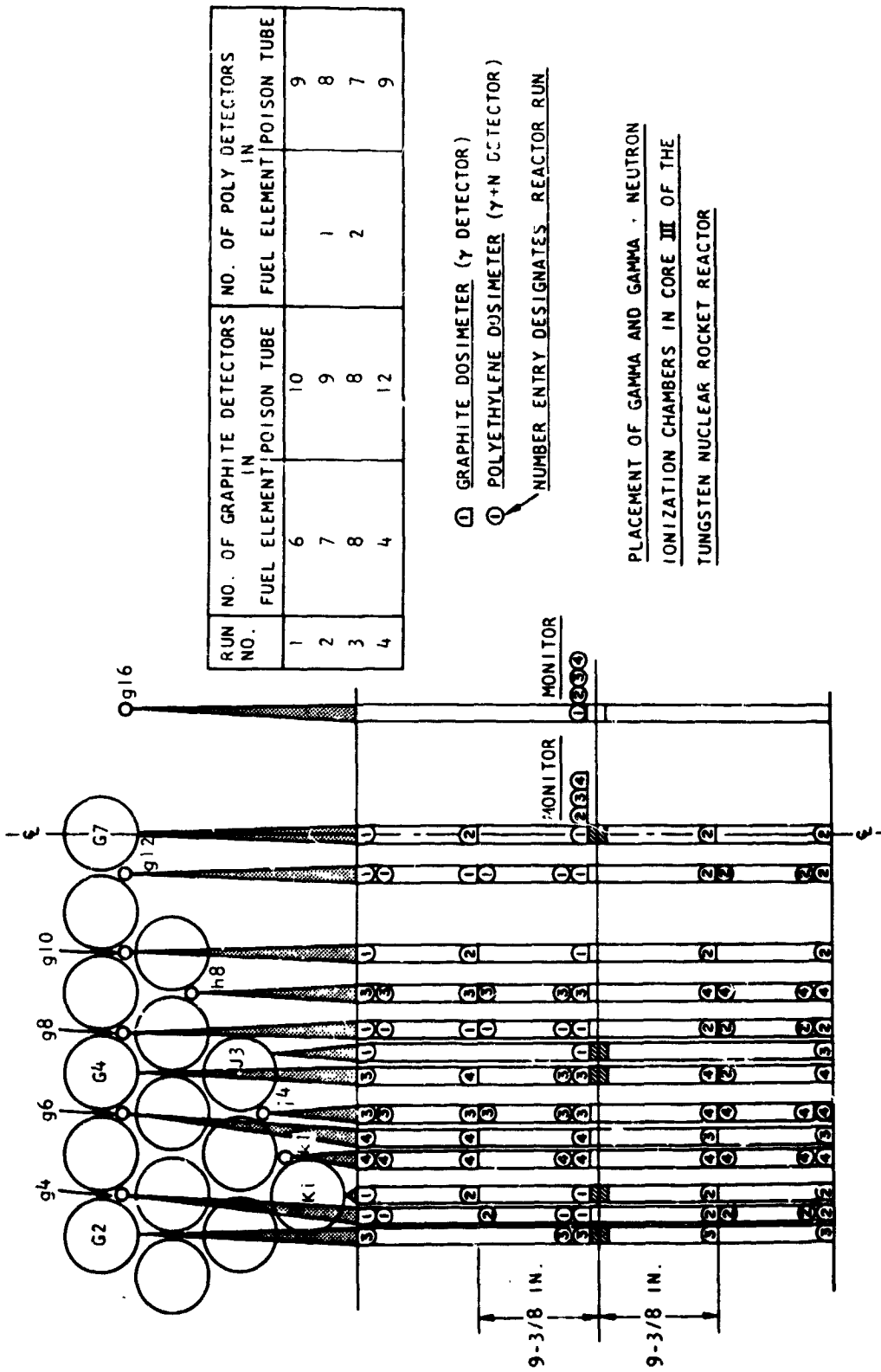


Fig. 3.32 -- Placement of dosimeters in Core III of the tungsten nuclear rocket reactor

against fast neutrons was used. The recorded output of this detector provided a measurement of the relative gamma intensity from the reactor core as a function of time. The contribution of delayed gammas to the prompt radiation is illustrated in Figs. 3.33 to 3.36.

The scintillating solution used in the gamma detector employed the nonhydrogenous hexafluorobenzene ( $C_6F_6$ ) as a solvent<sup>(7, 8)</sup> in order to discriminate against fast neutrons. Small concentrations of two hydrogenous scintillators were used in solution; para-terphenyl at 4 grams per liter and dimethyl POPOP at one gram per liter. The binary solution was sealed in a ten-milliliter pyrex flask in an argon atmosphere to prevent oxygen quenching<sup>(9)</sup> of the scintillations which were observed by a DuMont 6292 photomultiplier tube. The output current from the photomultiplier varied between  $1.5 \times 10^{-8}$  ampere and  $4.5 \times 10^{-7}$  ampere and was recorded on a graphic recorder.

The detector was positioned about two feet above the beryllium reflector at the edge of the core. The relative intensity of the gamma radiation was measured as a function of time for each of the four reactor operating runs in which the gamma and neutron fluxes were mapped using the carbon and polyethylene ion chambers.

The relative gamma intensity as a function of time for runs 1 through 4 is illustrated in Figs. 3.33 through 3.36 respectively. Typical of each curve is the exponential increase in intensity on the 30-second period of the reactor as it is brought up to power, leveling off at a constant value of 84.2 watts. Each run was continuous for approximately 40 minutes with the exception of run 1 in which a scram occurred during the run.

These graphs have been corrected for background effects, including residual nuclear radiation and detector dark current. An examination of each of the curves confirms the expected buildup in intensity of delayed gammas from fission during the run and the gradual decay after shutdown.

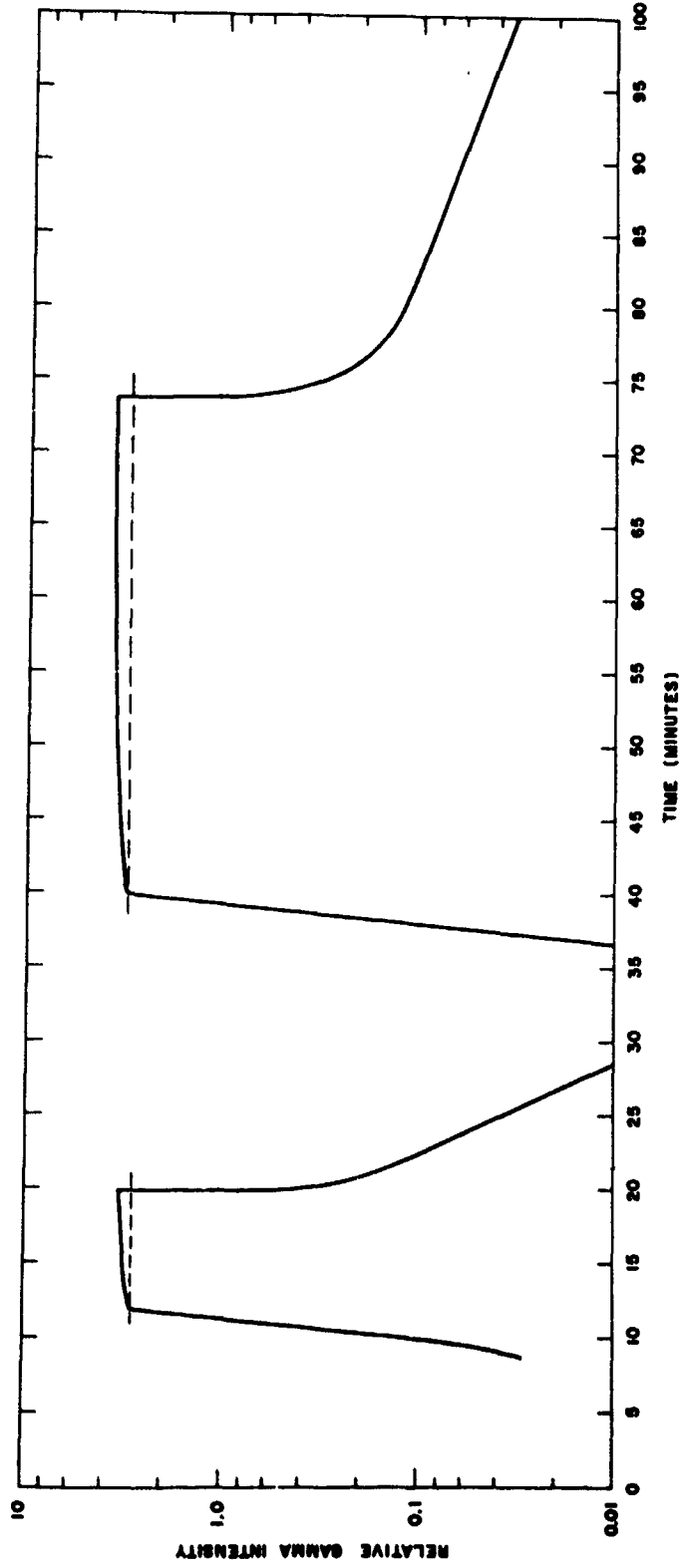


Fig. 3.33--Gamma intensity time history for dosimeter run one

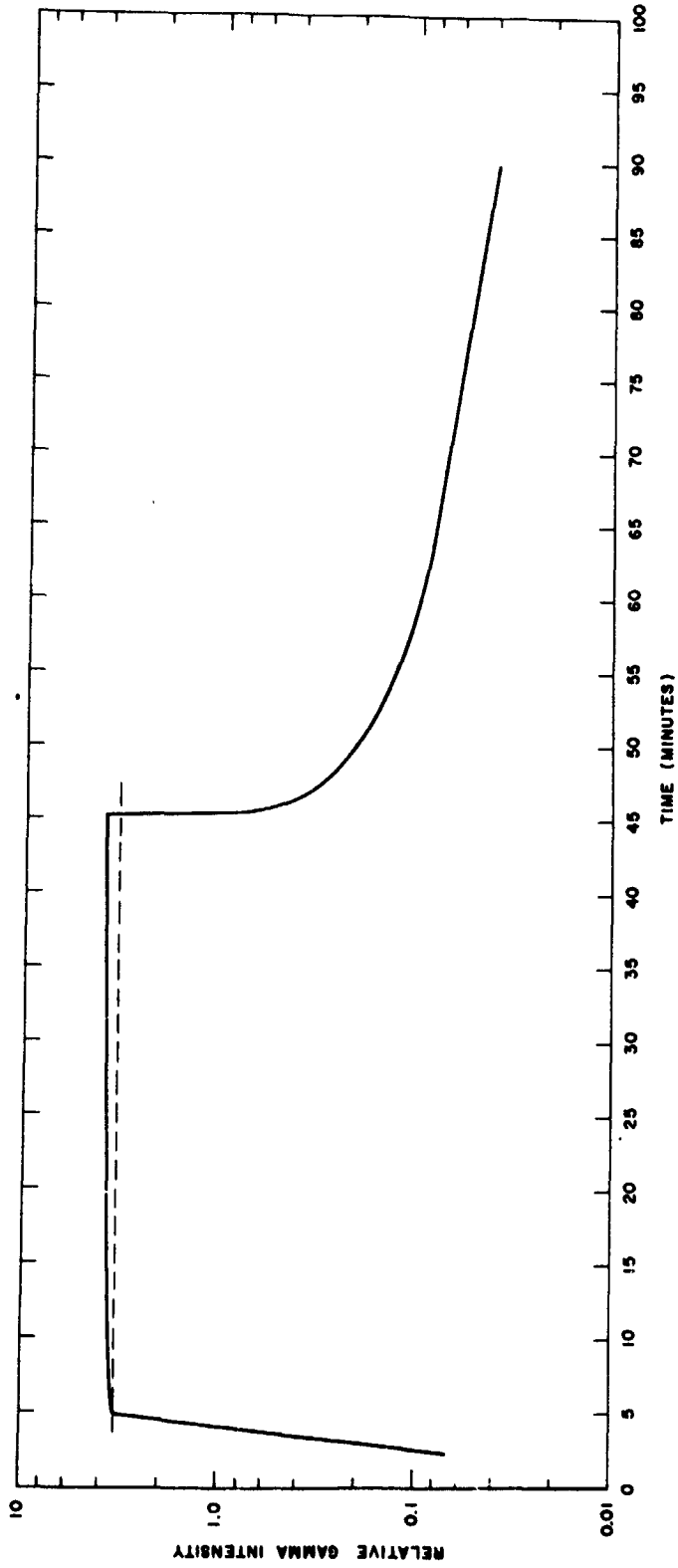


Fig. 3.34--Gamma intensity time history for dosimeter run two

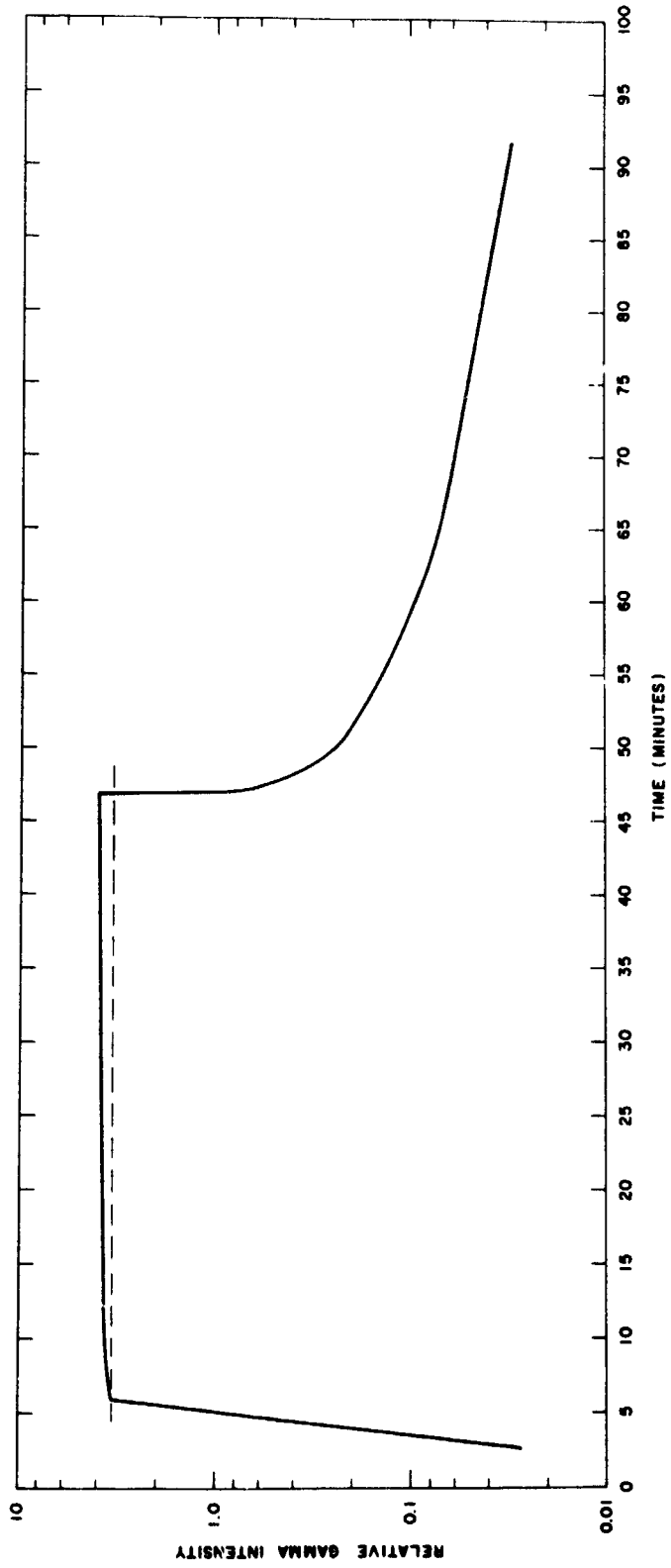


Fig. 3.35---Gamma intensity time history for dosimeter run three

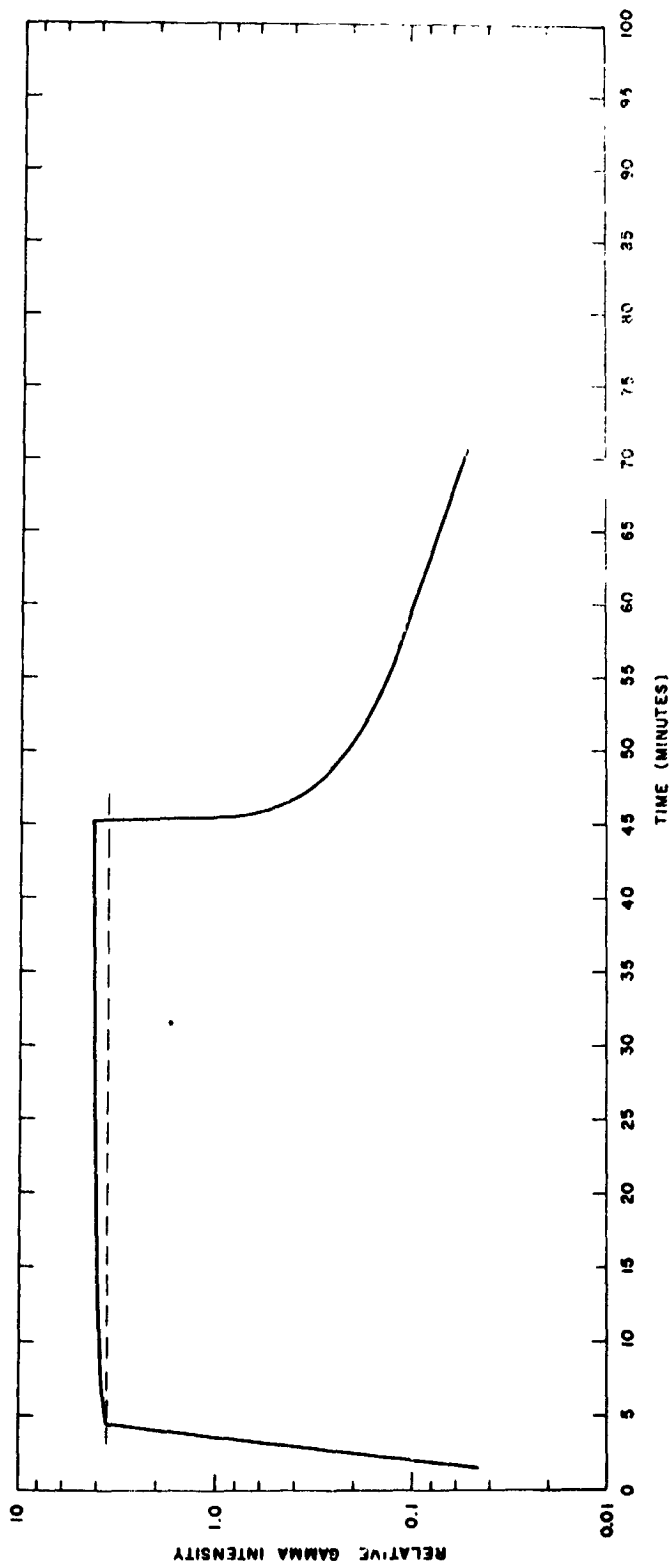


Fig. 3.36--Gamma intensity time history for dosimeter run four

For runs 2, 3, and 4 the intensity of delayed gamma radiation just prior to shutdown of the reactor is 19.7%, 18.9%, and 19.0% respectively, of the prompt gamma intensity. These numbers correspond very well with the point on the intensity curve where the exponential decay begins at reactor shutdown. The decay tail of delayed gammas is clearly a composite of several decay modes: the longest mode measured here, using the data for runs 2 and 3, corresponds to a half-life of approximately 40 minutes.

### 3.6.7 RESULTS AND DISCUSSIONS OF SOURCES OF ERROR IN THE ABSORBED DOSE MEASUREMENTS IN CORE III OF THE TUNGSTEN NUCLEAR ROCKET REACTOR

The results of the axial measurements of the gamma and neutron absorbed doses in Core III of the Tungsten Nuclear Rocket Reactor are graphed in Figs. 3.37, 3.38, 3.39, and 3.40 and tabulated in Table 3.29. The lines are the "best fit" to the data. The arrows on the graphs indicate possible defective data. The C-15 carbon dosimeter had an exceptionally high drift rate for which it was difficult to accurately correct. One reading of the C-1A carbon chamber reading is also suspect due to rough handling. The readings of the P-6 polyethylene dosimeter are suspect because the intercalibration ratio for the 7 MeV bremsstrahlung and the water calorimeter were different.

Two important considerations need to be elucidated. The polyethylene chambers were calibrated against a water calorimeter. This means that the absorbed dose for these chambers is characteristic of water and not polyethylene. Further, since they were calibrated in the TRIGA Mark I, the validity of their calibration is predicated on the basis that the gamma and neutron spectra in Core III of the Tungsten Nuclear Rocket Reactor is similar to that in TRIGA Mark I. The degree of accuracy of the calibration of the polyethylene dosimeters depends on the degree of accuracy of this assumption. The carbon dosimeters have been



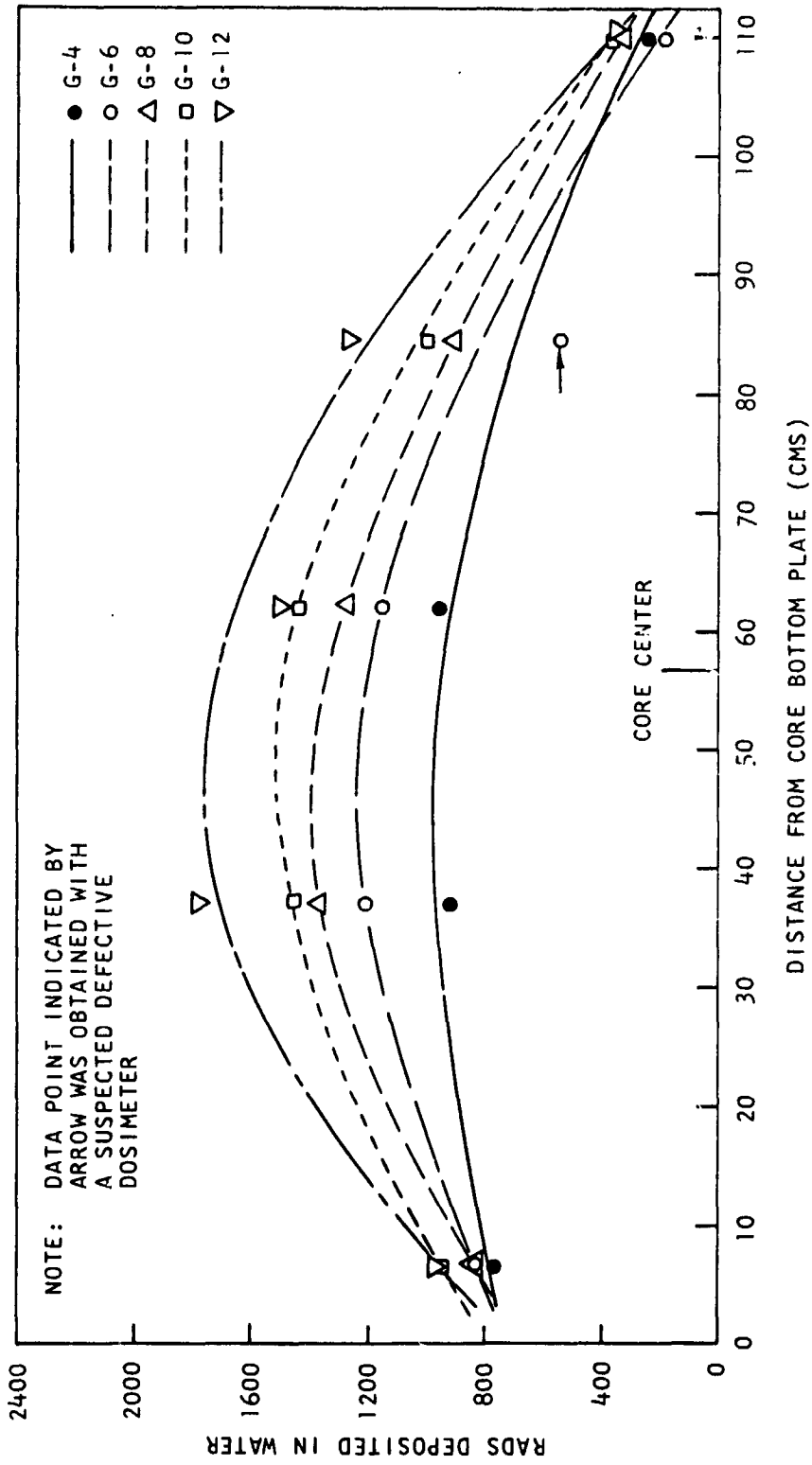


Fig. 3. 37--Absorbed dose in graphite dosimeters in nuclear  
rocket core poison tubes

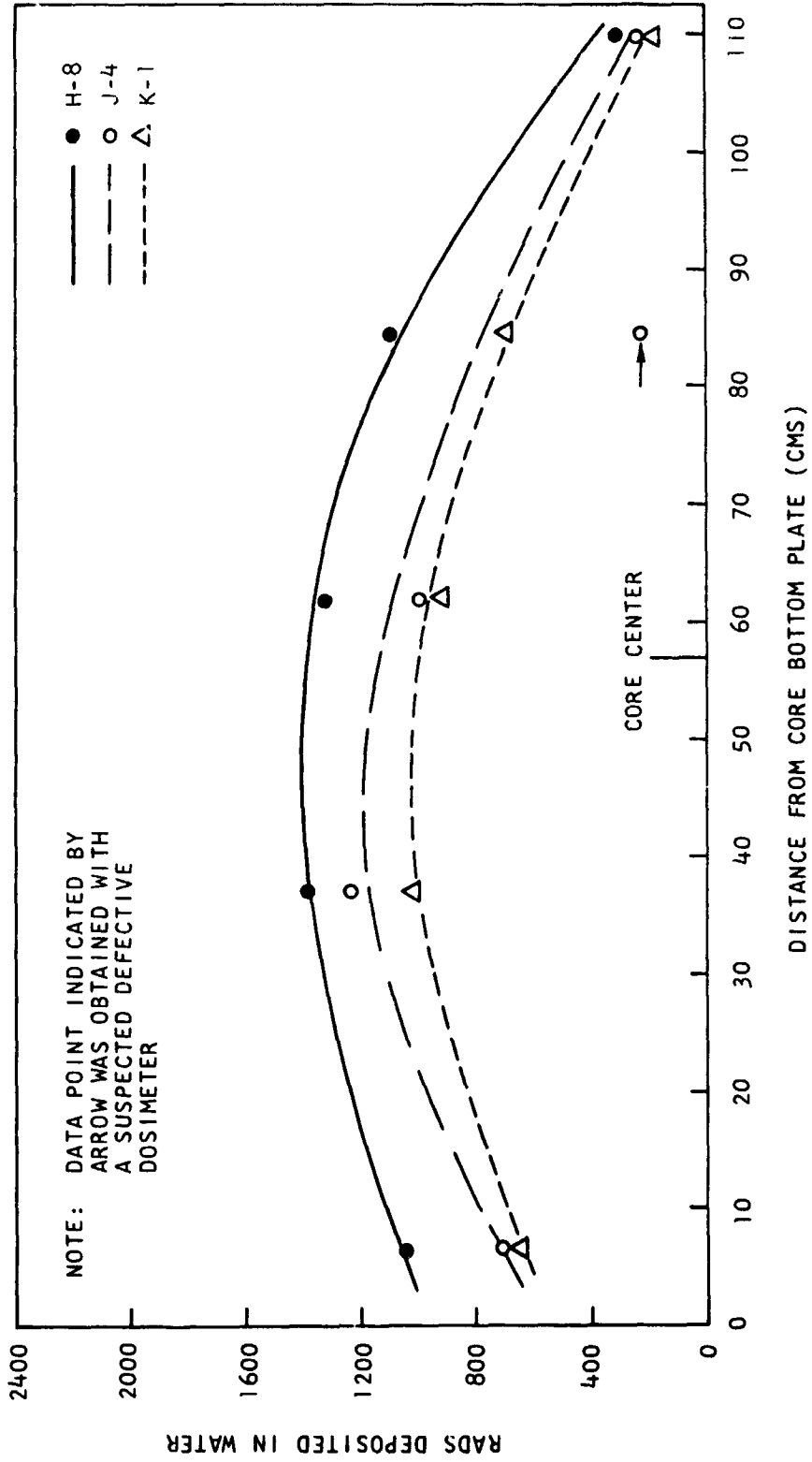


Fig. 3.38--Absorbed dose in graphite dosimeters in nuclear rocket core poison tubes

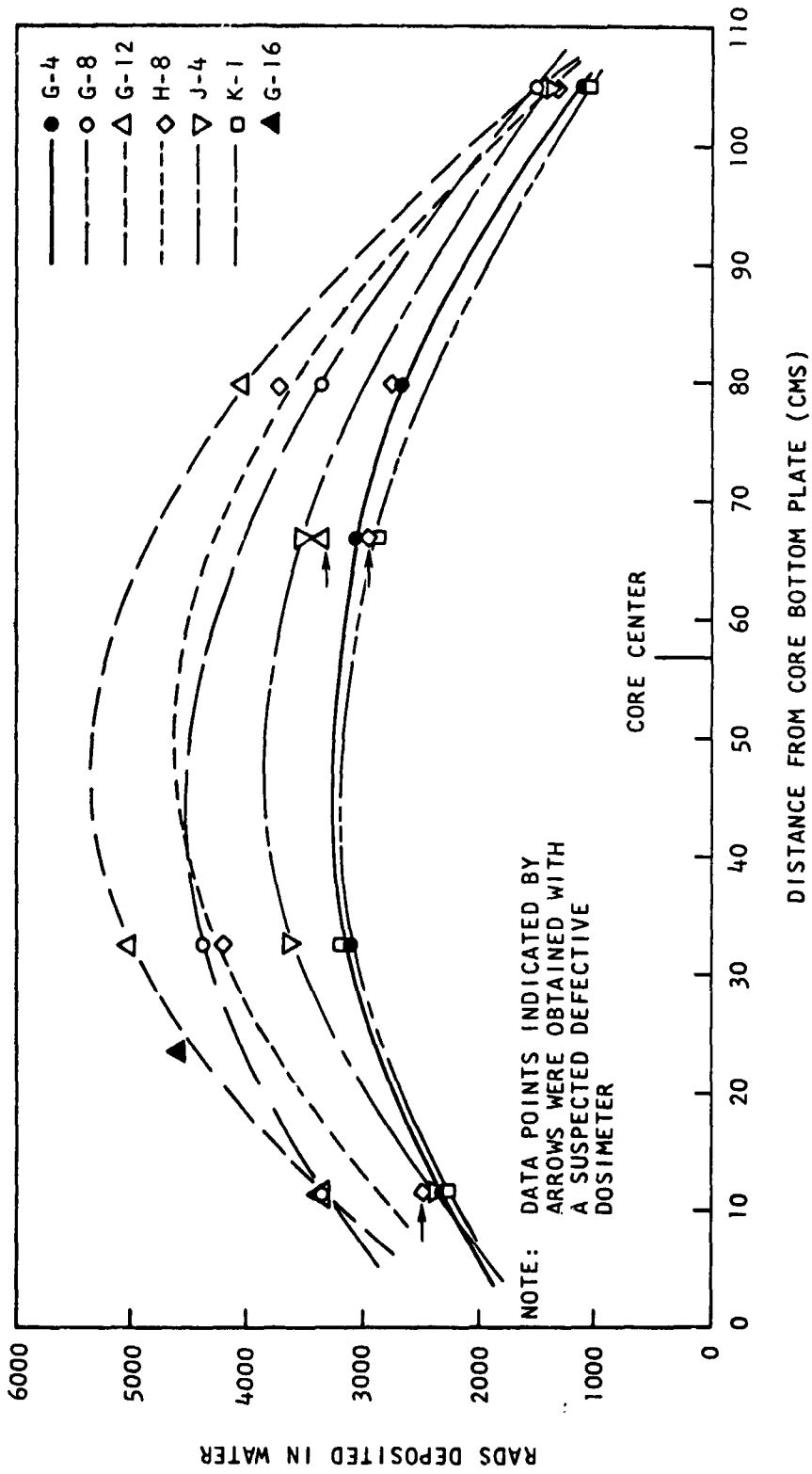


Fig. 3.39--Absorbed dose in polyethylene dosimeters in nuclear rocket core poison tubes

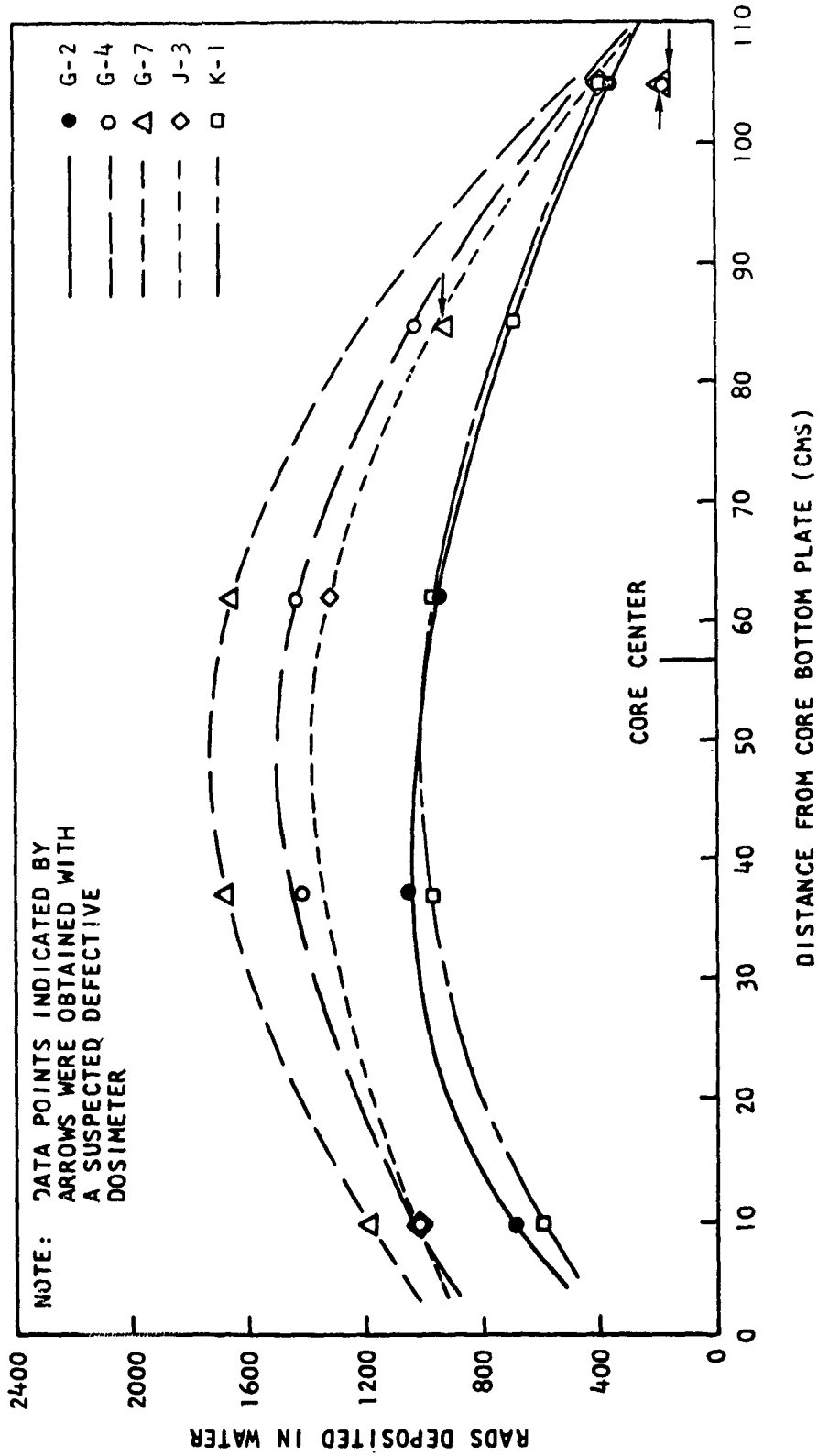


Fig. 3. 40--Absorbed dose in graphite dosimeters in nuclear rocket core fuel elements

Table 3.29  
 RESULTS OF IONIZATION CHAMBER MEASUREMENTS IN CORE III  
 OF THE TUNGSTEN NUCLEAR ROCKET REACTOR

Position Tube or Fuel Element	Distance from Core Bottom Plate Surface to Center of Dosimeter Active Volume, cm	Dosimeter Number C=Graphite P=Polyethylene	Dosimeter Reading in % of Full Scale (Corrected for Drift)	Normalizing Factor to Run 1 using C-14 as a Monitor	Absorbed Dose in Water at Point of Measurement Rads
G-2	9.4	C-16	19.2	1.021	684
G-2	37.1	C-11	24.8	1.021	1014
G-2	62.1	C-1	23.9	1.021	945
G-2	105.1	C-12	9.4	1.021	355
G-2	67.0	P-1	22.8	1.021	3000
G-4	9.4	C-5	26.0	1.009	1025
G-4	37.1	C-1	34.8	1.009	1406
G-4	62.1	C-6	35.1	1.021	1442
G-4	84.7	C-7	26.2	1.009	1029
G-4	105.1	*C-15	5.8	1.021	190
G-4	32.4	*P-6	28.8	1.026	3370
G-4	67.0	P-2	29.8	1.021	4540
G-7	9.4	C-5	30.0	1.026	1182
G-7	37.1	C-12	44.3	1.026	1673
G-7	62.1	(Run 1	43.1	1.000	1675
G-7	62.1	C-14 (Run 2	42.1	1.026	1636
G-7	62.1	(Run 3	42.3	1.021	1644
G-7	62.1	(R	42.8	1.009	1663
G-7	84.7	*C-15	22.9	1.026	907
G-7	105.1	*C-15	5.1	1.000	202
J-3	9.4	C-15	31.7	1.021	1012
J-3	62.1	C-12	35.1	1.000	1326
J-3	105.1	C-16	11.3	1.000	402
K-1	9.4	C-16	16.8	1.026	598
K-1	37.1	C-11	23.8	1.026	973
K-1	62.1	C-11	23.6	1.000	965
K-1	84.7	C-1	17.1	1.026	691
K-1	105.1	C-13	10.6	1.000	339
g-4	6.6	C-3	21.6	1.026	772
g-4	37.1	C-1A	25.3	1.026	922
g-4	62.1	C-1	23.6	1.000	953
g-4	110.0	C-3	6.6	1.000	236
g-4	11.4	P-1	17.8	1.026	2345
g-4	32.4	P-5	21.6	1.026	3150
g-4	67.0	P-2	20.6	1.000	3070
g-4	80.0	P-4	18.3	1.026	2670
g-4	105.3	P-1	8.6	1.000	1105

\*Suspected defective dosimeter

Table 3.29 (Continued)

Poison Tube or Fuel Element	Distance from Core Bottom Plate Surface to Center of Dosimeter Active Volume, cm	Dosimeter Number C=Graphite P=Polyethylene	Dosimeter Reading in % of Full Scale (Corrected for Drift)	Normalizing Factor to Run 1 using C-14 as a Monitor	Absorbed Dose in Water at Point of Measurement Rads
g-6	6.6	C-3	23.3	1.021	833
g-6	37.1	C-5	30.8	1.021	1214
g-6	62.1	C-12	30.5	1.009	1152
g-6	84.7	*C-15	13.6	1.009	538
g-6	110.0	C-13	5.6	1.009	179
g-8	6.6	C-2	23.1	1.026	837
g-8	37.1	C-6	33.5	1.026	1376
g-8	62.1	C-2	35.1	1.000	1271
g-8	84.7	C-1A	25.1	1.000	913
g-8	110.0	C-10	8.6	1.000	322
g-8	11.4	P-3	22.3	1.026	3370
g-8	32.4	P-2	28.6	1.026	4380
g-8	80.0	P-5	23.6	1.000	3360
g-8	105.3	P-4	10.6	1.000	1490
g-10	6.6	C-10	25.3	1.026	948
g-10	37.1	C-7	37.3	1.026	1465
g-10	62.1	C-5	36.6	1.000	1442
g-10	84.7	C-13	31.2	1.026	997
g-10	109.7	C-6	8.6	1.000	353
g-12	6.6	C-9	23.8	1.026	961
g-12	37.1	C-8	48.5	1.026	1765
g-12	62.1	C-7	38.1	1.000	1497
g-12	84.7	C-8	34.6	1.000	1259
g-12	110.0	C-9	8.6	1.000	347
g-12	11.4	P-7	27.0	1.026	3370
g-12	32.4	P-8	40.4	1.026	5030
g-12	67.0	*P-6	29.6	1.000	3375
g-12	80.0	P-8	32.6	1.000	4040
g-12	105.3	P-7	12.1	1.000	1470
h-8	6.6	C-16	29.5	1.009	1050
h-8	37.1	C-10	36.8	1.009	1379
h-8	62.1	C-7	33.5	1.021	1316
h-8	84.7	C-8	29.9	1.021	1088
h-8	110.0	C-9	7.3	1.021	295
h-8	11.4	*P-6	21.3	1.009	2450
h-8	32.4	P-5	29.3	1.009	4210
h-8	67.0	*P-6	25.8	1.021	3000
h-8	80.0	P-8	29.0	1.021	3660
h-8	105.3	P-7	10.8	1.021	1360

\*Suspected defective dosimeter

Table 3.29 (Continued)

Poison Tube or Fuel Element	Distance from Core Bottom Plate Surface to Center of Dosimeter Active Volume, cm	Dosimeter Number C=Graphite P=Polyethylene	Dosimeter Reading in % of Full Scale (Corrected for Drift)	Normalizing Factor to Run 1 using C-14 as a Monitor	Absorbed Dose in Water at Point of Measurement Rads
j-4	6.6	C-9	17.8	1.009	719
j-4	37.1	C-8	34.0	1.009	1237
j-4	62.1	C-2	27.5	1.021	996
j-4	84.7	*C-1A	5.9	1.021	215
j-4	110.0	C-10	6.7	1.021	251
j-4	11.4	P-7	19.6	1.009	2405
j-4	32.4	P-8	29.1	1.009	3630
j-4	67.0	P-3	24.4	1.021	3510
j-4	80.0	P-5	18.8	1.021	2730
j-4	105.3	P-4	9.0	1.021	1305
k-1	6.6	C-3	18.3	1.009	654
k-1	37.1	C-6	24.8	1.009	1019
k-1	62.1	C-2	25.0	1.009	906
k-1	84.7	C-11	16.9	1.009	691
k-1	110.0	C-1A	5.3	1.009	193
k-1	11.4	P-1	17.6	1.009	2285
k-1	32.4	P-2	21.1	1.009	3180
k-1	67.0	P-3	20.3	1.009	2890
k-1	105.3	P-4	7.3	1.009	1034
g-16	23.5	P-9	31.1	1.000	4540
g-16	23.5	P-9	30.8	1.026	4620
g-16	23.5	P-9	30.3	1.021	4530
g-16	23.5	P-9	31.3	1.009	4620

\*Suspected defective dosimeter

found to have an inherent response to neutrons. This response is difficult to determine precisely but has been estimated to be about 28%, and is also contingent upon the above discussed assumption. The neutron response of the carbon chamber was estimated by placing some of the carbon chambers in the same position as the calorimeter was placed. The ratio of the gamma dose in water to the dose in carbon is  $D_{H_2O}/D_C = 1.11$ .

The ratio of the neutron dose in water to the dose in carbon is  $D_{H_2O}^n/D_C^n =$

7.0. If the gamma dose in carbon is represented by A and the neutron dose in carbon by B then:

$$\text{Carbon: } A + B = R_1$$

$$\text{Water: } 1.11 A + 7 B = R_2$$

Where  $R_1$  and  $R_2$  are the rad values obtained for the carbon chamber and the water calorimeter respectively. <sup>(10)</sup> If these equations are solved simultaneously then the neutron response of the carbon chamber can be determined and is  $B/R_1$ . The data have not been corrected for the fast neutron response of the carbon chambers. It should be pointed out that the neutron response of the carbon chambers is a strong function of neutron energy and that additional calculations are required to determine the average response in the core spectrum.

It is estimated that the absolute calibration procedure for the polyethylene chambers gives the true absorbed dose in water within  $\pm 8\%$ .

The possible individual errors in this calibration are summarized below:

- $\pm 2\%$  in the reading of the Landsverk dosimeter
- $\pm 2\%$  in the relative monitor of the TRIGA power level
- $\pm 2\%$  in the uncertainty in time of the insertion of the dosimeters in the TRIGA core.



- ± 7% in the calibration of the calorimeter
- ± 1% in the dosimeter position corrective factor.

The possible individual errors in the measurements in Core III of the Tungsten Nuclear Reactor are summarized below:

- ± 2% in the reading of the Landsverk dosimeter
- ± 8% in the absolute calibration of the polyethylene chamber
- ± 5% in the absolute calibration of the carbon dosimeters
- ± 3% in the time at which the reactor is at maximum power level.

A negligible error was in the dose received by the chambers while being removed from the poison tubes and fuel elements. The fuel elements were reading an average of 2 r/hr at the surface and the dosimeters remained in the fuel elements for a maximum of 15 minutes after the run.

On this basis the probable error in the measurements using the polyethylene chambers is ± 9%; for the carbon dosimeters it is ± 6%.

#### IV. ANALYTICAL METHODS

##### 4.1 COMPUTATION OF THE SPATIAL FINE STRUCTURE IN A CELL

A unit hexagonal cell was defined, and homogeneous atom densities appropriate to this cell were obtained. The thermal spectrum (0 to 2.38 eV) was calculated in the P-1 approximation, using the GATHER-II code.<sup>(11)</sup> The scattering kernel as developed by Nelkin was used for hydrogen bound in water. One-hundred and one pointwise values of the cross sections were averaged over the thermal spectrum to obtain multigroup thermal cross sections for the spatial fine structure calculations. The fast spectrum (2.38 eV to 14.9 MeV) was calculated in the B-1 approximation, using the GAM-II<sup>(12)</sup> code with a U-235 fission source. Ninety-nine group values of the cross sections were then averaged over the calculated fast spectrum to obtain multigroup epithermal cross sections for the spatial fine structure calculations.

Once the multigroup cross sections were obtained, the spatial fine structure of the flux in the unit cell was computed to obtain cell disadvantage factors. The disadvantage factor in energy group "i" for nuclide "n" was defined in the following manner:

$$g_n^i = \frac{\int N_n(\bar{r}) \phi^i(\bar{r}) d^3 r}{\frac{1}{V} \int \phi^i(\bar{r}) d^3 r \int N_n(\bar{r}) d^3 r}, \quad (4.1)$$

where  $\phi$  is the scalar flux,  $N$  is the atom density, and  $V$  is the total cell volume. Since the flat flux assumption in the high energy region is invalid for highly heterogeneous cells, high energy as well as thermal disadvantage factors (sometimes called advantage factors in the high energy region) were obtained in the epithermal region ( $\gtrsim 60$  keV) of the spectrum. The details of this calculation, and in particular the validation of the white boundary condition for high energy fine structure calculations in the Wigner-Seitz<sup>(13)</sup> approximation, are discussed below.

The Carlson discrete angle  $S_n$  method<sup>(14)</sup> was used for all cell calculations. The disadvantage factors for all nuclides except cadmium were obtained by representing the hexagonal unit cell in the Wigner-Seitz approximation and utilizing the white boundary condition. (The cadmium poison was treated separately, and the calculation of the cadmium disadvantage factors is discussed in Section 4.11.) Terms through  $P_1$  were retained in the scattering kernels. The high energy disadvantage factors were obtained from one-dimensional calculations in the  $S_8$  approximation using the GAPLSN code.<sup>(15)</sup> Thermal group disadvantage factors were computed in the  $S_4$  approximation and the calculations were performed in both one-dimensional and two-dimensional  $r$ - $z$  geometry.

## 4.2 HIGH ENERGY DISADVANTAGE FACTORS

Highly heterogeneous reactor cells may exhibit fine structure in the high energy neutron flux that must be considered in an accurate calculation of the fast neutron effective cross sections. In particular, the proper spatial flux weighting of the cross sections in a water lattice is necessary for an accurate evaluation of the high energy leakage. Hardy and Klein<sup>(16)</sup> have measured the fast neutron fine structure in a series of uranium-water lattices, and have analyzed the experiment with Monte-Carlo calculations. It is desirable, however, to compute the fast flux fine structure with conventional transport cell calculations, in the same manner that the thermal neutron fine structure is usually computed.

Survey calculations of thermal neutron disadvantage factors in reactor cells are generally accomplished in the Wigner-Seitz (WS) cylindrical-cell approximation. Thie<sup>(17)</sup> demonstrated that high order transport calculations of small cells in the WS approximation together with the reflective-boundary condition can lead to significant errors in the disadvantage factors. Thie studied six tightly-packed square lattices, with moderator ( $H_2O$ ) thicknesses less than 0.5 mean free path in the equivalent cylindrical cell. Several authors<sup>(18, 19, 20, 21)</sup> have subsequently discussed this problem. Honeck<sup>(19)</sup> suggested an isotropic flux return at the boundary of the WS cell, which he implemented by surrounding the moderator with an optically thick, pure isotropic scatterer. Weiss and Stamm'ler<sup>(21)</sup> subsequently verified that Honeck's "white" boundary condition, used in conjunction with a transport calculation in the WS approximation, gives good agreement with Monte Carlo results (which were confirmed using a collision probability technique) for the Thie lattices.

In the calculation of high energy disadvantage factors, the question of the appropriate cylindrical cell boundary condition arises because the cell dimensions are generally small in comparison with a neutron mean free path. A re-examination of the issue is justified because of basic differences between the thermal and the high energy problems. In the high energy problem, the source is in the fuel zone rather than in the moderator. Furthermore, the flux in the moderator is likely to be highly anisotropic, which brings to suspect a boundary condition based upon an isotropic flux return.

To examine this problem, transport calculations were performed using both reflective and white boundary conditions in the cylindrical cell approximation, and the results were compared with equivalent two-dimensional calculations for simple two-zone cells. The two-dimensional calculations, referred to as "exact", treat the physically realistic square lattice cell incorporating the reflective-boundary condition. The fuel

zone consists primarily of a homogenized mixture of highly enriched uranium and aluminum with a radius of 3.29 cm. The moderator zone consists primarily of water; moderator thicknesses of 0.92 (Cell No. I) and 1.84 cm (Cell No. II) were examined.

The cylindrical cell calculations were performed with the GAPLSN code, whereas the Los Alamos DDK code was used for the two-dimensional calculations. Both sets of calculations were performed in the  $S_6$  approximation and included first order anisotropic scattering ( $P_1$ ). A constant isotropic fission source was utilized in the fuel zone. (The effect on the disadvantage factors of the flat source approximation was shown to be negligible by comparing the results with a multigroup calculation which computed a realistic fission source distribution.) The fuel zone was approximated in the two-dimensional calculation by a fine mesh of jagged boundaries which preserved the total area. Two energy groups were used - the first covering the energy range from 2.02 to 14.9 MeV, the second from 0.067 to 2.02 MeV.

The results of the calculations are given in Table 4.1. The reflective-boundary condition grossly overestimates the disadvantage factor in the high energy group. The agreement is considerably better in the low energy group, although the white boundary condition still gives better results. Physically, the curvature artificially introduced by the WS approximation accentuates the reflection to the fuel zone of the forward-peaking flux near the boundary. The white boundary condition has the effect of "smearing" the angular flux near the boundary, and, as shown in Fig. 4.1 eliminates the artificially high flux gradient near the boundary.

The effect of including high energy disadvantage factors in a calculation of the poisoned mockup reference core<sup>(22)</sup> is demonstrated in Table 4.2. The Fermi age leakage fraction, and multiplication factor were calculated in three ways - without high energy disadvantage factors and with high energy disadvantage factors calculated in the WS approximation using

Table 4. 1

DISADVANTAGE FACTORS,  $\bar{\phi}_{\text{FUEL}}/\bar{\phi}_{\text{MOD}}$ 

Cell No.	Neutron Energy Range (MeV)	Fuel Radius (mean free path)	Moderator Thickness (mean free path)	Two-Dimensional "Exact"	One-Dimensional Reflective Boundary Condition	One-Dimensional White Boundary Condition
I	2.02-14.9	0.346	0.186	1.171	1.467	1.175
	0.067-2.02	0.457	0.513	1.191	1.232	1.160
II	2.02-14.9	0.346	0.372	1.408	1.752	1.427
	0.067-2.02	0.457	1.03	1.400	1.443	1.378

4-5

Table 4. 2

## AGE, LEAKAGE FRACTION, AND EFFECTIVE MULTIPLICATION FACTOR OF THE MOCKUP REFERENCE CORE

	No High Energy Disadv. Factors	High Energy Disadv. Factors from White Bndry. Condition	High Energy Disadv. Factors from Reflective Bndry. Condition
Age (to 2.38 eV) cm <sup>2</sup>	83.4	90.6	96.1
Leakage/Source Neutron	0.1777	0.1880	0.1951
k <sub>eff</sub>	1.0107	1.0000	0.9929
δk <sub>eff</sub>	+1.07%	-	-0.71%

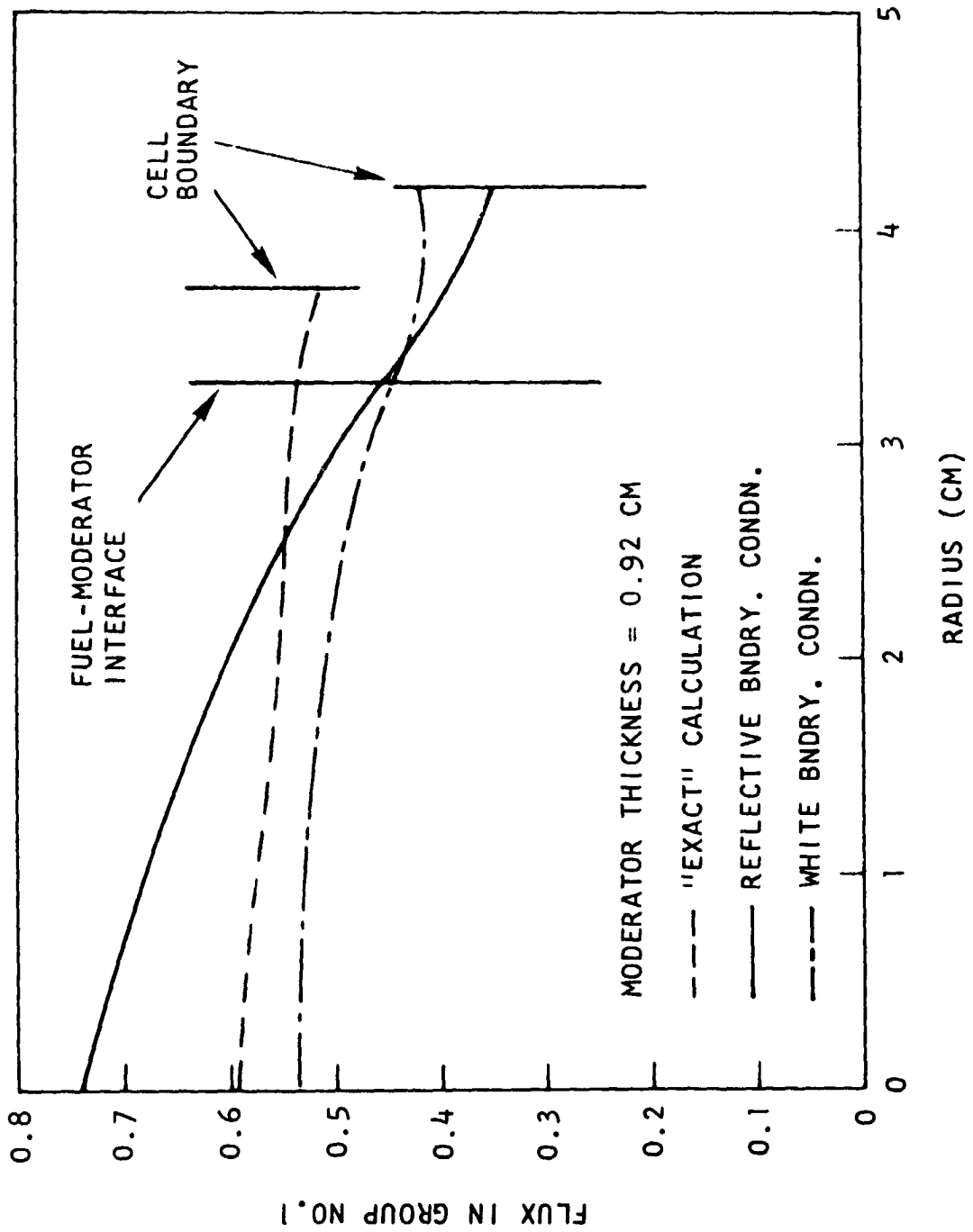


Fig. 4.1--Group 1 flux vs cell radius

both white and reflective boundary conditions. The age, as calculated by GAM, is defined in the following way:

$$\tau(E)_n = \frac{\Phi_{20}(E)_n}{\Phi_{00}(E)_n},$$

where:

$$\Phi_{nl}(E) = \frac{1}{n!} \int_{-\infty}^{\infty} Z^n \Phi_l(Z, E) dZ.$$

It is seen that the correct consideration of high energy disadvantage factors increases the Fermi age by more than 8%. The effect on  $k_{\text{eff}}$  is approximately 1%. A calculation of  $k_{\text{eff}}$  which utilizes the reflective-boundary condition is in error by approximately 0.7%.

#### 4.3. COMPUTATION OF $k_{\infty}$

Once the disadvantage factors were obtained, the thermal and fast spectra were recalculated, weighting the atom densities with the disadvantage factors to reflect spatial self-shielding. Gross core leakage is taken into account in the GAM-II calculation of the fast spectrum through the overall core buckling which was obtained in the subsequent multi-group diffusion calculation of  $k_{\text{eff}}$ . This portion of the calculation, then, depended upon an iterative procedure. The buckling was obtained from the group-diffusion calculation as:

$$B_i^2 = \frac{\sum_{i=1}^N (\text{Leakage})_i}{\sum_{i=1}^N D_i \phi_i} \quad (4.2)$$



where  $D_i$  is the diffusion coefficient for group  $i$ ,  $\phi_i$  is the integrated flux in group  $i$ , and  $N$  is the total number of groups in the calculation. The resonance calculation was initially performed in the constant source approximation using the Nordheim integral technique<sup>(23)</sup> for the solution of the energy-dependent integral equations. The details of the resonance treatments are described in Section 4.11.

Broad-group fast and thermal cross sections, used in subsequent multigroup-diffusion calculations, were averaged over the final GAM-II and GATHER-II spectra, and were weighted by the disadvantage factors. The infinite multiplication factor was then obtained, after an appropriate normalization between the fast and thermal fluxes, from the relationship,

$$k_{\infty} = \frac{\sum_j \nu_j \Sigma_{fj} \phi_j \Delta_j}{\sum_j \Sigma_{aj} \phi_j \Delta_j} \quad (4.3)$$

where  $\Sigma_f$  is the macroscopic fission cross section,  $\Sigma_a$  is the macroscopic absorption cross section,  $\phi$  is the scalar flux,  $\nu$  is the number of neutrons produced per fission.

#### 4.4 TRANSPORT CROSS SECTION

##### 4.4.1 TRANSPORT CROSS SECTION IN THE P-1 APPROXIMATION

The energy dependent P-1 equations may be written

$$\bar{\nabla} \cdot \bar{J}(\bar{r}, E) + \Sigma_t(\bar{r}, E)\phi(\bar{r}, E) = \int_0^{\infty} dE' \Sigma_{s0}(\bar{r}, E' \rightarrow E)\phi(\bar{r}, E') + S(\bar{r}, E) \quad (4.4)$$

$$\frac{1}{3} \bar{\nabla} \phi(\bar{r}, E) \Sigma_t(\bar{r}, E) \bar{J}(\bar{r}, E) = \int_0^{\infty} dE' \Sigma_{s1}(\bar{r}, E' \rightarrow E) \bar{J}(\bar{r}, E'), \quad (4.5)$$

where  $\varphi$  is the scalar flux,  $\bar{J}$  is the current, and  $\Sigma_t$  is the total cross section. The source term,  $S(\bar{r}, E)$ , includes neutrons produced by fission, and is assumed to be isotropic in the laboratory system. The Legendre expansion coefficients of the scattering kernel are given by

$$\Sigma_{s_\ell}(\bar{r}, E' \rightarrow E) = 2\pi \int_{-1}^1 d\mu P_\ell(\mu) \Sigma_s(\bar{r}, E' \rightarrow E, \mu), \quad (4.6)$$

where  $P_\ell(\mu)$  is the  $\ell^{\text{th}}$  order Legendre polynomial and  $\Sigma_s$  is the scattering kernel.

The transport cross section,  $\Sigma_{tr}(\bar{r}, E)$ , is defined by manipulation of Eq. (4.5). We have

$$-\frac{1}{3} \bar{\nabla} \varphi(\bar{r}, E) = \Sigma_t(\bar{r}, E) \bar{J}(\bar{r}, E) - \int_0^\infty dE' \Sigma_{s_1}(\bar{r}, E' \rightarrow E) \bar{J}(\bar{r}, E'). \quad (4.7)$$

It is assumed that the direction of the current is independent of energy; i. e., we can write

$$\bar{J}(\bar{r}, E) = \bar{\kappa} J(\bar{r}, E), \quad (4.8)$$

where  $J(\bar{r}, E)$  is a scalar function of space and energy and  $\bar{\kappa}$  is a unit vector denoting the direction of the current. Then Eq. (4.7) can be written

$$\bar{J}(\bar{r}, E) = - \frac{1}{3 \Sigma_{tr}(\bar{r}, E)} \bar{\nabla} \varphi(\bar{r}, E), \quad (4.9)$$

where the transport cross section is defined by

$$\sum_{tr}(\bar{r}, E) = \sum_t(\bar{r}, E) - \int_0^{\infty} dE' \sum_{s_1}(\bar{r}, E' \rightarrow E) \frac{J(\bar{r}, E')}{J(\bar{r}, E)} \quad (4.10)$$

A spatially independent current spectrum,  $J(E)$ , is generally obtained and used in the integral on the right-hand side of Eq. (4.10).

One frequently encounters an alternate definition of the transport cross section

$$\sum_{tr}(\bar{r}, E) = \sum_t(\bar{r}, E) - \bar{\mu} \sum_{s_0}(\bar{r}, E), \quad (4.11)$$

where  $\bar{\mu}$  is given by

$$\bar{\mu} = \frac{\int_{-1}^1 d\mu \mu \sum_s(\bar{r}, E' \rightarrow E, \mu)}{\int_{-1}^1 d\mu \sum_s(\bar{r}, E' \rightarrow E, \mu)} \quad (4.12)$$

Referring to Eq. (4.6), Eq. (4.11) can be written:

$$\sum_{tr}(\bar{r}, E) = \sum_t(\bar{r}, E) - \sum_{s_1}(\bar{r}, E) \quad (4.13)$$

This definition of the energy dependent transport cross section is an artifice, and the relationship given by Eq. (4.11) is strictly valid only within the realm of monoenergetic P-1 theory. However, when  $\sum_{s_1}(\bar{r}, E' \rightarrow E)$  in Eq. (4.10) is significant only in the energy range where  $J(\bar{r}, E')/J(\bar{r}, E) \simeq 1$ , and if the energy degradation in scattering is insignificant, Eq. (4.10) reduces to Eq. (4.13). These assumptions, of course, are synonymous with the limit of monoenergetic diffusion, and thus this alternate definition of the transport cross section is only justifiable for scattering from heavy elements.

The procedure for energy averaging of the transport cross section within the realm of multigroup diffusion theory has formed the basis for considerable controversy over the years. Pomraning<sup>(24)</sup> has discussed this problem in some length. The point is that the averaging procedure depends upon the stage at which the space-energy separation is performed. If the space-energy separation is made after the energy-dependent P-1 equations are written down

$$\varphi(\bar{r}, E) = \Phi(\bar{r})\varphi(E), \quad (4.14)$$

then a parallel average of the transport cross section over the spectrum is appropriate

$$\langle \sum_{tr}(\bar{r}) \rangle_i = \frac{\int_i dE \varphi(\bar{r}, E)}{\int_i dE \frac{1}{\sum_{tr}(\bar{r}, E)} \varphi(\bar{r}, E)}. \quad (4.15)$$

(This is equivalent to a series average of the transport cross section over the spectrum of the current.) If, however, one begins by writing down the energy dependent Boltzmann equation, and separating the angular flux

$$\psi(\bar{r}, \Omega, E) = \psi(\bar{r}, \bar{\Omega})\varphi(E), \quad (4.16)$$

the current and flux spectra are identical. Using this approach, Pomraning<sup>(25)</sup> has arrived at a series average of the transport cross section over the spectrum

$$\langle \sum_{tr}(\bar{r}) \rangle_i = \frac{\int_i dE \sum_{tr}(\bar{r}, E) \varphi(\bar{r}, E)}{\int_i dE \varphi(\bar{r}, E)}. \quad (4.17)$$

Generally energy dependent diffusion theory is preferred, and the parallel average given by Eq. (4.15) is applied.

#### 4.4.2 TRANSPORT APPROXIMATION OF THE MULTIGROUP BOLTZMANN EQUATION

The energy dependent Boltzmann equation may be written

$$\bar{\Omega} \cdot \bar{\nabla} \psi(\bar{r}, E, \bar{\Omega}) + \sum_t(\bar{r}, E) \psi(\bar{r}, E, \bar{\Omega}) = \iint dE' d\bar{\Omega}' \sum_s(\bar{r}, E' \rightarrow E, \bar{\Omega} \cdot \bar{\Omega}') \psi(\bar{r}, E', \bar{\Omega}'), \quad (4.18)$$

where  $\psi(\bar{r}, E, \bar{\Omega})$  is the angular flux. The source is neglected for simplicity. The scattering kernel is generally expanded in Legendre coefficients, resulting in the following equation

$$\bar{\Omega} \cdot \bar{\nabla} \psi(\bar{r}, E, \bar{\Omega}) + \sum_t(\bar{r}, E) \psi(\bar{r}, E, \bar{\Omega}) = \frac{1}{4\pi} \sum_{\ell=0}^{\infty} (2\ell + 1) \int dE' \sum_{s_\ell}(\bar{r}, E' \rightarrow E) \int d\bar{\Omega}' P_\ell(\bar{\Omega} \cdot \bar{\Omega}') \psi(\bar{r}, E', \bar{\Omega}'). \quad (4.19)$$

The Legendre expansion coefficients are defined by Eq. (4.6). The expansion is generally truncated so that all terms with  $n \geq 2$  are set equal to zero. In this way an isotropic and a first order anisotropic component of the scattering kernel are retained.

Frequently computer memory size limitations allow only the isotropic scattering component to be retained in a numerical quadrature of Eq. (4.19). Since anisotropic scattering plays a significant role in systems containing light elements, it is desirable when making this approximation to somehow account for anisotropic scattering in the cross sections. We refer to such a scheme as the transport approximation of the Boltzmann equation.

Rakavy and Yeivin<sup>(26)</sup> first demonstrated this transport approximation by subtracting an arbitrary function,  $X(\bar{r}, E, \bar{\Omega})$ , from both sides of Eq. (4.18). Defining

$$\alpha(\bar{r}, E, \bar{\Omega}) = \sum_t (\bar{r}, E) - X(\bar{r}, E, \bar{\Omega})$$

and

$$\beta(\bar{r}, E' \rightarrow E, \bar{\Omega} \cdot \bar{\Omega}') = \sum_s (\bar{r}, E' \rightarrow E, \bar{\Omega} \cdot \bar{\Omega}') - X(\bar{r}, E, \bar{\Omega}) \delta(E - E') \delta((\bar{\Omega} \cdot \bar{\Omega}') - 1), \quad (4.20)$$

where  $\delta$  is the Dirac delta function,  $\beta$  is expanded in a Legendre expansion through the second term

$$\begin{aligned} \bar{\Omega} \cdot \bar{\nabla} \psi(\bar{r}, E, \bar{\Omega}) + \alpha(\bar{r}, E, \bar{\Omega}) \psi(\bar{r}, E, \bar{\Omega}) &= \frac{1}{4\pi} \sum_{\ell=0}^{\ell=1} (2\ell + 1) \int dE' \beta_{\ell}(\bar{r}, E' \rightarrow E) \\ &\int d\bar{\Omega}' P_{\ell}(\bar{\Omega} \cdot \bar{\Omega}') \psi(\bar{r}, E', \bar{\Omega}'). \end{aligned} \quad (4.21)$$

The transport approximation consists of setting the term with  $\ell = 1$  on the right-hand side of Eq. (4.21) equal to zero. Doing so, the arbitrary function,  $X$ , is evaluated

$$\begin{aligned} X(\bar{r}, E, \bar{\Omega}) &= \int_0^{\infty} dE' \sum_{s_1} (\bar{r}, E' \rightarrow E) \frac{\bar{\Omega} \cdot \bar{J}(\bar{r}, E')}{\bar{\Omega} \cdot \bar{J}(\bar{r}, E)} \\ &= \sum_t (\bar{r}, E) - \sum_{tr} (\bar{r}, E), \end{aligned} \quad (4.22)$$

using the definition of  $\sum_{tr}$  in Eq. (4.10) and assuming that the direction of the current is independent of the energy. Thus the transport approximation of the energy dependent Boltzmann equation becomes

$$\begin{aligned} \bar{\Omega} \cdot \bar{\nabla} \psi(\bar{r}, E, \bar{\Omega}) + \sum_{tr}(\bar{r}, E) \psi(\bar{r}, E, \bar{\Omega}) &= \frac{1}{4\pi} \int_0^\infty dE' \left\{ \sum_{s_0}(\bar{r}, E' \rightarrow E) \right. \\ &+ \left. \left[ \sum_{tr}(\bar{r}, E) - \sum_t(\bar{r}, E) \right] \delta(E - E') \right\} \varphi(\bar{r}, E'). \end{aligned} \quad (4.23)$$

The multigroup scheme is derived by integrating Eq. (4.23) over energy within group  $i$ , where the group angular flux is defined as

$$\varphi_i(\bar{r}, \bar{\Omega}) = \int_{E_{i-1}}^{E_i} dE \psi(\bar{r}, E, \bar{\Omega}). \quad (4.24)$$

At this stage, the angular flux is assumed separable within each energy group

$$[\psi(\bar{r}, E, \bar{\Omega})]_i = \psi_i(\bar{r}, \bar{\Omega}) \varphi_i(E), \quad (4.25)$$

and accordingly the scalar flux becomes

$$[\varphi(\bar{r}, E)]_i = \int_i d\bar{\Omega} \psi(\bar{r}, E, \bar{\Omega}) = \Phi_i(\bar{r}) \varphi_i(E). \quad (4.26)$$

Integrating Eq. (4.23) over energy in the  $i^{\text{th}}$  group, and using the separability assumption, we arrive at the multigroup scheme for the transport approximation of the Boltzmann equation:

$$\bar{\Omega} \cdot \bar{\nabla} \psi_i(\bar{r}, \bar{\Omega}) + \sum_{tr}^i(\bar{r}) \psi_i(\bar{r}, \bar{\Omega}) = \frac{1}{4\pi} \sum_{j=1}^N \left\{ \sum_{s_0}^{j \rightarrow i}(\bar{r}) + \delta_{ij} \left[ \sum_{tr}^i(\bar{r}) - \sum_t^i(\bar{r}) \right] \right\} \Phi_j(\bar{r}), \quad (4.27)$$

where  $\delta_{ij}$  is the Kronecker delta. Equation (4.27) differs from the simple isotropic scattering approximation in two ways: 1) the group averaged transport cross section appears in place of the total cross section on the left-hand side of the equation, and 2) the diagonal term of the  $P_0$  scattering matrix on the right-hand side of the equation contains the additional term in the straight brackets.

The group cross sections appearing in Eq. (4.27) are defined in the following way

$$\sum_{t, tr}^i(\bar{r}) = \frac{\int_{E_{i-1}}^{E_i} dE \sum_{t, tr}(\bar{r}, E) \varphi_i(E)}{\int_{E_{i-1}}^{E_i} dE \varphi_i(E)} \quad (4.28)$$

and

$$\sum_{s_0}^{j \rightarrow i}(\bar{r}) = \frac{\int_{E_{i-1}}^{E_i} dE \int_{E_{j-1}}^{E_j} dE' \sum_{s_0}(\bar{r}, E' \rightarrow E) \varphi_j(E')}{\int_{E_{j-1}}^{E_j} dE' \varphi_j(E')} \quad (4.29)$$



We see that all of the cross sections appearing in Eq. (4.27) are series averages over the spectrum of the flux. The separability approximation of Eq. (4.25) is implicit in obtaining this result, but this assumption is necessary to arrive at multigroup transport theory, since the neutron spectrum used for averaging is generally obtained from a zero dimensional spectrum calculation.

#### 4.5 NUMERICAL EXAMPLE

Three cell calculations, using the GAPLSN code in the  $S_4$  approximation, have been performed to obtain thermal disadvantage factors for a unit cell closely resembling that of the mockup reference cell.<sup>(22)</sup> The three cell calculations consist of the following approximations to the Boltzmann equation:

1. A  $P_0$  expansion of the scattering kernel; i. e., only the first term of the expansion on the right-hand side of Eq. (4.19) is retained.
2. A  $P_1$  expansion of the scattering kernel; i. e., the first two terms of the expansion on the right-hand side of Eq. (4.19) are retained.
3. The transport approximation discussed in Section 4.4.2 i. e., Eq. (4.27) is used.

The disadvantage factors obtained for each of the above three approximations are listed in Table 4.3. The calculations were performed with five thermal groups, and results for the five principal isotopes present in the cell are tabulated. It is seen that the maximum deviation between the  $P_1$  results and the transport approximation is 3%, whereas several of the  $P_0$  results differ by as much as 7% from  $P_1$  calculation.

Table 4.3

## UNIT CELL DISADVANTAGE FACTORS

	P <sub>0</sub> Calculation					P <sub>1</sub> Calculation					Transport Approx.				
	Group					Group					Group				
	1	2	3	4	5	1	2	3	4	5	1	2	3	4	5
	(eV)	(eV)	(eV)	(eV)	(eV)	(eV)	(eV)	(eV)	(eV)	(eV)	(eV)	(eV)	(eV)	(eV)	(eV)
H	1.10	1.34	1.51	1.63	1.82	1.08	1.28	1.45	1.57	1.78	1.11	1.30	1.45	1.58	1.78
W	0.920	0.745	0.631	0.551	.423	0.931	0.785	0.668	0.584	.447	0.911	0.769	0.662	0.579	0.442
U <sup>235</sup>	0.902	0.686	0.539	0.436	.276	0.913	0.721	0.571	0.463	.295	0.884	0.697	0.562	0.456	0.288
U <sup>238</sup>	0.956	0.865	0.802	0.763	.694	0.967	0.906	0.848	0.808	.724	0.966	0.906	0.848	0.805	0.726
Al	0.940	0.800	0.699	0.629	.517	0.950	0.832	0.731	0.657	.538	0.936	0.823	0.728	0.655	0.534

#### 4.6 COMPUTATION OF $k_{eff}$

The effective multiplication factor was computed using multigroup diffusion theory. Most of the multigroup diffusion calculations were performed by a synthesis of the two-dimensional assembly geometry using a one-dimensional buckling-iteration procedure with the GAZE-II code.<sup>(27)</sup> The buckling iteration consists of a radial-axial-radial scheme, which has been shown to converge  $k_{eff}$  for these cores to an error in  $k$  of less than  $10^{-4}$ . At each step of the procedure, bucklings were computed from Eq. 4.2 to use as transverse bucklings in the subsequent calculations. Two-dimensional multigroup diffusion calculations were performed using the GAMBLE-IV code.<sup>(28)</sup>

The void content of the fuel element gave rise to some concern that an axial streaming problem might exist which is not properly treated by the procedure outlined above. A Monte Carlo analysis of the high energy leakage from the reference mockup core<sup>(22)</sup> was made and good agreement was obtained between it and the leakage as calculated by multigroup diffusion theory.

#### 4.7 MONTE CARLO ANALYSIS OF HIGH ENERGY LEAKAGE

##### 4.7.1 PURPOSE OF MONTE CARLO CALCULATIONS

A Monte Carlo analysis of the high energy leakage from the mock-up core was made. The purpose was to investigate the validity of the results obtained using the more conventional methods.

##### 4.7.2 DESCRIPTION OF THE MONTE CARLO CODE

A slightly modified version of FMC-N, developed by GE-ANP<sup>(29)</sup> was used on the General Atomic IBM-7044 computer. This code allows explicit representation of any geometry and source, as well as accounting for inelastic scattering, elastic scattering, absorption, and fission. A summary of the major features of the code and its data requirements follows:

#### 4.7.2.1 Geometry Description

A hexagonal cell containing one fuel element with the surrounding water moderator was exactly represented. The fuel element configuration was that used in the Hazards Analysis with the tungsten inside the fuel rings and the U-238 ring outside the radiation shield. It is shown in Fig. 4.2. A bottom beryllium reflector and a top water reflector were exactly represented.

#### 4.7.2.2 Source Description

The code requires probability tables for the source as separable functions of radius, height, and energy. Source neutron parameters are then selected randomly from the tables with an isotropic angular distribution. In this analysis the radial distribution was represented by the probability table shown in Fig. 4.3. The figure is a graph of the probability table as a function of radius and was prepared from the radial distribution of the source obtained from a transport cell calculation.

The axial source distribution was obtained from a GAZE axial calculation. As shown in Fig. 4.4 it was divided into seven segments, each segment being used as a source for a separate problem. The results of the seven problems, when properly weighted and combined are equivalent to those obtained from a single complete source problem but require much less running time.

The energy distribution of the source was taken from the thermal fission spectrum of U-235.

#### 4.7.2.3 Energy Group Bounds

Although the code uses explicit neutron energies in following a history, it is convenient to represent input and output data averaged over a group structure. The group structure used was that which was convenient to GAM averaged cross sections, i. e., groups of multiples of 0.1 lethargy units in width. Microscopic cross sections, angular distribution

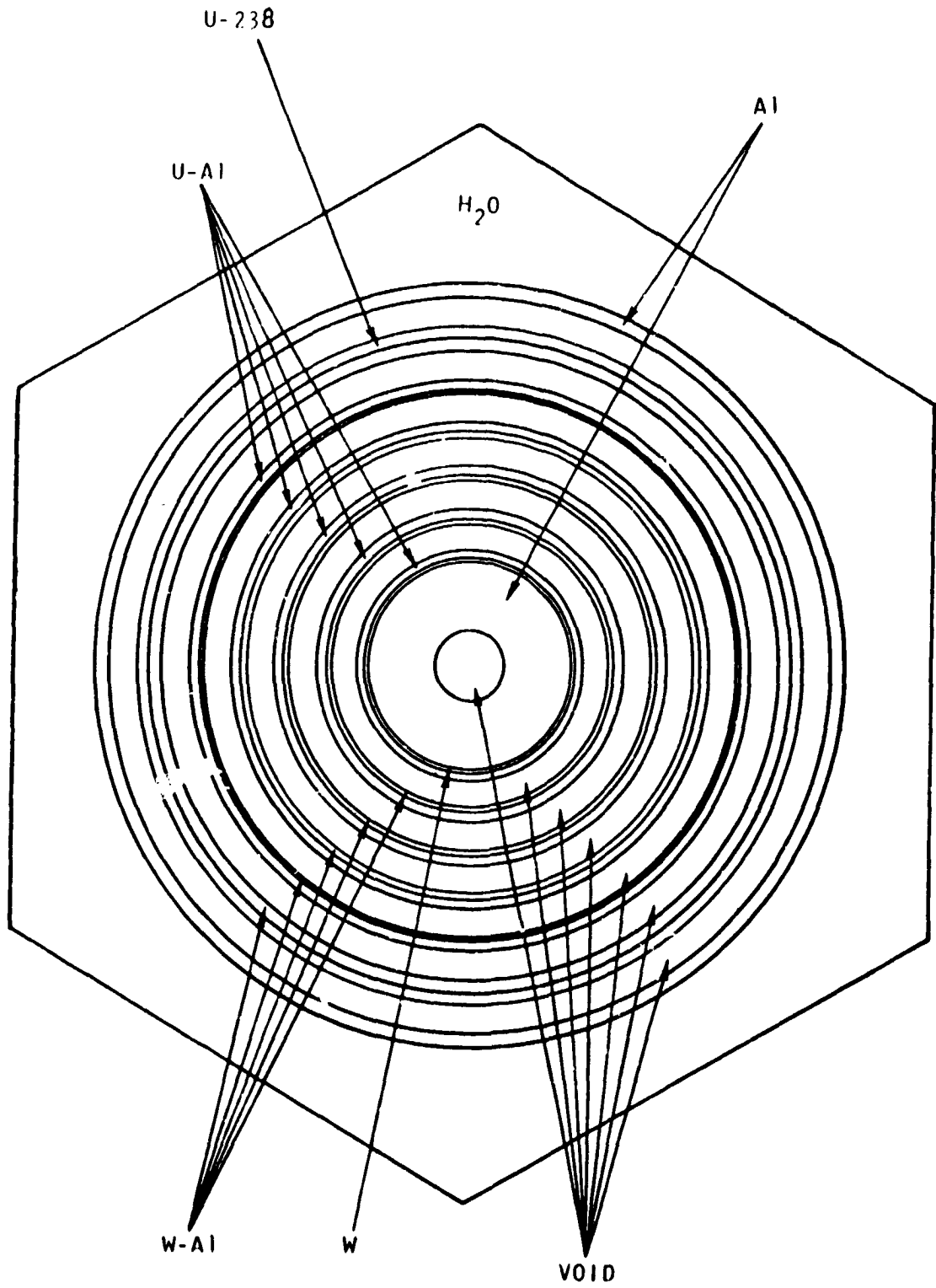
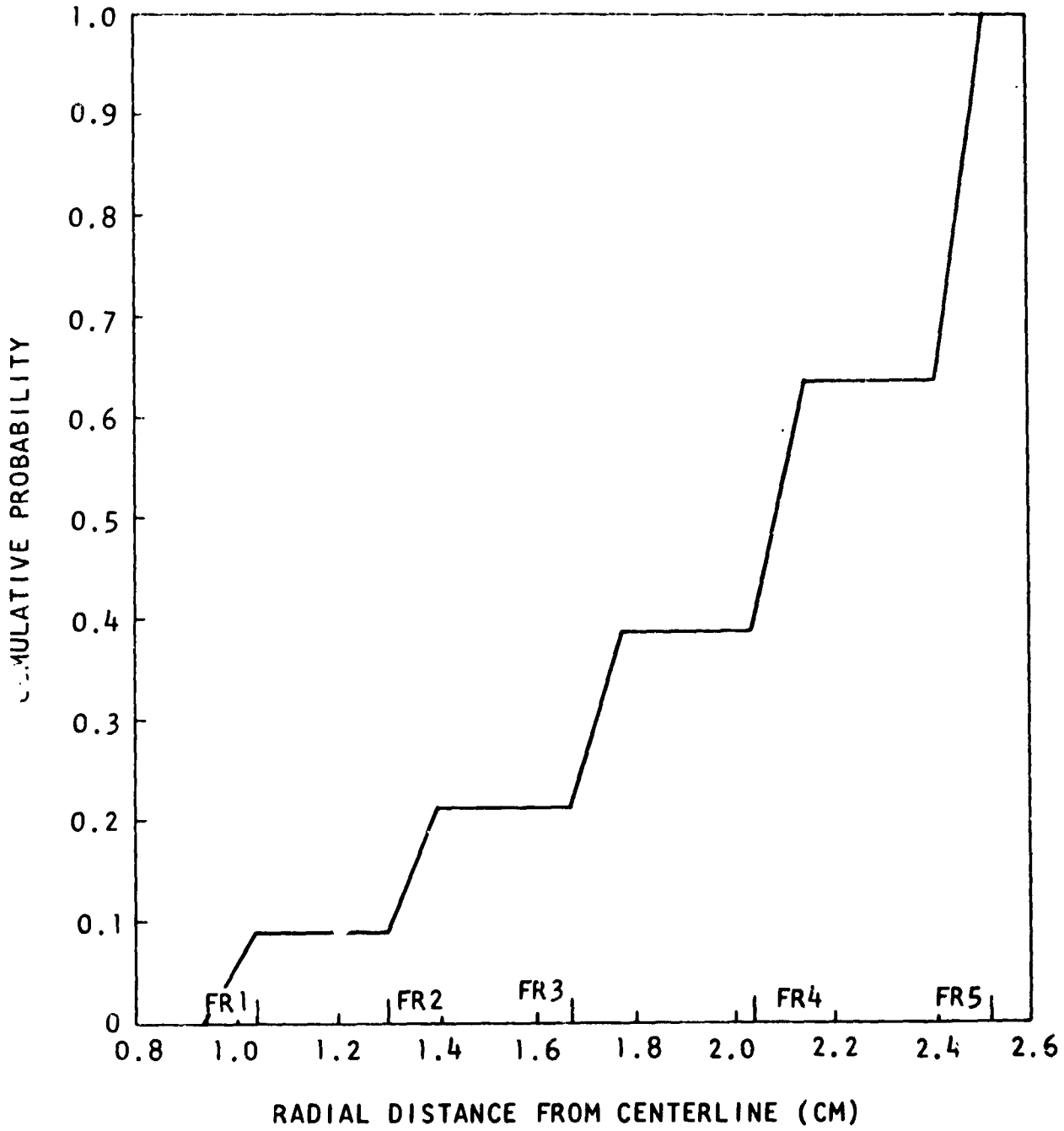


Fig. 4.2--Mockup fuel element and hexagonal cell used in Monte Carlo analysis



4.3

Fig. 4.3--Cumulative probability radial source distribution mockup 5-ring cell

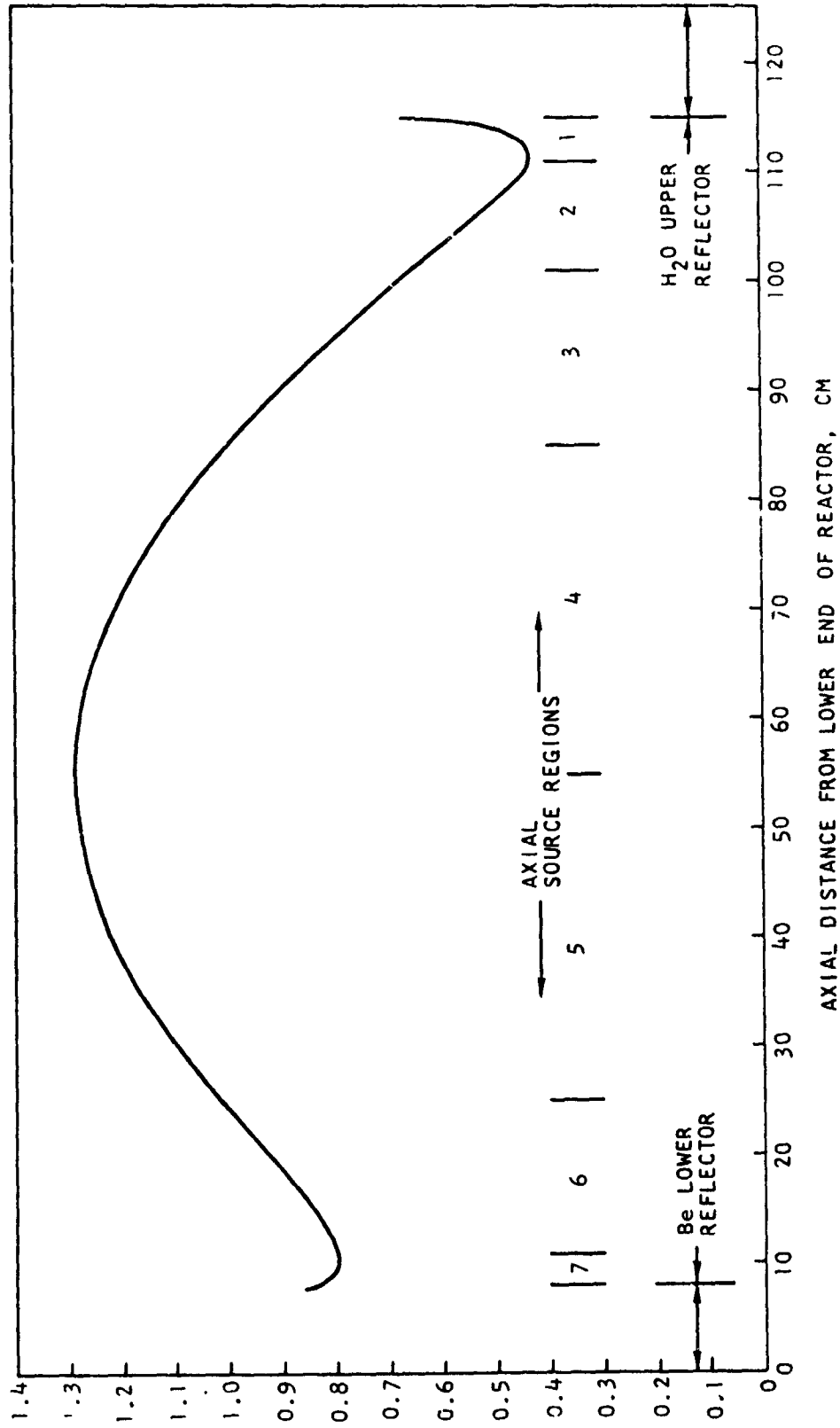


Fig. 4.4--Local/average fission rates vs. axial distances

probability tables, and fission spectrums were read into the code as average values over the group structure of Table 4.4.

The 26th group extends to zero energy and was merely used to terminate histories. Thus the problem was effectively cut off for energies below 86.5 keV.

Table 4.4  
ENERGY BOUNDS FOR INPUT DATA GROUP STRUCTURE

<u>Group</u>	<u>Top Energy (MeV)</u>
1	14.92
2	12.21
3	10.00
4	8.187
5	6.703
6	5.488
7	4.493
8	3.679
9	3.012
10	2.466
11	2.019
12	1.653
13	1.353
14	1.108
15	0.907
16	0.743
17	0.608
18	0.498
19	0.408
20	0.334
21	0.273
22	0.224
23	0.183
24	0.150
25	0.123
26	0.0865



#### 4.7.2.4 Fission and Total Cross Sections

The microscopic fission and total cross sections were obtained from the GAM-II program. The entries on these GAM-II data tapes are averaged with a  $1/E$  flux over each 0.1 lethargy interval and thus deviate from a flat average over such an interval by  $\pm 5\%$ . This is a very small error in the problem. The entries for each 0.1 lethargy interval were averaged to form values for the 0.2 lethargy intervals used in the Monte Carlo analysis.

Since  $n, 2n$  processes cannot be handled explicitly in FMC-N, they were considered to be a fission process with a yield of 2.0 neutrons/fission. The code stores fission events until all the source neutrons are used up and then returns to process the new neutrons originating from fast fission and, thus,  $n, 2n$  as well. The fast fission spectrum tables were modified to take into account the differing spectrum resulting from  $n, 2n$  processes.

#### 4.7.2.5 Inelastic Scattering Cross Sections

The inelastic cross sections for each nuclide were obtained from the GAM-II data tapes using the same weighting as in the total cross sections. The code requires the energy of the inelastically scattered neutron to be expressed in terms of a probability table. These tables were prepared for each nuclide by making use of the inelastic transfer arrays available for the GAM-II code. The probability of emission of a neutron in group  $j$  after an inelastic event in group  $i$  is simply

$$P_{i \rightarrow j} = \frac{\sigma_{i \rightarrow j}}{\sum_{j=1}^{99} \sigma_{i \rightarrow j}} \quad (4.30)$$

Tables can thus be constructed for each nuclide which give the probability of emission in any lower energy group following an inelastic event. These tables were prepared using a small data handling code, INELAS, written for this problem.

The angular distribution of the emitted neutron after an elastic event can also be controlled with probability tables. In this analysis, however, all inelastic events were assumed to result in an isotropically scattered neutron.

#### 4.7.2.6 Elastically Scattered Cross Sections

The elastic scattering cross sections were obtained from the GAM-II data tapes. For this type of event the code also requires a probability table to find the cosine of the polar scattering angle. The correction to lab coordinates is made after the polar scattering angle is chosen, and the energy of the scattered neutron is then calculated. The construction of these probability tables expressing the cosine of the polar scattering angles was based on the sets of Legendre coefficients available at General Atomic for each of the nuclides. The elastic scattering cross section  $\sigma_s(E, \mu)$  has been previously analyzed as

$$\sigma_s(E, \mu) = \frac{\sigma_s(E)}{4\pi} \sum_{\ell=0}^6 (2\ell + 1) f_{\ell}(E) P_{\ell}(\mu), \quad (4.31)$$

where  $\sigma_s(\sigma, \mu)$  is the scattering cross section per unit solid angle in the center of mass system for a neutron of energy  $E$  scattered through an angular deflection given by  $\cos^{-1} \mu$ . Since the Legendre coefficients  $f_{\ell}(E)$ , are conveniently available at General Atomic on cards for each nuclide, a data handling code, CUMTAB, was written to process the cards and make up probability tables. The probability of a neutron of energy  $E$  having a polar scattering angle whose cosine lies between  $\mu_1$  and  $\mu_2$  may be written as

$$P(E, \mu_1, \mu_2) = \frac{\int_{\mu_1}^{\mu_2} \sigma_s(E, \mu) d\mu}{\int_{-1}^1 \sigma_s(E, \mu) d\mu} \quad (4.32)$$

### 4.7.3 RESULTS OF ANALYSIS

#### 4.7.3.1 Number of Histories

The accuracy of a Monte Carlo analysis is based not only on the quality of the input data but also on the number of neutron histories. One thousand neutrons were used in each of the seven source regions. Each 1000 neutrons required about 0.16 hour on the computer.

#### 4.7.3.2 Calculation by other Methods

The results were compared to those obtained using the methods of Section 4.1. These methods may be summarized as follows:

- a. A one-dimensional  $S_{16}$  cell calculation using the  $P_1$  approximation was made with 15 groups between 14.9 MeV and 67.0 keV. The spatial source description was from a thermal neutron transport cell calculation.
- b. Disadvantage factors for each nuclide from the high energy transport calculation were used in a zero dimensional code, GAM-II, for a spectrum calculation using over 50 groups in this energy range. Diffusion coefficients were obtained using the formula

$$\sigma_{tr}(E) = \sigma_T(E) - \frac{1}{3} \int_E^{\infty} \frac{\sigma_{s1}(E' \rightarrow E) J(E') dE'}{J(E)} \quad (4.33)$$

- c. The leakage was then calculated for a homogenized core using the GAZE-II code.

4.7.3.3 Comparison of Results

The number of neutrons escaping from the assembly is shown in Table 4.5.

Table 4.5

MONTE CARLO ESTIMATE OF LEAKAGE FROM  
MOCKUP CORE (14.9 MeV-87.5 keV)

<u>Source Region</u>	<u>Integrated Source</u>	<u>Leakage/1000 Neutrons</u>	<u>Leakage/Source Neutron</u>
1	0.0182	205.0	0.00373
2	0.0497	89.1	0.00443
3	0.1252	33.5	0.00419
4	0.3336	2.93	0.00098
5	0.3338	7.53	0.00251
6	0.1168	45.3	0.00529
7	<u>0.0227</u>	120.6	<u>0.00274</u>
Sum	1.0000		0.02387

As shown in Table 4.5, each source region has roughly equal weight in leakage, as desired from a statistical viewpoint. The Monte Carlo axial leakage from the assembly shows excellent agreement to the value of 0.02381 found from the comparable GAZE diffusion calculation.

Core leakage into the reflector is a more important quantity from the standpoint of one-dimensional buckling iteration calculations. A direct comparison between the results from GAZE and FMC-N is possible in the Be bottom reflector. The results are shown in Table 4.6.

Table 4.6

<u>Code</u>	<u>Leakage/Source Neutron</u>
FMC-N	0.0294
GAZE	0.0240

The agreement is good, and indicates that the methods outlined in Section 4.1 are adequate for the calculation of high energy leakage in these cores.

It might be expected that the high energy spatial distribution of the flux would similarly show good correspondence between the FMC-N and transport cell calculations. The volume averaged flux in various regions of the cell is compared for the two methods in Table 4.7. The Monte Carlo results show slightly less flux buildup in the center of the cell than the transport results. This may be caused by the difference in the axial dimension.

Table 4.7

COMPARISON OF VOLUME AVERAGED FLUX IN  
VARIOUS CELL REGIONS (14.9 MeV-87.5 keV)

$$\int \phi dV / \int dV$$

	<u>GAPLSN Transport</u>	<u>FMC-N Monte Carlo</u>
Fuel Ring No. 1 (innermost)	1.495	1.470
Fuel Ring No. 2	1.499	1.451
Fuel Ring No. 3	1.488	1.455
Fuel Ring No. 4	1.454	1.407
Fuel Ring No. 5	1.386	1.384
U <sup>238</sup> Ring	1.316	1.235
Moderator	1.000	1.000

The transport cell calculation implies an infinite length cell. Some difference must occur in the U<sup>238</sup> ring also since it occupied a slightly different position closer to the moderator in the Monte Carlo calculation. Nevertheless the correspondence is good between the two calculations.

High energy disadvantage factors were calculated for a particular energy group from the FMC-N results for comparison to those obtained from the transport calculation. To eliminate statistical fluctuation, two FMC-N groups were averaged to form a group from 2.466 MeV to 1.653 MeV. The disadvantage factor for each material was then obtained from Formula 4.1. The results are shown in Table 4.8 compared to a comparable group from a transport calculation. The largest discrepancy is in the  $U^{238}$  and is probably caused by the different position in the two calculations. In general, the correspondence is good, indicating the validity of the high energy disadvantage factor calculational method.

Table 4.8  
COMPARISON OF DISADVANTAGE FACTORS

<u>Nuclide</u>	<u>GAPLSN (2.02-1.83 MeV)</u>	<u>FMC-N (2.466-1.653 MeV)</u>
H and O	0.749	0.799
Al	1.149	1.159
W	1.222	1.183
$U^{235}$	1.285	1.252
$U^{238}$	1.109	0.992

#### 4. .4 CONCLUSIONS

The Monte Carlo analysis showed that the methods previously described are adequate for the calculation of high energy leakage in these cores. The Monte Carlo results also showed good agreement with the one-dimensional transport calculation of the fast flux distribution in a cell and the high energy disadvantage factors.

#### 4.8 ONE-DIMENSIONAL CALCULATIONS

The one-dimensional cell calculations were performed with the GAPLSN code. The geometry of the unit cell, in a cross sectional cut through the fueled region, was represented explicitly in cylindrical geometry. The geometry of the fuel channel is given in Table 4.9. The influence of the cadmium poison tubes was represented in these calculations by homogenizing the cadmium throughout the entire moderator region of the cell. The mesh spacing,  $\delta$ , was chosen to satisfy the following condition for most of the problems:

$$\delta \leq \lambda_{t \min} \bar{\mu}_{\min},$$

where  $\lambda_{t \min}$  is the shortest mean free path of all groups in the problem, and  $\bar{\mu}_{\min}$  is the smallest value of the average cosine used in the  $S_n$  approximation.

#### 4.9 TWO-DIMENSIONAL CALCULATIONS

The two-dimensional cell calculations were performed with the DDF code, a FORTRAN language modification of the Los Alamos two-dimensional  $S_n$  code, DDK. Two-dimensional r-z calculations were performed to explicitly represent the 1/8 in. gap between fuel stages in the calculation of the thermal disadvantage factors. The details of the calculation are identical to those described above for the one-dimensional cell calculations, with two exceptions. To accommodate the problem within the memory block of the computer, the mesh spacing criterion was relaxed somewhat, and only the thermal portion of the fine structure calculation was performed, with a slowing down source specified in the moderator.

Table 4.9  
 DIMENSIONS OF THE MOCKUP UNIT CELL

	<u>Inside Radius (cm)</u>	<u>Outside Radius (cm)</u>
Al center post	0.6350	0.9690
Tungsten	0.9843	0.9970
Fuel A	0.9970	1.1036
Al tube	1.2763	1.3652
Tungsten	1.3805	1.3932
Fuel B	1.3932	1.4999
Al tube	1.6726	1.7615
Tungsten	1.7767	1.7894
Fuel C	1.7894	1.8961
Al tube	2.0688	2.1577
Tungsten	2.1730	2.1857
Fuel D	2.1857	2.2923
Al tube	2.4651	2.5540
Tungsten	2.5692	2.5819
Fuel E	2.5819	2.6886
Tungsten	2.7064	2.7140
U <sup>238</sup> ring	2.7140	2.8156
Pressure tube	3.0886	3.2537
Moderator	3.2537	4.2088



In the two-dimensional calculation of thermal cell disadvantage factors, a different scheme for taking into account the influence of the cadmium poison on the thermal fine structure was used. This scheme consisted of representing the cadmium as a thin ring at the outer boundary of the cell and thus preserving the actual volume and nuclear density of the cadmium solution belonging to the unit cell.

#### 4.10 CALCULATION OF THE CADMIUM THERMAL DISADVANTAGE FACTORS

The methods used for calculating the thermal disadvantage factors of the cadmium poison represented a departure from the methods used for the other disadvantage factors of the cell. Two methods have been used; they are described in detail below.

##### 4.10.1 ONE-DIMENSIONAL TUBE-CENTERED CALCULATION

The first method, referred to as the tube-centered calculation, is an attempt to represent the actual poison-tube-centered geometry, sketched in Fig. 4.5a, in one dimension. The one-dimensional approximation to this geometry, sketched in Fig. 4.5b, preserves the total amount of material and volume in the moderator and the fuel, both regions represented as annular rings surrounding the poison tube. Cadmium disadvantage factors were then obtained from GAPLSN calculations in the  $P_1S_4$  approximation.

The cadmium disadvantage factors obtained in the one-dimensional approximation described above are corrected for two-dimensional effects by the following procedure. The cadmium disadvantage factors in the tube-centered geometry of Fig. 4.5b were first computed by diffusion theory using the GAZE code. The actual two-dimensional geometry was then represented by a symmetric slice of the cell shown in Fig. 4.6. The cadmium disadvantage factors were calculated in this X-Y approximation to the actual geometry with the GAMBLE diffusion theory code. The

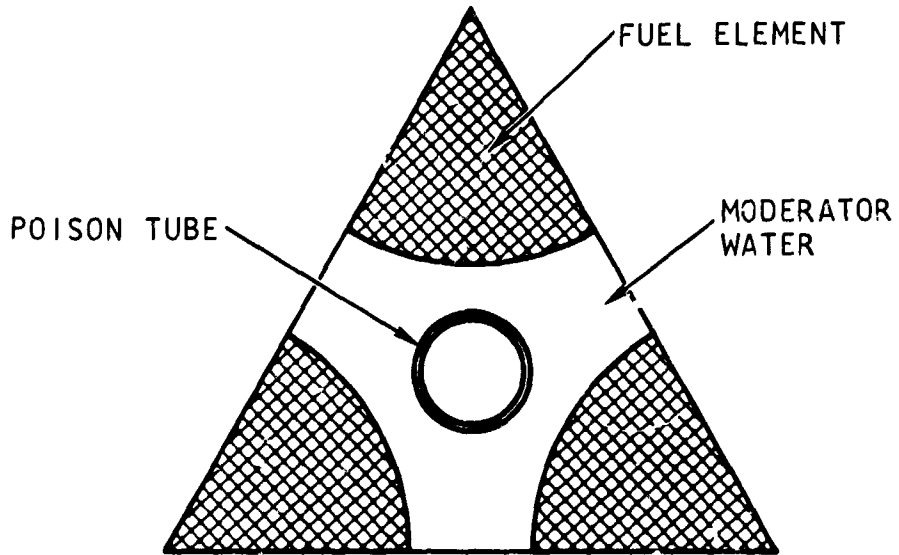


Fig. 4.5a--Actual geometry of poison tube in lattice

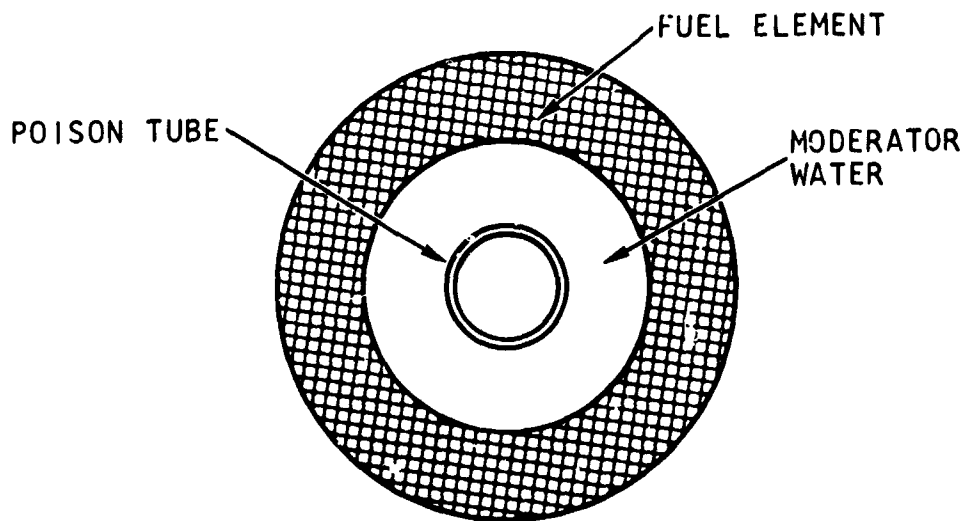


Fig. 4.5b--One-dimensional approximation for disadvantage factor calculation

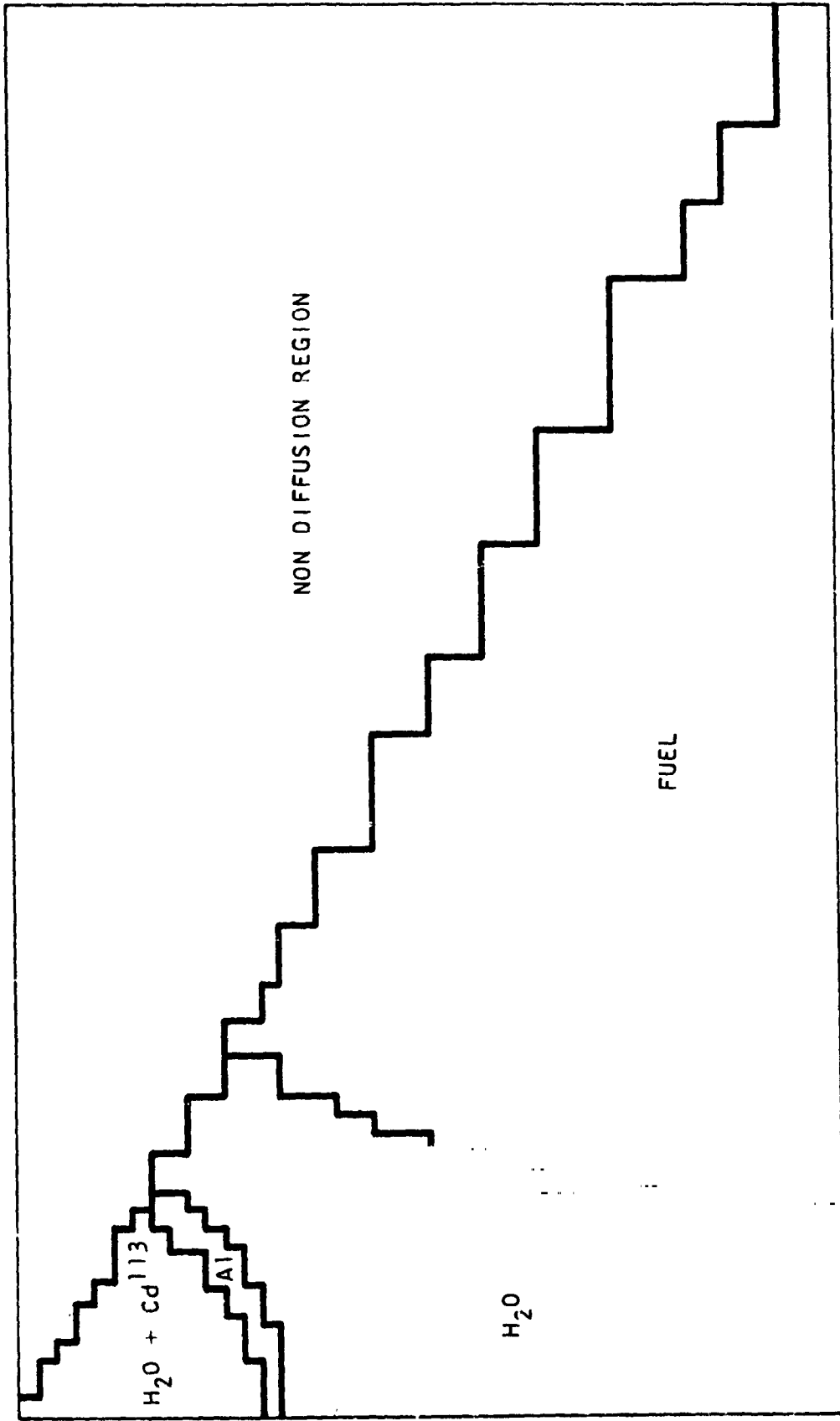


Fig. 4.6--Geometry of GAMBLE XY cell calculation

ratio of the disadvantage factors computed by two-dimensional diffusion theory to those obtained from one-dimensional diffusion theory were used as a correction to the one-dimensional transport disadvantage factors. Thus the final group-dependent cadmium disadvantage factors obtained in the tube-centered approximation were given by:

$$g_{\text{Cd}}^i = \left( g_{1-D}^i \right)_{\text{Tr.}} \left( \frac{g_{2-D}^i}{g_{1-D}^i} \right)_{\text{Diff.}} \quad (4.34)$$

In order to appreciate the magnitude of the two-dimensional correction, the average thermal group disadvantage factor before correction,  $\bar{g}_{1-D}^i$ , and the corrected average thermal group disadvantage factor,  $\bar{g}_{\text{Cd}}^i$ , are plotted as a function of cadmium concentration in Fig. 4.7. The results are shown for the 3.0-in. core. The average thermal group disadvantage factor was defined as:

$$\bar{g}^i = \frac{\sum_i \sigma_i \phi_i g^i}{\sum_i \phi_i} \quad (4.35)$$

where  $\sigma_i$  is the cadmium microscopic absorption cross section for group  $i$ ,  $\phi_i$  is the total cell flux in group  $i$ , and  $g^i$  is the group  $i$  disadvantage factor. The summation is over all thermal groups.

#### 4.10.2 TWO-DIMENSIONAL TRANSPORT CALCULATION

The second method for computing the cadmium disadvantage factors was a two-dimensional transport calculation, using the  $S_n$  code,

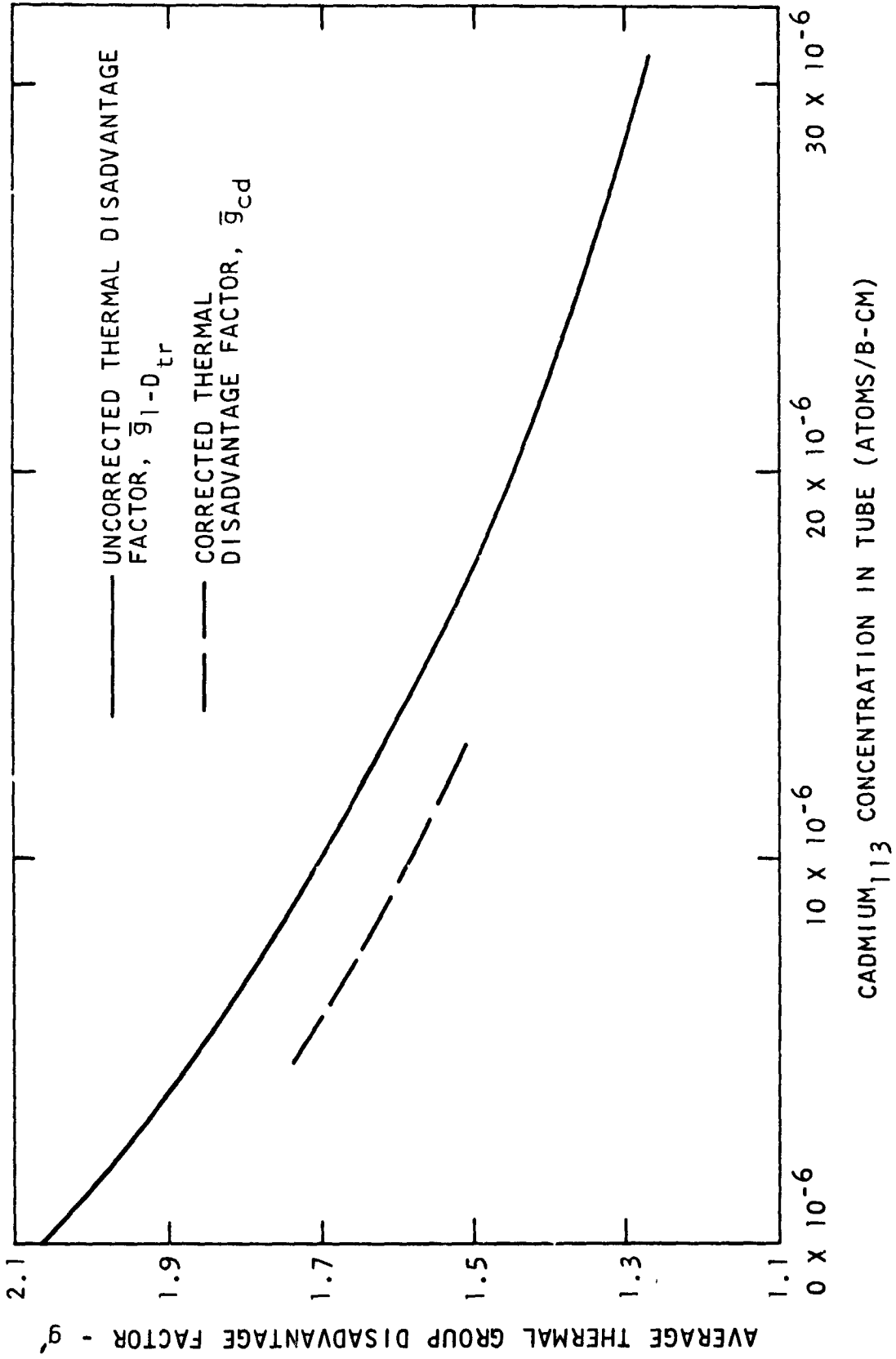


Fig. 4.7--Average thermal group disadvantage factor of cadmium as a function of cadmium atom density

2 DXY. <sup>(30)</sup> The unit cell considered, shown in Fig. 4.8 was a symmetric portion of the hexagonal array. The curved boundaries of the fuel channel and poison tube, shown on the right side of the figure, were represented in X-Y geometry throughout the entire cell by the jagged boundaries drawn on the left side of the figure. The material comprising the inner four fuel-W rings in the fuel element was homogenized into one central region. The material comprising ring E, including the uranium 238, tungsten and fuel was homogenized into an outer ring, and the void, pressure tube, and cadmium solution were explicitly represented. This homogenization procedure has been shown in separate calculations to give good results for the over-all flux distribution. Atom densities in the cell were adjusted slightly when necessary to preserve the correct material loadings of each region. The calculations were made in the  $S_4$  approximation and used the  $P_0$  transport approximation for the scattering cross sections (see Section 4.4). The thermal calculations were made using a slowing-down source in the moderator.

In order to correct for the slight error associated with the transport approximation, additional calculations were performed in the one-dimensional tube-centered cell configuration of Fig. 4.5b using both the  $P_0$ -transport and the  $P_1$  approximations for the scattering cross sections. The two-dimensional results were multiplied by the ratio of the one-dimensional  $P_1$  disadvantage factors to the one-dimensional  $P_0$ -transport disadvantage factors. Thus the final group-dependent cadmium disadvantage factors obtained by the two-dimensional transport calculations are:

$$g_{Cd}^i = \left( g_{2-D}^i \right)_{P_0} \left( \frac{g_{P_1}^i}{g_{P_0}^i} \right)_{1-D} \quad (4.36)$$

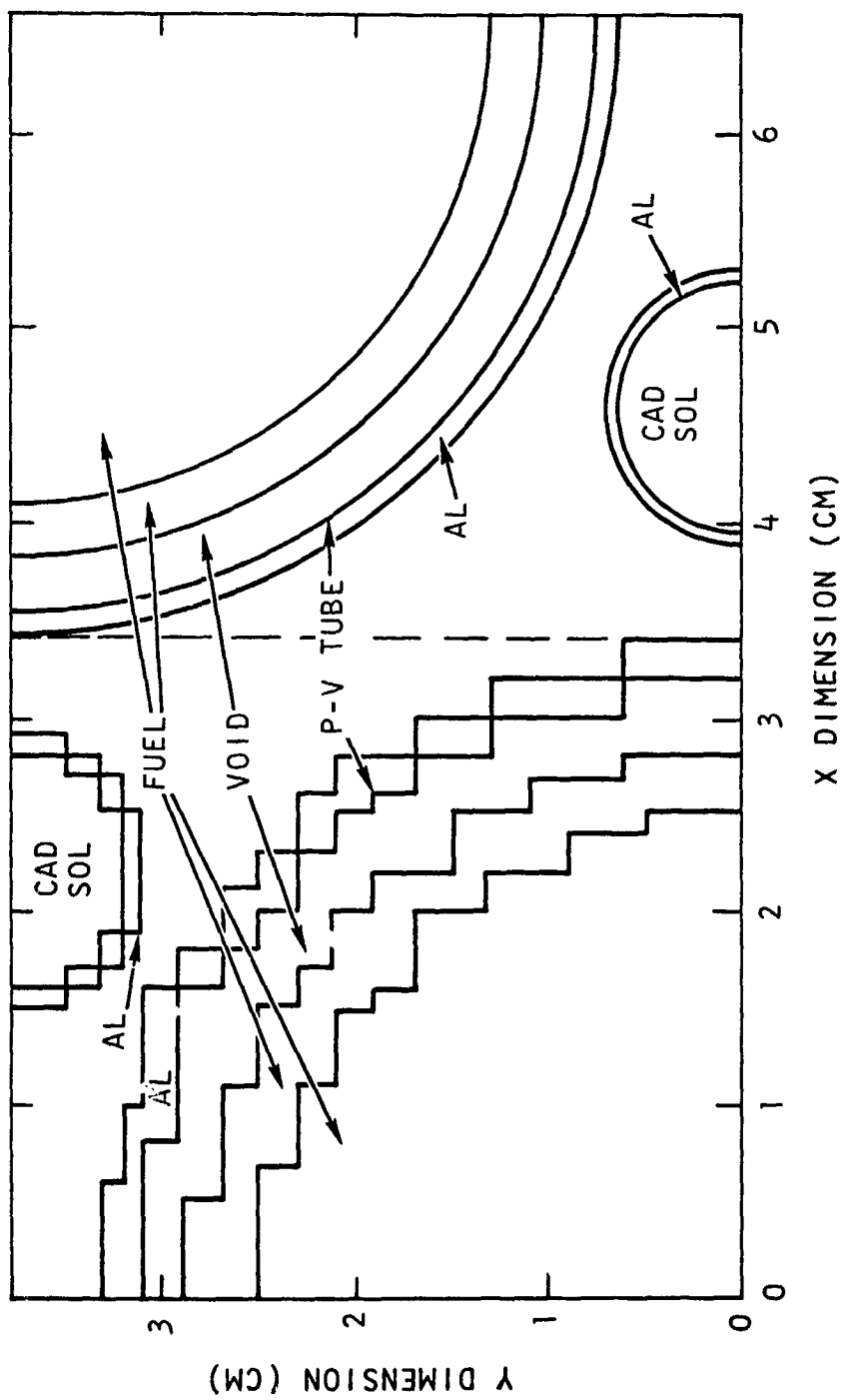


Fig. 4.8--Two-dimensional cell description

The correction for the transport approximation was less than 2% for all groups and all cadmium concentrations studied.

#### 4. 11 TREATMENT OF RESONANCE ABSORPTION

##### 4. 11. 1 CONVENTIONAL TREATMENT USING GAM-II

A comprehensive discussion of the conventional resonance absorption treatment as applied in the GAM-II code has been reported by Nordheim.<sup>(23)</sup> Basically, the moderator flux is assumed to be  $1/E$ , and the following integral equation is solved for the absorber flux:

$$\Sigma_{tA} \phi_A = P_c \frac{N_A}{1 - \alpha_A} \int_E^{E/\alpha_A} \frac{dE'}{E'} \phi_A(E') \sigma_{SA}(E') + \frac{(1 - P_c) \Sigma_{tA}}{E}, \quad (4. 37)$$

where  $\phi_A$  is the absorber flux,  $\Sigma_{tA}$  is the total macroscopic absorber cross section,  $\sigma_{SA}$  is the microscopic scattering cross section of the absorber,  $N_A$  is the absorber atom density,  $E$  is the energy,  $\alpha = \left(\frac{A-1}{A+1}\right)^2$  and  $P_c$  is the collision probability of the absorber lump. The absorber flux was obtained by Nordheim's integral method, a numerical quadrature of Eq. 4. 37, in which each individual resonance is broken up into a fine mesh of energy points. Once the absorber flux is obtained, the effective GAM cross section for nuclide  $n$  in fine-group  $k$  is calculated from the following expression:

$$\overline{\sigma_{cell_k}^n} = \frac{\int_{u_k}^{u_{k-1}} du \sigma^n(u) \phi_A(u)}{\Delta u_k}, \quad (4. 38)$$



The resonance line shapes including Doppler broadening, the resonance wing corrections, and the resonance treatment in the unresolved region are discussed in reference 12.

The collision probabilities,  $P_c$ , were obtained by a cylinder equivalence principle. The multiple-body concentric ring structure shown in Fig. 4.9 can be considered as a non-reentrant body in the absence of material between absorber rings. Then the chord length,  $l(\bar{\Omega})$ , is defined as the sum of individual paths through the material in the rings. The chord distribution<sup>(31)</sup> is defined by:

$$\varphi(l)dl = \frac{\int dA \int_{\bar{\Omega}=\bar{\Omega}(l)} \bar{\Omega} \cdot \hat{n} d\Omega}{\int dA \int_{\bar{\Omega}} \bar{\Omega} \cdot \hat{n} d\Omega} \quad (4.39)$$

where the numerator is integrated over all angles,  $\bar{\Omega}(l)$ , for a fixed chord length,  $l$ . The denominator is integrated over all angles, and is equal to  $\pi A$ , where  $A$  is the outside area of the outer ring. Then the mean chord length,  $\bar{l}$ , is given by:

$$\bar{l} = \int l \varphi(l) dl = \frac{1}{\pi A} \int dA \int \bar{\Omega} \cdot \hat{n} d\Omega \quad (4.40)$$

As is the case for a solid cylinder, the double integral yields a value of  $4\pi V$ , and the mean chord length for the ring structure becomes:

$$\bar{l} = \frac{4V}{A} \quad (4.41)$$

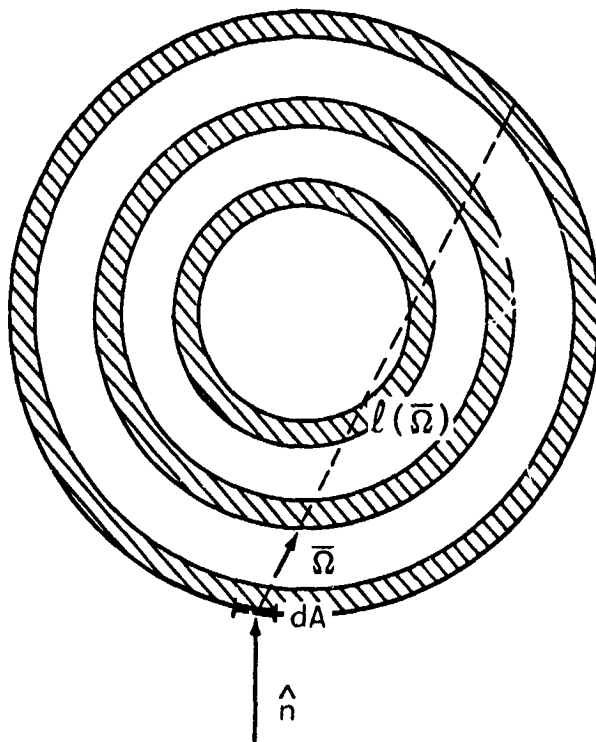


Fig. 4.9--Configuration for mean-chord length derivation

This is the usual expression for the mean chord length; however, for the multiple ring structure  $V$  is the total volume of the rings and  $A$  is the circumferential area of the outer ring.

Once the mean chord length has been obtained, the flat source approximation is assumed, in which case the collision probabilities are obtained in Case, de Hoffman, and Placzek<sup>(31)</sup> for the equivalent cylinder. That is,  $P_c = P_c(\Sigma\bar{a})$ , where  $\bar{a} = \bar{l}/2$ . The collision probabilities were corrected for the interaction between cells by the expression introduced by Nordheim:<sup>(23)</sup>

$$P_0^* = \frac{P_0(1 - C)}{1 - (1 - \Sigma\ell P_0)C} \quad , \quad (4.42)$$

where  $P_0$  is the escape probability ( $P_0 = 1 - P_c$ ),  $P_0^*$  is the escape probability corrected for the interaction between cells, and  $C$  is the Dancoff-Ginzburg factor.<sup>(32)</sup> The values for the Dancoff-Ginzburg factor,  $C$ , are obtained in ANL-5800<sup>(33)</sup> for a homogeneous mixture of materials exterior to the outside absorber ring.

#### 4.11.2 TREATMENT OF THE INTERSTITIAL CELLULAR MATERIAL

In theory, the material in the interstices between absorber rings can be handled as an additional scattering region, and the resonance treatment may be applied within the framework of the constant source approximation. Assuming, as usual, a  $\frac{1}{E}$  flux in the moderator, the collision density in each region is given by:

$$\begin{aligned}
V_A \Sigma_t \phi_A &= \frac{P_{A \rightarrow A} V_A}{1 - \alpha_A} \int_E^{E/\alpha_A} \frac{dE'}{E'} \phi_A(E') \Sigma_s(E') \\
&+ \frac{P_{I \rightarrow A} V_I}{1 - \alpha_I} \int_E^{E/\alpha_I} \frac{dE'}{E'} \phi_I(E') \Sigma_s(E') + \frac{P_{A \rightarrow M} V_A \Sigma_t}{E} \phi_A
\end{aligned} \quad (4.43)$$

$$\begin{aligned}
V_I \Sigma_t \phi_I &= \frac{P_{I \rightarrow I} V_I}{1 - \alpha_I} \int_E^{E/\alpha_I} \frac{dE'}{E'} \phi_I(E') \Sigma_s(E') + \frac{P_{A \rightarrow I} V_A}{1 - \alpha_A} \int_E^{E/\alpha_A} \frac{dE'}{E'} \phi_A(E') \Sigma_s(E') \\
&+ \frac{P_{I \rightarrow M} V_I \Sigma_t}{E} \phi_I,
\end{aligned} \quad (4.44)$$

where the subscript A refers to the absorber, I refers to the interstitial region, and M refers to the moderator. The nomenclature is conventional,  $\phi$  is the flux,  $\Sigma$  the macroscopic cross section (subscript s for scattering and t for total), V is the volume, E is the energy,  $\alpha = \left(\frac{A-1}{A+1}\right)^2$ , and  $P_{i \rightarrow j}$  is the probability that a neutron born in region i will suffer its first collision in region j.

The system of equations (4.43) and (4.44) are cumbersome and have not been programmed for the computer. The main drawback lies in the requirement for two independent sets of collision probabilities,  $P_{A \rightarrow j}$ , which must be derived from separate fixed source calculations. Furthermore, the complexity of the system obviates the utility of the usual reciprocity relationships, making it necessary to utilize several separate collision probability tables in the solution of Eqs. (4.43) and (4.44).

Two approximations are feasible which permit the use of existing numerical techniques and a single set of collision probability tables. The first involves the assumption that the flux in the interstitial region, as well as that in the moderator, is  $1/E$ . Introducing this approximation, Eqs. (4.43) and (4.44) reduce to the single equation:

$$V_A \Sigma_{tA} \phi_A = \frac{P'_{A \rightarrow A} V_A}{1 - \alpha_A} \int_E^{E/\alpha_A} \frac{dE'}{E'} \phi_A(E') \Sigma_{sA}(E') + \frac{(1 - P'_{A \rightarrow A}) V_A \Sigma_{tA}}{E} \quad (4.45)$$

In Eq. (4.45) the collision probability,  $P'_{A \rightarrow A}$ , is derived from a single transport calculation in which the interstitial material is explicitly represented by its potential scattering cross section. (Any resonance structure of the interstitial material, if it exists, is neglected and treated separately as a resonance interference phenomenon.)

A second limiting case is that for which the flux in the interstitial region is roughly equal to the flux in the absorber. If such is the case, the effect of the interstitial material may be approximated by homogenizing the interstitial material into the absorber rings, resulting in the equation

$$V_A \Sigma_{tA} \phi_A = P_{A \rightarrow A} V_A \left\{ \frac{1}{1 - \alpha_A} \int_E^{E/\alpha_A} \frac{dE'}{E'} \phi_A(E') \Sigma_{sA}(E') + \frac{V_I/V_A}{1 - \alpha_I} \int_E^{E/\alpha_I} \frac{dE'}{E'} \phi_A(E') \Sigma_{sI}(E') \right\} + \frac{(1 - P_{A \rightarrow A}) V_A \Sigma_{tA}}{E} \quad (4.46)$$

The collision probability,  $P_{A \rightarrow A}$ , in Eq. (4.46) is the conventional collision probability for the absorber rings alone.  $P_{A \rightarrow A}$  may be obtained from flat source transport calculations, or may be quite accurately approximated by the cylinder equivalence (see Section 4.4.1).

The best approximation for estimating the effect of the interstitial material was chosen in the following manner. The mockup tungsten ring configuration was explicitly represented in a GAPLSN cell calculation. The aluminum and fuel rings were homogenized into the interstices between the tungsten rings in their proper proportions, yielding the configuration sketched in Fig. 4.10. The  $W^{182}$  resonance at 4.15 eV was selected for the "exact" calculation. A 45-group structure between 2.38 eV and 8.315 eV was constructed, with group-averaged elastic transfer coefficients calculated from the equation

$$\sigma_{s_n}^{i \rightarrow j} = \frac{1}{E_{i-1} - E_i} \int_{E_j}^{E_{j-1}} dE \int_{E_i}^{E_{i-1}} dE' \frac{\sigma_s^n(E')}{E' (1 - \alpha_n)}, \quad (4.47)$$

for the  $n^{\text{th}}$  nuclide. A  $1/E$  slowing-down source in the cell materials as well as the moderator was calculated from the following relationship:

$$S_{i_n} = \int_{E_i}^{E_{i-1}} dE \int_{8.315 \text{ eV}}^{E/\alpha_n} \frac{dE'}{E'} \frac{\Sigma_s^n(E')}{E' (1 - \alpha)}. \quad (4.48)$$

The GAPLSN calculation was performed in the  $S_8$  approximation.

The results of the GAPLSN calculations are compared with the results obtained by solving Eqs. (4.45) and (4.46) in Table 4.10. The

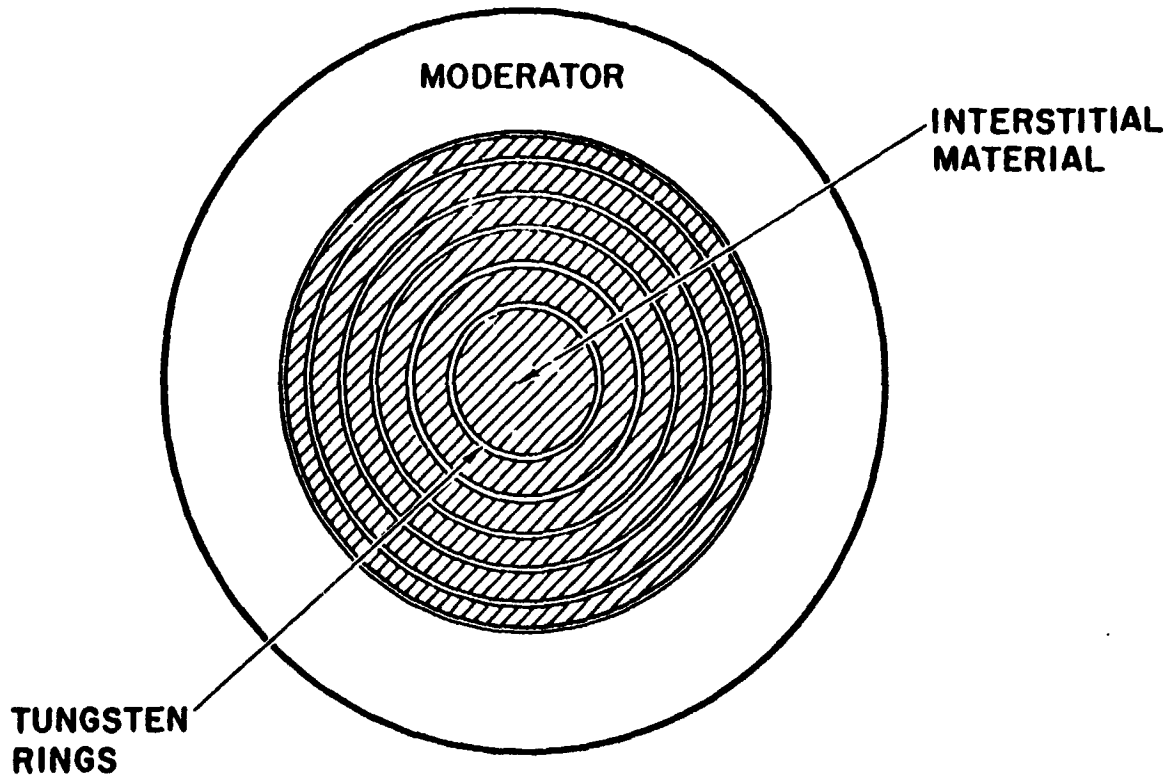


Fig. 4.10--Multiple body annular ring configuration

GAROL<sup>(34)</sup> code was used to solve the equations and by Nordheim's integral method. Figure 4.11 is a histogram of the spectra obtained from the GAPLSN calculation. The continuous line was obtained from a 500-point GAROL calculation.

Table 4. 10  
EFFECTIVE ABSORPTION CROSS SECTION OF  
 $W^{182}$  FROM 2.38 TO 8.32 eV

<u>Method</u>	$\overline{\sigma}_a$ (barns)		<u>Relative Effect</u>
	<u>Without Interstitial Material</u>	<u>Including Interstitial Material</u>	
1/E Flux in Interstitial Material (Eq. 4.45)	44.39	49.22	+10.9%
Homogenization of Interstitial Material (Eq. 4.46)	44.39	46.18	+ 4.0%
45-Group GAPLSN	43.80	45.91	+ 4.8%

As seen in Table 4.10, the assumption of 1/E flux in the interstitial material provides an overestimate of the effect. The departure from 1/E is clearly shown in Fig. 4.11, where it is seen that the flux in the interstitial material is actually depressed slightly below the flux in the absorbing rings. On the other hand, the homogenization procedure appears to provide a good estimate of the effect. This could be anticipated from the spectrum of the interstitial material flux, which is roughly equivalent to the flux in the absorbing tungsten rings.

A radial flux plot for two energy groups in an earlier 40-group GAPLSN calculation is given in Fig. 4.12. An explanation for the depression in the spatially integrated interstitial material flux is afforded by this figure. It is seen that despite some spatial flux recovery in the interstitial material, the strong rise in the outer two tungsten rings compensates to give a higher integrated flux in the rings.



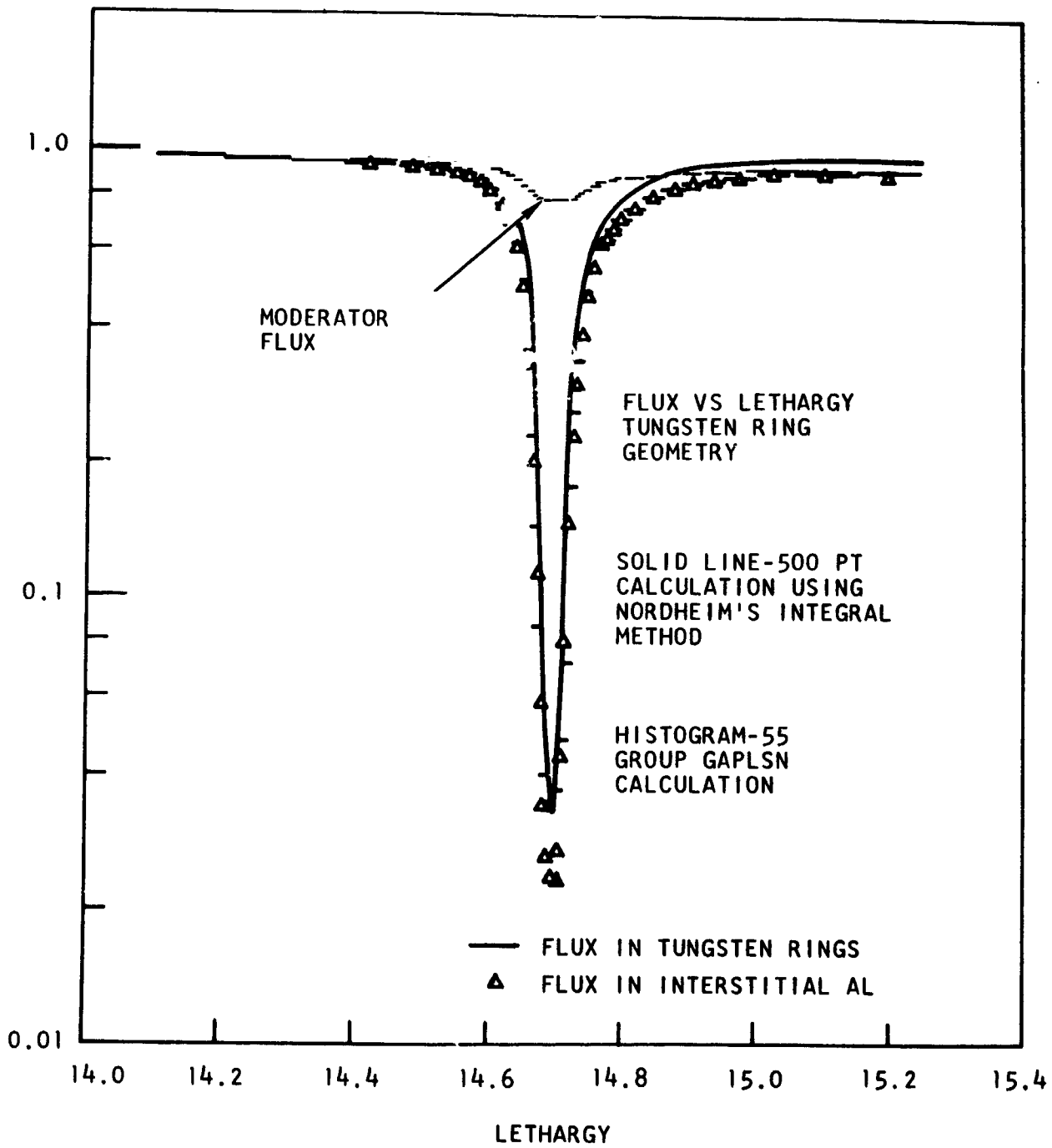


Fig. 4. 11--Flux in tungsten rings and interstitial material

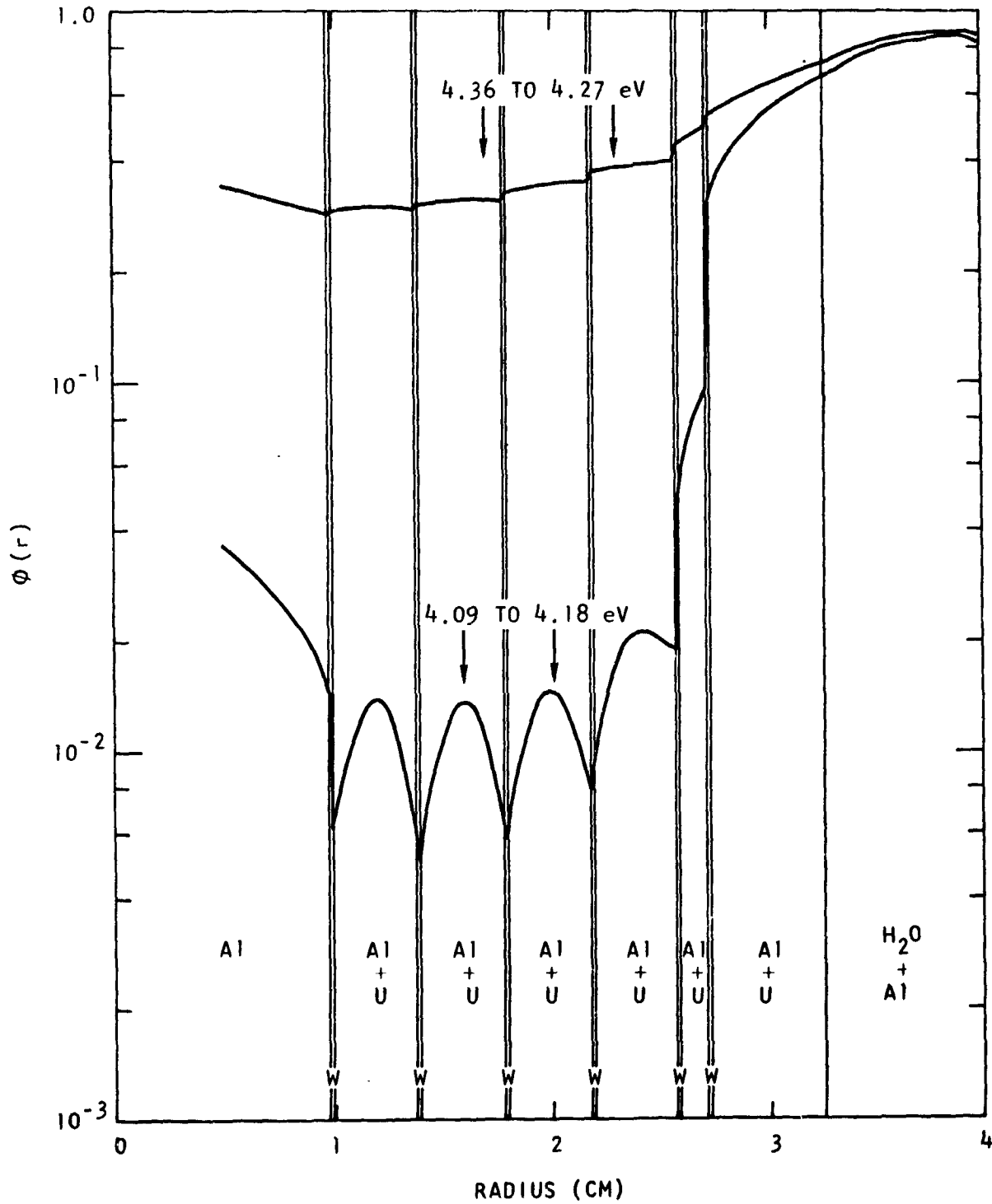


Fig. 4.12--Radial flux plot for fuel element with interstitial material, from 40GP GAPLSN

It should be pointed out that only the interstitial aluminum exerts an influence in the resonance calculation. This was concluded after performing GAROL W<sup>182</sup> calculations with and without interstitial uranium and background tungsten (the potential scattering contribution of W<sup>183</sup>, W<sup>184</sup>, and W<sup>186</sup>). No significant change was observed in the calculated absorption cross section. The same held true for the "exact" GAPLSN calculation; the effect of including interstitial uranium was insignificant.

In the fuel element, several nuclides are present in the interstices between the absorbing rings. For the tungsten resonance treatment, the fuel rings and aluminum tubes were considered as interstitial material, and tungsten itself is included in the U<sup>238</sup> ring resonance treatment. These materials essentially act as isotropic scattering sources to the resonance absorbers, thus effectively increasing the surface area and raising the resonance integral.

The effect of the interstitial material was taken into account in the resonance treatment by homogenizing the interstitial aluminum into the absorber rings. The effect of other interstitial nuclides was negligible. When including interstitial aluminum in the resonance calculation, Eq. 4.37 becomes:

$$\Sigma_{tA} \phi_A = P_c \left\{ \frac{N_A}{1 - \alpha_A} \int_E^{E/\alpha_A} \frac{dE'}{E'} \phi_A(E') \sigma_{SA}(E') \right. \\ \left. + \frac{(V_I/V_A)N_I}{1 - \alpha_I} \int_E^{E/\alpha_I} \frac{dE'}{E'} \phi_A(E') \sigma_{SI}(E') \right\} \\ + \frac{(1 - P_c) \Sigma_{tA}}{E} , \quad (4.49)$$

where the subscript I denotes the interstitial aluminum.

## 4.11.3 RESONANCE INTERFERENCE

Since several resonance absorbing nuclides are present in the fuel element the effects of interference between different nuclides had to be considered. The four isotopes of tungsten, in their natural abundances, comprise the tungsten rings. Uranium 238 is present to a small extent in the fuel rings, in addition to comprising the depleted uranium ring, which is completely separated spatially from the tungsten rings. The GAM resonance treatment, which is described in part in Section 4.4.1, treats each resonance of each nuclide separately. In other words, the GAM calculation entirely neglects any overlap between resonances of two different nuclides as well as interference between resonances of the same nuclide.

Overlap was treated using a more refined resonance calculation with the GAROL code.<sup>(34)</sup> The GAROL code allows several nuclides and all resonances in the region comprising the absorber lump to be treated simultaneously. This is accomplished by subdividing the energy region under consideration into a fine mesh and calculating cross sections at the points comprising this mesh from the individual resonance parameters. Then, for a  $1/E$  flux in the moderator, the following equation is solved for the flux in the absorber lump:

$$\Sigma_{tA} \phi_A = P_c \sum_{i=1}^M \frac{N_i}{1 - \alpha_i} \int_E^{F/\alpha_i} \frac{dE'}{E'} \phi_A(E') \sigma_{S_i}(E') + \frac{(1 - P_c) \Sigma_{tA}}{E} \quad (4.50)$$

where the summation is performed over all resonance nuclides comprising the absorber lump. Since this equation is solved over the entire energy region of interest in the resonance calculation, interference between neighboring resonances of the same nuclide is explicitly included. Although the  $U^{238}$  ring is spatially distinct from the tungsten ring structure the  $U^{238}$  was homogenized into the absorber region.

#### 4.11.4 $U^{235}$ RESONANCE CALCULATION

The inadequacy associated with the conventional GAM self-shielding treatment for  $U^{235}$ , where an attempt is made to fit the resonance cross sections with single-level Breit-Wigner parameters, has been pointed out by Stevens and Joanou.<sup>(35)</sup> The core calculations which use the conventional GAM treatment utilize  $U^{235}$  epithermal cross sections in the infinite dilution limit in the fine groups. The GAROL code, uses pointwise cross section data on a fine mesh basis. The resonance self-shielding calculation for  $U^{235}$  using the GAROL code, therefore, is in principle no more difficult than calculations involving resonances which are accurately represented by single-level parameters.

Self-shielding calculations of  $U^{235}$  in the fuel rings were carried out in the energy range 2.38 to 961 eV. GAROL fine mesh cross section values were obtained by linear interpolation from the pointwise cross section data given in Reference (36). The spatial treatment was based upon the cylindrical equivalence principle previously discussed.

#### 4.11.5 TWO-REGION RESONANCE CALCULATION

The resonance treatment discussed until now employed the  $1/E$  approximation in the moderator region of the cell. This simplification permits, in essence, a single absorber region calculation represented by a single integral equation for the flux in the lump. The GAROL code provides for an explicit treatment of the two-region cell, by solving the following coupled set of integral equations:

$$\begin{aligned}
V_A \Sigma_{t_A} \phi_A &= P_{A \rightarrow A} V_A \sum_{i=1}^I \frac{N_i}{1 - \alpha_i} \int_E^{E/\alpha_i} \frac{dE'}{E'} \phi_A(E') \sigma_{s_i}(E') \\
&+ P_{M \rightarrow A} V_M \sum_{j=1}^J \frac{N_j}{1 - \alpha_j} \int_E^{E/\alpha_j} \frac{dE'}{E'} \phi_M(E') \sigma_{s_j}(E') \quad (4.51)
\end{aligned}$$

$$\begin{aligned}
V_M \Sigma_{t_M} \phi_M &= P_{M \rightarrow M} V_M \sum_{j=1}^J \frac{N_j}{1 - \alpha_j} \int_E^{E/\alpha_j} \frac{dE'}{E'} \phi_M(E') \sigma_{s_j}(E') \\
&+ P_{A \rightarrow M} V_A \sum_{i=1}^I \frac{N_i}{1 - \alpha_i} \int_E^{E/\alpha_i} \frac{dE'}{E'} \phi_A(E') \sigma_{s_i}(E'), \quad (4.52)
\end{aligned}$$

where the subscript A denotes the absorber region and M the moderator region of the cell. The sum over i denotes all materials in the absorbing lump and that over j all materials in the moderator region. The collision probability,  $P_{a \rightarrow b}$ , is defined as the probability that a neutron born in region a will suffer its first collision in region b.

The explicit treatment of the moderator region makes it possible to relax the  $1/E$  approximation in obtaining the fine-group effective cell cross sections. Thus Eq. 4.38 is replaced by the more correct expression:

$$\overline{\sigma}_{\text{cell}_k}^n = \frac{(V_1 + V_2) \int_{u_k}^{u_{k-1}} du \sigma^n(u) \phi_A(u)}{V_1 \int_{u_k}^{u_{k-1}} du \phi_A(u) + V_2 \int_{u_k}^{u_{k-1}} du \phi_M(u)} \quad (4.53)$$

for the effective cell cross section of absorbing nuclide  $n$  in fine group  $k$ . Consideration of the proper flux-volume weighting of absorber nuclides alone, however, is inadequate. Cross sections of the moderator nuclides are also subject to cell fine-structure considerations in the resonance region of the energy spectrum. Of all the moderator resonance region cross sections, the most significant influence on reactivity is exerted by the elastic downscattering matrix, the terms of which for nuclide  $n$  are given by:

$$\begin{aligned} \overline{\sigma}_{\text{cell } k \rightarrow j}^n &= \frac{(V_1 + V_2) \int_{u_j}^{u_{j-1}} du \int_{u_k}^{u_{k-1}} du' \sigma_s^n(u' \rightarrow u) \varphi_M(u')}{V_1 \int_{u_k}^{u_{k-1}} du \varphi_A(u) + V_2 \int_{u_k}^{u_{k-1}} du \varphi_M(u)} \\ &\equiv W_k \frac{\int_{u_j}^{u_{j-1}} du \int_{u_k}^{u_{k-1}} du' \sigma_s^n(u' \rightarrow u) \varphi_M(u')}{\int_{u_k}^{u_{k-1}} du' \varphi_M(u')} \end{aligned} \quad (4.54)$$

$W_k$  in Eq. 4.54 may be considered as an epithermal "advantage factor." The expression to the right of  $W_k$  in Eq. 4.54 is the conventional integral for the elastic downscattering matrix used in GAM, where  $\varphi_M(u') = 1$  ( $1/E$  flux in the moderator). In applying the results of the two-region resonance calculation, the approximation that  $\varphi_M(u') = 1$  in Eq. 4.54 is retained. (In separate calculations, the result of this approximation was deemed insignificant.) However, the advantage factors,  $W_k$ , are applied to the cross sections of the moderator nuclides in the fine groups of the GAM calculation.

#### 4. 11. 6 SPECIAL COLLISION PROBABILITY TABLES

As previously discussed, the cylinder equivalence principle is applied in obtaining collision probabilities for the concentric ring resonance absorbers in the mockup fuel element. This permits the utilization of tabulated<sup>(31)</sup> collision probabilities for cylinders. For purposes of examining the validity of the cylinder equivalence principle, and in performing the resonances calculations for the tungsten ring configurations of the Lewis Critical Experiments, special collision probability tables were generated.

The specific calculation of collision probabilities in annular ring geometries is carried out in the following fashion. The actual geometry of the ring structure is explicitly represented in a GAPLSN cylindrical geometry  $P_0$  calculation. The outer boundary of the absorber is treated as a vacuum, and a uniformly distributed source (flat source approximation), whose volume integral is normalized to unity, is specified in the absorber rings. A series of calculations are performed, in which the total cross section of the absorber is varied. The collision probability, then, is equivalent to the total number of collisions in the absorber, and this quantity is tabulated as a function of  $\Sigma$ . The collision probability in the moderator is obtained from the reciprocity theorem.

#### 4. 12 TREATMENT OF THE BORON PLATE BOUNDARY IN THE BERYLLIUM-REFLECTED CORE

The radial beryllium reflector in the beryllium-reflected core has an outside 1/4-in. plate of aluminum mixed with  $B_4C$  to represent a nonreentrant boundary to thermal neutrons. Outside of the boron plate is a water reflector that is neutronicly infinite, but which returns some epithermal neutrons through the plate to the beryllium and thus to the core. Diffusion theory is inadequate to correctly represent black or nearly black regions, and therefore it is necessary to terminate radial diffusion theory



calculations of the beryllium-reflected core at the boral plate by specifying the correct boundary condition.

The conventional diffusion theory boundary condition is specified in terms of the linear extrapolation distance,  $d$ . For a totally black slab boundary, transport theory specifies that  $d = .7104 \lambda_{tr}$ , where  $\lambda_{tr}$  is the transport mean free path. This condition is adequate at the boral plate boundary for thermal neutrons, but is a gross underestimation of the extrapolation distance for neutrons of higher energy, where the transmission through the boral plate becomes significant. To determine a reasonable linear extrapolation distance for epithermal neutrons, a radial transport calculation was performed. In this  $P_1S_4$  calculation, the boral plate and the adjoining water reflector were explicitly represented. Values for the epithermal linear extrapolation distances were then obtained from the transport calculation by the following expression:

$$d = -\varphi_0 / \text{grad } \varphi_0, \quad (4.55)$$

where the subscript denotes values of the flux and its gradient at the boral plate boundary. The boundary condition is used in the GAZE diffusion theory code in terms of the group-dependent parameter,  $l_i$ , which is given by:

$$l_i = d_i / D_i, \quad (4.56)$$

where  $D_i$  is the diffusion coefficient for group  $i$ .

The validity of the above method for treating the boral plate boundary in a diffusion calculation may be evaluated by referring to Figs. 4.13 and 4.14. These are plots of the radial flux distribution in an epithermal energy group from 67 to 500 keV and a thermal group from 0.05 to 0.09 eV, respectively. The top lines represent the transport solution,

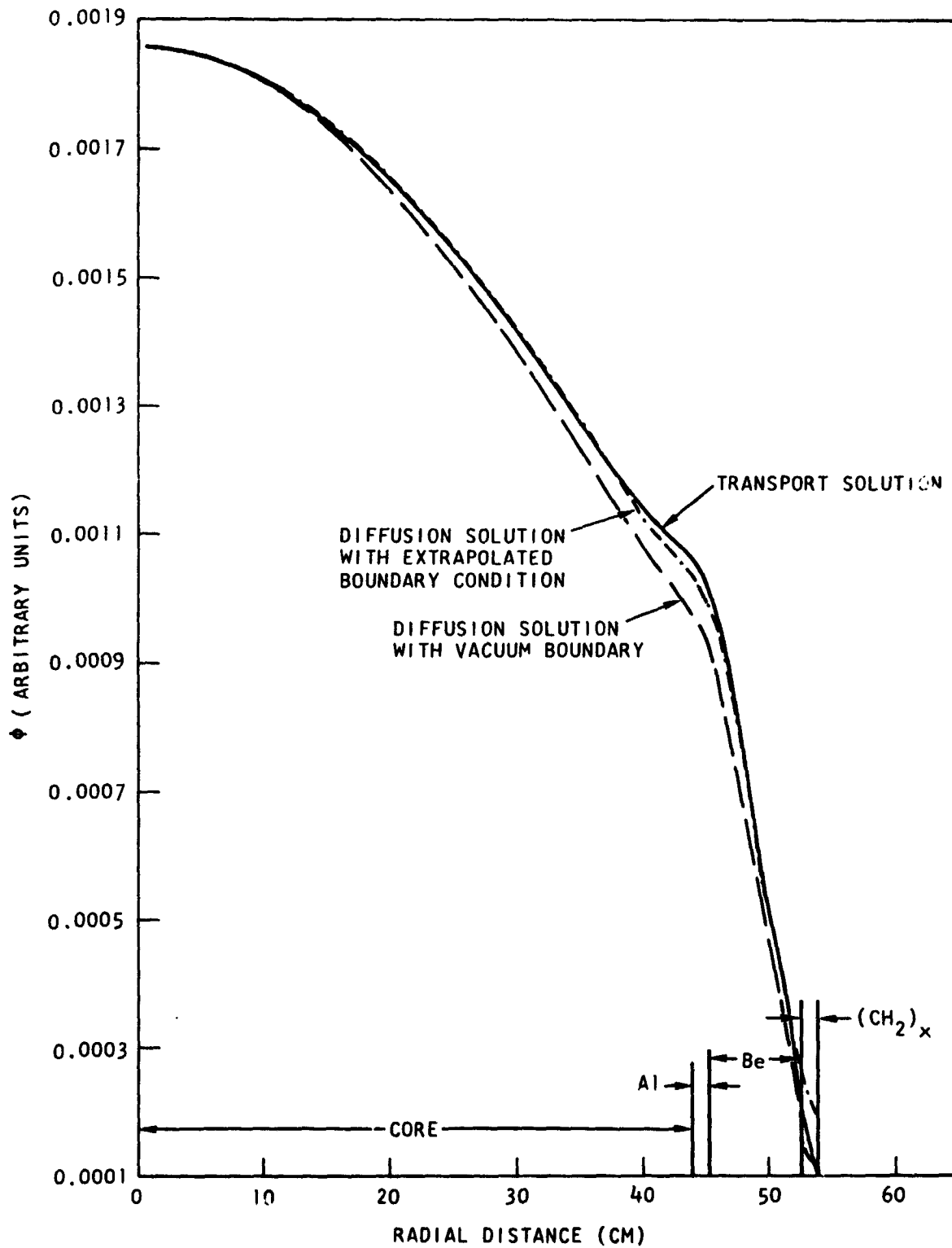


Fig. 4. 13--Neutron flux in energy region of 500 to 67 keV

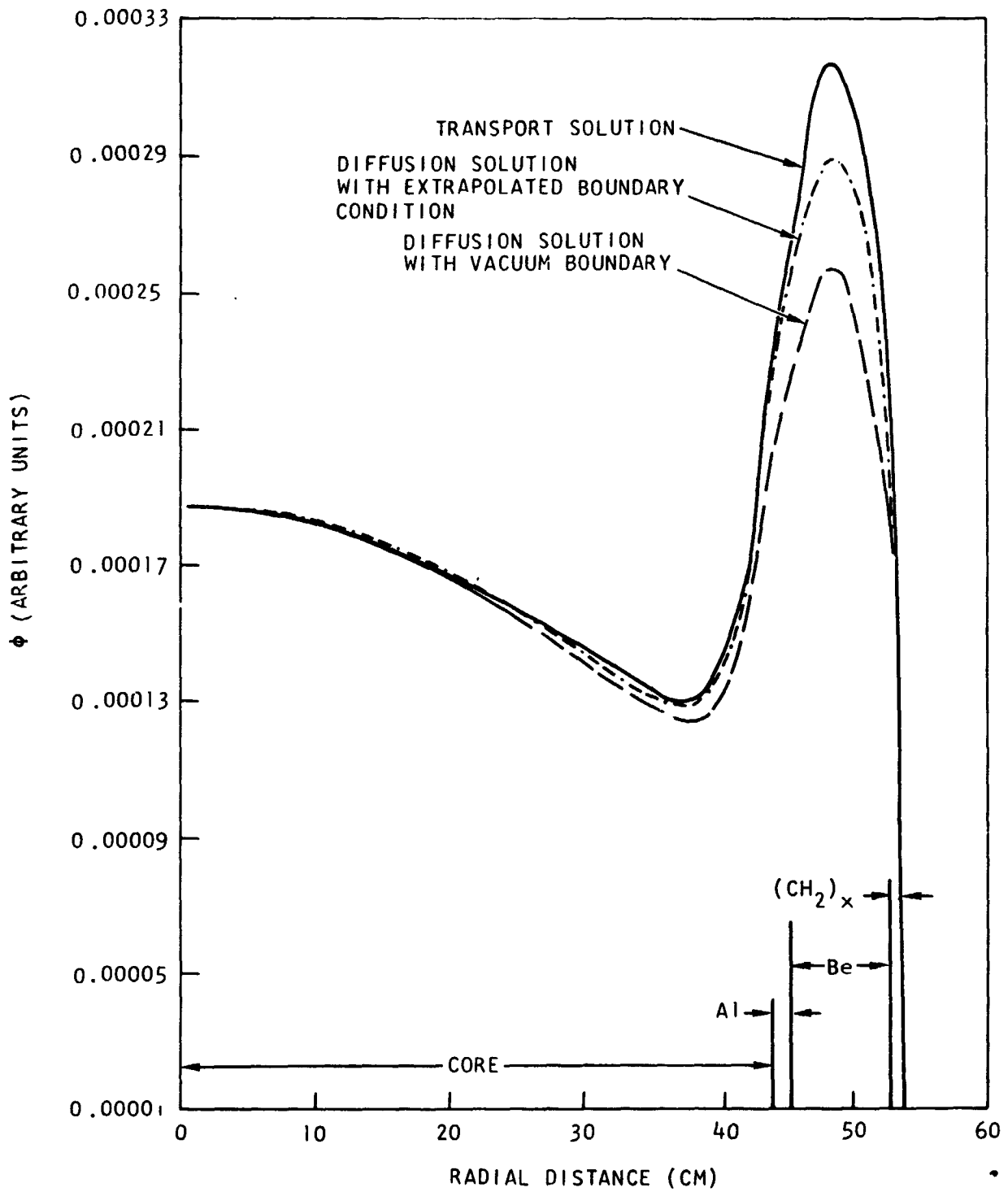


Fig. 4. 14--Neutron flux in energy region of 0.05 to 0.09 eV

the bottom lines represent the diffusion theory solutions when all energy groups are treated by the nonreentrant boundary condition at the boron plate ( $d = 0.7104 \lambda_{tr}$ ), and the middle lines are the diffusion theory solutions when the epithermal extrapolation distances calculated from transport theory are used. It is seen that the transport core fluxes are closely represented by the diffusion theory solution employing calculated extrapolation distances. Although the thermal flux boundary condition remains at  $0.7104 \lambda_{tr}$ , the improvement in the thermal flux comes about from a better description of the epithermal flux, which serves as a source to the thermal energy region.

#### 4.13 CALCULATION OF THE EFFECTIVE DELAYED NEUTRON FRACTION

Following the notation of Henry, <sup>(37)</sup> the total effective delayed neutron fraction (assumed to be time independent) is given by:

$$\beta_{\text{eff}} = \sum_i (\beta_{\text{eff}})_i = \frac{1}{F} \int_V \int_u \int_{u'} d^3r \, du \, du' \frac{\nu}{\nu_0} \cdot \sum_i \sum_j \nu^j(u') f_i(u) \beta_i^j \Sigma_f^j(\bar{r}, u') \varphi_0^*(\bar{r}, u) \varphi_0(\bar{r}, u) \quad , \quad (4.57)$$

where  $\frac{\nu}{\nu_0}$  is the fundamental eigenvalue of the static Boltzmann equation,  $f_i(u)$  is the delayed neutron spectrum for precursor group  $i$ , and  $\varphi_0$  and  $\varphi_0^*$  are the scalar flux and its adjoint, respectively. The sums are over precursor groups ( $i$ ) and fissile species ( $j$ ). The quantity  $F$  is the conventional normalization integral, defined by:

$$F = \int_V \int_u \int_{u'} d^3 r du du' \sum_i \sum_j [f^j(u)(1 - \beta^j) + f_i^j(u)\beta_i^j] \cdot \nu^j(u') \Sigma_f^j(\bar{r}, u') \varphi_0^*(\bar{r}, u) \varphi_0(\bar{r}, u'), \quad (4.58)$$

where  $f^j(u)$  is the fission spectrum for fissile species  $j$ . Finally, the time independent reactivity,  $\rho$ , is given by:

$$\rho = \frac{1}{F} \int_V \int_u d^3 r du \left\{ -\delta \Sigma(\bar{r}, u) \varphi_0^*(\bar{r}, u) \varphi_0(\bar{r}, u) + \int_{u'} du' \delta \left[ \Sigma_s^0(\bar{r}, u', u) + \frac{\nu}{\nu_0} \sum_i \sum_j \{f^j(u)(1 - \beta^j) + f_i^j(u)\beta_i^j\} \nu^j(u') \Sigma_f^j(\bar{r}, u') \right] \varphi_0^*(\bar{r}, u) \varphi_0(\bar{r}, u') \right\}, \quad (4.59)$$

where  $\Sigma$  is the total cross section,  $\Sigma_s^0$  is the  $P_0$  component of the scattering cross section, and  $\delta$  indicates the difference between perturbed and unperturbed quantities.

The total effective delayed neutron fraction may be evaluated as a function of eigenvalues of perturbed and unperturbed systems in the following way. If the delayed neutron fractions in Eq. (4.59) are doubled, and the eigenvalue  $\nu/\nu_0$  is adjusted to  $\nu'/\nu_0$  so that the net reactivity vanishes, Eq. (4.59) becomes:

$$0 = \int_V \int_u \int_{u'} d^3 r du du' \left[ \frac{\nu'}{\nu_0} \sum_i \sum_j \sum_n \{f^j(u)(1 - \beta^j) \right.$$

$$\begin{aligned}
 & + f_i(u)(1 + \delta_{in})\beta_i^j \} - \frac{\nu}{\nu_0} \sum_i \sum_j \{ f^j(u)(1 - \beta^j) \\
 & + f_i(u)\beta_i^j \} ] \cdot \nu^j(u') \Sigma_f^j(\bar{r}, u') \varphi_0^*(\bar{r}, u) \varphi_0(\bar{r}, u'), \quad (4.60)
 \end{aligned}$$

where  $\delta_{in}$  in Eq. (4.60) is the Kronecker delta, and the sum over  $n$  is over all precursor groups. Referring to Eqs. (4.57) and (4.58), Eq. (4.60) can be written:

$$0 = \frac{\nu'}{\nu_0} F - \frac{\nu}{\nu_0} F + \frac{\nu'}{\nu} \beta_{\text{eff}} F. \quad (4.61)$$

Then in terms of the multiplication factors,

$$k' = \frac{1}{\nu'/\nu_0}; \quad k = \frac{1}{\nu/\nu_0}. \quad (4.62)$$

the effective delayed neutron fraction can be obtained from the multiplication factors of two calculations:

$$\beta_{\text{eff}} = \frac{k' - k}{k^2}, \quad (4.63)$$

where  $k$  is obtained from the initial criticality problem, and  $k'$  is obtained from a calculation with the delayed neutron spectrum augmented by the following amount,

$$\int_u du \sum_n \sum_j f_n(u) \beta_n^j.$$

In practice the problem is solved by a multigroup scheme, where integrals over lethargy are divided into finite groups:

$$\int_u du g(u) = \sum_k \int_k^{k+1} du g(u). \quad (4.64)$$

Then two multigroup GAZE diffusion problems are solved, the first with the fission spectrum given by:

$$S^k = \sum_i \sum_j \left\{ f_i^{j,k} (1 - \beta^j) + f_i^{k,j} \beta_i^j \right\} \quad (4.65)$$

and the second with the following fission spectrum:

$$S^{i,k} = \sum_i \sum_j \left\{ f_i^{j,k} (1 - \beta^j) + 2f_i^{k,j} \beta_i^j \right\}. \quad (4.66)$$

Two fissile species are present in these cores. However, inasmuch as fissions in  $U^{238}$  contribute a small fraction to the spectrum, the presence of  $U^{238}$  is treated in an approximate manner by assuming that the prompt and delayed neutron spectra of  $U^{235}$  and  $U^{238}$  are identical. Then the presence of  $U^{238}$  is taken into account by correcting the delayed neutron fraction for  $U^{235}$  in the following fashion:

$$\beta^{235'} = \beta^{235} \frac{\iint d^3 r du \varphi_o(\bar{r}, u) \left[ \nu^{235}(u) \Sigma_f^{235}(\bar{r}, u) + \frac{\beta^{238}}{\beta^{235}} \nu^{238}(u) \Sigma_f^{238}(\bar{r}, u) \right]}{\iint d^3 r du \varphi_o(\bar{r}, u) \left[ \nu^{235}(u) \Sigma_f^{235}(\bar{r}, u) + \nu^{238}(u) \Sigma_f^{238}(\bar{r}, u) \right]} \quad (4.67)$$

For the 3.0-in. core,  $\beta^{235'}/\beta^{235} = 1.02$ .

It is assumed that the ratio,  $\beta_{\text{eff}}/\beta$ , is independent of the precursor group, such that  $(\beta_{\text{eff}})_i/\beta_i = \beta_{\text{eff}}/\beta$ . Thus each precursor group is corrected by the enhancement of the total delayed neutron spectrum. This is deemed to be an adequate approximation for these cores. A more refined analysis could be carried out in which the enhancement of each precursor group could be obtained separately by eliminating the summation over  $n$  in Eq. (4.60).

The delayed neutron spectrum,  $\left\{ \sum_i \beta_i' f_i \right\}^K$ , from a compilation by Keepin, <sup>(38)</sup> is tabulated in the third column of Table 4.11. The  $U^{235}$  fission spectrum,  $(1-\beta') f^k$ , as obtained from the GAM library, is given in the second column of this table. The  $U^{235}$  delayed neutron fraction was corrected for the presence of U-238, as discussed earlier. Keepin reports the following values for the total delayed neutron fractions of  $U^{235}$  and  $U^{238}$ :

$$\begin{aligned} \beta^{235} &= 0.0065 \pm 0.0002 \\ \beta^{238} &= 0.0147 \pm 0.0009 \end{aligned}$$

Table 4.11

URANIUM 235 FISSION SPECTRUM AND  
DELAYED NEUTRON SPECTRUM

Group No.	Fission Spectrum $(1 - \beta') f^k$	Delayed Neutron Spectrum $\left\{ \sum_i \beta_i' f_i \right\}^k$
1	3.01 to 14.92 MeV	0.20535
2	1.35 to 3.01 MeV	0.36419
3	0.91 to 1.35 MeV	0.14885
4	0.41 to 0.91 MeV	0.17507
5	0.11 to 0.41 MeV	0.08465
6	61.4 eV to 0.11 MeV	0.01527
7	2.38 to 61.4 eV	0.0



## V. MEASUREMENT AND EVALUATION OF NEUTRON CROSS SECTIONS

### 5.1 INTRODUCTION

The cross sections of U-235, U-238, Be, Cd, W-182, W-183, W-184, W-186 and Al were evaluated in the energy range 0.01 eV to 15.0 MeV and reports were issued giving the results of these evaluations. These reports are listed below.

1. "Neutron Cross Sections for U-238," G. D. Joanou and C. A. Stevens, General Atomic report, GA-6087 Rev. (1965).
2. "Neutron Cross Sections for the Tungsten Isotopes," G. D. Joanou and C. A. Stevens, General Atomic report GA-5885 (1965).
3. "Neutron Cross Sections for Aluminum," G. D. Joanou and C. A. Stevens, General Atomic report GA-5884 (1965).
4. "Neutron Cross Sections for U-235," G. D. Joanou and C. A. Stevens, General Atomic report GA-5944 (1965).
5. "Neutron Cross Sections for Be," G. D. Joanou and C. A. Stevens, General Atomic report GA-5905 (1965).
6. "Neutron Cross Sections for the Cd Isotopes," M. K. Drake, General Atomic report (unpublished).

## 5.2 EPITHERMAL U<sup>235</sup> CROSS SECTIONS

It is well known that a discrepancy exists between the integral measurements of  $\alpha$  for U<sup>235</sup> and the calculated values from differential data. Alpha is defined as the ratio of the infinite dilution capture integral to the fission integral, both integrations performed over 1/E spectra above the cadmium cutoff energy (generally taken to be 0.50 eV); i. e. :

$$\alpha^{235} = \frac{\int_{E_c}^{\infty} \frac{dE}{E} \sigma_c^{235}(E)}{\int_{E_c}^{\infty} \frac{dE}{E} \sigma_f^{235}(E)} \quad (5.1)$$

The integral measurements for  $\alpha$  may be as low as 20% below the calculated values from differential data, <sup>(39)</sup> depending upon the set of differential data selected. Clean critical experiments, such as those performed in recent years at Livermore, KAPL, and Brookhaven appear to favor the lower values of  $\alpha$  suggested by the integral measurements.

Our concern with the epithermal fission cross sections arises from the fact that approximately 30 percent of the total fissions in the assemblies are epithermal (above 0.414 eV). Thus, roughly, a 10 percent uncertainty in  $\alpha$  represents more than one percent uncertainty in reactivity. Some recent measured values of the fission integral (the denominator of Eq. 5.1) and the epithermal value of  $\alpha$  are summarized in Table 5.1. These are compared with calculated values based upon the recent U<sup>235</sup> cross section report. <sup>(36)</sup>

Because of the uncertainty surrounding the epithermal U<sup>235</sup> cross sections, a study was undertaken to determine the effect of normalizing the present set of infinite-dilution cross sections <sup>(36)</sup> on the reactivity of the 3.0-in. pitch core. The normalization was performed in the energy range from 2.38 to 100.0 eV, where it is felt that the greatest uncertainty

exists in the  $U^{235}$  differential cross section data. The normalization was done in the following manner. The infinite dilution fission integral from 14.9 MeV to 0.50 eV was adjusted to a value of 276 barns by normalization of the magnitude of  $\sigma_f$  on the GAM data tape from 2.38 to 100.0 eV. The value of 276 barns for the fission integral corresponds roughly to the mean of the measured values given in Table 5.1. The capture integral was then adjusted by normalization of the values of  $\sigma_{n,\gamma}$  on the GAM data tape between 2.38 and 100 eV so as to yield the desired value of  $\alpha$  between 14.9 MeV and 0.50 eV. Two normalized values of  $\alpha$  were examined - 0.52 and 0.48. Admittedly the above procedure contains a high degree of arbitrariness, since the energy region where the actual difficulty might exist in the differential data is unknown. However, since the effect of the fission cross section enters into the reactor calculation in an integral fashion, it is felt that the normalization procedure gives rise to a semi-quantitative estimate of the effect of variation in the epithermal  $U^{235}$  cross sections on reactivity.

Table 5.1  
MEASURED VALUES OF THE  $U^{235}$  FISSION INTEGRAL AND  $\alpha$

<u>Investigator</u>	<u>Fission Integral (barns)</u>	<u>Cutoff (eV)</u>	<u><math>\alpha</math></u>
Hardy	274 $\pm$ 11	0.50	
Clayton	271 $\pm$ 25	0.49	
Feiner (KAPL) <sup>a</sup>	292 $\pm$ 18	0.50	.486 $\pm$ 0.025
Conway (Bettis) <sup>b</sup>	288 $\pm$ 18	0.50	.550 $\pm$ 0.040
Bigham	272 $\pm$ 8	0.45	
Baumann	263 $\pm$ 9	0.60	
Hellestrand	278 $\pm$ 9	0.50	
Calculated	280.5	0.414	.536
	258.2	0.532	.570

<sup>a</sup>Published in Trans. Am. Nucl. Society, Vol. 7, No. 1, June 1964.  
Recent corrections in the data indicate a value for  $\alpha$  of 0.51.

<sup>b</sup>Published in Trans. Am. Nucl. Society, Vol. 7, No. 1, June 1964.  
According to a recent private communication, the latest measurements and data treatment indicate a preliminary value for  $\alpha$  of 0.49.

The results of the calculations are given in Table 5.2. In addition to the two normalized sets of  $U^{235}$  cross sections, a third set suggested by KAPL<sup>(40)</sup> was examined. For completeness, the fission integral and value of  $\alpha$  to 0.50 eV according to Eq. (5.1) are given in Table 5.2 for each set of cross sections. The effect on  $k_{\infty}$  of the 3.0-in. pitch core is summarized in Column 4.

Table 5.2  
RESULTS OF THE EXAMINATION OF VARIOUS  
EPITHERMAL  $U^{235}$  CROSS SECTION SETS

$U^{235}$ Cross Section Set	Fission Integral to 0.50 eV (barns)	$\alpha$ to 0.50 eV	$k_{\infty}$ of 3.0 in. Pitch Core	$\delta k\%$
Standard Set (GA-5944)	265	0.563	1.2403	-
Normalized to $\alpha = 0.52$	276	0.516	1.2533	+ 1.0
Normalized to $\alpha = 0.48$	276	0.480	1.2587	+ 1.5
KAPL Data Set	287	0.557	1.2511	+ 0.9

The results demonstrate that the mockup core is quite sensitive to the epithermal  $U^{235}$  cross sections. Both the set normalized to  $\alpha = .52$  and the KAPL set lead to approximately one percent increase in  $k$ . The further normalization to  $\alpha = .48$  gives rise to an additional 0.5% increase in reactivity. It appears that the initial adjustment of the fission integral to a value of 276 barns accounts for approximately 0.5% of the increase in  $k$ , and that each renormalization step in  $\alpha$  gives rise to an additional 0.5% increase. It should be noted that on the basis of the integral measurements, neither a fission integral magnitude of 276 barns nor a value of  $\alpha = 0.48$  is unreasonable. Indeed, reference to the error bars given in Table 5.1 indicates that a further increase in the fission

integral of as much as 10 barns could be justified. The arbitrariness rests in the energy range to which the correction should be applied, as well as the actual magnitude of the correction itself. We may conclude from this study that all of the evidence points to more  $U^{235}$  fissions and less parasitic captures in the epithermal region, and that the error in the epithermal  $U^{235}$  cross sections may account for as much as 1.0 to 1.5% in reactivity for the 3.0-in. pitch core.

### 5.3 THE ENERGY DEPENDENCE OF NEUTRON CAPTURE CROSS SECTION OF TUNGSTEN ISOTOPES FROM 0.01 TO 10.0 eV

#### 5.3.1 INTRODUCTION

Tungsten has become of interest as a structural material for high temperature reactor applications due to its very high melting point. Since the thermal neutron capture cross section of tungsten is not small it is important to have accurate capture cross sections in the region of the Maxwellian neutron velocity distribution. Due to the large temperature difference between startup and operation, the energy dependence of the capture cross section must be known over an appreciable energy interval. The capture cross section shape may deviate from a  $1/v$  dependence due to both positive and negative energy levels near the neutron binding energy of the compound nucleus, and hence knowledge of the 2200 m/sec value is not sufficient.

Several techniques have been employed to obtain capture cross sections in the low energy region:

1. Pile oscillator technique: <sup>(41)</sup>

This method requires that the cross section have a  $1/v$  dependence, or a known energy dependence with which the value obtained can be corrected.

2. Activation measurements: (42)

This technique can be employed to obtain capture cross sections if the decay scheme of the product nucleus is known and if states with suitable half lives are present.

3. Total cross section measurements:

Information about the capture cross section can be obtained from this kind of measurement provided the scattering cross section is either small or well known, neither of which is the case for tungsten. Complications arise when using this method due to the crystalline binding effects, and hence it is usually the practice to measure the total cross section at energies below the Bragg cutoff and to extrapolate to thermal energies assuming a  $1/v$  cross section dependence. (43) A correction must still be made for incoherent scattering, however. (44)

4. Calculations using resonance parameters:

The low energy cross section can be calculated from measured resonance parameters, however, resonance parameter determinations are subject to analytic and experimental limitations which usually result in undesirably large errors. The calculations are further hampered by the lack of information on resonances outside the measured region, particularly negative energy levels.

Obviously a direct energy-dependent measurement of the capture cross section is desirable. To date there has been no such measurement on any isotope reported in the literature. In this section we shall describe the capture cross section measurements on the four most abundant tungsten isotopes,  $W^{182}$ ,  $W^{183}$ ,  $W^{184}$  and  $W^{186}$ . No attempt was made to obtain the cross sections in the Lorentzian part of the low energy resonances,

where the multiple scattering effects are large and strongly dependent upon resonance parameters.

### 5.3.2 EXPERIMENTAL TECHNIQUES

#### 5.3.2.1 Detector Efficiency

In the work reported here, the capture cross section was measured by observing the prompt gamma rays which are emitted by the compound nucleus upon neutron capture. In general several gamma rays will be emitted whose spectral distribution is a function of the capturing isotope and the neutron energy. The total energy of the gammas is very nearly equal to the neutron binding energy of the compound nucleus. The difference between the prompt gamma ray energy and the neutron binding energy is the kinetic energy of the capturing neutron, which is very small at the neutron energies considered here, and may also be caused by long lived product nucleus activity. Since it is usually not possible to make corrections for changes in gamma spectra with neutron energy, it is important that the gamma-ray detector have a gamma detection efficiency which is independent of the gamma spectrum. This has been achieved by the high efficiency large liquid scintillator which was used in these measurements at General Atomic.<sup>(45)</sup> A cross sectional view of the scintillator is shown in Fig. 5.1.

The calculated probability for at least one interaction by a gamma ray before escaping the scintillator is shown in Fig. 5.2. It is not possible to make a direct experimental check on this calculated intrinsic efficiency since gammas which completely escape cannot contribute to the observed pulse height distribution. It can be noted from the observed pulse height distributions shown in Figs. 5.3 and 5.4 that small pulses are relatively infrequent. Since small pulses are due to high energy gammas which lose only a small part of their energy in the scintillator it can be argued that

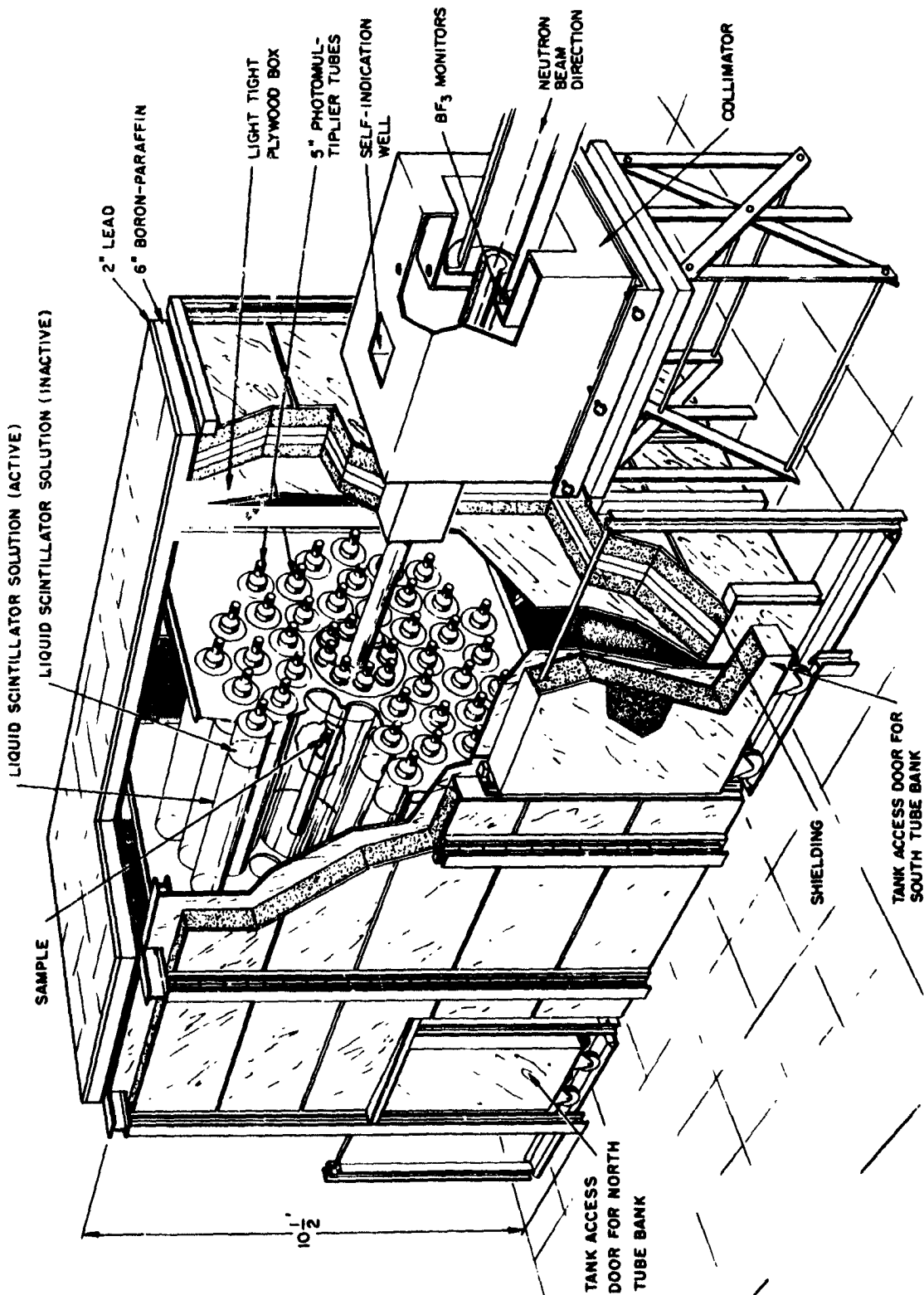


Fig. 5. 1.--View of large liquid scintillator showing the associated shielding and collimation.



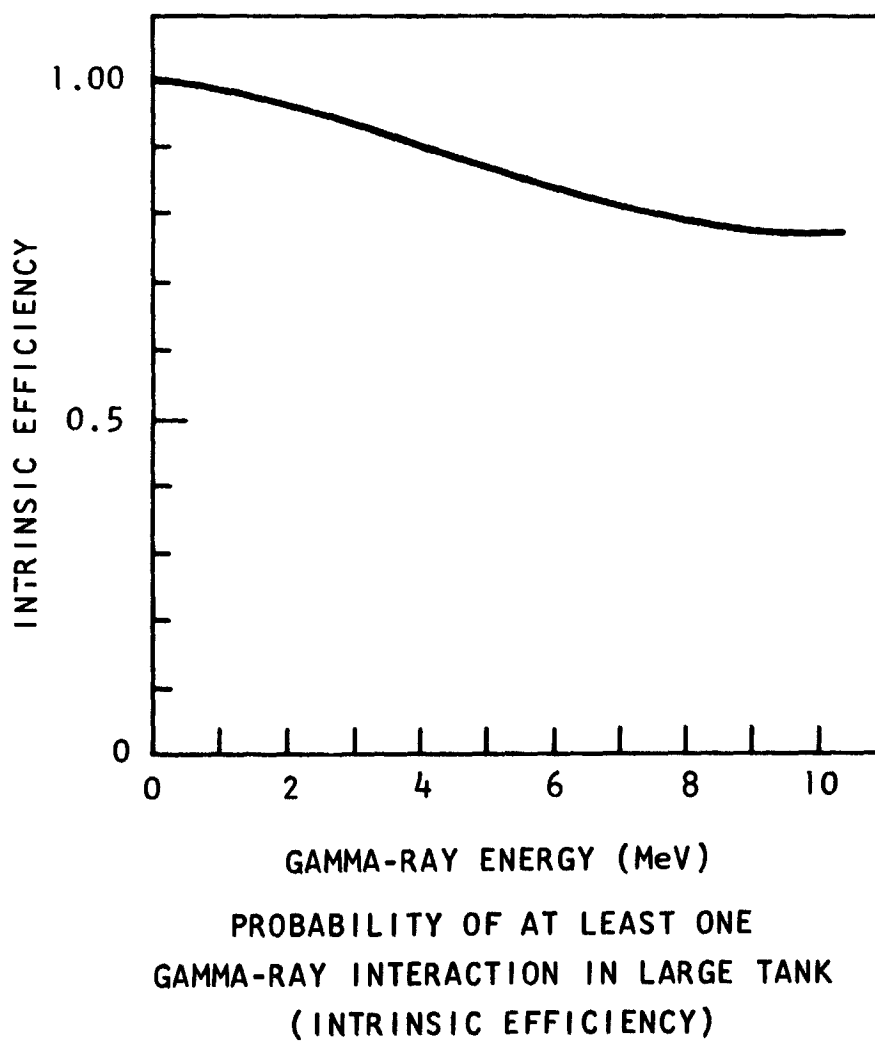


Fig. 5.2--Calculated first interaction probability for a single gamma to interact before escaping the large liquid scintillator.

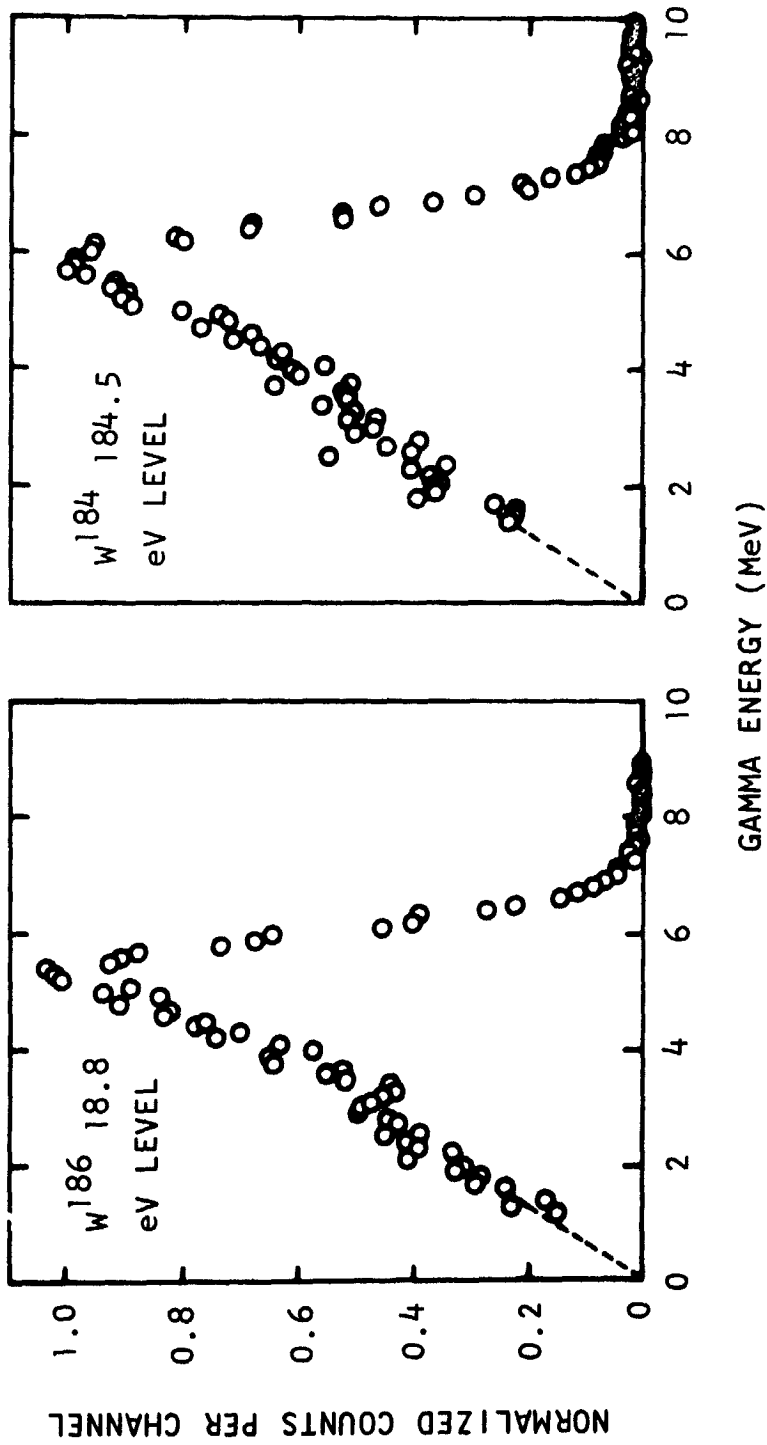


Fig. 5.3 -- Pulse height distributions due to captures in  $W^{182}$  and  $W^{183}$ .

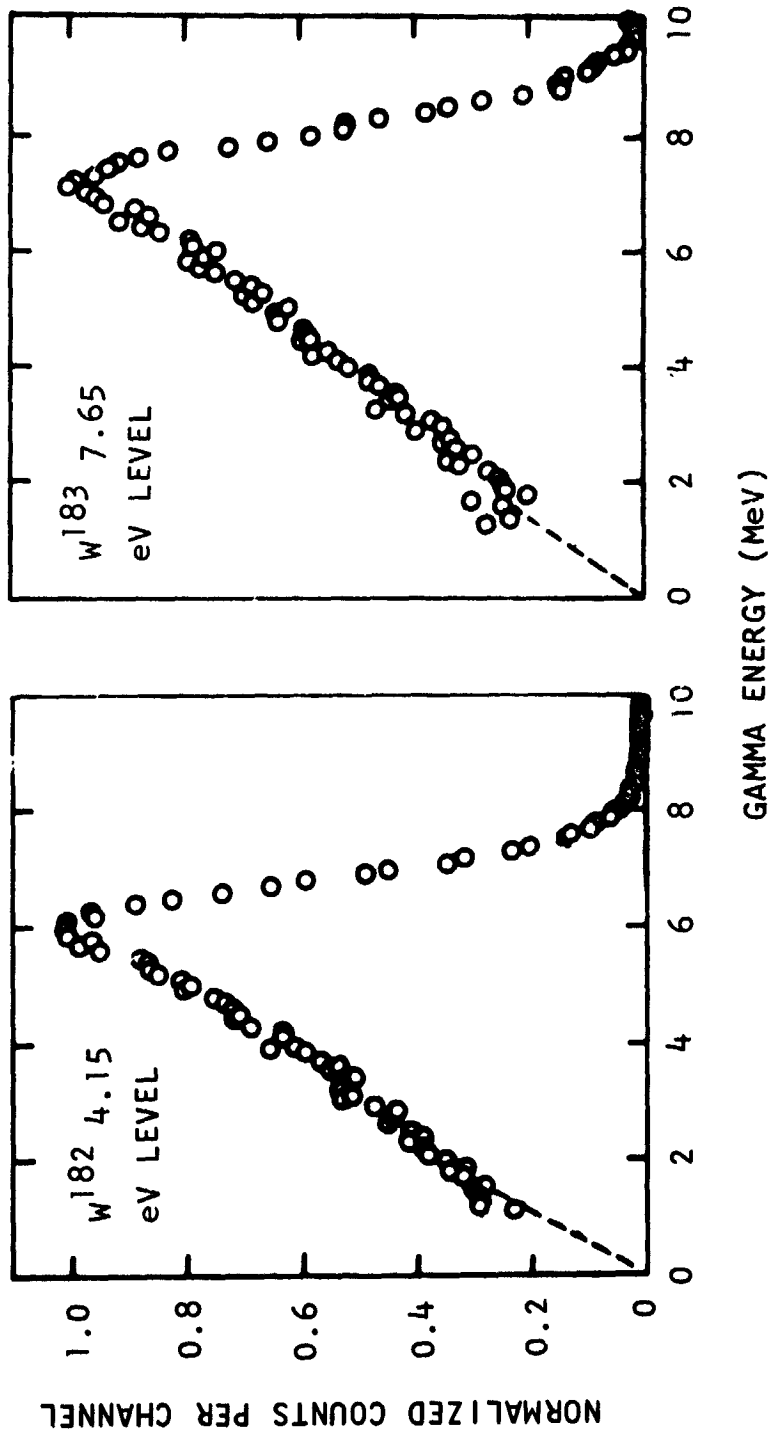


Fig. 5. 4--Pulse height distributions due to captures in  $W^{184}$  and  $W^{186}$ .

the probability of no pulse at all is also small since energy loss by Compton scattering, which is the dominant process, is a monotonic function of the scattering angle.

A second check can be obtained by observing the capture rate at zero bias for black samples of two different isotopes with markedly different gamma spectra. Since the incident flux is the same, the capture rates will differ by their relative intrinsic efficiencies. A good example is gold, which is known to have a large fraction of high energy gammas and  $W^{182}$  which has a much softer spectrum.<sup>(46)</sup> The observed capture rates agreed to within 2.5%.

It has been experimentally confirmed in every measurement to date that the pulse height distribution from neutron capture into various resonant states of the same isotope which have the same ingoing orbital angular momenta are identical. An example of this is shown in Fig. 5.5 for the 4.15 and 21.2 eV levels in  $W^{182}$ . This insensitivity to gamma spectra changes owing to capture in various resonant states is a strong indication that the fraction of capture events which exceed the lower level bias (3 to 4 MeV) will not be varied by the changing contributions to the isotropic cross section from various levels.

#### 5.3.2.2 Apparatus

The neutron source used in these measurements was the General Atomic linear accelerator. The machine parameters used were; electron energy of 28 MeV, currents of .3 to 1 Amp, and burst widths of .05 to 4.5  $\mu$  sec at 22.5 pulses per second. The shorter burst widths were used to reduce the counting rate for the high cross section sample runs and to obtain high resolution flux calibration data. The electron target assembly is shown in Fig. 5.6. The electrons slowing down in the Fansteel target produce bremsstrahlung which in turn produces high energy neutrons with a broad maximum near 1 MeV. These neutrons were slowed down

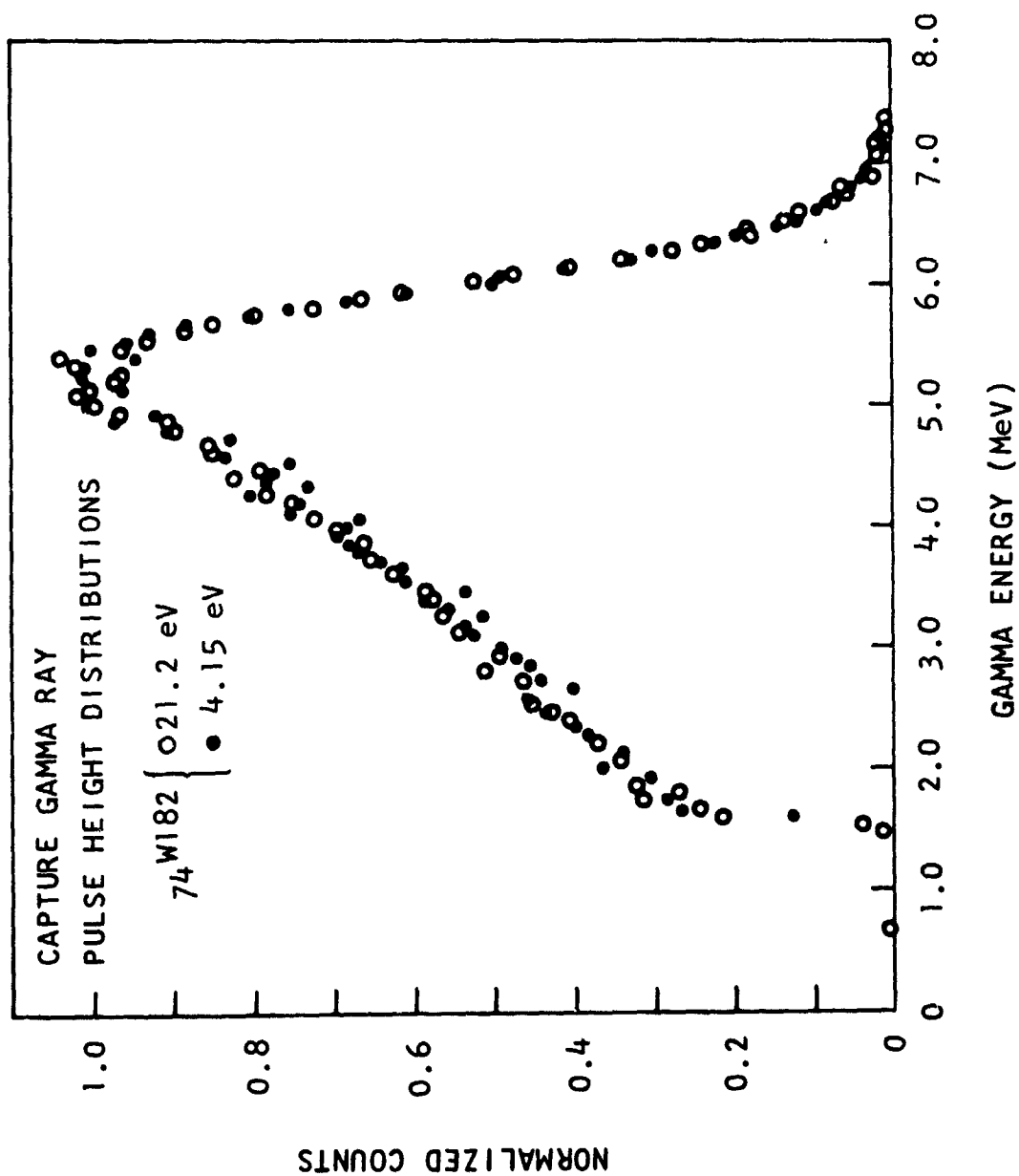


Fig. 5.5--Comparison of capture gamma ray pulse height distributions obtained from the 4.15 and 21.2 eV levels in W182.

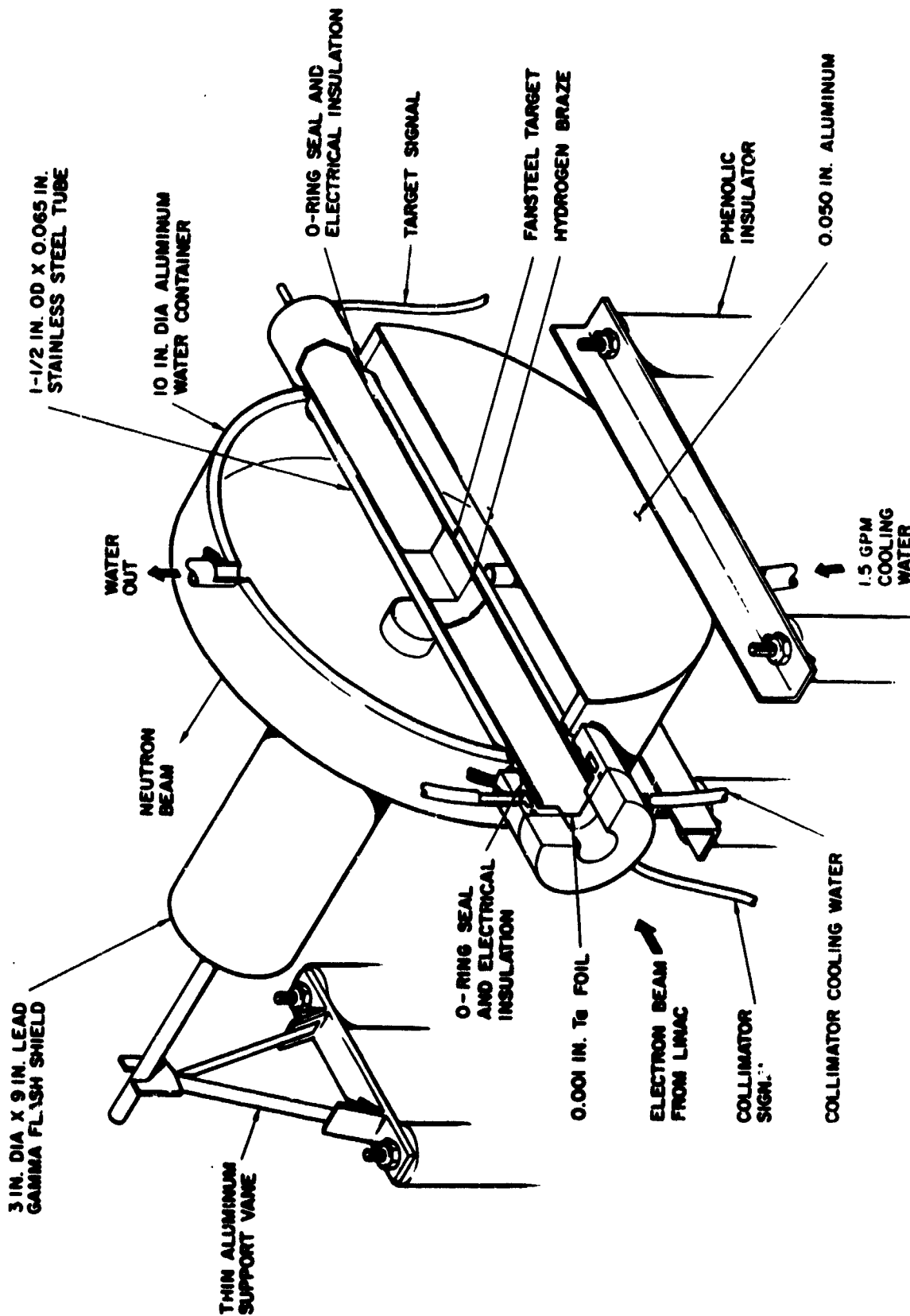


Fig. 5.6--Cross sectional view of electron target and moderator assembly.

to the epithermal and thermal region by the water container which also acts as a coolant for the target.

The neutron energy was determined by conventional time-of-flight techniques. The effective flight path length was  $18.61 \pm 0.01$  meters which includes a 0.03 meter correction for neutron slowing down time and the neutron scattering mean free path in the moderator. The entire flight path was maintained at a pressure of less than 150 microns, including an additional 2.5 meters beyond the sample. The electronics used for the time of flight and pulse height data acquisition are shown in Fig. 5.7. Not shown are the two independent  $\text{BF}_3$  flux monitoring channels which sample the penumbra of the beam just before it enters the scintillator. The sum of the counts in the two monitors was taken to be proportional to the neutron flux at the sample. The signals from the monitors are turned off for 50  $\mu\text{sec}$  following the accelerator burst to eliminate effects due to accelerator noise pickup and bremsstrahlung.

### 5.3.2.3 Flux Shape

The flux data above 1 eV were taken with two different  $\text{BF}_3$  detectors placed at the point at which the neutron beam leaves the scintillator. The smaller of the two was 1 in. in diameter with a 20 cm Hg filling pressure, and the larger one was 2 in. in diameter with a 76 cm Hg filling pressure. The smaller counter was assumed to have a response proportional to the  $1/v$  boron cross section and the larger counter was corrected for self protection which amounted to 3.0% at 1 eV and was proportionately less at higher energies. After this correction the data from both counters could be fitted to a high degree of accuracy by a smoothing function  $\phi(t) = KE^\alpha$ , where K is a flux normalization constant, E is the neutron energy in eV and  $\alpha$  is a constant dependent upon the size and type of moderator.

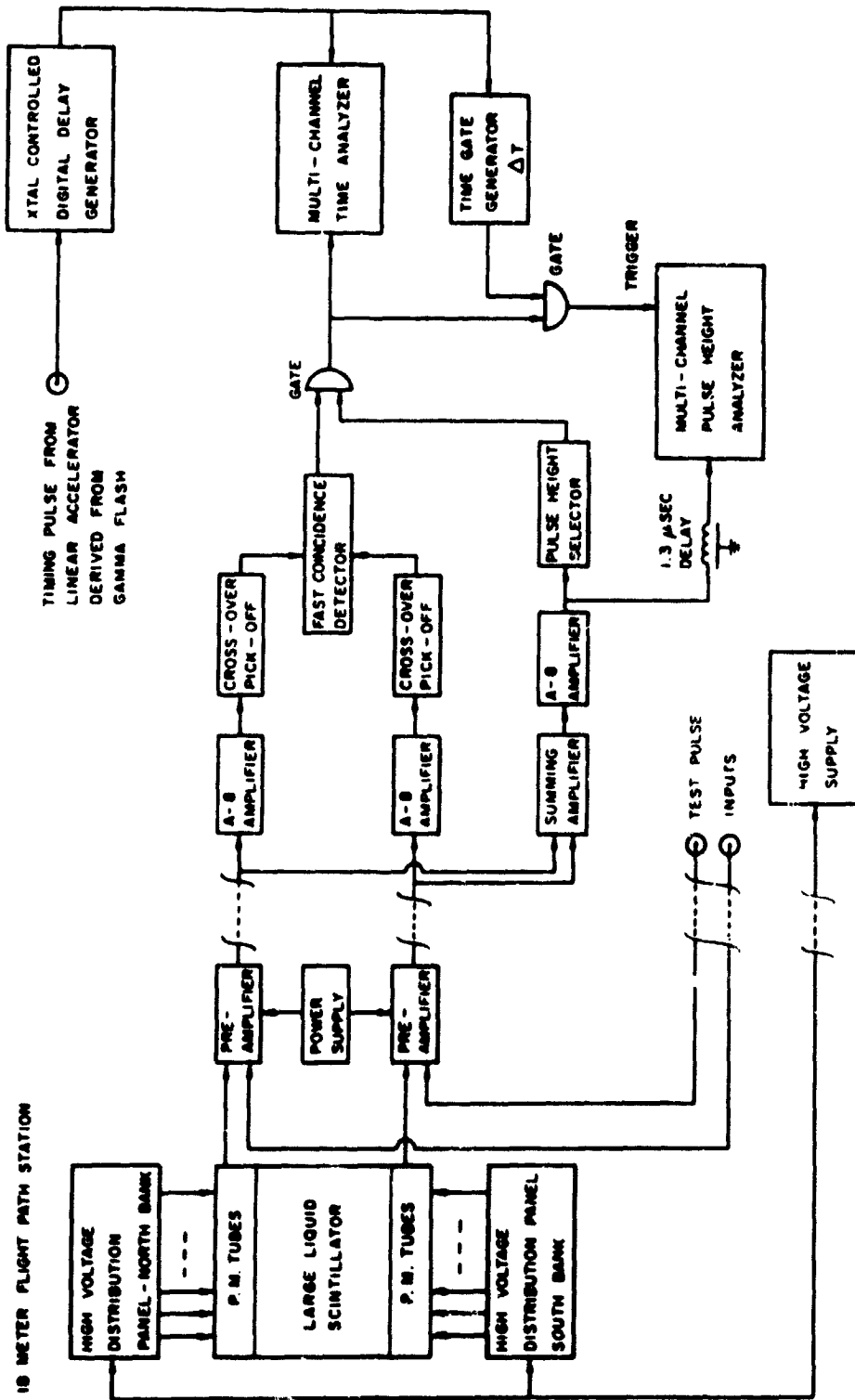


Fig. 5.7--Schematic of electronic configuration used in time-of-flight and pulse height data acquisition.



The determination of the flux shape below 1 eV proved to be more difficult. Consequently five techniques were investigated in an attempt to obtain the relative neutron flux incident on the sample. These techniques were:

1. A 2-in. diameter, 0.7-in. thick indium disk.
2. Five 2-in. diameter, 0.1-in. thick indium disks spaced approximately 1 in. apart.
3. A 2-in. diameter, 0.4-in. thick natural boron disk. (In this measurement the modular construction of the scintillator was utilized by turning off the outer cylinders and using only the central annulus which allowed the low energy boron capture gamma to be observed under low background conditions.)
4. A 2-in. diameter, 0.03-in. thick cadmium disk.
5. A 1-in. diameter  $\text{BF}_3$  detector with 20 cm Hg filling pressure placed downstream from the sample position.

Methods (1) through (4) depended upon the detection of capture gamma rays in the large liquid scintillator.

The indium disks were "black" (< 1% transmission) below 2 eV, the boron was black below 1.2 eV and the cadmium below .28 eV. All of these black samples were placed at the same location in the scintillator as the capture sample.

There are several possible sources of error in the techniques employing the detection of gamma rays.

1. The gamma biasing efficiency may be neutron energy dependent due to varying contributions to the capture cross section by isotopes with different binding energies.
2. The energy dependence of the fraction of the scattered neutrons which are not captured before leaving the sample.
3. In general some of the capture gammas will be absorbed or degraded in energy before leaving the capturing sample. Since the mean distance that the neutrons penetrate into the sample before the first interaction depends upon the total cross section, the attenuation of the gammas in the

sample will be neutron energy dependent. This effect arises from the exponential nature of the attenuation. For s-wave capture the capture gammas are emitted isotropically and hence the gamma transmission for a capture occurring on the surface of an infinite slab can be written:

$$T_s = \frac{1}{2} + \frac{1}{2} \frac{\int_0^1 e^{-\mu \frac{d}{x}} dx}{\int_0^1 dx} \quad (5.2)$$

and at the center:

$$T_c = \frac{\int_0^1 e^{-\mu \frac{d}{2x}} dx}{\int_0^1 dx} \quad (5.3)$$

where;

$x = \cos \theta$ ,

$\mu$  = effective gamma-ray attenuation coefficient,

$d$  = sample thickness,

$\theta$  = scattering angle.

Now  $T_c < T_s$  and hence a cross section dependence of the gamma attenuation can be expected.

Effect (1) is small in the case of indium and cadmium since the low energy cross section is dominated by a single low energy resonance. In the case of boron it is completely absent since the branching ratio to the 470 keV level in  $B^{11}$  is energy independent in the energy region of interest.

Effect (2) can be estimated from the ratio of scattering to total cross section. This ratio has a maximum value of 1% for cadmium, 3% for indium and 5% for boron. Since a large portion of the scattered neutrons are captured before leaving a black sample, the errors due to this effect should be small compared to the above percentages.

Effect (3) will be small for the 0.03-in. cadmium since experience has shown that attenuation of gammas in samples of this thickness is small and hence the second order effect described above should be negligible. The 0.4-in. boron slab is intermediate in thickness. An upper bound on the second order sample attenuation effect can be obtained by using the mass absorption coefficient for the 470 keV capture gamma in boron. The difference in transmission for an event at the face of and at the center of an infinite slab is about 5%. Since edge effects and detection of Compton scattered gammas reduce this effect the actual distortion is much less than this even if an extreme change in cross section is assumed, which is of course not the case.

Because of the much higher atomic number of indium and the unknown effective absorption for the capture gamma spectrum, the cross section dependent gamma-ray attenuation is not so easy to estimate in this case. Experimental comparisons discussed later will indicate the magnitude of this effect.

The thin  $\text{BF}_3$  data were corrected for self protection and absorption in the counter walls using the manufacturer's specifications. The correction was about 1.8% at 0.01 eV.

Figure 5.8 shows the normalized ratio of the cadmium to boron shapes from 0.01 to 0.28 eV and that of the normalized  $\text{BF}_3$  to boron shapes from 0.28 to 1.2 eV. It can be seen that these shapes are consistent within statistics in the regions of comparison. Above 0.28 eV the cadmium becomes thin and cannot be used. Below 0.2 eV the  $\text{BF}_3$  data showed a systematic departure from the boron and cadmium shapes which was about 3% at 0.01 eV. The reason for this departure is not apparent. The  $\text{BF}_3$  was placed in the scintillator in order to check the

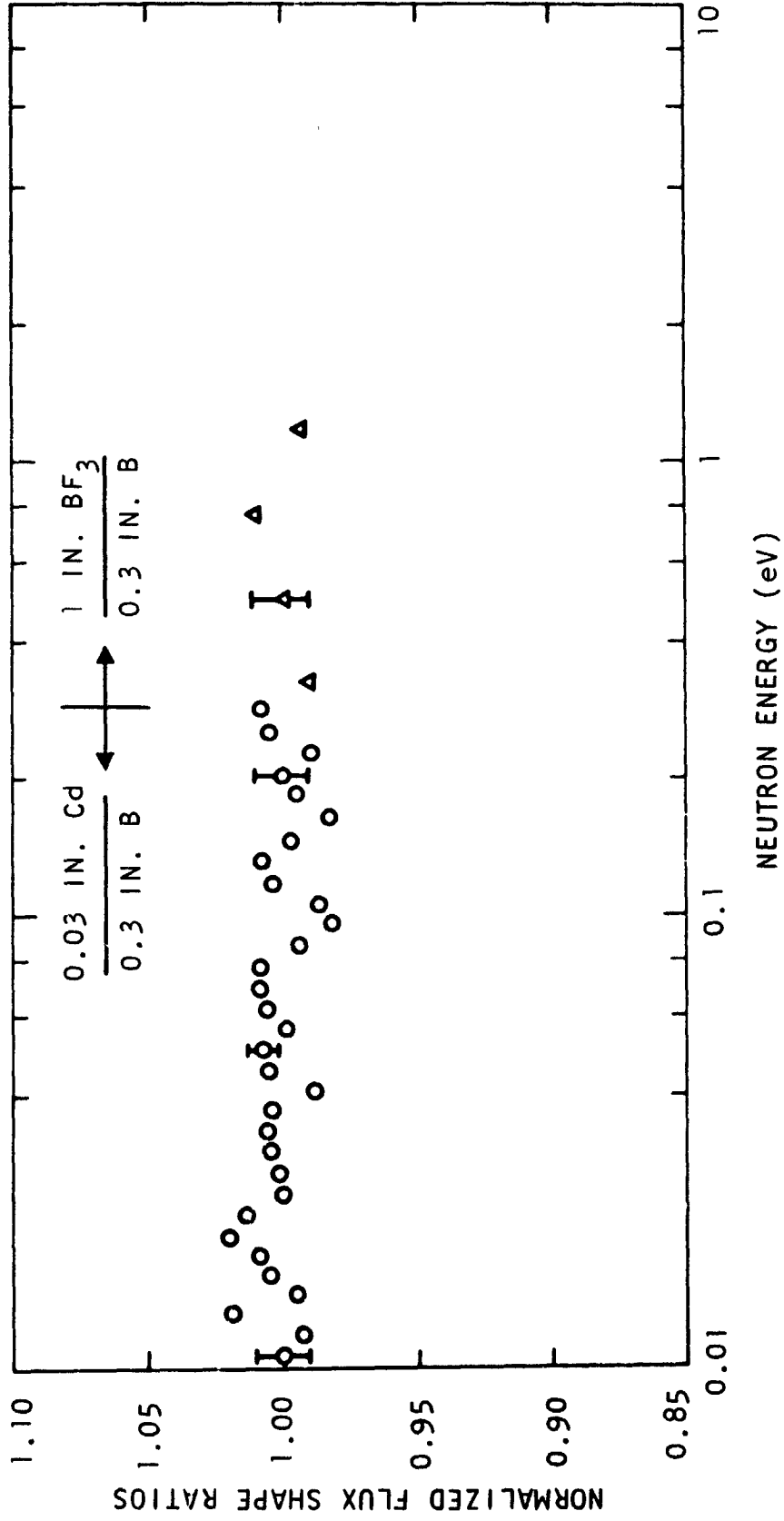


Fig. 5.8--Flux shape comparisons using thick boron slab and cadmium samples and a thin BF<sub>3</sub> tube with a 1/v resonance.

cross section of the counter walls. Good agreement with the copper cross section was obtained. The absorption in the 0.02-in. aluminum window at the end of the drift tube could account for only about 0.1% of the discrepancy. The error could be due to a boron deposit on the inside of the counter wall, but this possibility could not be checked without destroying the tube.

The 0.7-in. indium flux shape (1) also showed a systematic departure from the boron shape. The deviation shown in Fig. 5.9 has a shape analogous to the indium cross section which tends to confirm the hypothesis that the second order gamma attenuation effect discussed is important. The five spaced indium slabs (2) showed a similar deviation which was slightly smaller in magnitude due to the reduced gamma absorption.

One of the best known capture cross sections is that of gold, and hence measurements on gold were included as a check on the techniques employed in the tungsten measurements.

In the case of gold it is possible to obtain information about the capture cross section from the activation cross section since the decay scheme of  $^{198}\text{Au}$  is well known.<sup>(47)</sup> A recent compilation of the low energy cross section data on gold has been made<sup>(48)</sup> and points derived from a fit to these data are shown in Fig. 5.10. The calculated capture cross sections obtained from the published resonance parameters using the high and low limits on the product  $\Gamma_{\gamma} \Gamma_n$  for the 4.906 eV resonance, as listed in BNL-325, and the best values of the remaining resonances up to 1 keV, as measured at Saclay,<sup>(49)</sup> are shown in the figure. A statistical calculation<sup>(50)</sup> was used to include the contribution of resonances above 1 keV. These two curves are reasonably representative of the uncertainty in the calculated cross section since the low energy cross section is dominated by the 4.906 eV resonance. The "total minus scattering" curve was obtained by subtracting the scattering cross section calculated from the above parameters from the total cross section curve of BNL-325. The potential scattering cross section of  $11.1 \pm .3$  barns determined by Seth<sup>(51)</sup> et al., was used in the calculation. The interference between resonant and potential scattering was included only for the 4.906 eV level since the

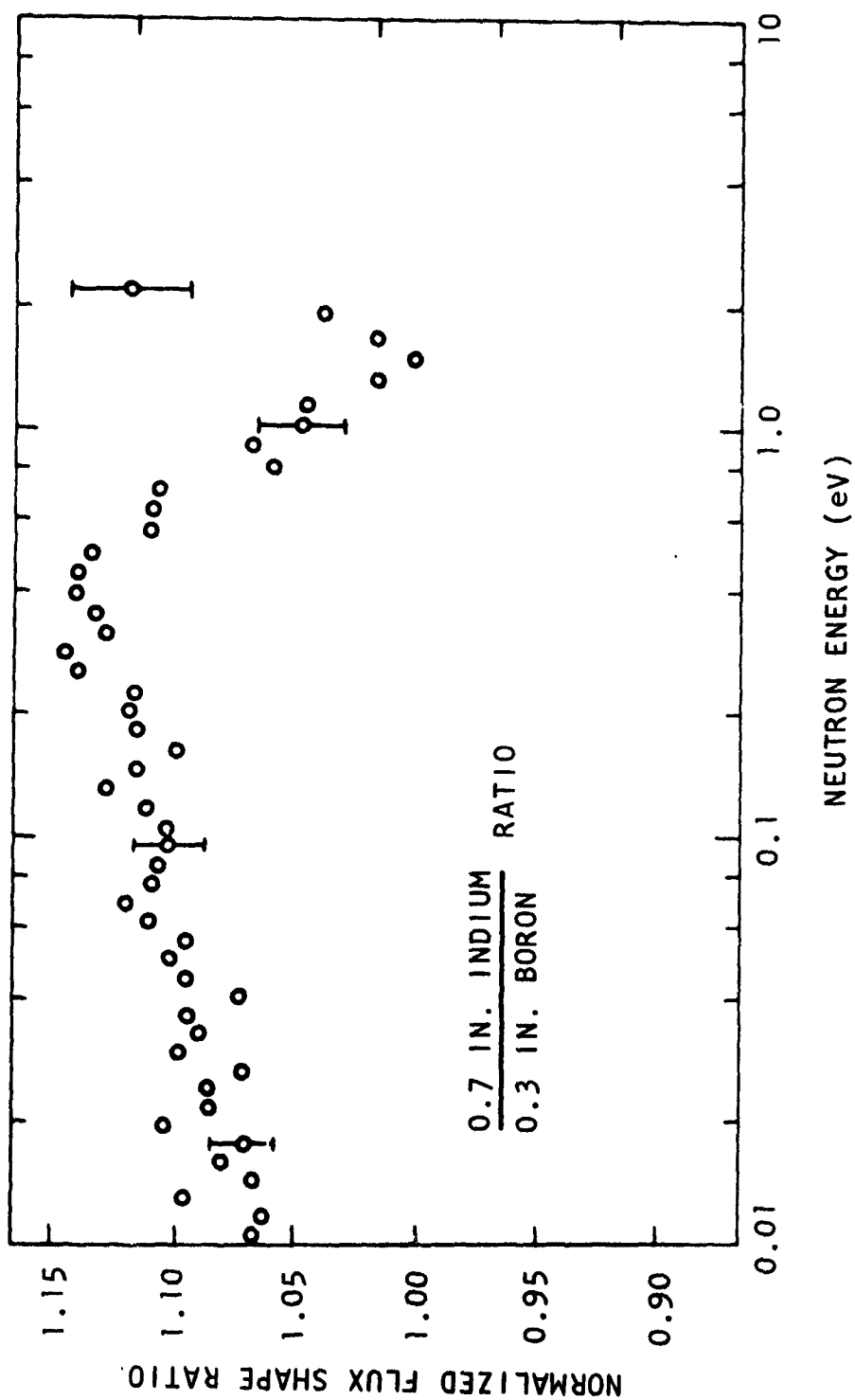


Fig. 5.9--Comparison of flux shapes measured with thick indium and boron slab samples.

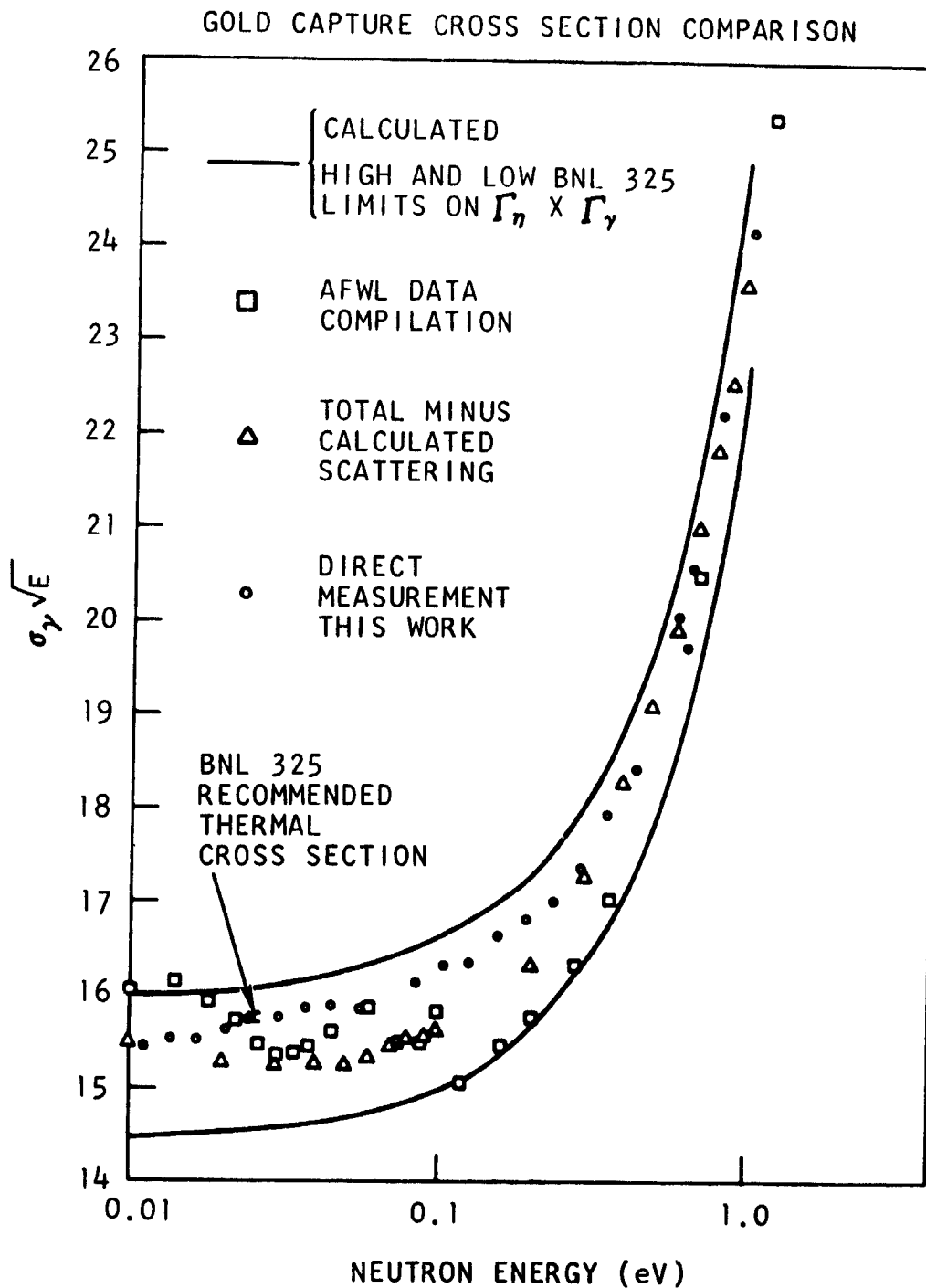


Fig. 5.10--Low energy gold cross sections obtained from various sources.

interference contributions of the other levels can be expected to cancel. The data points in the figure were obtained below 1 eV using the boron flux shape described above. The excellent agreement between the data points and the calculated curve tends to confirm the conclusions drawn previously about the reliability of the boron flux shape.

#### 5.3.2.4 Flux Calibration

The flux shape was made absolute by employing the saturated resonance technique. This involves the measurement of the capture rate in some energy interval in which the sample transmission is negligible. It is important that capture predominate over scattering to reduce the correction required for neutrons lost from the sample due to scattering collisions, and the thickness of the sample must not be so large as to produce appreciable gamma ray attenuation effects.

These two conditions were fulfilled only by the 4.15 eV resonance in  $W^{182}$  and the 4.906 eV resonance in gold for the isotopes investigated in this work. Typical flux calibration data are shown in Fig. 5.11. The saturated energy interval is indicated by a flattening of the resonance peak. The energy interval indicated in the figure was chosen for the calibration, and the data in this interval were corrected for resolution and multiple scattering<sup>(52)</sup> effects using the parameters obtained by Bernabie<sup>(53)</sup> in the case of  $W^{182}$ , and the BNL 325<sup>(54)</sup> parameters for gold. These corrections were from 1 to 3% and are relatively insensitive to the values of the resonance parameters. Hence the error in the calibration correction used is negligible. Since the  $W^{182}$  thermal cross section was measured with the same gamma energy bias which was used for the flux calibration, no corrections for biasing efficiency were required for this isotope. The other three tungsten isotopes do not have the same neutron binding energy as  $W^{182}$ , and their bias efficiencies cannot be expected to be the same.



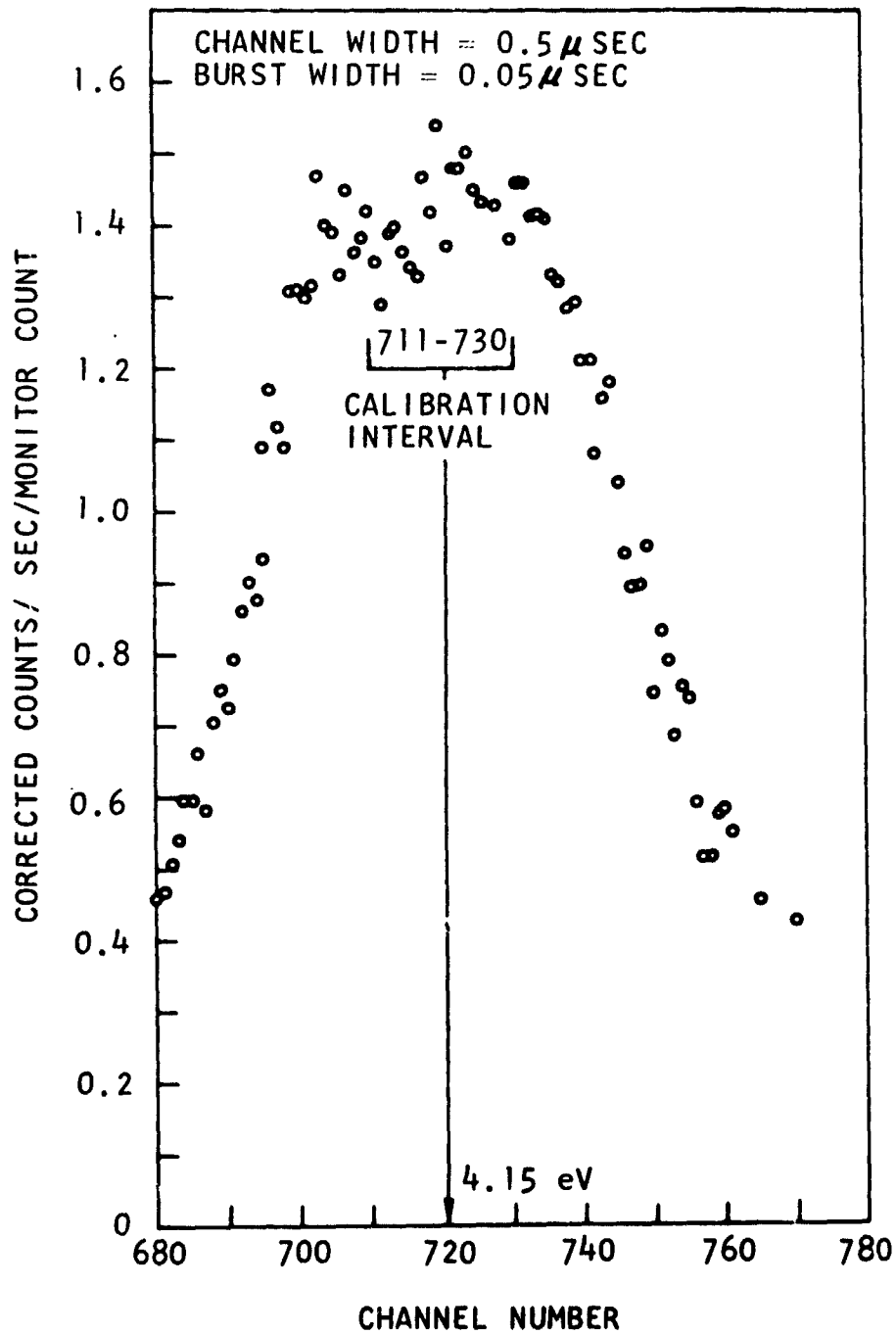


Fig. 5. 11--Flux calibration data using the 4.15 eV resonance in  $W^{182}$ . The sample is .01 inch natural tungsten.

In order to correct for these spectrum differences, time gated pulse height distributions were taken for captures in the lowest energy resonance in each of the isotopes. In order to minimize errors due to background subtractions the "sliding window" method of background accumulation was employed. In this technique the sample is left in position and the time window is moved to flight times slightly earlier and then slightly later than the time corresponding to the resonance in question. Since the time dependent backgrounds vary only slightly within the width of a typical resonance, the average background accumulated in this fashion is representative of the background in the resonance itself. Using this technique the pulse height data were reliable down to  $\approx 1.5$  MeV. Below this energy an extrapolation to zero bias is necessary. As can be seen from the measured pulse height distributions shown in Figs. 5.3 to 5.5, a linear extrapolation is consistent with the shape of the distributions. The area under the curves below 1.5 MeV is about 4% of the total. It is highly improbable that the extrapolation could be in error by more than  $\pm 50\%$ , and hence a 2% error was assumed. The exponential flux shape above 1 eV was normalized to the absolute flux at the calibration energy and the boron flux shape was in turn normalized to the exponential flux between 1.05 and 1.20 eV. The measured absolute flux shape is shown as a function of time in Fig. 5.12.

The gold and natural tungsten data were taken using high purity metallic disks of 2 in. in diameter. The sample thicknesses were  $7.294 \times 10^{-4}$  and  $1.795 \times 10^{-3}$  atoms/barn respectively. The tungsten isotopic cross section data were acquired using tungsten trioxide powder with the thicknesses and enrichments listed in Table 5.3.

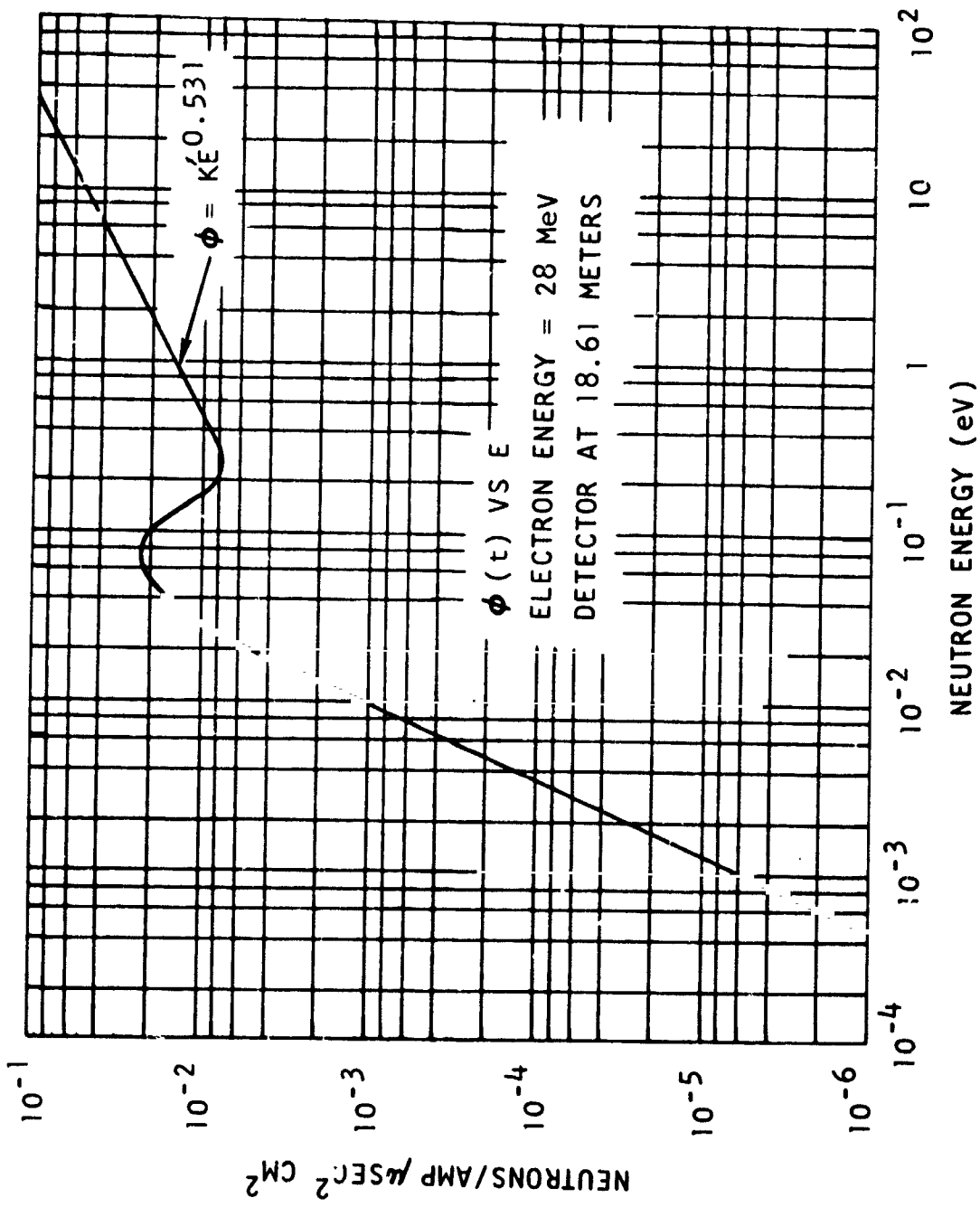


Fig. 5.12--Absolute neutron flux as a function of time.

Table 5.3  
ABUNDANCES

<u>Enriched Isotope</u>	<u>180</u>	<u>182</u>	<u>183</u>	<u>184</u>	<u>186</u>	<u>Thickness atoms/barn</u>
182	<.0003	0.945	0.0209	0.0234	0.0109	$2.423 \times 10^{-3}$
183	<.001	0.052	0.813	0.073	0.062	$8.685 \times 10^{-4}$
184	<.0005	0.0174	0.0174	0.942	0.0235	$2.452 \times 10^{-3}$
186	<.001	0.0057	0.0041	0.0183	0.972	$1.2697 \times 10^{-3}$

The trioxide powder was placed in three different types of containments in order to detect errors which might arise due to scattering and capture in the container materials. The containers used were:

1. Pressed caked with aluminum foil cover
2. Pressed with 10% by weight Plexiglas binder
3. Pressed into thin wall aluminum cans.

The samples in container (1) proved to be extremely fragile and were used only in the first set of measurements. The Plexiglas binder used in containment (2) increased the multiple scattering corrections required by a considerable amount and hence data acquired with the samples in this form were used only to check the cross section at the peak of the Maxwellian velocity distribution (.0253 eV) where energy changes of the scattered neutron can be assumed to cancel. The 2200 m/sec cross section obtained in this way agreed very well with that obtained with the samples in forms (1) and (3).

The aluminum cans in form (3) had 0.02-in. walls and a 0.125 in. thick rim. The tungsten trioxide was pressed into the cans using a special die under 2 tons/sq in. pressure. Radiographs indicated that the samples were uniform within  $\pm 5\%$ . The weights of all the cans were adjusted to

the same value (10 grams) and an empty can placed in the neutron beam was used to measure the capture rate in the aluminum. This data was used to correct the tungsten data for captures in aluminum.

The effect of scattering from aluminum on the tungsten capture rate was taken into account by adjusting the energy independent component of the tungsten trioxide scattering cross section in each case.

### 5.3.3 METHOD OF ANALYSIS

The equation which relates the capture rate in the  $i^{\text{th}}$  isotope to the cross section is given by:

$$C_i(t) = \epsilon_i s \phi(t) (1 - e^{-N\sigma_T}) \frac{a_i \sigma_{\gamma i}}{\sigma_T f_0} \quad (5.4)$$

where:

- $\epsilon_i$  = efficiency for detection of captures in isotope  $i$
- $\phi(t)$  = neutron flux in neutrons/cm<sup>2</sup>
- $N$  = number of sample atoms/cm<sup>2</sup>
- $\sigma_T$  = total cross section in cm<sup>2</sup>
- $a_i$  = abundance of the  $i^{\text{th}}$  isotope
- $\sigma_{\gamma i}$  = capture cross section of the  $i^{\text{th}}$  isotope
- $s$  = sample area in cm<sup>2</sup>
- $f_0$  = probability of capture of an incident neutron on the first interaction
- $f$  = total neutron capture probability.

If more than one isotope is present, then  $C = \sum_i C_i$ . Solving for  $\sigma_{\gamma i}$  in this sum we obtain:

$$\sigma_{\gamma i} = \left[ \frac{C(t)\sigma_{Tf_0}}{s\phi(t)(1-e^{-N\sigma_T})f} - \sum_{k \neq i} a_k \epsilon_k \sigma_{\gamma k} \right] (a_i \epsilon_i)^{-1} \quad (5.5)$$

where  $C(t)$  is the number of capture counts observed at time  $t$ . The sum over the depleted isotopes in Eq. (5.5) corrects for captures in isotopes other than the enriched one. It should be noted in Eq. (5.5) that the  $\sigma_{\gamma k}$  are in general unknown. Hence Eq. (5.5) must be solved by iteration employing a data set corresponding to each of the enriched isotopes. A computer code was used to solve Eq. (5.5) at each time point for the four tungsten isotopes and gold.

In the cases of natural tungsten and gold where the sum of the abundance weighted isotopic capture cross sections is being measured, Eq. (5.5) becomes:

$$\sigma_{\gamma T} = \frac{C(t)\sigma_{Tf_0}}{\epsilon_T(t)s\phi(t)(1-e^{-N\sigma_T})f} \quad (5.6)$$

where  $\epsilon_T(t)$  is the efficiency for detecting a capture in a natural sample given by:

$$\epsilon_T(t) = \frac{\sum_i \epsilon_i a_i \sigma_{\gamma i}(t)}{\sum_i a_i \sigma_{\gamma i}(t)} \quad (5.7)$$

The solution of Eqs. (5.5) and (5.6) requires a knowledge of the multiple scattering effect, i. e.,  $f_0/f$ . The multiple scattering correction employed is a first order analytic calculation of the fraction  $f_1$  of neutrons which capture after the first scattering collision. The scattering cross sections for tungsten were those calculated from the resonance parameters listed in Ref. 55.\* The low energy scattering cross sections listed in Ref. 54 were used for oxygen and aluminum.

---

\*The low energy scattering cross sections listed in Ref. 55 seem to be in error.

The calculation ignores energy changes of the scattered neutron and the effects of thermal motion of the scattering nucleus. These effects are appreciable in the Lorentzian portion of the low energy resonances and hence no attempt was made to analyze the data in these regions.

The sample was considered to be an infinite slab which is justified by the large diameter-thickness ratios for the samples employed. The geometric series approximation  $\frac{f_0}{f} = 1 - f_1$  was used as the correction for the total of all scattered neutron captures.

The cross section data shown in Fig. 5.13 through 5.18 represent the weighted average of data acquired on six different dates. In each case the flux shape and backgrounds as well as flux calibration and pulse height distribution data were taken. In this way the effects of changes in the apparatus between data runs were eliminated.

The time-of-flight data, after being corrected for analyzer dead time and backgrounds, were grouped and interpolated on a set of energy points. These energy points correspond to the data points shown in the figures. In all cases the neutron energy resolution width is much smaller than the energy difference between the points shown. Equation (5.5) was solved for each of these energy groups, and hence contains a "resolution" error which becomes appreciable when the flux shape or cross section varies rapidly with energy. This occurs only in the low energy resonances, and since, as explained earlier, the data in the vicinity of these resonances are unreliable, the data points in these energy regions were omitted from the figures.

The measured  $W^{182}$  cross section shown in Fig. 5.13 is significantly higher than that calculated from positive energy resonances including a statistical term for the unresolved region. The discrepancy can be accounted for by postulating a  $1/v$  contribution from negative energy levels. The choice of parameters for such a level is arbitrary with the sole restriction that the "resonance" energy be much less than -10 eV in order that its contribution vary essentially as  $1/v$  in the region of the measurement.

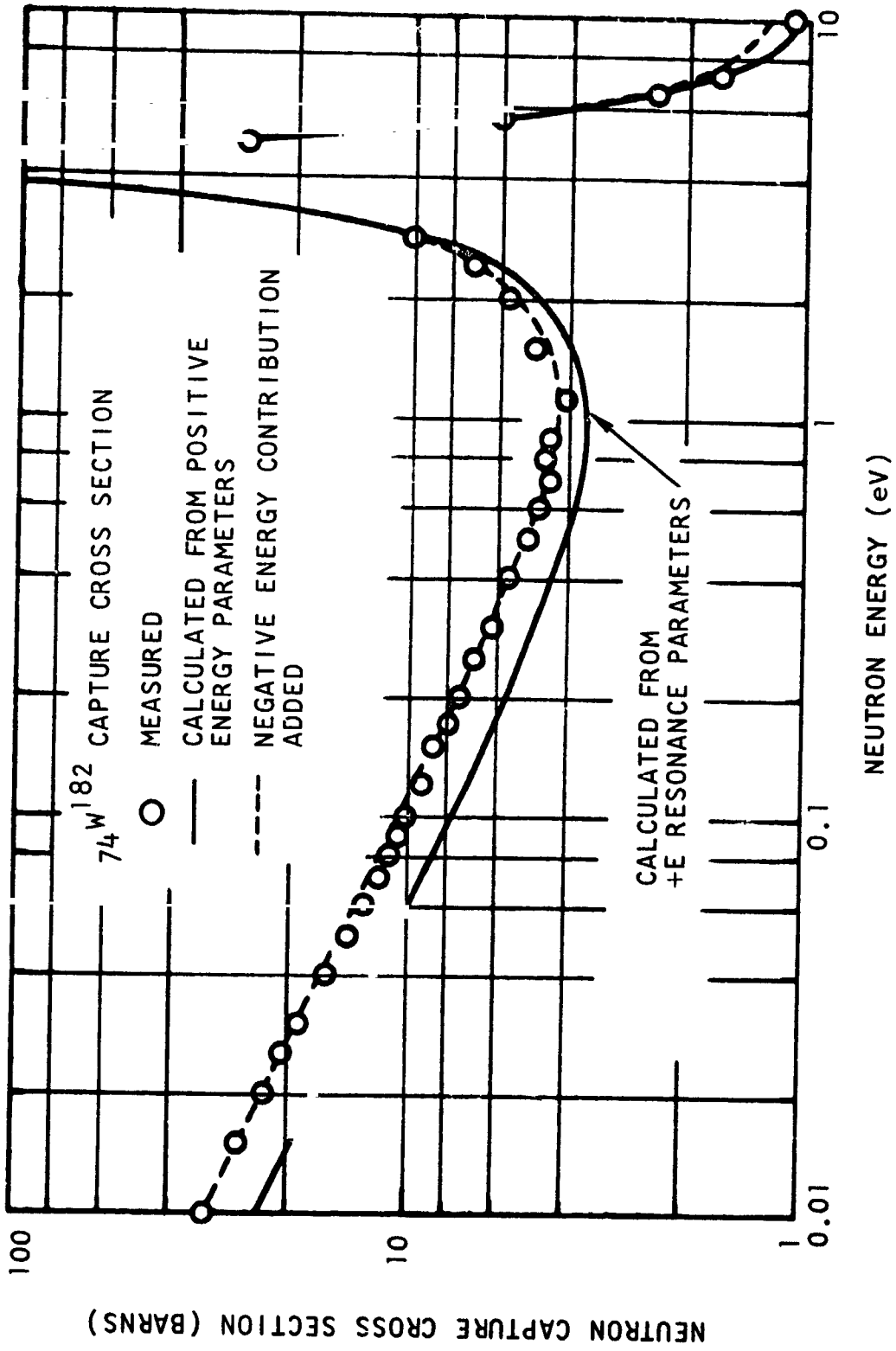


Fig. 5.13--Tungsten 182 cross section



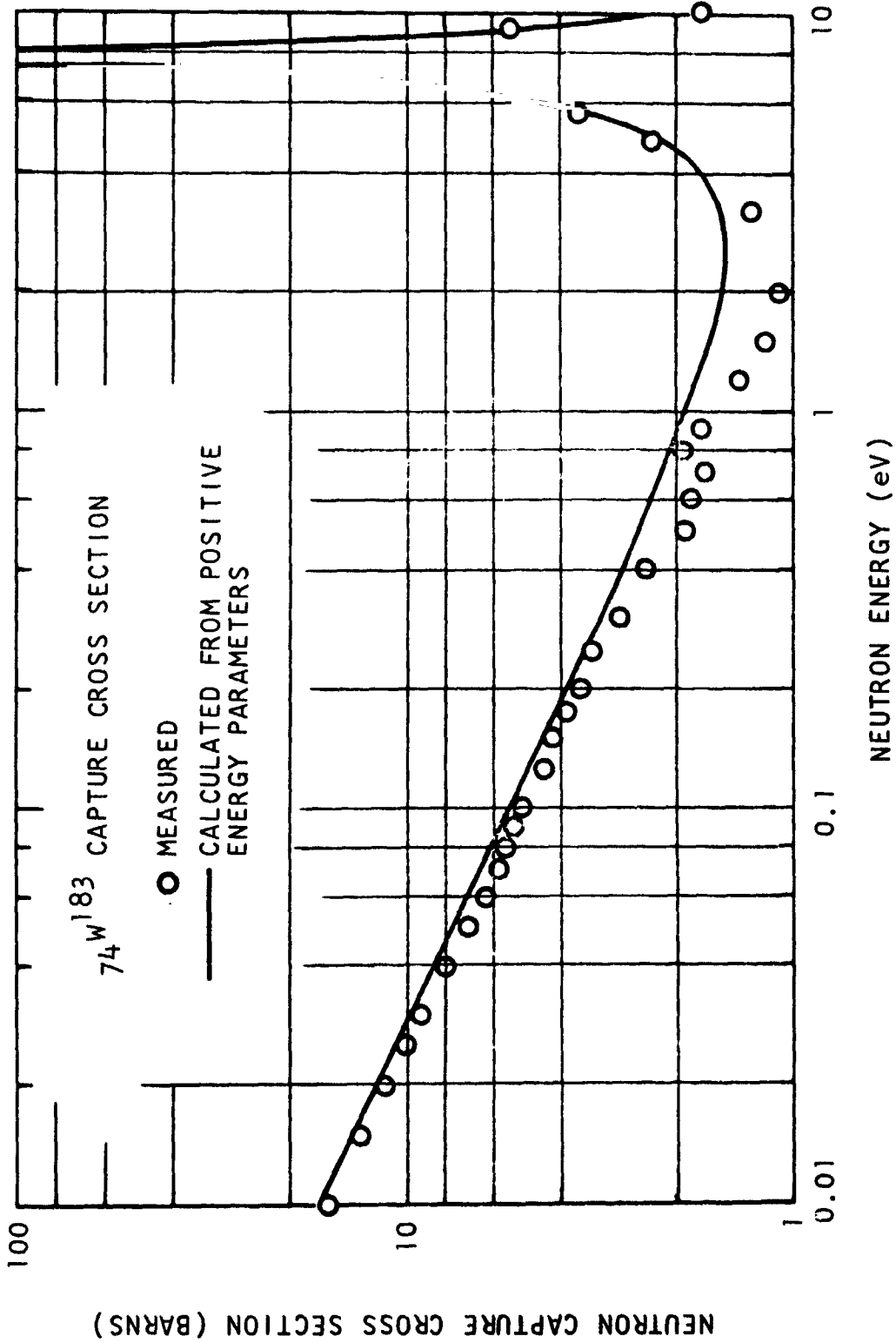


Fig. 5.14--Tungsten 183 cross section

THE INFORMATION CONTAINED HEREIN IS UNCLASSIFIED EXCEPT WHERE SHOWN OTHERWISE

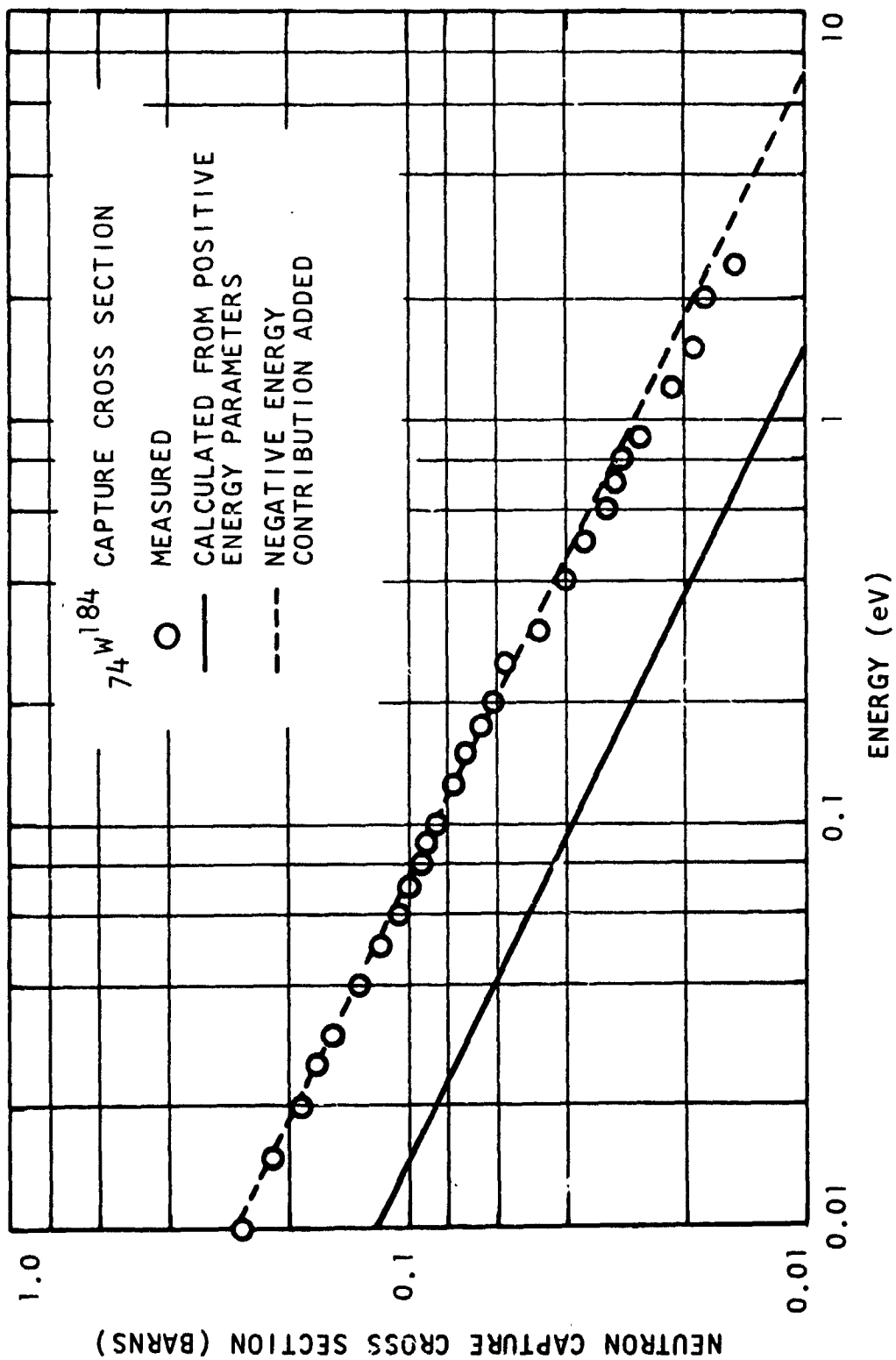


Fig. 5.15--Tungsten 184 cross section

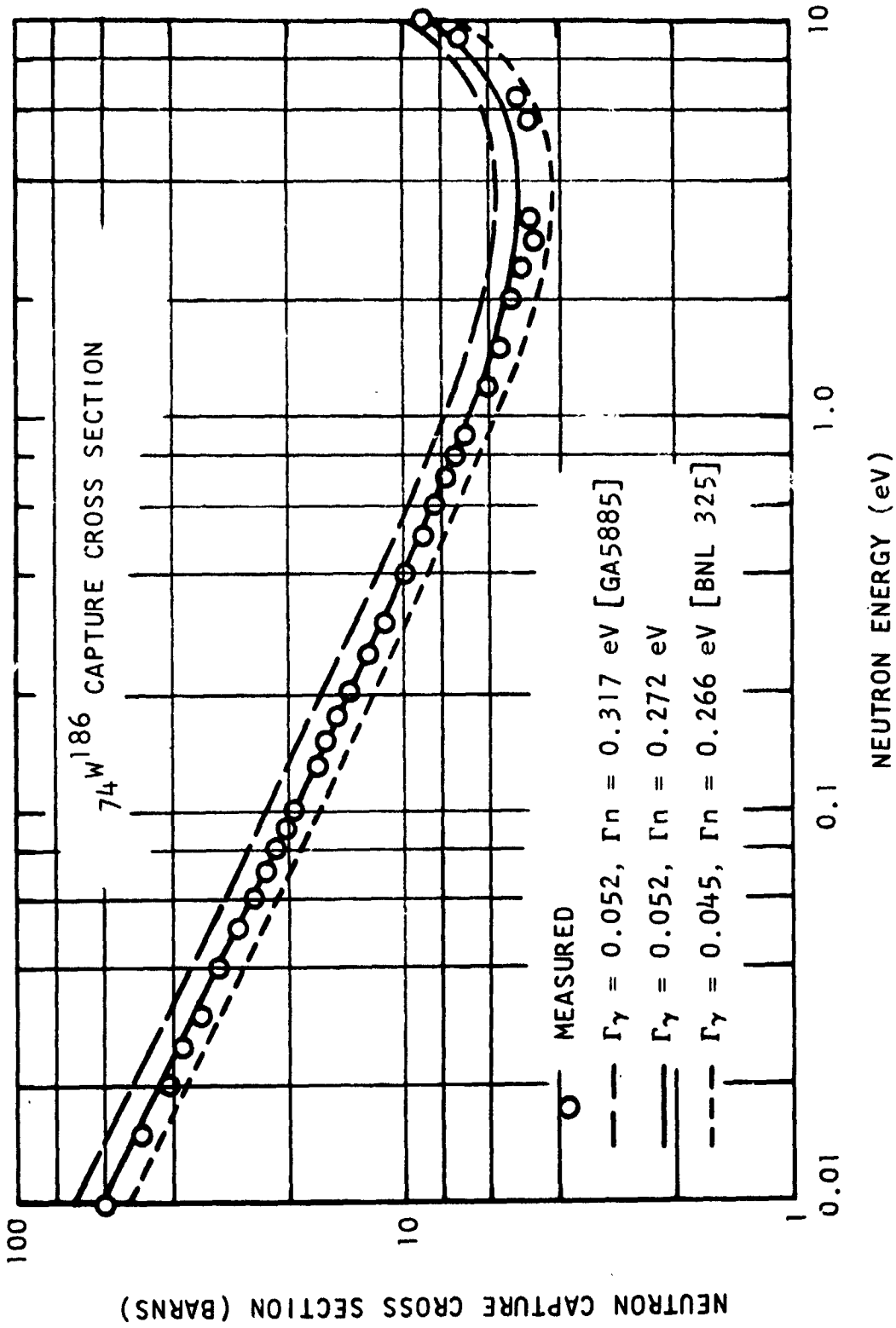


Fig. 5.16--Tungsten 186 cross section

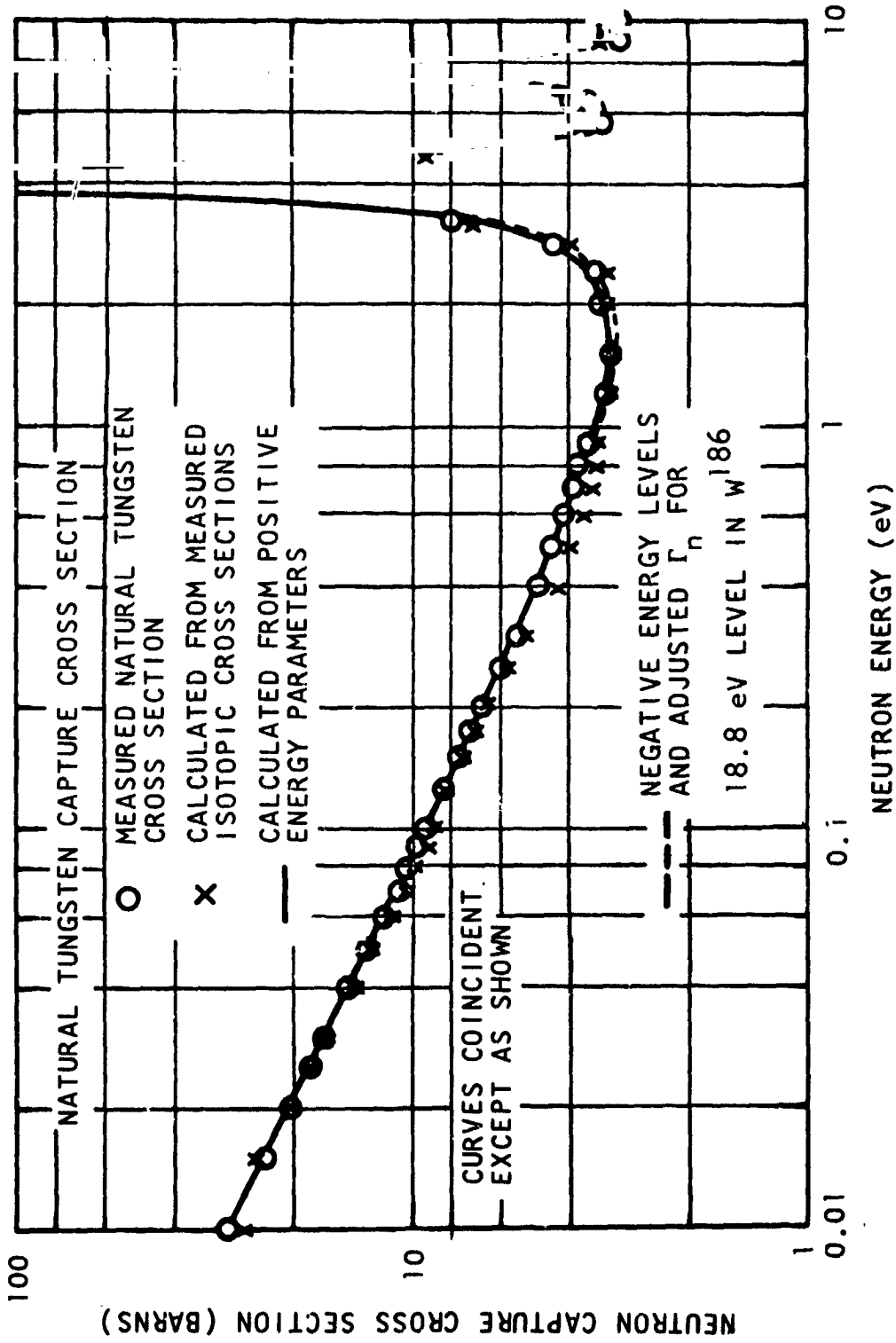


Fig. 5.17--Natural tungsten cross section

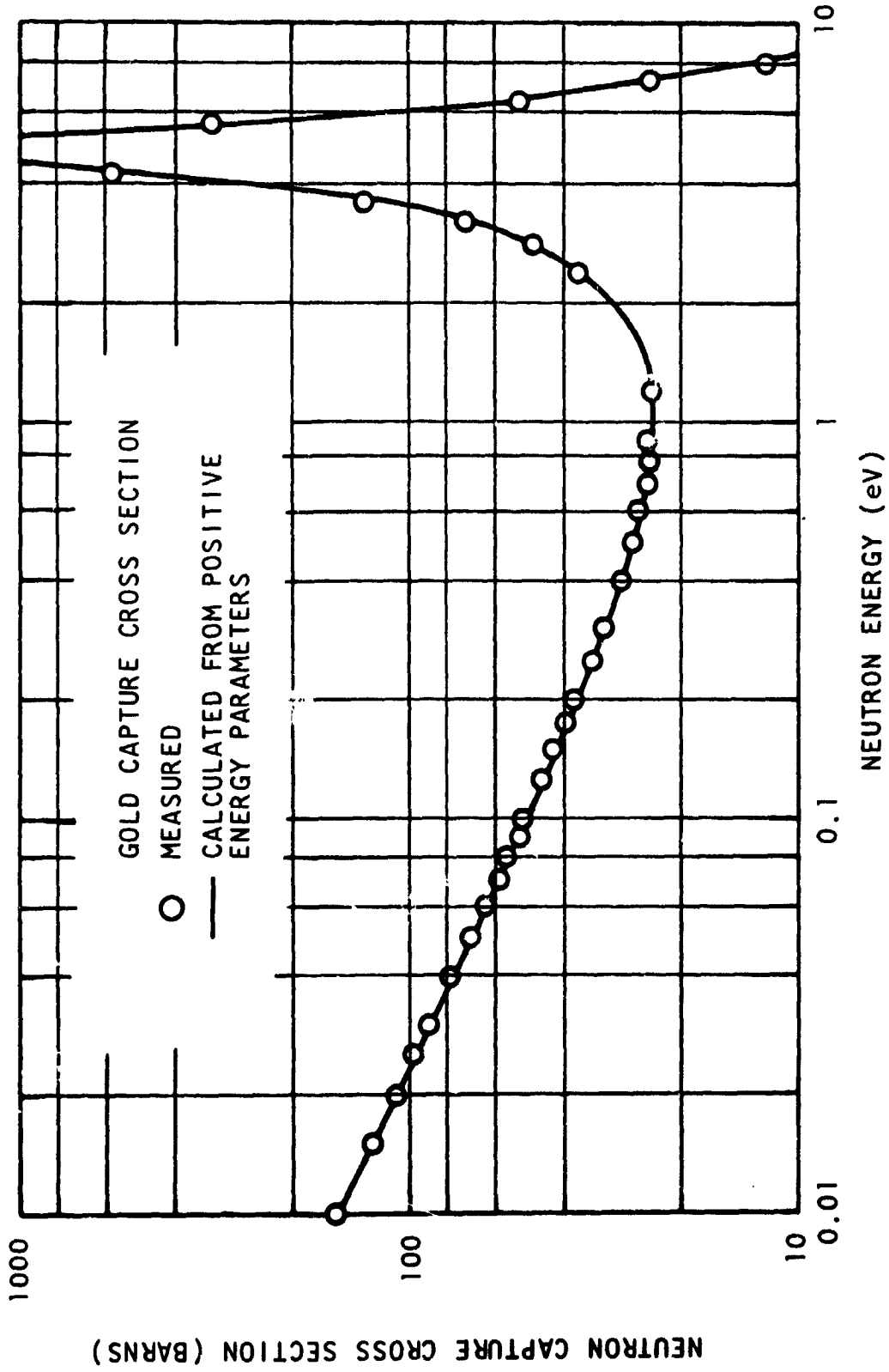


Fig. 5. 18--Gold cross section

Since  $W^{182}$  is an even-even nucleus,  $g = 1$ . The best choice of  $\Gamma_\gamma$  is the average radiation width of the positive energy levels, i. e., 57 meV. The average reduced neutron width of  $20 \text{ meV/eV}^{1/2}$  was chosen, which yields a resonant energy of  $-30.7 \text{ eV}$ , sufficiently small to make only a  $1/v$  contribution. The dashed curve shown in Fig. 5.13 was obtained by adding this contribution to that of the positive energy levels. There is some indication that the negative energy contribution does not quite vary as  $1/v$  due to the systematic deviation near 10 eV. No attempt was made to improve the fit by the inclusion of a non  $1/v$  negative energy contribution due to the doubtful significance of the deviation.

The  $W^{183}$  cross section shown in Fig. 5.14 is slightly below the calculated curve by an amount which exceeds the errors in this measurement. The discrepancy is thought to be due to errors in the resonance parameters used.

The  $W^{184}$  data points shown in Fig. 5.17 lie well above the calculated curve which again indicates a negative energy contribution. The "parameters" for the negative energy level obtained in the same fashion as those for  $W^{182}$  are:  $g=1$ ,  $\Gamma_\gamma = 57 \text{ meV}$ ,  $\Gamma_n^0 = 48.4 \text{ meV/eV}^{1/2}$ ,  $E_0 = -110 \text{ eV}$ . Again there is an indication of a non  $1/v$  negative energy contribution, but the significance of this deviation is again doubtful.

Three calculated cross section curves for  $W^{186}$  are shown in Fig. 5.16. The upper one was obtained from the parameters listed in Ref. 55 and the lower one from those listed in Ref. 56. It can be seen that the data points lie at an intermediate position. Since the cross section is dominated by the 18.8 eV level, the error can probably be ascribed to the  $\Gamma_n \Gamma_\gamma$  product for this level which is  $1.413 \times 10^{-2} \text{ eV}^2$  for the measured curve as opposed to  $1.648 \times 10^{-2} \text{ eV}^2$  for the upper calculated curve and  $1.197 \times 10^{-2} \text{ eV}^2$  for the lower one. Since the radiation width used in the upper curve is probably more reliable than the neutron width, the latter quantity was adjusted to force agreement at thermal energy. The result is the dashed curve which is in good agreement with the data throughout the measured energy interval.

The measured natural tungsten cross section is shown in Fig. 5.17 along with a calculation from the positive energy parameters listed in Ref. 55. Also shown is the calculated cross section including the two negative energy levels evaluated earlier as well as the adjusted neutron width of the 18.8 eV level in  $W^{186}$ . These two curves agree below 1 eV due to a fortuitous cancellation of the errors in the isotopic cross sections calculated from the positive energy parameters. The natural tungsten cross section obtained by abundance weighting the measured isotopic cross sections are also shown. The natural tungsten cross section obtained in this way is in very good agreement with the measured cross section of natural tungsten except in the region near 10 eV where statistical uncertainties are appreciable.

Finally in Fig. 5.18 the measured gold cross section is compared to that obtained from the best set of resonance parameters. It can be seen that the agreement is very good throughout the energy region investigated.

#### 5.3.4 EXPERIMENTAL RESULTS

The values obtained in this work for the thermal cross section of  $W^{182}$ ,  $W^{183}$ ,  $W^{184}$  and  $W^{186}$  are given in Table 5.4. Also included are the values recommended in BNL 325 and the values calculated from the measured resonance parameters of the positive energy states.

The natural tungsten cross sections listed in Table 5.4 were obtained using the abundances listed in the Handbook of Physics and Chemistry. The relative contribution of the various isotopes to the natural tungsten thermal cross section can be seen in Table 5.5.

Table 5.4  
CAPTURE CROSS SECTION AT .0253 eV

<u>Isotope</u>	<u>BNL 325</u>	<u>From Parameters</u>	<u>This Work</u>
180	60.0 ± 60.0	a	
182	20.0 ± 2.0	13.5	20.70 ± 0.5
183	11.0 ± 1.0	9.5	9.97 ± 0.3
184	2.0 ± 0.3	1.87	1.71 ± 0.1
186	35.0 ± 3.0	44.2 <sup>b</sup>	37.8 ± 1.2
Natural	19.2 ± 1.0	19.9	18.29 ± 0.5
Calculated <sup>c</sup>	17.5	18.2	18.29 ± 0.5
Gold	98.8 ± 0.3	97.0	98.7 ± 1.8

<sup>a</sup> There are no reported parameters for W<sup>180</sup>; however, a resonance at 15.8 eV has been assigned to this isotope. (57)

<sup>b</sup> A recent infinite dilution resonance integral measurement on W<sup>186</sup> (58) yielded a value 20% lower than that calculated from resonance parameters, which may indicate that the reported neutron width of the 18 eV level is too large.

<sup>c</sup> Calculated abundance-weighted cross section using 60 barns for W<sup>180</sup>. The agreement between the measured and calculated natural cross section of this work is fortuitous.

Table 5.5

<u>Isotope</u>	<u>Natural Abundance</u>	<u>Thermal Capture Cross Section (barns)</u>	<u>Thermal Contribution (barns)</u>	<u>% of Total</u>
180	.00126	(60.0 ± 60.0) <sup>a</sup>	0.076 ± 0.076	0.4 ± 0.4
182	.2631	20.7 ± 0.5	5.45 ± 0.13	29.8 ± 0.7
183	.1428	9.97 ± 0.3	1.42 ± 0.04	7.76 ± 0.2
184	.3064	1.71 ± 0.1	0.52 ± 0.03	2.84 ± 0.2
186	.2864	37.8 ± 1.2	10.83 ± 0.34	59.21 ± 1.9

<sup>a</sup> BNL 325 value used



The error sources involved in the cross section determination fall into three classes. These are: (1) errors which affect the normalization, (2) errors which affect the energy scale, and (3) errors which affect the shape of the curve relative to the normalization point. Some of the errors involved are not analytic in nature, and hence only subjective estimates can be given. Table 5.6 enumerates all known sources of errors and their estimated magnitude for each of the isotopes.

### 5.3.5 CONCLUSIONS

The magnitudes of the 2200 m/sec cross sections for  $W^{182}$ ,  $W^{183}$ ,  $W^{184}$ , and  $W^{186}$  have been obtained with appreciably smaller errors than have been previously reported. The capture cross section shapes reported here for the tungsten isotopes are the first in this energy region, and illustrate the utility of the technique as a check on measured low energy resonance parameters and in the determination of negative energy level effects. The agreement between the natural tungsten cross section as measured directly with that obtained from isotopic cross sections, as well as the agreement of the gold cross section with the best values available lend support to the belief that the techniques used here will be of value in obtaining accurate low energy capture cross sections for most of the isotopes of interest in reactor physics.

Table 5.6  
CLASS (1) ERRORS IN NORMALIZATION

Error Type	% Error	
	Tungsten	Gold
1-1 Parameters of flux calibration resonances (4.15 eV in W <sup>182</sup> and 4.906 eV in Au <sup>187</sup> )	<0.01	<0.01
1-2 Resolution correction to flux calibration.	0.04	<0.01
1-3 Analyzer dead time correction	<0.01	<0.01
1-4 Statistical errors in calibration interval	0.7	0.6
1-5 Background subtraction in calibration	<0.01	<0.01
1-6 Purity and deviation from formula weight	1.0	0.1
1-7 Extrapolation to zero bias	2.0 <sup>a</sup>	0
1-8 Gain shift after normalization	0.8	0.7
1-9 Gamma attenuation in sample	0-1	0
1-10 Error in flux shape exponent	0.9	1.7

## CLASS (2) ERRORS IN ENERGY SCALE

Error Type	All Isotopes
2-1 Flight path length	0.1
2-2 Frequency or analyzer clock	0.2
2-3 Analyzer start time	1.0-0.02

## CLASS (3) SHAPE ERRORS

Error Type	W <sup>182</sup>	W <sup>183</sup>	W <sup>184</sup>	W <sup>186</sup>	Au <sup>197</sup>
	3-1 Scattering cross section used in multiple scattering calculation	0.5	0.3	0.8	0.3
3-2 Assumption of no energy change in scattered neutrons, infinite slab approximation and isotropic scattering approximation in multiple scattering calculation	<0.1 <sup>b</sup>	<0.1	<0.1	<0.1	<0.01
3-5 Effect of WO <sub>3</sub> on aluminum capture	0.01	0.3	0.6	<0.01	0
3-6 Isotropic abundancies	0.5	0.5	0.5	0.5	0
3-7 Subtraction of captures due to contaminating isotopes <sup>c</sup>	0.1	0.6	3.8	0.02	0
3-8 Statistical uncertainty in points	.2-3.	.1-5.	1.-10.	.1-3.	.1-3.
3-9 Boron flux shape	1.0	1.0	1.0	1.0	1.0
3-10 Analyzer dead time correction	<0.01	<0.01	<0.01	<0.01	<0.01
3-11 Insensitivity to gamma spectrum changes	0.1	0.1	0.1	0.1	0.1
3-12 Flux-capture flight path differences	<0.7	<0.7	<0.7	<0.7	<0.7
3-13 Background subtraction <sup>d</sup>	<0.3	1, 3-5.	2, -11.	<0.2	<0.3
3-14 Error in flux shape exponent <sup>e</sup>	<0.9	<0.9	<0.9	<0.9	<0.9

a 0.0 for W<sup>182</sup>

b These limits might be exceeded in the 5 to 7.5 eV region in W<sup>182</sup> and the 9 to 1.0 region in W<sup>183</sup> due to the large energy loss in oxygen scattering which might scatter neutrons into the low energy resonances in these isotopes.

c These errors are exceeded near the low energy resonances

d Errors due to backgrounds are largest near 1 and 10 eV, and are very much smaller at other energies

e 1 to 10 eV only

## VI. ANALYTICAL RESULTS AND COMPARISON WITH EXPERIMENT

### 6.1 CRITICALITY

#### 6.1.1 VARIATION OF THE MULTIPLICATION FACTOR WITH LATTICE PITCH

The relationship between the fuel element spacing and the multiplication factor of the assembly has been calculated for the 121-fuel element core reflected both by water and by beryllium side and bottom reflectors. The cadmium poison was omitted from these calculations. The reflector configuration for the beryllium-reflected core calculations consisted of the following - a side reflector represented as 1.7 cm of aluminum, 7.3 cm of beryllium, and 5 cm of water; a bottom reflector represented as 3.0 cm of aluminum on top of 10.0 cm of beryllium; and a top reflector represented as 25.0 cm of water.

In these calculations, the conventional resonance treatment using GAM-II was used, the cell disadvantage factors were obtained by the one-dimensional treatment, and the one-dimensional buckling iteration sequence was employed in obtaining  $k_{\text{eff}}$ . Both the fine structure calculation and the over-all diffusion calculations utilized a ten-group energy structure shown in Table 6.1.

The results, for both the water- and beryllium-reflected cores at seven values of the lattice pitch are shown in Table 6.2 and plotted in Fig. 6.1.

Table 6.1  
TEN-GROUP STRUCTURE FOR EIGENVALUE  
CALCULATIONS

<u>Group</u>	<u>Energy Range</u>
1	2.73 to 14.9 MeV
2.	0.498 to 2.73 MeV
3	0.0674 to 0.498 MeV
4	0.0614 to 67.4 keV
5	2.38 to 61.4 eV
6	0.414 to 2.38 eV
7	0.09 to 0.414 eV
8	0.05 to 0.09 eV
9	0.03 to 0.05 eV
10	0.0 to 0.03 eV

Table 6.2  
VARIATION OF EIGENVALUE WITH  
FUEL ELEMENT PITCH (121-ELEMENT CORE)

<u>Pitch (in.)</u>	<u>Equivalent Cell Radius (cm)</u>	<u>H/U<sup>235</sup></u>	<u>k<sub>∞</sub></u>	<u>k<sub>eff</sub> (Be Side and Bottom Reflector)</u>	<u>k<sub>eff</sub> (Water Reflector)</u>
2.800	3.734	34.65	1.325	1.055	0.960
2.916	3.889	47.67	1.367	1.126	1.045
3.000	4.001	57.42	1.385	1.161	1.090
3.156	4.209	76.25	1.396	1.202	1.144
3.290	4.387	93.13	1.389	1.214	1.166
3.450	4.601	114.4	1.359	1.210	1.171
3.637	4.850	140.3	1.313	1.179	1.148

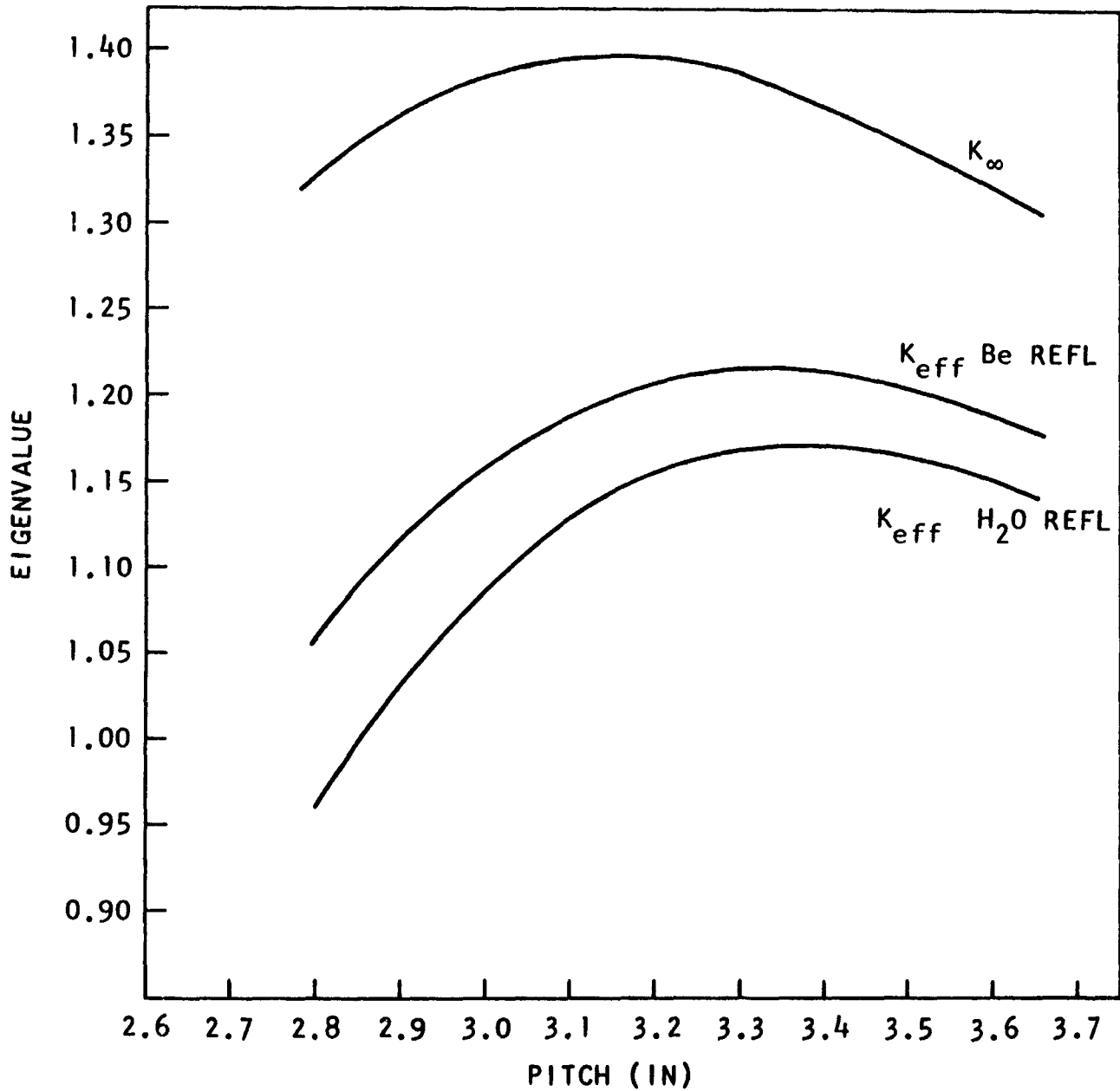


Fig. 6. 1--Variation of eigenvalue with fuel element pitch

### 6.1.2 CRITICALITY RESULTS FOR THE 3.0-in. PITCH, WATER-REFLECTED CORE

The initial calculation of the 3.0-in. pitch water-reflected core, referred to as the "precritical" calculation, utilized methods previously described. In particular, cell and cadmium disadvantage factors were obtained by one-dimensional analyses, the conventional GAM-II resonance treatment was employed, and the one-dimensional buckling iteration sequence was utilized to obtain the effective multiplication factor. The ten-group energy structure, given in Table 6.1, was again used. The homogenized atom densities in the core and reflector are given in Table 6.3. Cadmium was omitted in the radial description beyond 40.8 cm, to account for the lack of a full poison complement for the outer ring of fuel elements.

The result of the calculation, the cadmium concentration in the poison tubes for a critical 121-element core, was 0.0953 moles of cadmium nitrate per liter. The initial loading of the core containing this cadmium concentration reached criticality at 112 fuel elements. Using the measured worth of a fuel element in the outer ring, the estimated multiplication factor for the entire 121-element core at this cadmium concentration was 1.021. Thus the precritical estimate of reactivity was low by 2.1%  $\Delta k/k$ .

A recalculation of the critical 121-element core, which contained the as-loaded 0.1225 moles per liter of cadmium nitrate, was performed. This "refined" calculation incorporated the following features. The cell and cadmium disadvantage factors were obtained by two-dimensional analyses and the resonance treatment included the effect of the interstitial material, resonance interference,  $U^{235}$  resonance self-shielding, and the two-region cell. The effective multiplication factor was computed with two-dimensional diffusion theory as well as a one-dimensional buckling iteration. A drawing of the geometrical configuration used in the two-dimensional calculation is shown in Fig. 6.2. The results of the calculations are shown in Table 6.4. The significant discrepancy between theory

Table 6.3  
HOMOGENIZED ATOM DENSITIES FOR THE  
3.0-IN. PITCH CORE

<u>Nuclide</u>	<u>Atom Density (atoms/b-cm)</u>	
	<u>Core (0 to 44.01 cm)</u>	
H	2.172 x 10 <sup>-2</sup>	
O	1.085 x 10 <sup>-2</sup>	
Al	1.845 x 10 <sup>-2</sup>	
Ni	4.4 x 10 <sup>-5</sup>	
Zr	9.83 x 10 <sup>-5</sup>	
Cd <sup>113</sup> (0 to 40.8 cm)	3.545 x 10 <sup>-7</sup>	
Cd <sup>113</sup> (40.8 to 44.01 cm)	0.0	
W <sup>182</sup>	2.519 x 10 <sup>-4</sup>	
W <sup>183</sup>	1.374 x 10 <sup>-4</sup>	
W <sup>184</sup>	2.920 x 10 <sup>-4</sup>	
W <sup>186</sup>	2.710 x 10 <sup>-4</sup>	
U <sup>235</sup>	3.735 x 10 <sup>-4</sup>	
U <sup>238</sup>	1.521 x 10 <sup>-3</sup>	
<u>Side Reflector (44.01 to 59.01 cm)</u>		
H	6.677 x 10 <sup>-2</sup>	
O	3.339 x 10 <sup>-2</sup>	
<u>Top and Bottom Reflectors (25 cm)</u>		
H	2.172 x 10 <sup>-2</sup>	
O	1.085 x 10 <sup>-2</sup>	
Al	8.49 x 10 <sup>-3</sup>	

and experiment, suggested by the precritical calculations, was eliminated. Neutron balances from the precritical and "refined" one-dimensional calculations of the 3.0-in. pitch, water-reflected core are compared in Table 6.5.

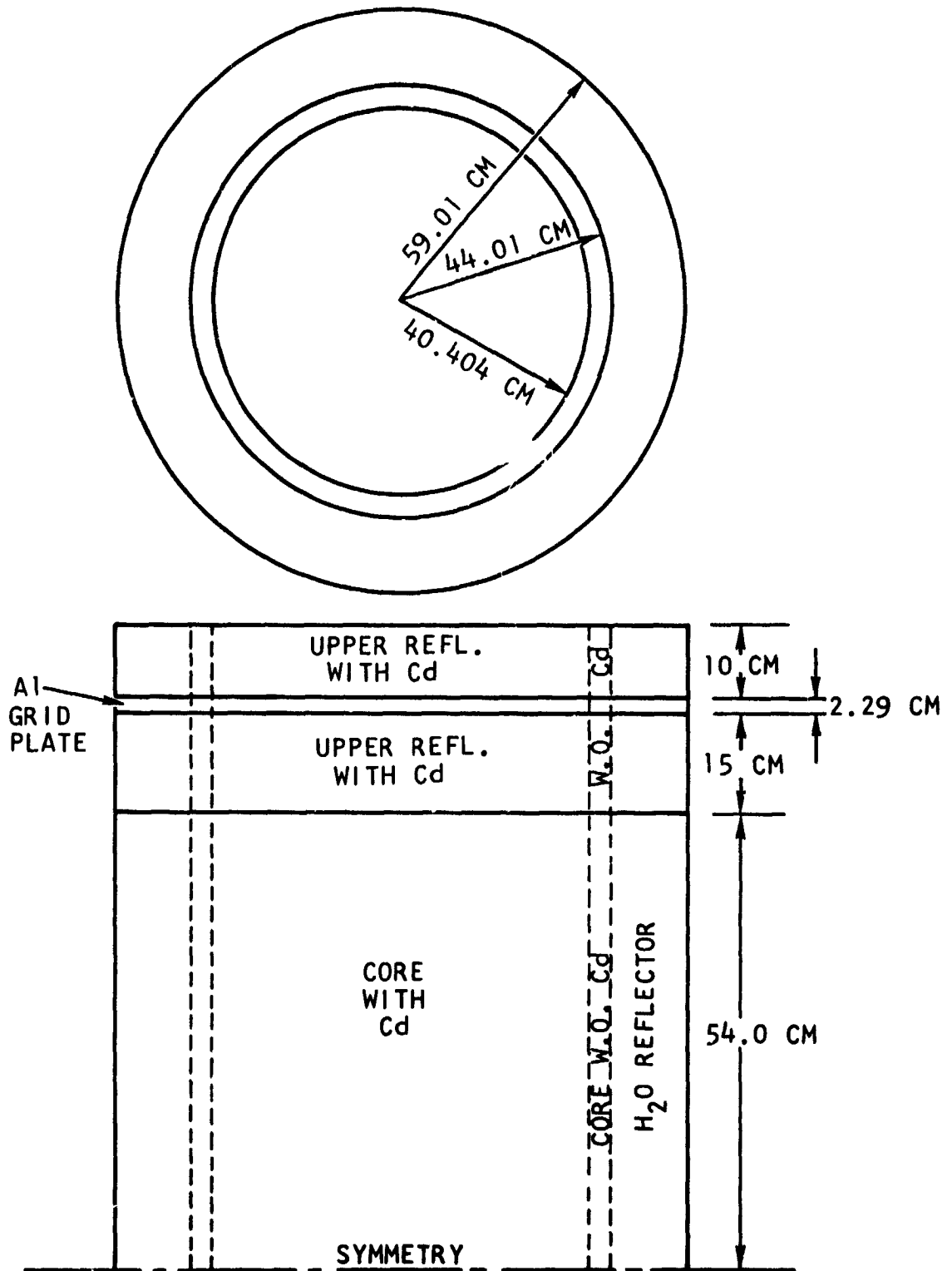


Fig. 6.2--Two-dimensional core configuration



Table 6.4

RESULTS OF THE REFINED CALCULATION  
OF THE 3.0-IN. PITCH, WATER-REFLECTED CORE

	$k_{\text{eff}}$		<u>% Dev.</u>
	<u>Calculated</u>	<u>Measured</u>	
One-Dimensional Buckling Iteration	0.9989	1.0007 <sup>1</sup>	- 0.18%
Two-Dimensional Calculation	1.0056 ± .0010 <sup>3</sup>	1.0011 <sup>2</sup>	± 0.45 ± 0.10%

1. The experimental value of 1.0000 has been corrected for the existence of the stainless steel guides and source tube to bring the experimental configuration in line with the calculated configuration.
2. Same as above, but in addition the experimental configuration has been adjusted to include 10 cm additional top reflector contained in the calculation.
3. Extrapolated from  $k_{\text{eff}} = 1.0036$ .

Table 6.5

NEUTRON BALANCES FOR 3.0-IN. PITCH, WATER-REFLECTED  
CORE FROM ONE-DIMENSIONAL RADIAL DIFFUSION CALCULATION

Nuclide	Precritical Calculation		Refined Calculation	
	<u>Absorptions/Source Neutron</u>			
	Epithermal (2.38 eV to 14.9 MeV)	Thermal (0 to 2.38 eV)	Epithermal (2.38 eV to 14.9 MeV)	Thermal (0 to 2.38 eV)
H	0.0015	0.0342	0.0017	0.0325
Ø	0.0013	0.0000	0.0013	0.0000
Al	0.0031	0.0088	0.0030	0.0086
Ni	0.0001	0.0006	0.0001	0.0006
Zr	0.0002	0.0001	0.0001	0.0001
Cd	0.0000	0.0504	0.0000	0.0600
W <sup>182</sup>	0.0197	0.0090	0.0213	0.0095
W <sup>183</sup>	0.0210	0.0022	0.0222	0.0024
W <sup>184</sup>	0.0025	0.0010	0.0027	0.0010
W <sup>186</sup>	0.0201	0.0204	0.0191	0.0214
U <sup>235</sup> (captures)	0.0564	0.0563	0.0397	0.0599
U <sup>235</sup> (fissions)	0.0926	0.3106	0.0736	0.3291
U <sup>238</sup> (captures)	0.0397	0.0115	0.0398	0.0116
U <sup>238</sup> (fissions)	0.0065	0.0000	0.0066	0.0000
		<u>Leakage/Source Neutron</u>		
Radial		0.1671		0.1676
Axial		0.0507		0.0509
Total		0.2178		0.2185

### 6.1.3 CRITICALITY RESULTS FOR THE 2.9-IN. PITCH WATER-REFLECTED CORE

The 2.9-in. pitch core was analyzed as outlined at the beginning of Section 6.1.2. The homogenized atom densities in the core and reflector are given in Table 6.6. One refinement was incorporated into the calculation, i. e., the inclusion of interstitial material in the resonance treatment. Drawing upon the initial experience with the 3.0-in. pitch core, the effective multiplication factor was normalized to 0.98 in the calculation of the critical cadmium concentration.

The calculated critical cadmium loading for a 121-element core was 0.0474 moles of cadmium nitrate per liter. The actual as-loaded cadmium concentration was 0.0431 moles/liter of cadmium nitrate. This cadmium concentration led to a computed multiplication factor of 0.986. The core was critical after 119 fuel elements were loaded. Using the measured worth of an outer ring fuel element, and the associated cadmium poison tubes, the estimated multiplication factor for the entire 121-element core was 1.008. Thus the predicted estimate of reactivity was low by about 2.2%. A neutron balance for the 2.9-in. pitch core is given in Table 6.7.

An unpoisoned 2.9-in. pitch core was also assembled. A symmetric loading of 85 fuel elements with no poison tubes was found to have a multiplication of 1.0056. The calculated multiplication factor of this assembly was 0.9899. The predicted estimate of reactivity for an unpoisoned 2.9-in. pitch core was thus low by 1.57%.

Refined calculations were not performed for the 2.9-in. pitch core. As discussed in Section 8.1, it is expected that a calculation similar to the refined calculation of the 3.0-in. pitch water-reflected core would diminish the discrepancy between analysis and experiment.

Table 6.6  
 HOMOGENIZED ATOM DENSITIES FOR THE  
 2.9-IN. PITCH, WATER REFLECTED CORE

<u>Nuclide</u>	<u>Atom Density (atoms/b-cm)</u>
<u>Core (height = 108. cm, radius = 42.54 cm)</u>	
H	$1.856 \times 10^{-2}$
O	$0.928 \times 10^{-2}$
Al	$1.974 \times 10^{-2}$
Ni	$4.708 \times 10^{-5}$
Zr	$1.052 \times 10^{-4}$
Cd <sup>113</sup> (0 to 39.43 cm radius)	$1.885 \times 10^{-7}$
Cd <sup>113</sup> (39.43 to 42.54 cm radius)	0.0
W <sup>182</sup>	$2.695 \times 10^{-4}$
W <sup>183</sup>	$1.470 \times 10^{-4}$
W <sup>184</sup>	$3.124 \times 10^{-4}$
W <sup>186</sup>	$2.899 \times 10^{-4}$
U <sup>235</sup>	$3.996 \times 10^{-4}$
U <sup>238</sup>	$1.627 \times 10^{-3}$
<u>Side Reflector (42.54 to 57.54 cm radius)</u>	
H	$6.677 \times 10^{-2}$
O	$3.339 \times 10^{-2}$
<u>Top and Bottom Reflectors (25. cm thick)</u>	
H	$1.856 \times 10^{-2}$
O	$0.928 \times 10^{-3}$
Al	$0.908 \times 10^{-3}$
Cd <sup>113</sup>	$1.885 \times 10^{-7}$

Table 6.7  
 NEUTRON BALANCE FOR THE 2.9-IN. PITCH, WATER-  
 REFLECTED CORE FROM RADIAL DIFFUSION CALCULATION

<u>Nuclide</u>	<u>Absorptions/Source Neutron</u>	
	<u>Epithermal</u> <u>(2.38 eV to 14.9 eV)</u>	<u>Thermal</u> <u>(0 to 2.38 eV)</u>
H	0.0013	0.0024
Ø	0.0012	0.0000
Al	0.0034	0.0083
Ni	0.0001	0.0005
Zr	0.0002	0.0000
Cd	0.0000	0.0220
W <sup>182</sup>	0.0213	0.0086
W <sup>183</sup>	0.0240	0.0021
W <sup>184</sup>	0.0029	0.0009
W <sup>186</sup>	0.0213	0.0194
U <sup>235</sup> (captures)	0.0617	0.0536
U <sup>235</sup> (fissions)	0.1023	0.2944
U <sup>238</sup> (captures)	0.4601	0.0109
U <sup>238</sup> (fissions)	0.0072	0.0000

Leakage/Source Neutron

Radial	0.1909
Axial	0.0568
Total	0.2477

#### 6.1.4 CRITICALITY RESULTS FOR THE 3.0-IN. PITCH, BERYLLIUM-REFLECTED CORE

The calculations for the 3.0-in. pitch, beryllium-reflected core were also performed by the method outlined at the beginning of Section 6.1.2. The homogenized atom densities in the core and reflectors are given in Table 6.8. Two refinements were incorporated into the calculation, the inclusion of the interstitial material in the resonance treatment and the utilization of two-dimensional calculations for the cadmium disadvantage factors. The beryllium-boron boundary was treated in the one-dimensional diffusion calculations by the method discussed in Section 4.5. A crystal kernel was used for beryllium, although the results were nearly identical when a free gas kernel was used. The effective multiplication factor was normalized to a value of 0.98, as was done in the case of the 2.9-in. pitch core.

The calculated critical cadmium loading for a 121-element core was 0.232 moles of cadmium nitrate per liter. The actual as-loaded cadmium concentration was 0.220 moles/liter of cadmium nitrate. This cadmium concentration led to a computed multiplication factor of 0.9865. The core was critical with 121 fuel elements loaded, with an estimated multiplication factor of 1.0024. Thus the predicted estimate of reactivity was low by 1.6%. A neutron balance for the beryllium-reflected core is given in Table 6.9.

Refined calculations were not performed for the beryllium-reflected core. As discussed in Section 8.1, it is expected that a calculation similar to the refined calculation of the 3.0-in. pitch, water-reflected core would diminish the discrepancy between analysis and experiment.

#### 6.1.5 SUMMARY OF CRITICALITY RESULTS

Table 6.10 gives a summary of the criticality results reported in this section.

Table 6.8  
 HOMOGENIZED ATOM DENSITIES FOR THE 3.0-IN.  
 PITCH BE-REFLECTED CORE

<u>Nuclide</u>	<u>Radial Description</u>	<u>Atom Density</u>
	<u>Core (0 to 44.01 cm)</u>	
H		$2.172 \times 10^{-2}$
O		$1.085 \times 10^{-2}$
Al		$1.845 \times 10^{-2}$
N <sub>i</sub>		$4.4 \times 10^{-5}$
Zr		$9.83 \times 10^{-5}$
Cd <sup>113</sup>	(0 to 40.41 cm)	$8.627 \times 10^{-7}$
Cd <sup>113</sup>	(40.41 to 44.01 cm)	0.0
W <sup>182</sup>		$2.519 \times 10^{-4}$
W <sup>183</sup>		$1.374 \times 10^{-4}$
W <sup>184</sup>		$2.920 \times 10^{-4}$
W <sup>186</sup>		$2.710 \times 10^{-4}$
U <sup>235</sup>		$3.735 \times 10^{-4}$
U <sup>238</sup>		$1.521 \times 10^{-3}$
	<u>Side Reflector (44.01 to 53.77 cm)</u>	
Al	(44.01 to 45.51 cm)	$6.02 \times 10^{-2}$
Be	(45.51 to 52.79 cm)	$1.228 \times 10^{-1}$
H	(52.79 to 53.77 cm)	$7.98 \times 10^{-2}$
C	(52.79 to 53.77 cm)	$3.99 \times 10^{-2}$
	<u>Axial Description</u>	
	<u>Bottom Reflector (0 to 23.5 cm)</u>	
H	(0 to 10 cm)	$6.677 \times 10^{-2}$
O	(0 to 10 cm)	$3.339 \times 10^{-2}$
Be	(10 to 20 cm)	$1.228 \times 10^{-1}$
Al	(20 to 23.5 cm)	$6.02 \times 10^{-2}$
	<u>Top Reflector (131.5 to 136.5 cm)</u>	
H		Same as core
O		Same as core
Al		$4.740 \times 10^{-3}$
Cd		Same as core

Table 6.9

NEUTRON BALANCE FOR THE 3.0-IN. PITCH, BE-REFLECTED  
CORE FROM RADIAL DIFFUSION CALCULATION

<u>Nuclide</u>	<u>Absorptions/Source Neutrons</u>	
	<u>Epithermal (2.38 eV to 14.9 eV)</u>	<u>Thermal (0 to 2.38 eV)</u>
H	0.0018	0.0310
Ø	0.0014	0.0000
Al	0.0033	0.0082
Ni	0.0001	0.0005
Zr	0.0002	0.0000
Cd	0.0000	0.0914
W <sup>182</sup>	0.0231	0.0087
W <sup>183</sup>	0.0248	0.0021
W <sup>184</sup>	0.0030	0.0009
W <sup>186</sup>	0.0230	0.0194
U <sup>235</sup> (captures)	0.0642	0.0529
U <sup>235</sup> (fissions)	0.1046	0.2900
U <sup>238</sup> (captures)	0.0483	0.0107
U <sup>238</sup> (fissions)	0.0069	0.0000
	<u>Leakages/Source Neutron</u>	
Radial	0.1246	
Axial	0.0495	
Total	0.1741	



Table 6.10

## SUMMARY OF CRITICALITY RESULTS

<u>Core</u>	<u>Calculation</u>	<u>Cadmium Loading (moles/liter)</u>	<u>Predicted <math>k_{eff}</math></u>	<u>Measured <math>k_{eff}</math></u>	<u><math>\delta k_{eff}</math></u>
3.0-in. Pitch, Water-Reflected	Precritical	0.0953	1.000	1.021	- 2.1%
	"Refined" - 1 Dimensional	0.1225	0.999	1.001	- 0.2%
	"Refined" - 2 Dimensional	0.1225	1.0056 $\pm$ .001	1.001	+0.45 $\pm$ .10%
2.9-in. Pitch, Water-Reflected	Precritical (including Interstitial Material in resonance calculation)	0.0431	0.986	1.008	- 2.2%
2.9-in. Pitch, Water-Reflected, Unpoisoned	Precritical (including Interstitial Material in resonance calculation)	0.0000	0.990	1.006	- 1.6%
3.0-in. Pitch, Beryllium-Reflected	Precritical (including Interstitial Material and 2-D Cadmium Disadvantage Factors)	0.2202	0.986	1.002	- 1.6%

## 6.2 REACTIVITY

### 6.2.1 PROMPT NEUTRON LIFETIME

A value of the prompt neutron lifetime was calculated for each of the critical assemblies constructed. The calculations were carried out by inserting a uniformly distributed  $1/v$  absorber in a ten-group GAZE calculation. The lifetime was then found from the relationship:

$$l = \frac{\Delta k}{\alpha}, \quad (6.1)$$

where  $\Delta k$  is the change in eigenvalue caused by the  $1/v$  absorber, and the asymptotic decay constant,  $\alpha$ , is equivalent to the atom density of the  $1/v$  absorber.

The values found by this analysis are compared to the experimentally measured values in Table 6.11.

Table 6.11

#### COMPARISON OF MEASURED AND CALCULATED VALUES OF THE PROMPT NEUTRON LIFETIME

<u>Pitch</u> <u>(in.)</u>	<u>Reflector</u>	<u>Fuel</u>	<u>Poison</u>	<u>Measured</u> <u>Lifetime</u> <u>(<math>\mu</math>sec)</u>	<u>Calculated</u> <u>Lifetime</u> <u>(<math>\mu</math>sec)</u>
2.9	Water	85	none	28.9	28.8
2.9	Water	119	195 "H" 5 "D"	29.9	25.0
3.0	Water	121	206 "C"	28.9	25.0
3.0	Beryllium	120	194 "K"	31.6	26.6

The results are discussed in Section 8.2.

### 6.2.2 EFFECTIVE DELAYED NEUTRON FRACTION

The effective delayed neutron fraction was calculated for each of the three critical assemblies using the method suggested by Henry, which is described in detail in Section 4.13. In summary, the initial criticality problem (with the normal fission spectrum) was solved in the GAZE diffusion code using a buckling iteration scheme to account for transverse leakage. The contribution of delayed neutrons to the fission spectrum was then doubled and the problem again solved. The value of  $\beta_{\text{eff}}$  was calculated from the equation

$$\beta_{\text{eff}} = \frac{k' - k}{k^2} \quad (6.2)$$

where  $k'$  is the eigenvalue of the perturbed problem and  $k$  is the eigenvalue of the initial problem. The results for each core are listed in Table 6.12.

Table 6.12  
CALCULATED VALUES FOR THE EFFECTIVE  
DELAYED NEUTRON FRACTION

<u>Core</u>	<u><math>\beta_{\text{eff}}</math></u>
2.9-in. pitch, water-reflected	0.00724
3.0-in. pitch, water-reflected	0.00712
3.0-in. pitch, beryllium-reflected	0.00702

The values of  $\beta_{\text{eff}}$  tend toward the infinite medium value of 0.0065 as leakage decreases. This trend may be seen in the data of Table 6.12.

## 6.2.3 REACTIVITY AND THE ASYMPTOTIC PERIOD

The relationship between the asymptotic period and the reactivity of the mockup core was determined for each assembly from the inhour equation,

$$\rho = \frac{1}{\beta_{\text{eff}}} \left[ \frac{l\omega}{l\omega + 1} + \frac{1}{l\omega + 1} \sum_i \frac{\beta_i \omega}{\omega + \lambda_i} \right], \quad (6.3)$$

where  $\rho$  is the reactivity in dollars,  $\omega$  is the inverse period,  $l$  is the prompt neutron lifetime, and  $\beta_i$  and  $\lambda_i$  are the delayed neutron fraction and decay constant of the  $i$ 'th delayed neutron group.

The delayed neutron fractions and decay constants used for  $\text{U}^{235}$  are shown in Table 6.13 for the 3.0-in. pitch, water-reflected core. The effective delayed neutron fraction for each group was obtained from  $\beta_{\text{eff}}$  using the abundances quoted by Keepin, et al. (59). The solution of the inhour equation using the above data is shown in Fig. 6.3 for the same core. This relationship is typical and changed only slightly from one configuration to another.

Table 6.13  
EFFECTIVE DELAYED NEUTRON FRACTIONS AND DECAY  
CONSTANTS FOR  $\text{U}^{235}$  IN 3.0-IN. PITCH CORE

Delayed Neutron Group	$t_{1/2}$ (sec)	Decay Constant ( $\text{sec}^{-1}$ )	Effective Delayed Neutron Fraction
1	55.7	0.0124	0.000235
2	22.7	0.0305	0.001559
3	6.22	0.111	0.001396
4	2.30	0.301	0.002812
5	0.613	1.13	0.000819
6	0.231	3.00	<u>0.000299</u>
			0.00712

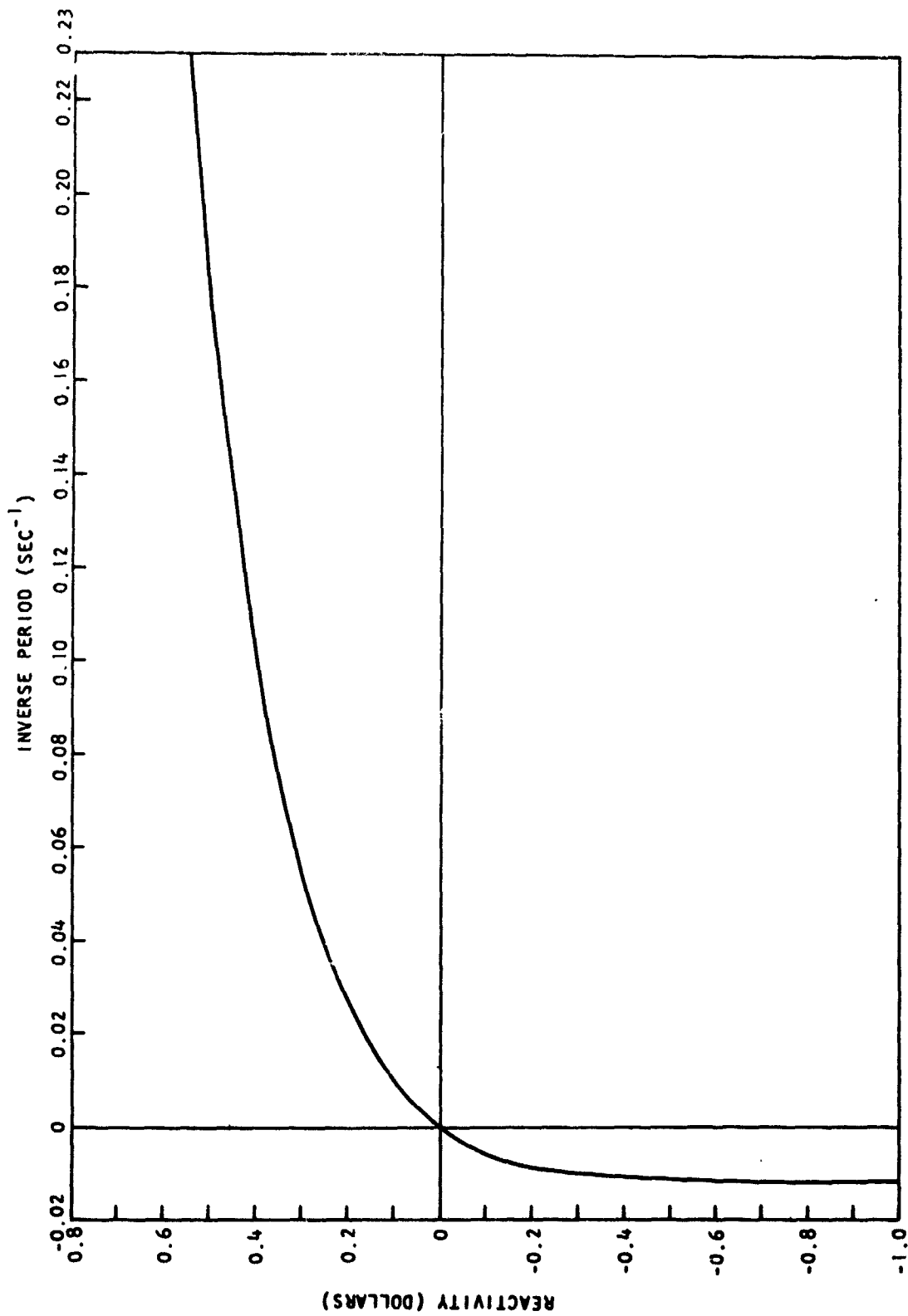


Fig. 6.3--Solution of the inhour equation for the  
3.0-in. pitch, water-reflected core

#### 6.2.4 CONTROL ROD WORTHS

The reactivity worths of the safety and regulating rods were calculated in the 3.0-in. pitch, water-reflected core. The calculations made use of a "black" boundary condition for the rod surface; a two-dimensional calculation of one quarter of the core was performed using the GAMBLE code in X-Y geometry.

The core and control rod representation used in the calculation is shown in Fig. 6.4. Region 1 of Fig. 6.4 represents the region in which cadmium tubes are present. Region 2 does not contain cadmium in order to account for the lack of poison tubes at the outside of the outer row of fuel elements. Region 4 was represented as a nondiffusion region in the calculations. (The use of jagged internal boundaries to represent curved internal boundaries introduces little error in this type of a problem.)

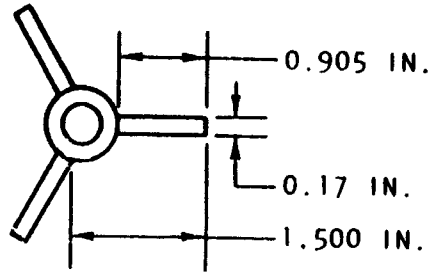
The safety and regulating rods were represented as "black" boundaries. At the rod surface the following boundary condition was used

$$\frac{D_i \text{ grad } \varphi_i}{\varphi_i} = \frac{-1}{2.1312}, \quad (6.4)$$

where  $\text{grad } \varphi_i$  is taken normal to the rod surface.

The five-group structure shown in Table 6.14 was chosen. Axial leakage was taken into account by using transverse bucklings derived from an axial GAZE calculation. The control rods were represented as black nondiffusion regions below 0.414 eV and by diffusion regions containing only cadmium above 0.414 eV.

The results are given in Table 6.15 for the cases of no rods, two regulating rods, and all eight rods. Case 4 is included to demonstrate the effect of rod absorptions above 0.414 eV. Case 5 gives the worth of the six safety rods, obtained by subtraction from Cases 2 and 3. Figures 6.5 and 6.6 are Group 5 flux plots along the X and Y axes, respectively, for



MEASURED ROD DIMENSIONS (IN.)

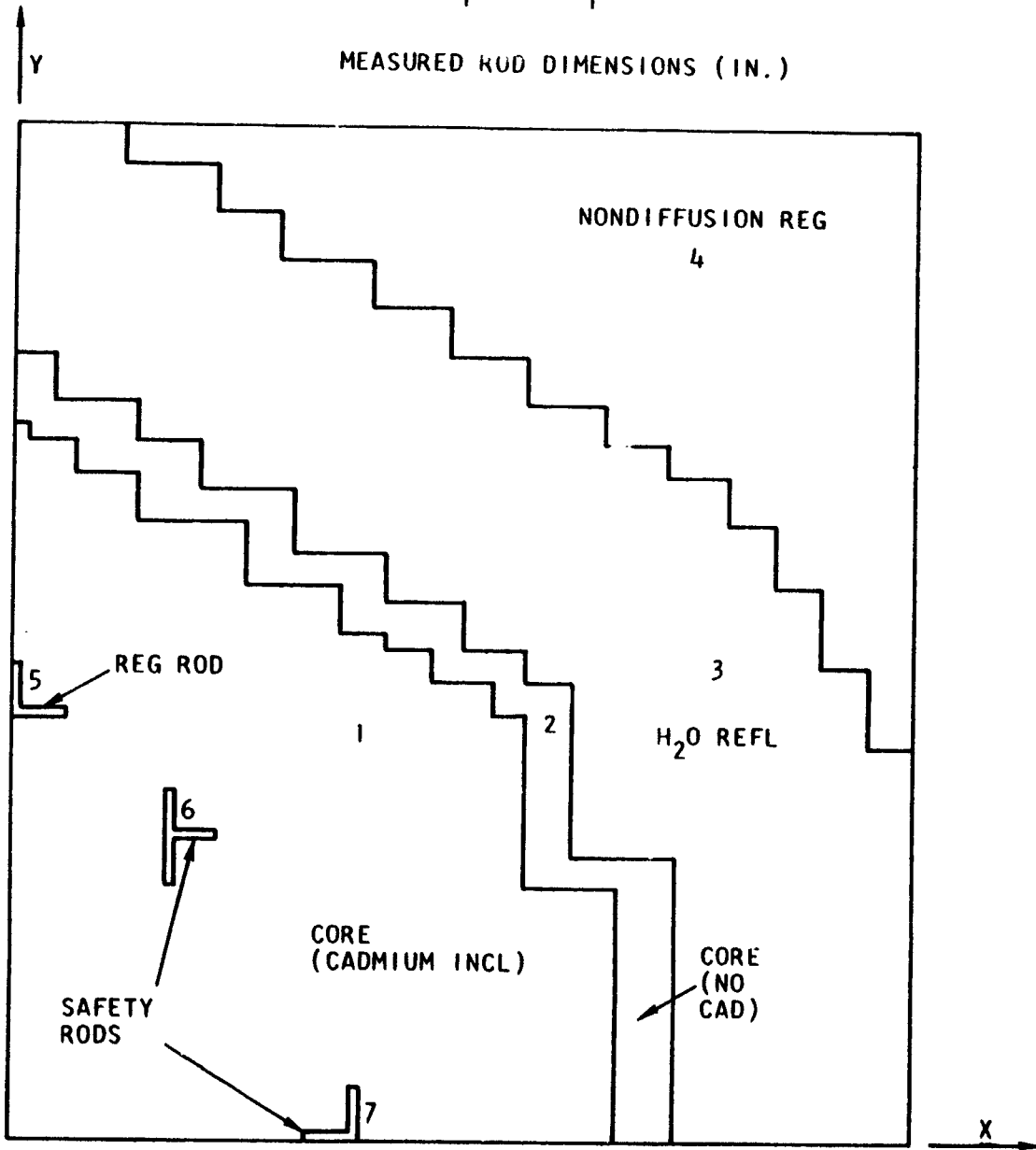


Fig. 6.4--XY GAMBLE Representation

Table 6.14  
 FIVE-GROUP STRUCTURE FOR CONTROL  
 ROD CALCULATIONS

<u>Group</u>	<u>Energy Range</u>
1	14.9 MeV to 67.4 keV
2	67.4 keV to 0.414 eV
3	0.414 eV to 0.09 eV
4	0.09 eV to 0.05 eV
5	0.05 eV to 0.0 eV

Table 6.15  
 ROD WORTH RESULTS

<u>Case No.</u>	<u>No. of Rods</u>	<u><math>k_{eff}^a</math></u>	<u><math>\Delta k_{eff}</math> Relative to Unrodded</u>	<u><math>\Delta\rho</math></u>	<u>Dollars/Rod (<math>\beta_{eff} = 0.00712</math>)</u>	<u>Comment</u>
1	0	0.998155	----	----	--	
2	2	0.991025	0.007130	0.007208	\$0.506	
3	8	0.964948	0.035207	0.036480	0.640	
4	2	0.993264	0.004891	0.004933	0.346	No rod absorption above 0.414 eV
5	6	----	----	0.029272	0.685	Calculated from Cases 2 and 3

<sup>a</sup>Extrapolated from GAMBLE



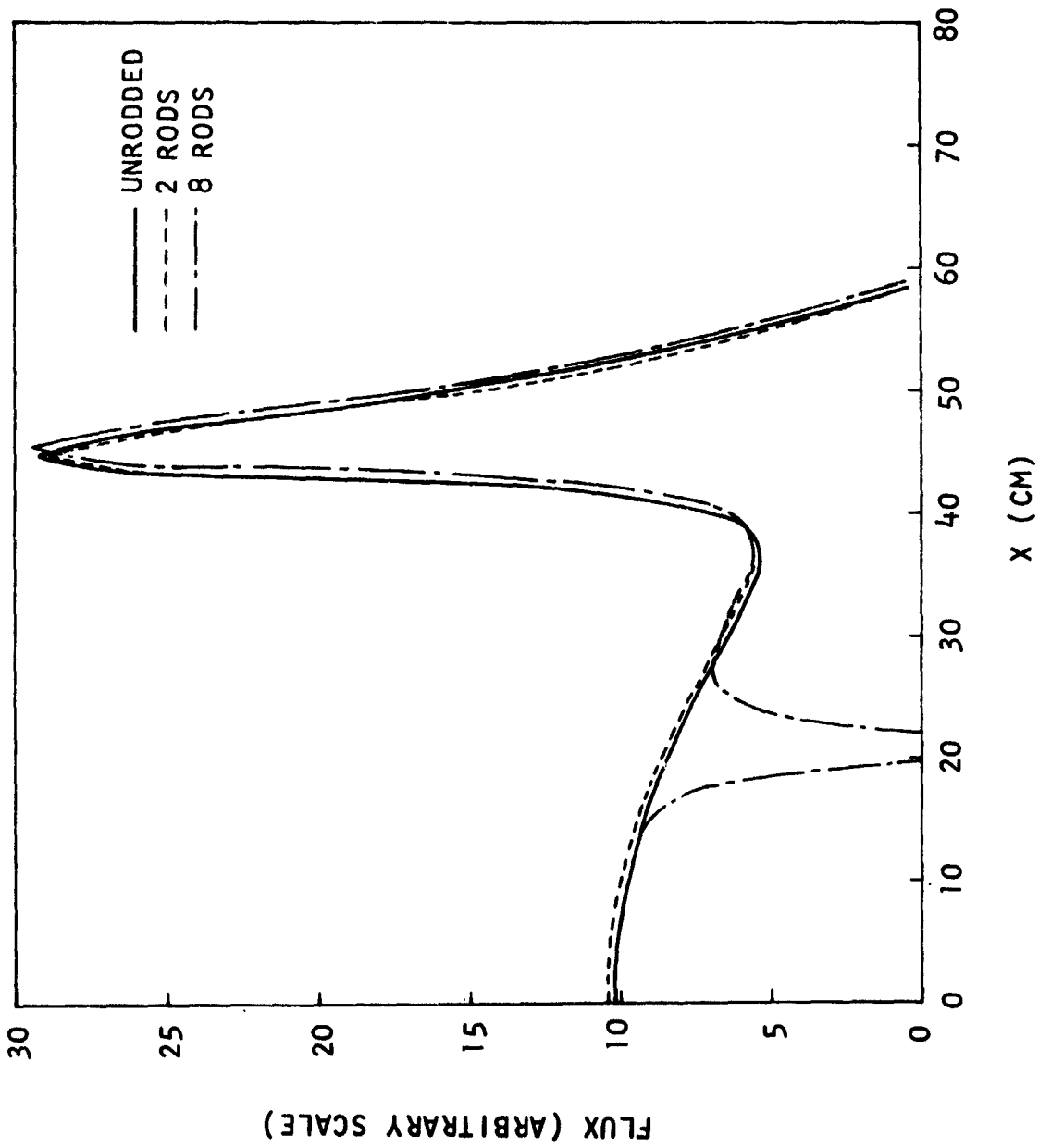


Fig. 6.5--Group 5 flux along X axis

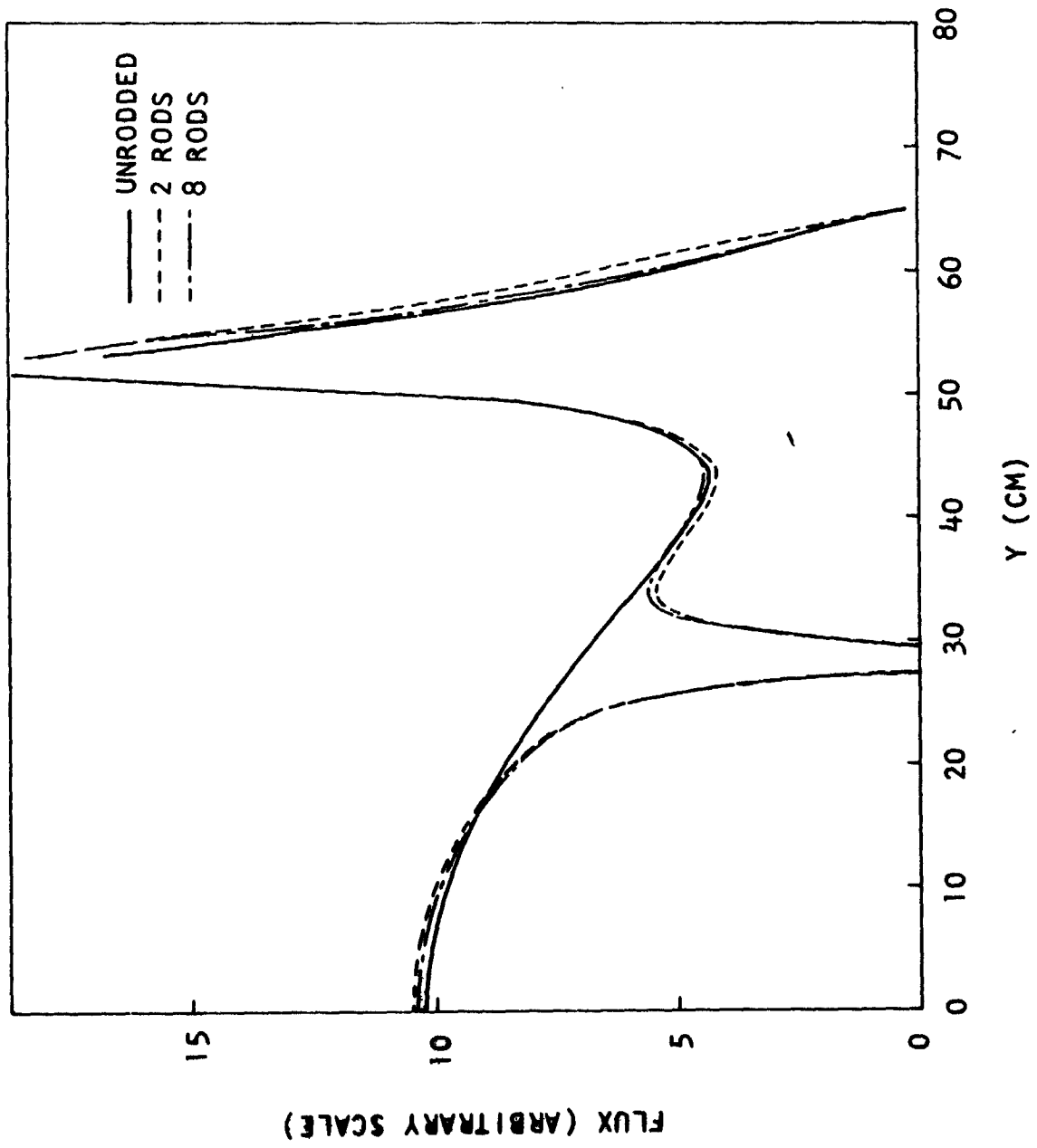


Fig. 6.6--Group 5 flux along Y axis

the three calculated configurations. The flux distributions suggest that interaction between rods is insignificant, thus lending credence to the subtraction scheme for obtaining the worth of the six safety rods.

The significant fraction of captures in the rods at energies greater than 0.414 eV prompted an investigation of the five-group structure used in the calculations. Since the contribution to the cadmium absorption cross sections in Group 2 is primarily from the small energy band between 0.414 and 2.38 eV, it was suspected that the effect of averaging the cross section over the large energy band from 0.414 eV to 67.4 keV might introduce a significant error into the calculations. Furthermore, the GAM spectrum in the important energy band of 0.414 to 2.38 eV is significantly different from the thermal spectrum in the same band computed by the GATHER code. In order to investigate these effects, identical GAMBLE calculations were performed, one with the five-group structure and the other with a ten-group structure incorporating GATHER cross sections up to 2.38 eV. No significant difference in rod absorptions above 0.414 eV was observed between the two calculations.

As shown in Table 6.15, single rod values of \$0.506 and \$0.685 were predicted for the regulating and safety rods respectively. They are in close agreement with the measured values for this core of \$0.525 and \$0.644.

#### 6.2.5 CALCULATION OF THE EXCESS REACTIVITY

The experimental mapping technique described in Section 3.2.3 was investigated analytically. The purpose of the analysis was to compare the calculated reactivity of a core with no cadmium to that predicted for the same core by summing the removal worth of small bands of cadmium. The 3.0-in. pitch, water-reflected core was represented in a series of GAZE radial calculations. This core had an equivalent radius of 44.01 cm; however, since 208 poison tubes were assumed to be loaded, the

cadmium was homogenized within a radius of 40.8 cm. A homogenized unshielded  $\text{Cd}^{113}$  atom density of  $6.8 \times 10^{-7}$  atom/b cm was used in the core to reduce  $k_{\text{eff}}$  to 1.0016, and the calculations were done in the ten-group energy structure of Table 6.1.

The worth of a one-cm thick annulus of homogenized cadmium was determined at 11 different radial positions by eigenvalue calculations. The calculated worths are plotted in Fig. 6.7. The function plotted in Fig. 6.7 is the worth of homogenized  $\text{Cd}^{113}$  for a core volume of  $\pi(r_2^2 - r_1^2)H$  where  $H$  is the core height and  $(r_2 - r_1) = 1.0$  cm. The area under this curve, which is the total worth of all the  $\text{Cd}^{113}$ , has a value of  $0.09172 \Delta k/k$ . This compares well with the total cadmium worth of 0.09012 obtained from the eigenvalues of the unpoisoned and poisoned cores. (Due to the preliminary nature of these calculations, the cadmium density is different than that reported in Section 3.)

The analysis showed that this experimental method of estimating the total cadmium poison worth was valid. Since the experiment was done by removing only one rod at a time at various radii, the experimental results resemble the curve shown in Fig. 6.8. This was obtained from the previous figure by dividing the calculated values by  $\pi(r_2^2 - r_1^2)$ , and thus represents the removal worth of a square cm of homogenized cadmium from a homogenized core.

The eigenvalue of each of the three poisoned cores was calculated with no cadmium. The methods were identical to those presented in Section 6.1 for precritical calculations. The calculated results are shown in Table 6.16.

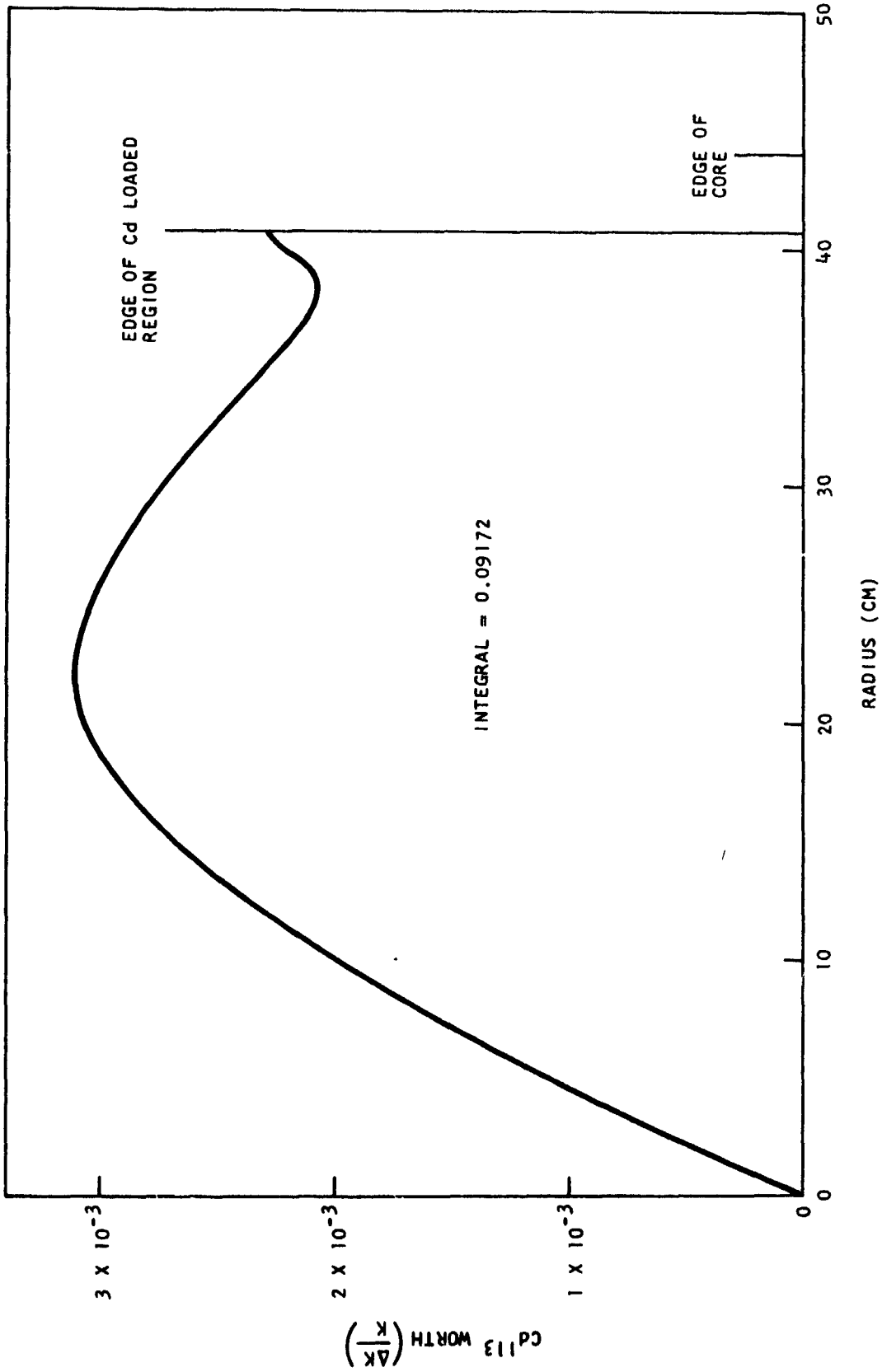


Fig. 6.7--Removal worth of 1 cm thick annulus of homogenized Cd<sup>113</sup>

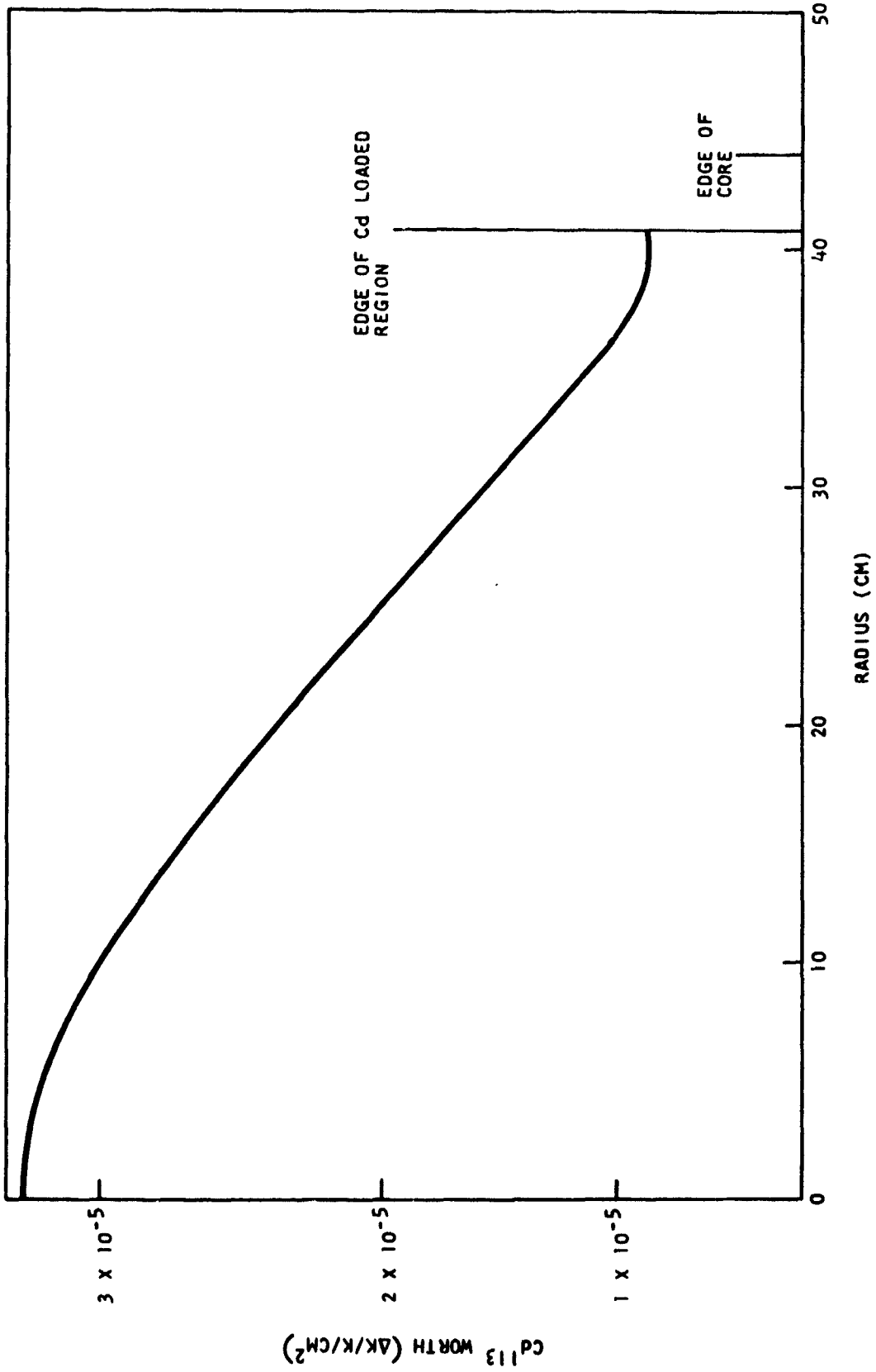


Fig. 6.8--Removal worth of homogenized Cd<sup>113</sup> per sq. cm of core area

Table 6. 16  
 COMPARISON OF PREDICTED AND  
 MEASURED EXCESS REACTIVITY

<u>Core</u>	<u>Calculated</u> k	$\frac{k - 1}{k\beta_{\text{eff}}}$ (%)	<u>Mapped</u> <u>Excess</u> <u>Reactivity</u> (%)	<u>Error</u> (%)
2.9-in. water refl.	1.0252	3.40	6.61	- 3.21
3.0-in. water refl.	1.0895	11.54	14.39	- 2.85
3.0-in. Be refl.	1.1429	17.81	20.55	- 2.74

(The calculated eigenvalue of the beryllium-reflected core is slightly lower than that of the lattice-pitch calculations reported in Section 6.1 because of the difference between the "as-built" beryllium reflector and the reflector considered in the lattice-pitch calculations.) The results are discussed in Section VIII.

#### 6.2.6 RADIAL WORTH OF THE CADMIUM POISON TUBES

The worth of a poison tube (0.1255 molar  $\text{Cd}(\text{NO}_3)_2$ ) compared to a dummy tube filled with water was measured at various radial locations in the 3.0-in. pitch, water-reflected core. The predicted worth as a function of radius for the same core was obtained using a perturbation analysis. The direct and adjoint flux at each radial position was calculated using the GAZE code with a ten-group energy structure. The worth was calculated from the relationship;

$$\begin{aligned}
\rho = & \frac{1}{F} \sum_i \sum_j \int \delta \Sigma_{(i \rightarrow j)}(r) \varphi_i(r) \varphi_j^*(r) d^3 r \\
& - \frac{1}{F} \sum_i \int \delta \Sigma_T^i(r) \varphi_i(r) \varphi_i^*(r) d^3 r \\
& + \frac{1}{kF} \sum_i \sum_j \chi_i \int \delta (\nu^i \Sigma_f^j(r)) \varphi_j(r) \varphi_i^*(r) d^3 r \\
& + \frac{1}{F} \sum_i \int \delta D_i(r) \text{grad } \varphi_i(r) \text{grad } \varphi_i^*(r) d^3 r \quad (6.5)
\end{aligned}$$

with

$$F = \sum_i \sum_j \chi_i \int \nu_j \Sigma_j^f(r) \varphi_j(r) \varphi_i^*(r) d^3 r. \quad (6.6)$$

The scalar flux and adjoint for group  $i$  at space point  $r$  are denoted by  $\varphi_i(r)$  and  $\varphi_i^*(r)$  in Eqs. (6.5) and (6.6);  $\Sigma_T^i$ ,  $\nu_i \Sigma_i^f$ , and  $\Sigma_{(i \rightarrow j)}$  represent the macroscopic cross sections in the  $i$ 'th group for total events, productions, and scattering to group  $j$  and  $\chi_i$  is the fraction of fission neutrons born in group  $i$ . The worths of the cadmium poison tubes calculated from Eqs. (6.5) and (6.6) are compared with the measured values in Table 6.17. The agreement is good for all but the last two locations which are affected by heterogeneities at the core reflector interface.



Table 6.17

COMPARISON OF EXPERIMENTAL AND ANALYTICAL  
POISON ROD WORTHS (0.1255 molar  $\text{Cd}(\text{NO}_3)_2$ )

<u>Tube Location</u>	<u>Radius (cm)</u>	<u>Measured Worth (\$)</u>	<u>Worth from Perturbation Analysis (\$)</u>
f-12	4.40	-0.1316	-0.1276
f-11	8.80	-0.1252	-0.1216
e-12	11.64	-0.1188	-0.1157
e-11	15.86	-0.1099	-0.1048
d-12	19.18	-0.0988	-0.0945
d-11	23.28	-0.0829	-0.0805
c-12	26.76	-0.0727	-0.0680
c-11	30.80	-0.0547	-0.0537
b-12	34.36	-0.0409	-0.0420
b-11	38.35	-0.0302	-0.0337
a-12	41.97	-0.0375	-0.0471

### 6.2.7 CADMIUM WORTH AS A FUNCTION OF CONCENTRATION

The worth, relative to water, of various concentrations of cadmium were calculated for poison tube location f-12 in the 3.0 in. pitch, water-reflected core. The worths were calculated from perturbation theory using Eqs. (6.5) and (6.6). The cadmium disadvantage factors were obtained by the two-dimensional calculation discussed in Section 4.10.2, which gave good results for  $\text{Cd}(\text{NO}_3)_2$  concentrations of up to 0.17 moles/liter. The results are shown in Table 6.18 and compared to the corresponding measurements. The agreement between the calculated and measured values is good.

### 6.2.8 WORTH OF FUEL ASSEMBLY COMPONENTS

The worth of the  $\text{U}^{238}$  rings, the tungsten foils, and the uranium-aluminum foils were measured at three locations in the 3.0-in. pitch core. Experimental details are given in Section 3.2.6. The worths were calculated by perturbation methods at all three locations and also by direct eigenvalue

Table 6. 18  
 COMPARISON OF EXPERIMENTAL AND CALCULATED  
 WORTHS FOR VARIOUS CADMIUM CONCENTRATIONS

<u>CdNO<sub>3</sub> Concentration</u> <u>moles/liter</u>	<u>Measured Worth</u> <u>\$</u>	<u>Calculated Worth</u> <u>\$</u>
0. 0314	0. 0387	0. 0361
0. 0628	0. 0736	0. 0690
0. 0956	0. 1062	0. 1007
0. 1108	0. 1207	0. 1147
0. 1255	0. 1320	0. 1288
0. 1677	0. 1613	0. 1618

calculation for one location at the center. The perturbation method was discussed in Section 6. 2. 6. The eigenvalue method consisted of representing the core before and after removal of the components of the center fuel elements in ten-group diffusion calculations. The worth was then computed from the relationship,

$$\Delta\rho = \frac{k_1 - k_2}{k_1 k_2} \quad (6.7)$$

Disadvantage factors of the H, O, and Al in the center cell were set equal to unity for the eigenvalue calculations following removal of the fuel. The results of the analysis are shown in Table 6. 19.

The reactivity worths of a poison tube, the W rings, and the U<sup>238</sup> ring were also calculated for the 2. 9-in. pitch core using the perturbation method. The cadmium disadvantage factors were obtained by the one-dimensional, tube-centered calculation discussed in Section 4. 10. The results are compared in Table 6. 20 with the experimental values. A discussion of the results is given in Section VII.

Table 6.19

COMPARISON OF EXPERIMENTAL AND ANALYTICAL  
FUEL ELEMENT COMPONENT WORTHS  
(3.0-in. Pitch, Water-Reflected Core)

<u>Material</u>	<u>Measured Worth</u> \$	<u>Calculated Worth from Eigenvalues</u> \$	<u>Worth from Perturbation Analysis</u> \$
<u>Location G-7 (Center)</u>			
U <sup>238</sup> ring	- 0.113	- 0.115	- 0.114
W foils	- 0.352	- 0.329	- 0.313
U-Al foils + Al structure	<u>+ 1.082</u>	+ 1.011	+ 0.665
Sum	\$ 0.617		
<u>Location B6 (Next to Outer Row)</u>			
U <sup>238</sup> ring	- 0.027		- 0.036
W foils	- 0.101		- 0.099
U-Al + Al structure	<u>+ 0.366</u>		+ 0.207
Sum	+ 0.238		
<u>Location A5 (Outer Row)</u>			
U <sup>238</sup> ring	- 0.019		- 0.025
W foils	- 0.071		- 0.071
U-Al + Al structure	<u>+ 0.358</u>		+ 0.192
Sum	\$ 0.268		

Table 6.20

COMPARISON OF EXPERIMENTAL AND ANALYTICAL FUEL  
ELEMENT COMPONENT WORTHS  
(Center Cell in the 2.9-in. Pitch Core)

<u>Material</u>	<u>Measured Worth</u>	<u>Calculated Worth</u>
Tungsten	- \$0.326	- \$0.331
U <sup>238</sup> ring	- \$0.110	- \$0.120
Cadmium tube (0.0431 molar)	- \$0.0478	- \$0.0483

## 6.2.9 WORTH OF UPPER REFLECTOR

The measured worth of various water heights in the upper reflector is reported in Section 3.2.8. Calculated values were obtained for two water heights in the 3.0-in. pitch, water-reflected core from ten-group axial diffusion calculations. The results are compared to measured values in Table 6.21. The agreement is good, lending confidence to the use of a homogenized reflector in the criticality calculations. The slight difference between measured and calculated values may be caused by a small difference in the reference point used for the core-reflector interface.

Table 6.21  
COMPARISON OF MEASURED AND CALCULATED  
TOP REFLECTOR WORTHS

<u>Water Height in Reflector</u> (in.)	<u>Measured Worth (Interpolated)</u> \$	<u>Calculated Worth</u> \$
1.772	0.286	0.301
5.906	0.606	0.615

## 6.2.10 NEUTRONIC SIMULATION EXPERIMENT

An analysis of the pseudo-reference fuel element was made for the configuration described in Section 3.2.7. The five-stage replacement contained seven tungsten rings enriched in  $W^{184}$  and one ring enriched in  $W^{183}$ ; the fuel rings were obtained from the corresponding mockup fuel stages.

High energy and thermal disadvantage factors were calculated for the pseudo-reference fuel stages using the GAPLSN code; a  $P_1$  expansion of the scattering cross sections and an  $S_4$  approximation for the angular flux was made in the standard ten-group structure. Broad group-averaged cross sections were then obtained for the simulated fuel stages; they were used in a perturbation analysis of the reactivity worths of the fuel components.

The perturbation equations solved are given in Section 6.2.6. In this experiment only five of the twenty-four stages in a mockup fuel element were replaced by the pseudo-reference fuel stages. For purposes of analysis they were assigned the average flux and adjoint flux in the axial direction, and the analysis was confined to a radial perturbation. The results thus illustrate the compensations in worth between the mockup and pseudo-reference elements. A complete two-dimensional analysis was not made because of the expense involved in separate direct and adjoint flux calculations.

The calculated values for  $k_{\infty}$  are given for the pseudo-reference and mockup stages in Table 6.22. The pseudo-reference stage had a  $k_{\infty}$  of 1.1791, just .0082  $\Delta k/k$  larger than the mockup element value of 1.1694. The measured reactivity of the five pseudo-reference stages was +\$.0008 greater than the mockup, which when converted to a full core accounts for about one-third of the small discrepancy. Thus the calculated values of  $k_{\infty}$  would be within .005  $\Delta k/k$  if the mockup and pseudo-reference stages were exactly matched in worth.

A fractional absorption table for the two cases is also given in Table 6.22. A comparison of the Fermi age to 2.38 eV in the same table shows the effect of the inelastic scattering of tungsten which lowers the age in the pseudo-reference case.

A comparison of removal worths for each isotope as calculated by the perturbation analysis is given in Table 6.23. The results are discussed in Section VIII.

### 6.3 FLUX AND POWER DISTRIBUTIONS

#### 6.3.1 POWER DENSITY IN THE FUEL RINGS

The measured power density in each ring of the central fuel element is shown in Table 3.17 for the 3.0-in. pitch assembly. Calculated values of the power density for this core were obtained from one-dimensional transport calculations described in Section 4.8. The calculated and measured values are compared in Table 6.24.

Table 6.22  
 COMPARISON OF NEUTRON BALANCE FOR  
 MOCKUP AND PSEUDO-REFERENCE FUEL STAGES

<u>Nuclide</u>	<u>Fractional Absorptions above 2.38 eV</u>		<u>Fractional Absorptions below 2.38 eV</u>	
	<u>Mockup</u>	<u>Pseudo-Reference</u>	<u>Mockup</u>	<u>Pseudo-Reference</u>
H	.0022	.0022	.0360	.0366
Ø	.0019	.0017	.0000	.0000
Al	.0044	.0042	.0096	.0116
Ni	.0002		.0006	
Zr	.0002	.0002	.0001	.0001
Cd	.0000	.0001	.1224	.1265
W <sup>182</sup>	.0287	.0201	.0102	.0058
W <sup>183</sup>	.0309	.0733	.0025	.0167
W <sup>184</sup>	.0038	.0235	.0011	.0137
W <sup>186</sup>	.0284	.0177	.0228	.0110
U <sup>235</sup>	.2113	.2092	.4005	.4196
U <sup>238</sup>	.0699	.0061	.0125	.0001
Sum	.3819	.3583	.6183	.6417
$k_{\infty}$	1.1694	1.1791		
$\tau$ (2.38 eV)	102.6 cm <sup>2</sup>	95.3 cm <sup>2</sup>		

Table 6.23  
 REMOVAL WORTH OF NUCLIDES IN MOCKUP AND  
 PSEUDO-REFERENCE ELEMENT

<u>Nuclide</u>	<u>Mockup Element</u>	<u>Pseudo-Reference Element</u>
<u>Removal Worth of Parasitic Capture (Cents)</u>		
H	1.88	1.86
Ø	0.06	0.06
Al	0.63	0.72
W <sup>132</sup>	1.62	1.04
W <sup>183</sup>	1.32	3.62
W <sup>184</sup>	0.20	1.56
W <sup>186</sup>	2.24	1.21
U <sup>235</sup>	6.17	6.19
U <sup>238</sup>	2.92	0.23
<u>Removal Worth of Fission Capture (Cents)</u>		
U <sup>235</sup>	21.97	22.14
U <sup>238</sup>	0.30	0.01
<u>Removal Worth of Fission Production (Cents)</u>		
U <sup>235</sup>	- 41.19	- 41.49
U <sup>238</sup>	- 0.88	- 0.02
<u>Removal Worth of Scattering (Cents)</u>		
H	- 9.10	- 9.21
Ø	- 0.19	- 0.20
Al	- 0.41	- 0.41
W <sup>182</sup>	- 0.02	- 0.01
W <sup>183</sup>	- 0.02	- 0.07
W <sup>184</sup>	- 0.03	- 0.35
W <sup>186</sup>	- 0.03	- 0.01
U <sup>235</sup>	- 0.02	- 0.02
U <sup>238</sup>	- 0.15	~ 0.0
<u>Total Removal Worth (Cents)</u>		
	- 12.73	- 13.15

Table 6.24

COMPARISON OF CALCULATED  
AND MEASURED POWER DENSITY

(Fuel Rings in Central Element of 3.0-in. Pitch Core)

Fuel Ring	Measured Power Density	Calculated Power Density
A	0.653	0.640
B	0.670	0.663
C	0.723	0.722
D	0.824	0.823
E	1.000	1.000

The measured values are the averages of the two points measured in each fuel ring. Both sets are normalized to unity in the outer ring (Ring E). The agreement between the measured and calculated values is excellent.

### 6.3.2 GOLD CADMIUM RATIOS

Experimental values of the gold cadmium ratio are reported in Section 3.3.6. The measurements were made on the exterior surface of the  $U^{238}$  ring using 0.022 in. thick cadmium covers.

The cadmium ratio was calculated as

$$C. R. = \frac{\int_0^{\infty} \sigma_a(E)\phi(E)dE}{\int_{0.414 \text{ eV}}^{\infty} \sigma_a(E)\phi(E)dE} \quad (6.8)$$



Values of the absorption cross section for Au<sup>197</sup> were calculated in the resonance region by the GANIT<sup>(60)</sup> code using the Nordheim integral technique. Gold resonances through the 194 eV resonance were included in the calculation of the absorption cross section, which was averaged over each GAM-II fine group below 194 eV. Broad group cross sections for the standard epithermal group structure were then computed using the average cell flux obtained from a GAM-II calculation as a weighting function.

The average thermal absorption cross sections for the five thermal groups were obtained by weighting a  $\frac{1}{v}$  absorber with the thermal flux cell spectrum calculated by the GATHER-II code. The thermal absorption cross sections were normalized to a 2200 m/sec value of 98.8 barns for Au<sup>197</sup>.

Equation (6.8) was then evaluated by the relationship

$$\text{C. R.} = \frac{\sum_{i=1}^{10} \bar{\sigma}_{ai} \bar{\phi}_i}{\sum_{i=1}^6 \bar{\sigma}_{ai} \bar{\phi}_i}, \quad (6.9)$$

where  $\bar{\phi}_i$  is the average flux in energy group  $i$  at the location of the foil. The fluxes at the surface of the U<sup>238</sup> ring were obtained in the standard ten-group structure from one-dimensional cell calculations. These fluxes are appropriate for an element in the center of the core, and were used to calculate the cadmium ratio at that location (element G-7). Fluxes for an explicit fuel element ring could not be calculated with confidence at the core edge due to the change in spectrum caused by the reflector; consequently the average group fluxes at the location of element A-4 were obtained from a GAZE diffusion calculation for the homogenized core. The results are shown in Table 6.25.

Table 6.25

COMPARISON OF EXPERIMENTAL AND  
CALCULATED CADMIUM RATIOS FOR GOLD

<u>Core Pitch</u>	<u>Foil Location</u>	<u>Calculated C. R.</u>	<u>Measured C. R.</u>
2.9 in.	U <sup>238</sup> ring, G-7	1.44	1.45
3.0 in.	U <sup>238</sup> ring, G-7	1.50	1.51
3.0 in.	U <sup>238</sup> ring, A-4	2.49	2.54

The agreement is excellent for measurements made at the center of the core and is reasonable for the measurement made at the core edge. A positioning uncertainty of only 0.04 cm would account for the 3% discrepancy at the core edge.

### 6.3.3 FLUX AND POWER DISTRIBUTIONS IN THE CORE

Axial flux traverses with Cu foils are shown in Fig. 3.9 for the 3.0-in. pitch, water-reflected core. The bare activations have been calculated using the ten-group axial flux profiles from a GAZE calculation. The infinite dilution resonance integral for Cu was used in the resonance energy region. The results are shown in Fig. 6.9 and compared to the experimental data. The agreement is good between the calculated and measured activations at all points aside from the bottom reflector. The deviation in the bottom reflector may be explained by the termination of the reflector at 25.0 cm in the calculations.

Radial power traverses along two radii were also made in the 3.0-in. pitch, water-reflected core, and are reported in Section 3.3.5. These activations can only be compared to homogenized radial calculations at equivalent cell positions. In such a comparison the cell disadvantage factors are constant from point to point and the over-all power distribution can then be compared to homogenized core calculations. This comparison is made in Fig. 6.10 for the "E" ring activations taken from the two radial

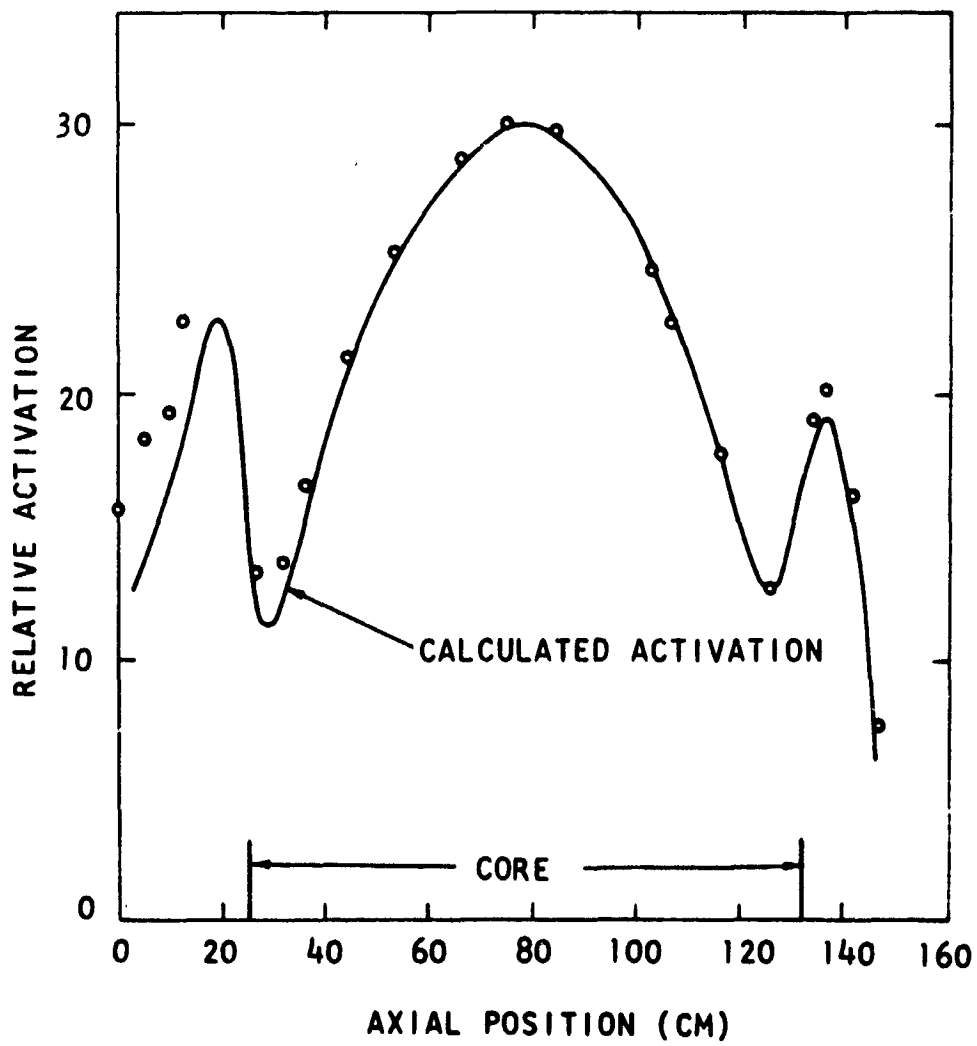


Fig. 6.9--Measured versus calculated activation for Cu foils  
3.0-in. pitch, water-reflected core

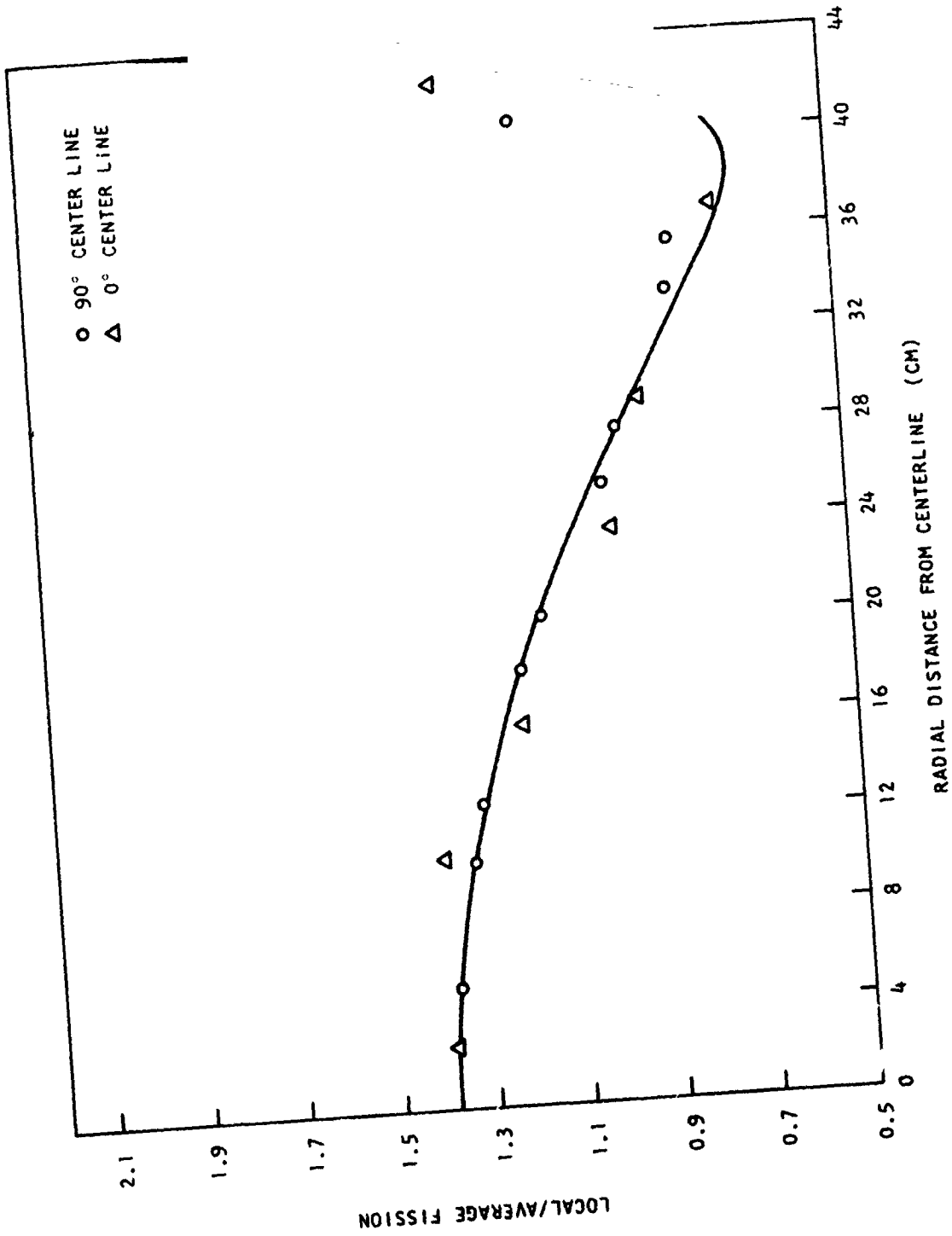


Fig. 6.10--Radial power distribution, 3.0-in. pitch water-reflected core

power distributions, Figs. 3.10 and 3.11. The calculated power distribution was obtained from a ten-group radial GAZE calculation. Aside from some scatter, the calculated power density curve is in good agreement with the measured points. The two measurements in the outer ring of fuel elements are higher than the calculated points, which may be explained by the proximity of the reflector interface.

The measured axial power distribution in the 3.0 in. pitch, beryllium-reflected core is compared with the results of a homogenized axial GAZE calculation in Fig. 6.11. A consistent deviation between the measured and calculated power density is apparent near the bottom beryllium reflector. The deviation is discussed in Section VIII.

Radial power density profiles in ring "E" were measured at five axial levels in the beryllium-reflected core. These data have all been normalized to the power density profile from a radial GAZE calculation and plotted in Fig. 6.12. The agreement is reasonable, aside from the points in the outermost fuel element.

#### 6.3.4 ANALYSIS IN SUPPORT OF THE GAMMA HEATING EXPERIMENT

The gamma heating experiment and the results of the measurements are discussed in Section 3.6. The results are contingent upon a calculation of the absolute core power. Additional calculations were performed to establish the general validity of the numerous measurements.

The measured power density in each ring was used to make the geometry correction in the ring activation measurements. The measured results shown in Table 3.20 may be compared with the calculated results of Table 6.24. The measured power densities from the gamma heating experiment are up to 6% higher than those from the transport cell calculation. The agreement is adequate to justify the use of the experimental data for counting geometry corrections.

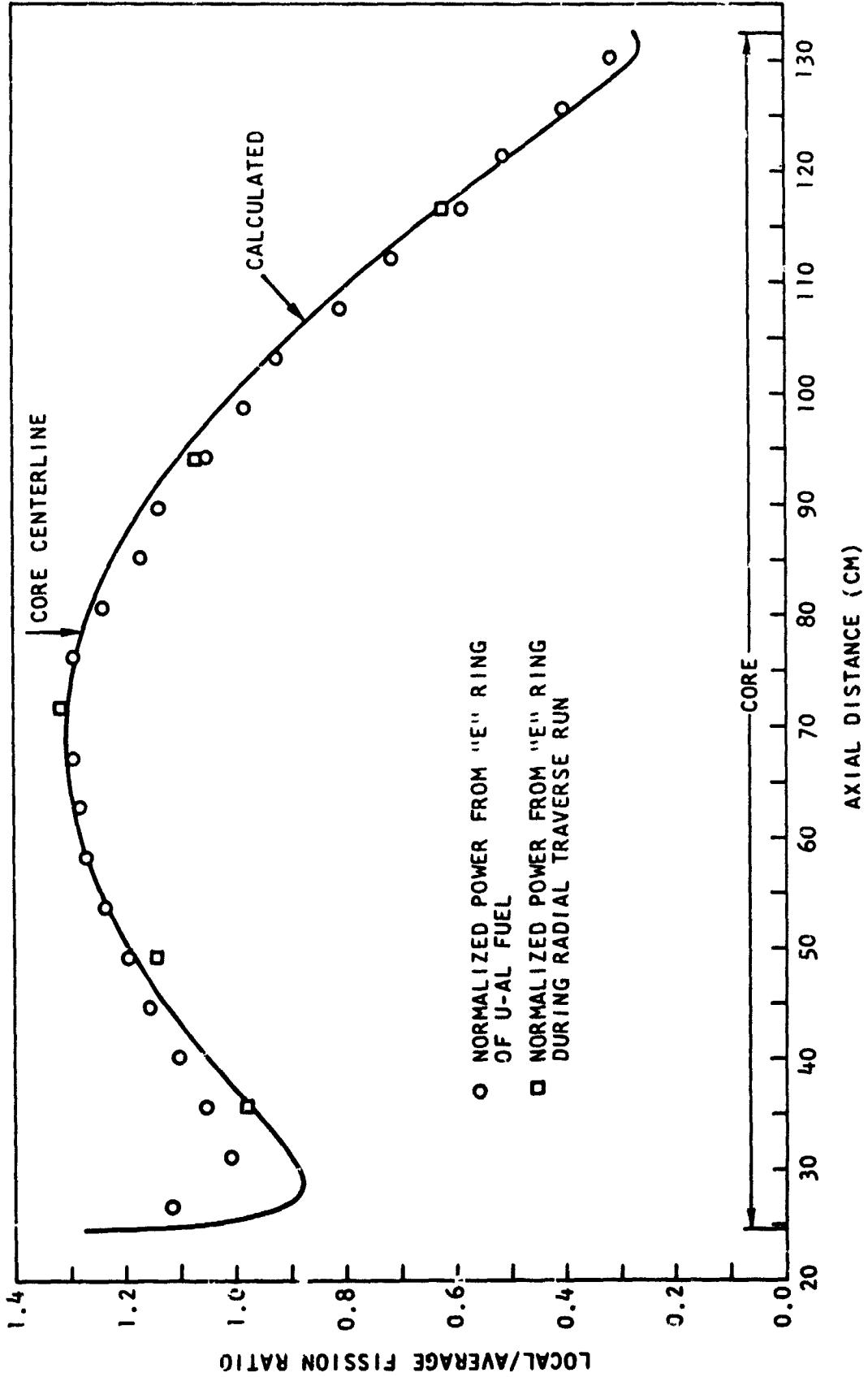


Fig. 6.11--Axial power traverse, 3.0-in. pitch, Be-reflected core

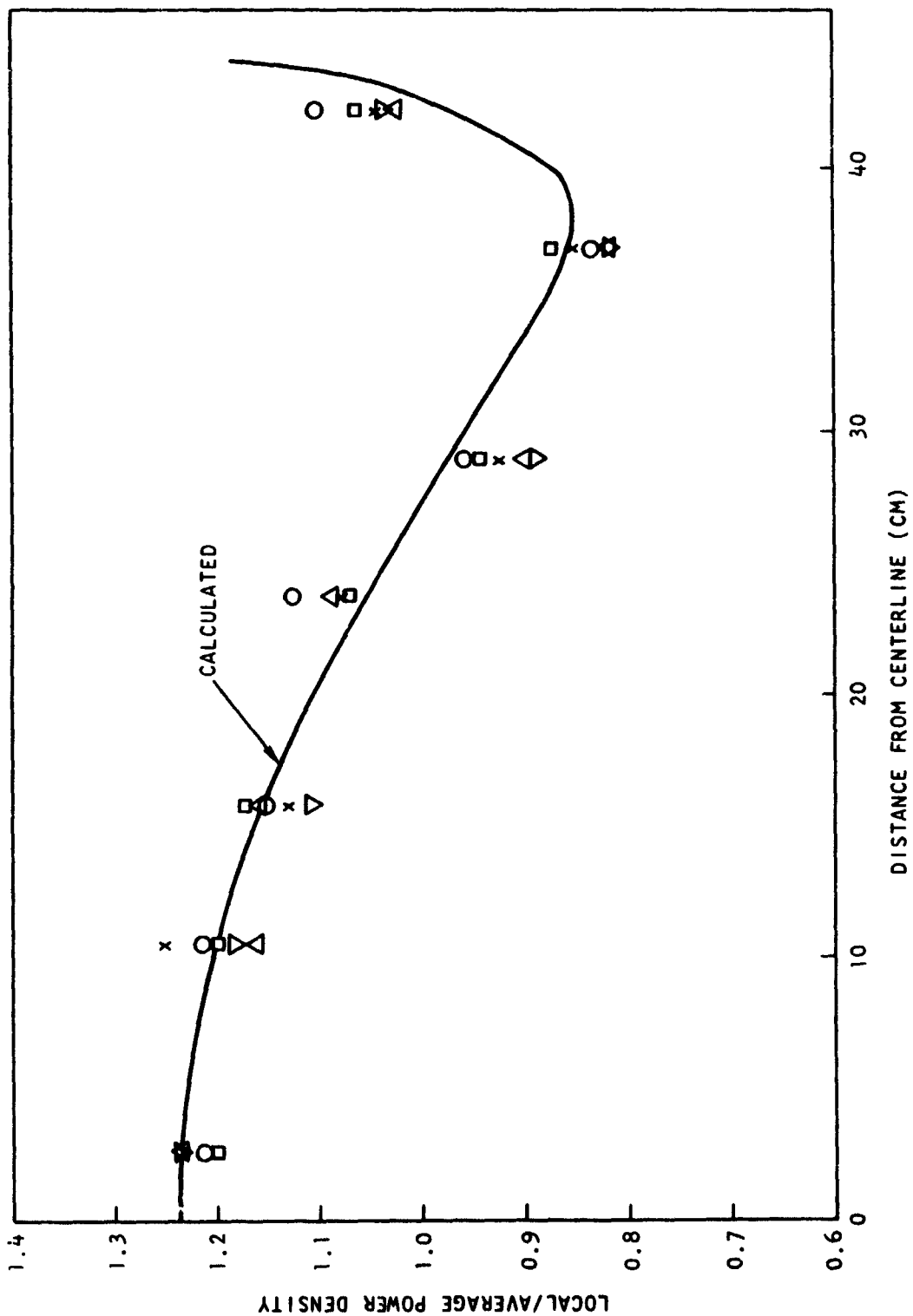


Fig. 6.12--Radial power distribution, 3-in. pitch, Be-reflected core

The relative power of Stage 12 in each fuel element position was measured to use in finding the total core power. Calculated values were also obtained from a GAMBLE calculation in which the entire core and reflector was represented. The power density at the Stage 12 level was then calculated by averaging over the radius occupied by each cell. The comparison between calculated and measured values is given in Table 6.26; the data are normalized to the center fuel stage in each case. The difference between the calculated and measured relative powers is less than 4% in every element except K-1, J-1, and H-1. These three elements are the outermost elements of the assembly and show in each case a higher actual power than that calculated in the homogenized core. The agreement justifies the use of the experimental data in calculating the total core power.

Both gold and manganese foils were activated on the outside of the  $U^{238}$  ring in Stage 12 of element G-7 in order to measure the flux level of the assembly. The actual power level could then be computed by normalization to the GAMBLE results. Thermal disadvantage factors appropriate to the position of the foils in the cell were taken from the corresponding transport cell calculation. The subcadmium flux (below 0.414 eV) found by the GAMBLE two-dimensional calculation was then used to find the saturated subcadmium activity of the foils. The calculated relative activity of the gold and manganese foils per watt of core power is given in Table 6.27.

#### 6.4 TEMPERATURE COEFFICIENTS

The reactivity of the 3.0-in. pitch, water-reflected and beryllium-reflected cores has been calculated as a function of temperature, and compared with the results of experiment. Four values of the temperature were chosen; 27°C, 50°C, 70°C, and 100°C for all of the calculations.



Table 6.26

COMPARISON OF MEASURED AND CALCULATED  
RELATIVE POWERS IN STAGE 12

<u>Element No.</u>	<u>Relative Power Per Element</u>		<u>% Difference</u>
	<u>Measured</u>	<u>Calculated</u>	
K-1	0.744	0.685	- 8.0
J-1	0.724	0.693	- 4.3
J-2	0.712	0.715	+ 0.4
J-3	0.800	0.808	+ 1.0
H-1	0.771	0.696	- 9.7
H-2	0.671	0.697	+ 3.9
H-3	0.781	0.793	+ 1.5
H-4	0.883	0.884	+ 0.1
H-5	0.949	0.947	- 0.2
G-2	0.709	0.686	- 3.2
G-3	0.733	0.750	+ 2.3
G-4	0.851	0.853	+ 0.2
G-5	0.938	0.933	- 0.5
G-6	0.983	0.982	- 0.1
G-7	1.000	1.000	

Table 6.27

FOIL ACTIVATION CALCULATION

<u>Nuclide</u>	<u>wt %</u>	<u>2200 m/sec Activation Cross Section (barns)</u>	<u>Subcadmium activation dis/sec (milligram - watt)</u>
gold	100.	98.8±.2	135.5±.2
manganese	80.	13.2±.1	51.9±.4

These calculations were used to estimate the core power in the gamma heating experiment.

The following physical changes were assumed to occur in the assembly with temperature.

- a. The water and beryllium density and cadmium concentration decrease with temperature by the reduction factors shown in Table 6.28.
- b. The grid plate and axial structural members freely expand with temperature in a linear fashion, according to the formula,  $l(T) = l_0 (1 + \gamma \Delta T)$ , where  $\gamma = 2.35 \times 10^{-5} \text{ } ^\circ\text{C}^{-1}$  (for aluminum).

The following nuclear changes were accounted for in the calculations:

- a. The appropriate hydrogen Nelkin kernel or beryllium crystal and gas kernels were used at each value of the temperature. Accordingly, the free gas kernel for oxygen was computed for the same temperature.
- b. Separate resonance calculations for the tungsten isotopes and  $\text{U}^{238}$  were performed at each value of the temperature.

Table 6.28

## WATER AND CADMIUM DENSITY REDUCTION FACTORS

<u>Temperature (<math>^\circ\text{C}</math>)</u>	<u>Density Reduction Factor</u>
27	1.00000
50	0.99198
70	0.98168
100	0.96172

## BERYLLIUM DENSITY REDUCTION FACTORS

<u>Temperature (<math>^\circ\text{C}</math>)</u>	<u>Density Reduction Factor</u>
27	1.000
50	0.9992
70	0.9986
100	0.9976

The methods used in the calculations correspond to the methods used in the precritical analysis of the 3.0-in. pitch, water-reflected core (see Section 6.1.2). The group structure in the thermal region was expanded, as shown in Table 6.29. This expansion was necessary, particularly in the calculation of the disadvantage factors, to adequately represent the component of the temperature coefficient associated with the thermal utilization (see Table 6.30). The calculations were converged to  $10^{-5}$  in  $k$ . The disadvantage factors for all of the calculations were obtained at a single value of the temperature, namely  $27^{\circ}\text{C}$ . In order to evaluate the effect on the temperature coefficient of the change in disadvantage factors with temperature, the calculation of the water-reflected core at  $100^{\circ}\text{C}$  was repeated with disadvantage factors appropriate to this temperature.

The final results of the calculations are shown in Tables 6.31 and 6.32. Table 6.31 shows the results for the water-reflected core and Table 6.32 for the beryllium-reflected core, using both the crystal and gas kernels for beryllium. The reactivity, relative to  $27^{\circ}\text{C}$ , is defined by:

$$\rho(T, 27^{\circ}) = \frac{k(T) - k(27^{\circ})}{\beta_{\text{eff}} k(T) k(27^{\circ})} \quad (6.10)$$

and the temperature coefficient between temperatures  $T_1$  and  $T_2$  is given by:

$$\Delta\rho = \frac{k(T_2) - k(T_1)}{\beta_{\text{eff}} k(T_2) k(T_1) [T_2 - T_1]} \quad (6.11)$$

Table 6.29

GROUP STRUCTURE FOR TEMPERATURE  
COEFFICIENT CALCULATIONS

<u>Group</u>	<u>Energy Range</u>
1	14.9 to 2.7 MeV
2	2.7 to .498 MeV
3	497.9 to 67.4 keV
4	67.4 keV to 61.4 eV
5	61.4 to 2.38 eV
6	2.38 to 1.9 eV
7	1.9 to 1.2 eV
8	1.2 to 1.0 eV
9	1.0 to .6 eV
10	0.6 to 0.414 eV
11	0.414 to 0.33 eV
12	0.33 to 0.23 eV
13	0.23 to .16 eV
14	0.16 to .12 eV
15	0.12 to .09 eV
16	0.09 to .075 eV
17	0.075 to .06 eV
18	0.06 to .05 eV
19	0.05 to .04 eV
20	0.04 to .03 eV
21	0.03 to .02 eV
22	0.02 to .01 eV
23	0.01 to 0.0 eV

Table 6.30

THERMAL UTILIZATION CALCULATED BY  
GATHER WITH 5- AND 18-GROUP DISADVANTAGE FACTORS

	$f^a$		$\frac{\delta f}{f}$
	<u>27°C</u>	<u>100°C</u>	<u>27°C→100°C</u>
5-Group	.711415	.712670	+.001763
18-Group	.704990	.707493	+.003545

<sup>a</sup>The magnitude of  $f$  should not be compared with subsequent values, as these calculations were performed with a constant cadmium concentration, as well as a different 27°C kernel.

Table 6.31

TEMPERATURE COEFFICIENT RESULTS FOR THE  
3.0-IN. PITCH, WATER-REFLECTED CORE

Temperature (°C)	$k_{\text{eff}}$	$\rho(T, 27^\circ)$ (cents)	$\Delta\rho$ (cents/°C)
27°	0.971037	--	+ 0.21
50°	0.971359	+ 4.8	- 0.86
70°	0.970206	- 12.4	- 1.45
100°	0.967306	- 55.8	

Table 6.32

TEMPERATURE COEFFICIENT RESULTS FOR THE 3.0-IN.  
PITCH, BERYLLIUM-REFLECTED CORE

Temp. °C	Crystal Kernel			Gas Kernel		
	$k_{\text{eff}}$	$\rho(T, 27^\circ)$ cents	$\Delta\rho$ cents/°C	$k_{\text{eff}}$	$\rho(T, 27^\circ)$ cents	$\Delta\rho$ cents/°C
27	0.988772	-	-1.04	0.988600	-	-1.03
50	0.987137	-23.9	-0.88	0.986984	-23.7	-0.87
70	0.985937	-41.5	-1.83	0.985797	-41.1	-1.81
100	0.982206	-96.6		0.982124	-95.3	

where  $\beta_{\text{eff}} = .00712$  for the water-reflected core and  $\beta_{\text{eff}} = .00700$  for the beryllium-reflected core. The calculated values of the reactivity are compared with the measured values in Fig. 6.13 . . . . .

The results given in Tables 6.31 and 6.32 are not quite complete, since they do not reflect the change in cell thermal disadvantage factors with temperature. As pointed out earlier, the effect of the change in cell thermal disadvantage factors was examined at a temperature of  $100^{\circ}\text{C}$  for the water-reflected core. Both the cadmium and cell disadvantage factors were recalculated, and the calculations reflect the diminution of water and cadmium densities as well as the change in the hydrogen and oxygen kernels. The results of these calculations are given in Table 6.33, where the reactivity and temperature coefficient between  $27^{\circ}\text{C}$  and  $100^{\circ}\text{C}$  are tabulated, both with and without consideration of the change in thermal disadvantage factors. The results are compared with the measured overall temperature coefficient, extrapolated from  $80^{\circ}\text{C}$ .

Table 6.33  
OVERALL TEMPERATURE COEFFICIENT  
(Water-Reflected Core)

Temperature ( $^{\circ}\text{C}$ )	$k_{\text{eff}}$	$\rho(T, 27^{\circ})$ (cents)	Calculated $\Delta\rho(100^{\circ}, 27^{\circ})$ (cents/ $^{\circ}\text{C}$ )	Measured $\Delta\rho(100^{\circ}, 27^{\circ})$
$27^{\circ}\text{C}$	0.971037	-----		
$100^{\circ}\text{C}$	0.967306	- 55.8	- 0.76	- 0.63 <sup>a</sup>
(change in thermal disadvantage factors neglected)			- 0.58	
$100^{\circ}\text{C}$	0.968215	- 42.1		
(change in thermal disadvantage factors considered)				

<sup>a</sup>Extrapolated from  $80^{\circ}\text{C}$

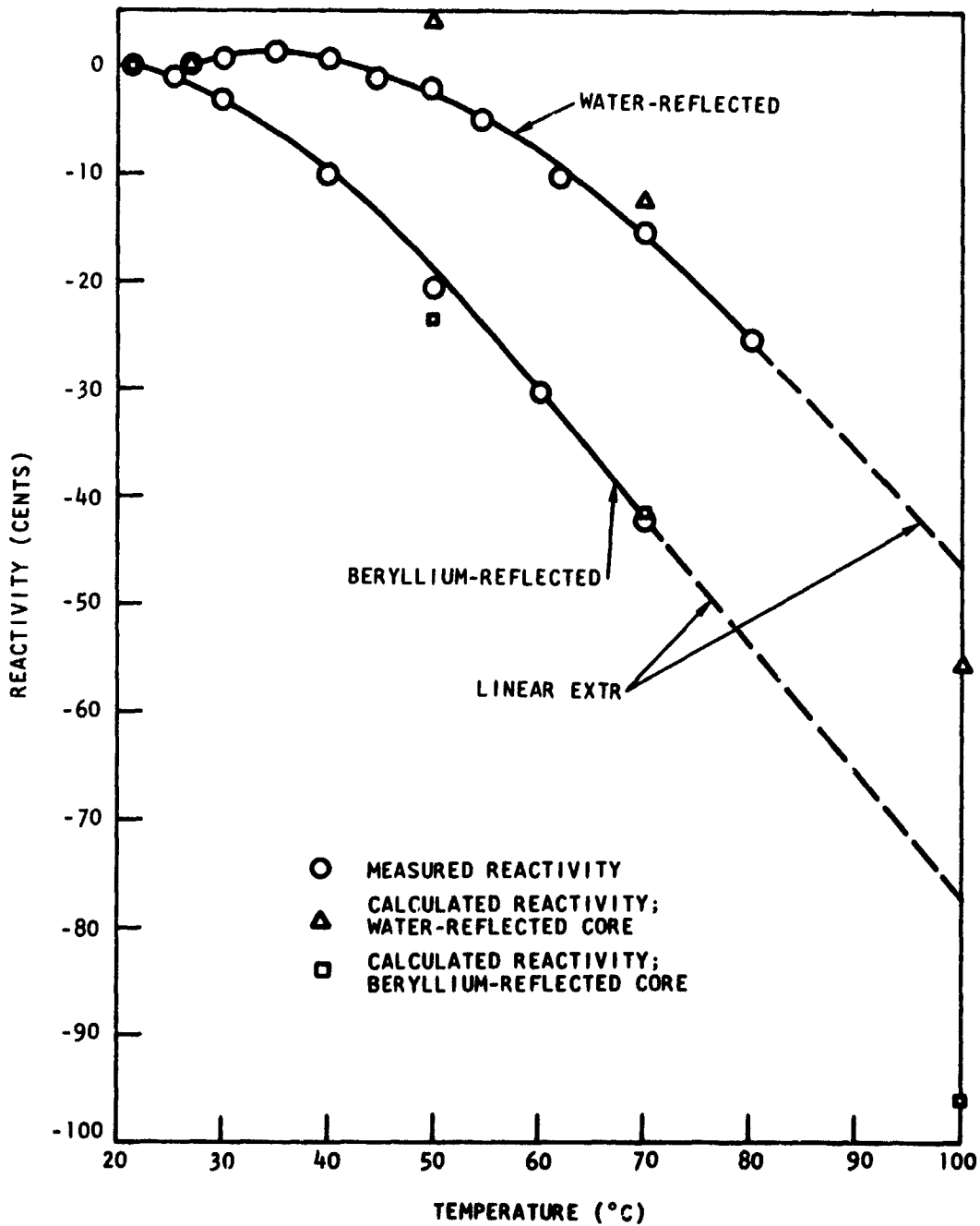


Fig. 6.13--Comparison of experimental and calculated values of the effect of temperature on reactivity

A better understanding of the temperature coefficient can be gained by dissociating the coefficient into its component parts. This has been done in Table 6.34 for the water-reflected core and in Table 6.35 for the beryllium-reflected core. The usual "generalized five-factor formula" components were computed from the final radial diffusion calculation. The individual components were defined as follows:

$$\eta = \frac{\int_{\text{core}} d^3r \int_0^{2.38 \text{ eV}} dE \nu(E) \Sigma_f(\bar{r}, E) \phi(\bar{r}, E)}{\int_{\text{core}} d^3r \int_0^{2.38 \text{ eV}} dE \Sigma_a^{\text{Fuel}}(\bar{r}, E) \phi(\bar{r}, E)}, \quad (6.12)$$

$$f = \frac{\int_{\text{core}} d^3r \int_0^{2.38 \text{ eV}} dE \Sigma_a^{\text{Fuel}}(\bar{r}, E) \phi(\bar{r}, E)}{\int_{\text{core}} d^3r \int_0^{2.38 \text{ eV}} dE \Sigma_a(\bar{r}, E) \phi(\bar{r}, E)}, \quad (6.13)$$

$$\epsilon = \frac{\int_{\text{core}} d^3r \int_0^{\infty} dE \nu(E) \Sigma_f(\bar{r}, E) \phi(\bar{r}, E)}{\int_{\text{core}} d^3r \int_0^{2.38 \text{ eV}} dE \nu(E) \Sigma_f(\bar{r}, E) \phi(\bar{r}, E)}, \quad (6.14)$$



Table 6. 34

COMPONENTS OF THE TEMPERATURE  
COEFFICIENT FOR THE 3. 0-IN. PITCH, WATER-REFLECTED CORE

Temp. (°C)	$\eta$	$\frac{1}{\beta\eta} \frac{\delta\eta}{\delta T}$ (cents/°C)	$\xi$	$\frac{1}{\beta\xi} \frac{\delta\xi}{\delta T}$ (cents/°C)	$\rho$	$\frac{1}{\beta\rho} \frac{\delta\rho}{\delta T}$ (cents/°C)	$P_{NL}$	$\frac{1}{\beta P_{NL}} \frac{\delta P_{NL}}{\delta T}$ (cents/°C)
27°	2. 05722	- 0. 13	1. 33300	+ 1. 50	. 65806	- 0. 57	. 78979	- 0. 46
50°	2. 05678	- 0. 16	1. 33281	+ 1. 89	. 65744	- 1. 57	. 78921	- 1. 45
70°	2. 05632	- 0. 20	1. 33390	+ 2. 20	. 65597	- 2. 25	. 78758	- 2. 03
100°	2. 05546		1. 33693		. 65282		. 78417	

Table 6. 35  
 COMPONENTS OF THE TEMPERATURE COEFFICIENT FOR  
 THE 3. 0-IN. PITCH, BERYLLIUM-REFLECTED CORE

Temp. (°C)	$\eta$	$\frac{1}{\beta} \frac{\delta \eta}{\delta T}$ (cents/°C)	$f$	$\frac{1}{\beta} \frac{\delta f}{\delta T}$ (cents/°C)	$\epsilon$	$\frac{1}{\beta} \frac{\delta \epsilon}{\delta T}$ (cents/°C)	$P$	$\frac{1}{\beta} \frac{\delta P}{\delta T}$ (cents/°C)	$\frac{P_{NL}}{\beta P_{NL}}$	$\frac{1}{\beta} \frac{\delta P_{NL}}{\delta T}$
27°	2.05496	- 0.14	.67148	+ 1.11	1.38636	+ 0.78	.63302	- 1.66	.82036	- 1.58
50°	2.05449	- 0.19	.67268	+ 1.62	1.38811	+ 1.93	63133	- 3.30	.81816	- 0.24
70°	2.05394	- 0.22	.67421	+ 1.99	1.39187	+ 2.14	.62843	- 3.69	.81782	- 2.26
100°	2.05298		.67704		1.39816		.62360		.81359	

$$p = \frac{\int_{\text{core}} d^3r \int_0^{2.38 \text{ eV}} dE \Sigma_a(\bar{r}, E) \varphi(\bar{r}, E)}{\int_{\text{core}} d^3r \int_0^{\infty} dE \Sigma_a(\bar{r}, E) \varphi(\bar{r}, E)}, \quad (6.15)$$

and

$$P_{NL} = \frac{\int_{\text{core}} d^3r \int_0^{\infty} dE \Sigma_a(\bar{r}, E) \varphi(\bar{r}, E)}{\int_{\text{core}} d^3r \int_0^{\infty} dE \Sigma_a(\bar{r}, E) \varphi(\bar{r}, E) - \int_{\text{core}} d^3r \int_0^{\infty} dE D(\bar{r}, E) \nabla^2 \varphi(\bar{r}, E)} \quad (6.16)$$

## 6.5 CALCULATION OF THE PROMPT NEUTRON DECAY CONSTANT

Measurements of  $\alpha$ , the prompt neutron decay constant, for the 3.0-in. pitch, water-reflected core were reported in Section 3.5. These data have been corrected to "standard" core values. (The "standard" core contains 204 poison tubes and 121 fuel elements.) Values of  $\alpha$  have also been calculated for the same three cases, using the  $1/v$  poison removal method.

In order to eliminate discrepancies the calculations utilized all of the refinements mentioned in Section 6.1.2 of this report. Thermal disadvantage factors for cadmium were obtained from two-dimensional X-Y transport cell calculations. Thermal disadvantage factors for the other fuel constituents were obtained from two-dimensional R-Z transport cell calculations. Fuel disadvantage factors were calculated for cells containing  $\text{Cd}(\text{NO}_3)_2$  concentration of 0.0 and 0.1255 moles/liter. The disadvantage factors for the two higher concentrations were then obtained by extrapolation since the changes were small and linear over a wide range of  $\text{Cd}(\text{NO}_3)_2$  molarities. The resonance treatment incorporated the refinements discussed in Section 4.11.

The standard ten-group energy structure was used and broad group cross sections were obtained from a calculation of the energy spectrum in each of the three cases.

The calculation of  $\alpha$  is based on the well known one-dimensional group-diffusion equation for a non-critical system:

$$\begin{aligned} \nabla \cdot D_i \nabla \phi_i + \left[ \Sigma_{a,i} + \frac{\alpha}{\bar{v}_i} + D_i B_i^2 + \sum_{j \neq i} \Sigma(i \rightarrow j) \right] \phi_i \\ = \chi_i (1-\beta) \sum_j \nu_j \Sigma_{f,j} \phi_j + \sum_{j \neq i} \Sigma(i \rightarrow j) \phi_j \end{aligned} \quad (6.17)$$

where  $\phi_i$  is the flux in energy group  $i$ ,  $\Sigma_{a,i}$ ,  $\Sigma_{f,i}$ , and  $\Sigma(i \rightarrow j)$  are the usual macroscopic cross sections for absorption, fission, and group transfer,  $\chi_i$  and  $\nu_j$  are the group fission yield and neutron yield per fission, and  $D_i B_i^2$  represents the transverse leakage. The value of  $\bar{v}_i$  is the inverse of the average inverse velocity. The quantity  $\chi_i (1-\beta)$  is the prompt neutron contribution to the total production rate in the group.

The GAZE code was used to find  $\alpha$  by means of a search routine in which the atom density of a  $1/\bar{v}$  absorber is adjusted everywhere in the assembly until the eigenvalue is just equal to  $1+\beta$ . The  $\alpha$  search was made in both axial and radial directions in a one-dimensional leakage synthesis. This procedure was followed in the three calculated cases. The results are shown in Table 6.36.

The values of reactivity were obtained in both the experimental and calculated cases from the equation,

$$\rho = \frac{1 + \frac{\lambda \alpha}{\beta_{\text{eff}}}}{1 + \lambda \alpha} \quad (6.18)$$

where an experimental value of 28.9 micro sec was used for the prompt neutron lifetime,  $\ell$ , and 0.00712 was used for  $\beta_{\text{eff}}$ , the effective delayed neutron fraction. The experimental values were further corrected to the standard core values given above. The results are discussed in Section VIII.

Table 6.36

COMPARISON OF CALCULATED AND MEASURED VALUES OF  $\alpha$   
(3.0-IN. PITCH, WATER-REFLECTED CORE)

Cadmium Conc. (moles/ liter)	$\alpha$ Measured (sec <sup>-1</sup> )	$\alpha$ Calculated (sec <sup>-1</sup> )	$\rho$ Measured (\$)	$\rho$ Calculated (\$)	Difference (\$)
0.1255	- 340.	- 685.	- 0.38	- 1.82	- 1.44
0.1677	- 941.	- 1539.	- 2.91	- 5.49	- 2.58
0.2899	- 2280.	- 3028.	- 9.02	-12.37	- 3.35

**VII. CRITICAL EXPERIMENTS PERFORMED BY  
NASA LEWIS RESEARCH CENTER**

**7.1 DESCRIPTION OF EXPERIMENTS**

Ten critical experiments were selected for analysis from among a number of experiments made at the Lewis Research Center. The experiments used aqueous solutions of uranium oxyfluoride and covered a range of moderator/uranium ratios as well as different core heights, varying numbers of penetrating tubes, and differing numbers of tungsten cylinders in the empty tubes. The ten experiments which were selected are listed in Table 7.1.

Table 7.1  
EXPERIMENTS SELECTED FOR ANALYSIS

	<u>Voided Tubes</u>	<u><math>N_H/N_{U^{235}}</math></u>	<u>Critical Height (in.)</u>	<u>Solution Density</u>
1	0	152.9	5.44	1.2071
2	0	995.0	10.76	1.0310
3	0	1650.0	29.95	1.0180
4	19	1240.0	29.69	1.0245
5	37	865.0	29.66	1.0359
6	37	634.0	20.25	1.0496
7	37	436.0	15.24	1.0727
8	37 (3W)	436.0	29.74	1.0727
9	37 (2W)	509.0	29.60	1.0621
10	37 (1W)	634.0	30.28	1.0496

Experiments 1, 2, and 3 display critical height vs the hydrogen to uranium-235 ratio (R) for nonvoid solutions. Experiments 3, 4, and 5 show the effect of increasing void fraction vs R for constant heights; and Experiments 5, 6, and 7, all having constant void fraction, show the variation of R with critical height. Experiments 8, 9, 10, and 5, all at constant critical height, provide a comparison of the effect of 3, 2, 1 and no tungsten cylindrical inserts, respectively, vs R.

A correction of -0.10 in. was applied to the solution heights given in Table 7.1 for Experiments 2 through 10 to account for the lower aluminum gridplate.

The ten experiments were done in cylindrical geometry, and were radially reflected with approximately six inches of water. The dimensions of the core and reflector vessels and the penetrating tubes are listed in Table 7.2. All vessel materials and tubes are fabricated of 6061 aluminum.

Table 7.2  
DIMENSIONS OF CRITICAL ASSEMBLIES

	o. d. (in.)	i. d. (in.)	Thickness	
			Wall (in.)	Base (in.)
Core Vessel	30.535	29.980	0.277	0.500
Reflector Vessel	43.475	42.475	0.50	0.50 sheet
Tubes	3.015	2.742	---	0.375

A triangular lattice pitch of 3.8 in. was used in all cases for the voided tubes.

Inserts of nested cylindrical tungsten tubes were used in Experiments 8-10. These tubes, fabricated of natural tungsten, were of the dimensions shown in Table 7.3.

Table 7.3  
DIMENSIONS OF TUNGSTEN TUBE INSERTS

	<u>o. d. (in.)</u>	<u>i. d. (in.)</u>	<u>Height (in.)</u>	<u>Av. Weight (gms)</u>
WL (Large)	2.637	2.597	36	1875
WM (Intermediate)	2.213	2.173	36	1612
WS (Small)	1.844	1.804	36	1287

Critical assemblies 4 through 10 which have penetrating tubes could not be represented by single region cores, since the cell structure did not extend over the entire assembly. For this reason these assemblies were considered to be two-region cores. The inner core region contained the tubes and had a diameter equivalent to that of a core of 37 hexagonal cells (19 in the case of Experiment 4). The region between the inner core diameter and the core vessel wall was calculated with a full density fuel solution. Volume fractions for the entire core are given in Table 7.4 along with the volume fractions of the Wigner-Seitz cell used in the inner core regions.

Table 7.4  
VOLUME FRACTIONS

Single Wigner-Seitz Cell of Experiments 4-10

Fuel Solution	0.4291
Aluminum Tube	0.0987
Central Space	<u>0.4722</u>
	1.0000

Entire Core (Excluding Reflector)

	<u>Dilute (Inner) Fuel Solution</u>	<u>Dense (Outer) Fuel Solution</u>	<u>Total</u>
Cores 1-3		1.000	1.000
Core 4	0.3367	0.6633	1.000
Cores 5-10	0.6555	0.3445	1.000



The inner core regions of Experiments 4-10 were uniformly homogenized into one mixture. The homogenized atom densities for all experiments are given in Table 7.5.

Table 7.5  
HOMOGENIZED ATOM DENSITIES

Lewis Critical Experiments  
(Atoms/b-cm multiplied by  $10^{14}$ )

Region of full density solution

Nuclide	<u>Experiment No.</u>									
	<u>1</u>	<u>2</u>	<u>3</u>	<u>4</u>	<u>5</u>	<u>6</u>	<u>7</u>	<u>8</u>	<u>9</u>	<u>10</u>
H	651.73	665.00	665.96	665.47	664.63	663.62	661.39	661.89	662.68	663.62
O	335.01	333.98	333.85	333.89	333.96	334.05	334.20	334.20	334.13	334.05
F	9.1510	1.4342	0.8661	1.1516	1.6488	2.2461	3.2577	3.2577	2.7938	2.2461
U <sup>234</sup>	0.0467	0.00733	0.00442	0.00589	0.00843	0.01147	0.01664	0.91664	0.01427	0.01147
U <sup>235</sup>	4.2640	0.6683	0.4036	0.5367	0.7684	1.0467	1.5181	1.5181	1.3019	1.0467
U <sup>236</sup>	0.0073	0.00114	0.00069	0.00092	0.00132	0.00180	0.00261	0.00261	0.00224	0.00180
U <sup>238</sup>	0.2570	0.04032	0.02429	0.03238	0.04635	0.06312	0.09154	0.09154	0.07848	0.06312

Region of voided tubes

Nuclide	<u>Experiment No.</u>							
	<u>4</u>	<u>5</u>	<u>6</u>	<u>7</u>	<u>8</u>	<u>9</u>	<u>10</u>	
H	285.55	285.19	284.76	284.02	284.02	284.36	284.76	
O	143.27	143.30	143.34	143.41	143.41	143.38	143.34	
F	0.4941	0.7075	0.9638	1.398	1.398	1.1988	0.9638	
Al	59.417	59.417	59.417	59.417	59.417	59.417	59.417	
W <sup>182</sup>	0.	0.	0.	0.	5.279	3.197	1.451	
W <sup>183</sup>	0.	0.	0.	0.	2.880	1.744	0.7916	
W <sup>184</sup>	0.	0.	0.	0.	6.119	3.705	1.682	
W <sup>186</sup>	0.	0.	0.	0.	5.679	3.439	1.561	
U <sup>234</sup>	0.002527	0.003617	0.00492	0.00714	0.00714	0.00612	0.00492	
U <sup>235</sup>	0.23029	0.3297	0.4491	0.6514	0.6514	0.5587	0.4491	
U <sup>236</sup>	0.000394	0.000566	0.000772	0.00112	0.00112	0.000961	0.000772	
U <sup>238</sup>	0.01389	0.01988	0.02708	0.03927	0.03927	0.03368	0.02708	

## 7.2 METHOD OF ANALYSIS

The procedure followed for analyzing the Lewis Critical Experiments adheres closely to the general procedure used in the precritical analyses of the Mockup Cores (see Section 6.1). More thermal groups were used, as seen in a listing of the group structure, given in Table 7.6. The B-1 approximation was used in solving for the epithermal spectra for all experiments, except Experiment 1, in which the B-3 approximation was employed. For this experiment, in which the core leakage is nearly 45 percent, particular care was exercised in using an accurate estimate of the core buckling in the spectrum calculation. Special collision probability tables were generated for the tungsten ring configurations in Experiments 8, 9, and 10, as discussed in Section 4.11.6.

Table 7.6

### SIXTEEN-GROUP STRUCTURE USED FOR LEWIS EXPERIMENT EIGENVALUE CALCULATIONS

<u>Group</u>	<u>Energy Range</u>		
1	3.68	to 14.9	MeV
2	2.02	to 3.68	"
3	0.907	to 2.02	"
4	0.0865	to 0.907	"
5	2.03	to 86.5	keV
6	0.0614	to 2.03	"
7	2.38	to 61.4	eV
8	0.414	to 2.38	"
9	0.100	to 0.414	"
10	0.070	to 0.100	"
11	0.050	to 0.070	"
12	0.040	to 0.050	"
13	0.030	to 0.040	"
14	0.020	to 0.030	"
15	0.010	to 0.020	"
16	0.0	to 0.010	"

Thermal disadvantage factors were also calculated for these three cores.

For Cores 1 through 3, one-dimensional buckling iterations in both the diffusion approximation and transport theory, were used to obtain  $k_{\text{eff}}$ . Cores 4 through 10 have two distinct radial regions. The inner, voided region was treated by simple homogenization. For these experiments, an axial geometric buckling was used to represent the transverse leakage from each of the two radial regions in radial transport and diffusion calculations. The group bucklings,  $B_i^2$ , were calculated from the equation:

$$B_i^2 = \left[ \frac{\pi}{H + 2(0.7104\lambda_{\text{tr}_i})} \right]^2, \quad (7.1)$$

where  $H$  is the core height and  $0.7104\lambda_{\text{tr}_i}$  is the extrapolation distance. The aluminum tank walls were explicitly represented in the radial calculations for all experiments, whereas the tank bottom was explicitly represented in the axial calculations of only Experiments 1 through 3. The worth of the tank bottom was calculated to be +0.1% in reactivity, and the quoted multiplication factors contain this correction.

The validity of the geometric buckling method for representing the axial leakage in Experiments 4 through 10 was assessed by performing transport calculations in the axial dimension for Cores 3, 5, and 8. The results are shown in Table 7.7, where the axial group leakages,  $L_i = D_i B_i^2 \phi_i$ , are compared for the two methods. Although significant differences in group leakages occur, the total axial leakages compare closely for all three cores.

Table 7.7  
AXIAL LEAKAGES/SOURCE NEUTRON

Group	Expt. 3 Entire Core H/U-235 = 1650		Expt. 5 Inner Core Region H/U-235 = 865		Expt. 8 Inner Core Region H/U-235 = 436	
	Geometric B <sup>2</sup> Method	Transport Method	Geometric B <sup>2</sup> Method	Transport Method	Geometric B <sup>2</sup> Method	Transport Method
1	4.05-3	2.84-3	5.62-3	5.07-3	3.73-3	3.61-3
2	6.51-3	4.84-3	10.32-3	9.36-3	6.80-3	6.54-3
3	6.53-3	4.91-3	11.35-3	10.03-3	7.58-3	7.07-3
4	7.96-3	6.58-3	15.05-3	13.74-3	10.72-3	10.46-3
5	3.58-3	3.76-3	7.40-3	7.73-3	5.36-3	5.79-3
6	2.30-3	2.80-3	5.15-3	5.68-3	2.97-3	3.88-3
7	1.89-3	2.38-3	4.37-3	4.82-3	1.89-3	2.12-3
Sub total	0.0328	0.0281	0.0593	0.0564	0.0391	0.0395
8	0.88-3	1.34-3	1.39-3	2.71-3	1.23-3	1.49-3
9	1.39-3	1.90-3	2.33-3	3.23-3	0.98-3	1.34-3
10	0.96-3	1.40-3	1.48-3	2.03-3	0.37-3	0.55-3
11	1.08-3	1.56-3	1.59-3	2.21-3	0.35-3	0.54-3
12	0.63-3	0.94-3	0.91-3	1.32-3	0.18-3	0.30-3
13	0.60-3	0.96-3	0.88-3	1.34-3	0.16-3	0.28-3
14	0.51-3	0.88-3	0.74-3	1.22-3	0.12-3	0.24-3
15	0.35-3	0.67-3	0.55-3	0.92-3	0.07-3	0.16-3
16	0.12-3	0.26-3	0.18-3	0.36-3	0.02-3	0.06-3
Sub total	0.0065	0.0099	0.0100	0.0153	0.0035	0.0050
Total	0.0393	0.0380	0.0693	0.0717	0.0426	0.0445

## 7.3 RESULTS

### 7.3.1 EXPERIMENT 1

The results for Experiment 1 are shown in Table 7.8. The first value of 0.952 for the multiplication factor resulted from diffusion calculations in both the axial and radial directions. The axial leakage was overestimated by the diffusion code. The same radial leakage was then used in a transport calculation of the axial problem. The results for both  $P_1$  anisotropic scattering and  $P_3$  anisotropic scattering show good agreement with the expected value of 1.0.

Table 7.8  
RESULTS FOR ZPR 1

<u>Method</u>	<u>k<sub>eff</sub></u>	<u>Radial Core Leakage</u>	<u>Axial Core Leakage</u>
GAZE radial	0.952	0.056	0.421
GAZE axial			
GAZE radial	0.991	0.056	0.404
GAPLSN P <sub>1</sub> S <sub>8</sub> axial			
GAZE radial	0.996	0.056	0.402
GAPLSN P <sub>3</sub> S <sub>8</sub> axial			

### 7.3.2 EXPERIMENT 2

The results of the one-dimensional synthesis are given in Table 7.9.

Table 7.9  
RESULTS FOR ZPR 2

<u>Method</u>	<u>k<sub>eff</sub></u>	<u>Radial Core Leakage</u>	<u>Axial Core Leakage</u>
GAZE radial	0.972	0.073	0.216
GAZE axial			
GAZE radial	0.993	0.073	0.200
GAPLSN P <sub>1</sub> S <sub>8</sub> axial			

The GAZE axial calculation is closer to the GAPLSN axial calculation as expected in this 10.76 in. high core.

### 7.3.3 EXPERIMENT 3

The results are given in Table 7.10.

Table 7.10  
RESULTS FOR ZPR 3

<u>Method</u>	<u>k<sub>eff</sub></u>	<u>Radial Core Leakage</u>	<u>Axial Core Leakage</u>
GAZE radial	0.988	0.083	0.041
GAZE axial			
GAZE radial	0.991	0.083	0.036
GAPLSN P <sub>1</sub> S <sub>4</sub> axial			

Since Experiment 3 was the first in the series to have a nominal height of 30 in., it is of interest to compare the neutron energy spectrum and radial flux shape for this one-region, very thermal assembly with other 30 in. assemblies. The infinite-media spectrum for Experiment 3 is shown in Figs. 7.1 and 7.2. The radial thermal ( $E < 2.38$  eV) flux shape is illustrated in Fig. 7.3. The thermal and fast spectra of Experiment 3 are characteristic of a well-moderated assembly.

#### 7.3.4 EXPERIMENT 4

This critical assembly was the first of the series to have a two-region core. The assembly contained nineteen void tubes. The inner core equivalent radius was 22.09 cm. Results of eigenvalue calculations are given in Table 7.11.

Table 7.11  
RESULTS FOR ZPR 4

<u>Method</u>	<u>k<sub>eff</sub></u>	<u>Radial Core Leakage</u>	<u>Axial Core Leakage</u>
GAZE radial	1.016	0.1321	0.0631
GAPLSN radial	1.029	0.1272	0.0624

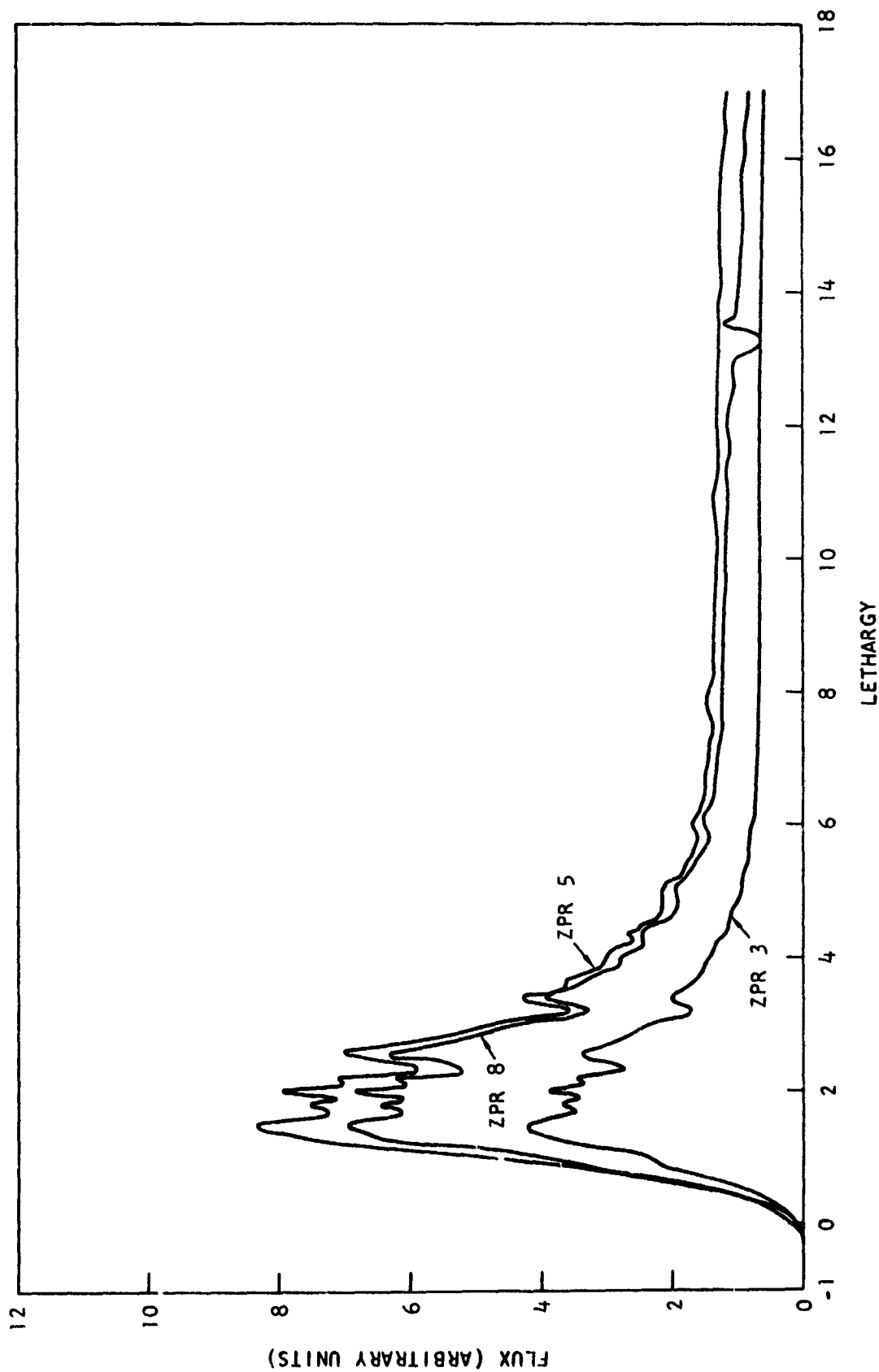


Fig. 7.1--Fast neutron spectra at inner regions of ZPR cores 3, 5, and 8  
(Normalized to one source neutron)

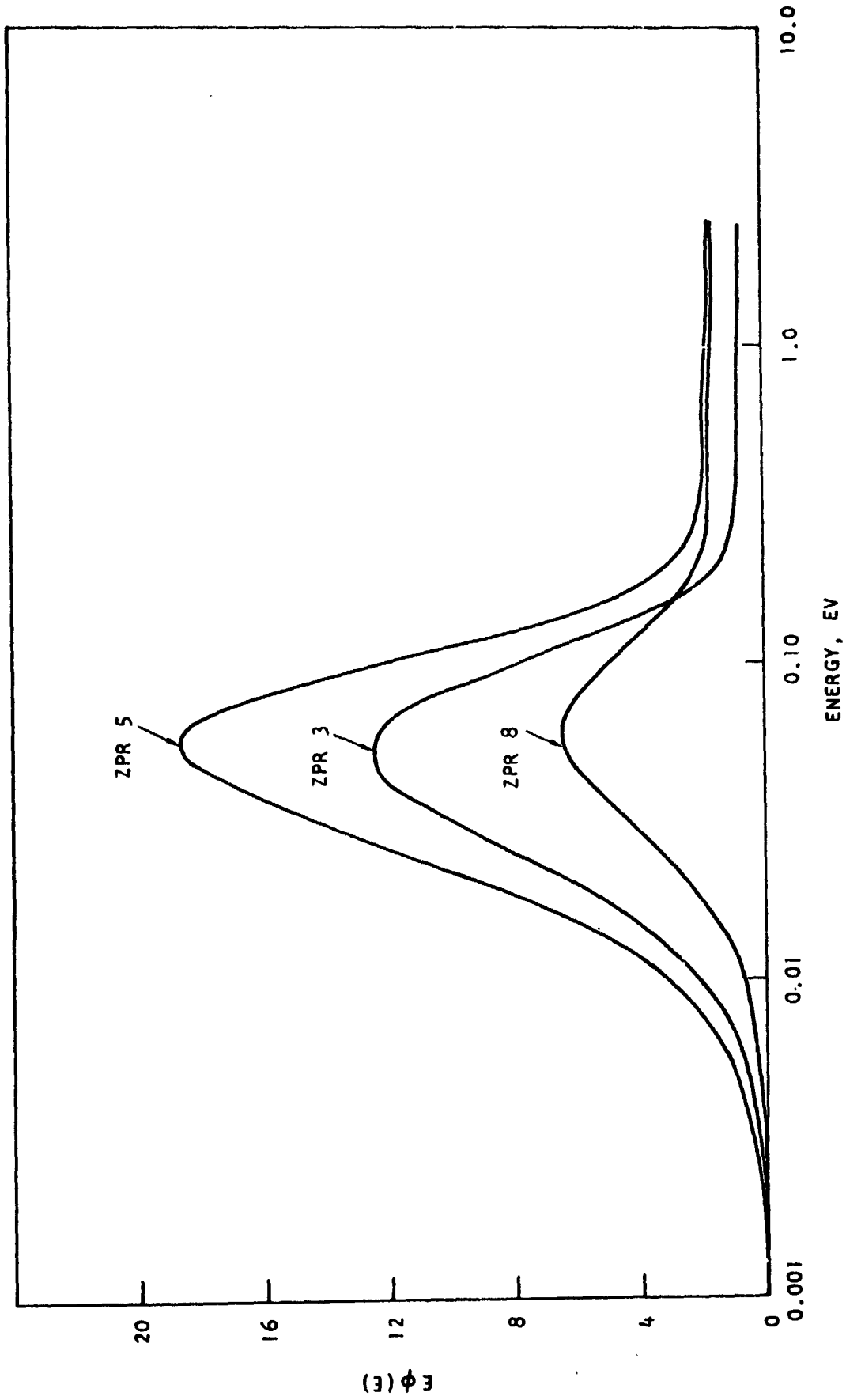


Fig. 7.2--Thermal neutron spectra at inner regions of ZPR cores 3, 5, and 8  
(Normalized to one neutron slowing down below 2.38 eV)



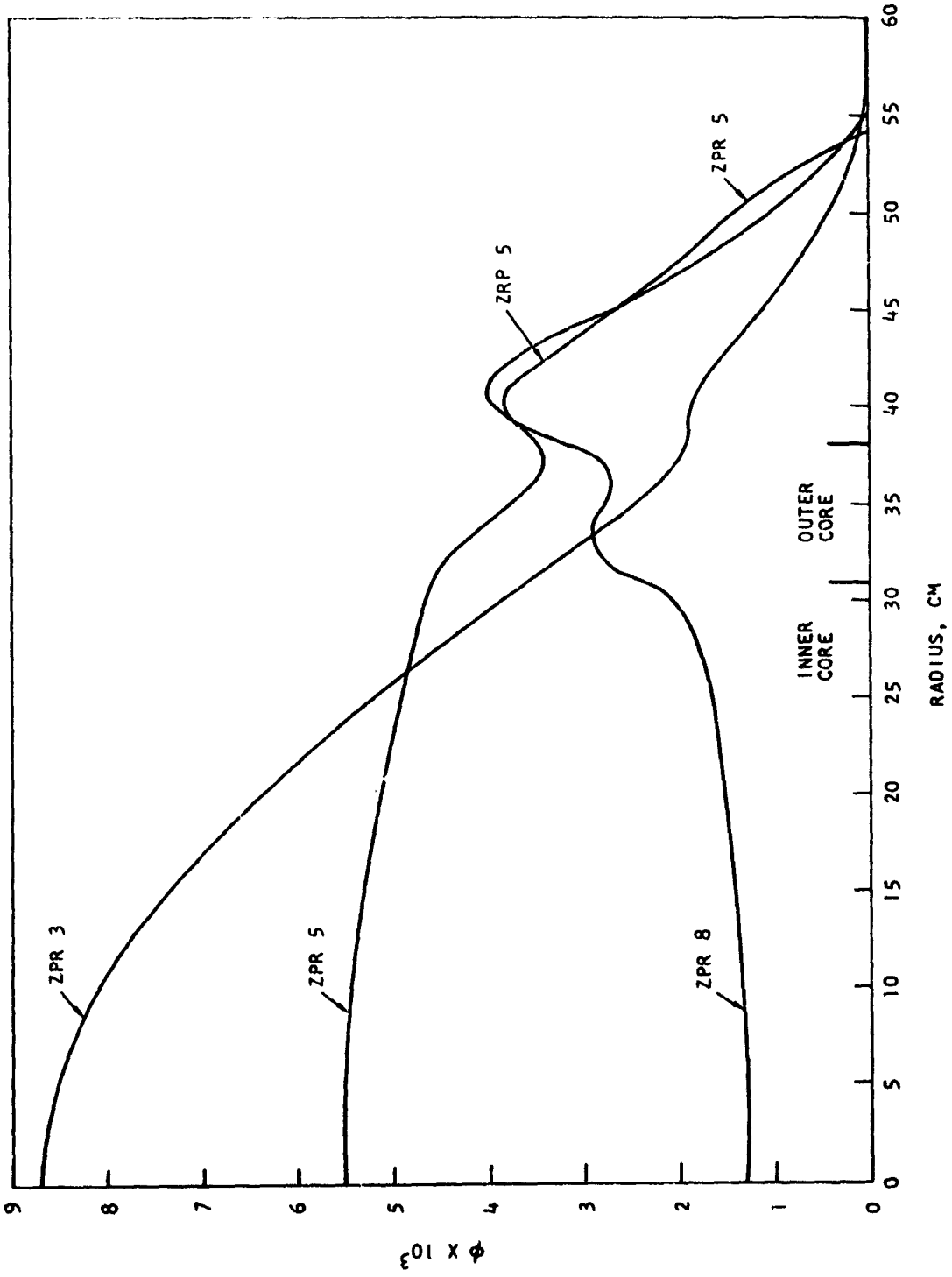


Fig. 7.3--Thermal radial flux profiles

## 7.3.5 EXPERIMENT 5

This critical assembly was the first in the series to have a whole complement of 37 tubes and the same height (nominal 30 in.) as those assemblies with tungsten inserts. As such it provides an endpoint for calculation of the effect of the tungsten inserts. The results for this experiment are given in Table 7.12. Infinite media spectra for the inner core region are shown in Figs. 7.1 and 7.2, and the thermal radial flux profile is shown in Fig. 7.3. The influence of the outer core region, or "driver," is apparent on the thermal flux.

Table 7.12  
RESULTS FOR ZPR 5

<u>Method</u>	<u>k<sub>eff</sub></u>	<u>Radial Core Leakage</u>	<u>Axial Core Leakage</u>
GAZE radial	1.024	0.1794	0.0822
GAPLSN radial	1.041	0.1721	0.0824

The inclusion of a Behrens' correction<sup>(61)</sup> was studied in this assembly. Anisotropic diffusion coefficients were derived for radial and axial directions in the inner core region. The resultant correction was applied to the transport cross sections and to the extrapolation distances appearing in the calculated leakage terms. The corrections to each group *i* were made through the formulae:

$$\frac{D_{1i}}{D_o} = 1 + 2\phi + \left\{ \phi^2 \left( \frac{2r}{\lambda} \right) \left[ \exp \left( \frac{2r}{\phi\lambda} \right) - 1 \right]^{-1} \right\} + \frac{2r\phi}{\lambda}, \quad (7.2)$$

and,

$$\frac{D_1}{D_0} = 1 + 2\phi + \left[ \phi^2 \left( \frac{2r}{\lambda} \right) \left[ \exp \left( \frac{2r}{\lambda} \right) - 1 \right]^{-1} \right] + \frac{r\phi}{\lambda}, \quad (7.3)$$

where:

- $\phi$  = volume of holes/volume of material
- $r$  = hydraulic radius
- $\lambda$  = mean free path through solid material
- $D_0$  = diffusion coefficient for solid material.

The resultant eigenvalue is 0.94, indicating that the axial leakage in the voided region is overestimated by this method. The Benoist<sup>(62)</sup> second- and third-order treatments gave similar results.

### 7.3.6 EXPERIMENT 6

The results for this 20-in. high core, which had 37 voided tubes, are given in the following table:

Table 7.13  
RESULTS FOR ZPR 6

<u>Method</u>	<u>k<sub>eff</sub></u>	<u>Radial Core Leakage</u>	<u>Axial Core Leakage</u>
GAZE radial	1.024	0.1752	0.1442
GAPLSN Radial	1.042	0.1674	0.1460

### 7.3.7 EXPERIMENT 7

This 15-in. high core also had 37 voided tubes. Results are shown in Table 7.14.

Table 7.14  
RESULTS FOR ZPR 7

<u>Method</u>	<u>k<sub>eff</sub></u>	<u>Radial Core Leakage</u>	<u>Axial Core Leakage</u>
GAZE Radial	1.011	0.1703	0.2073
GAPLSN Radial	1.020	0.1659	0.2120

As expected, the diffusion calculations on shorter cores consistently give eigenvalues somewhat lower than on the longer cores.

### 7.3.8 EXPERIMENT 8

Experiment 8 had three tungsten sleeves inserted in each tube. The results of the eigenvalue calculations are shown in Table 7.15.

Table 7.15  
RESULTS FOR ZPR 8

<u>Method</u>	<u>k<sub>eff</sub></u>	<u>Radial Core Leakage</u>	<u>Axial Core Leakage</u>
GAZE Radial	0.970	0.2000	0.0596
GAPLSN Radial	0.991	0.2034	0.0589

Infinite media spectra are shown in Figs. 7.1 and 7.2 for the inner core regions of Experiment 8. The resonance absorption of the tungsten-186 isotope is apparent at a lethargy of 13.25 in the slowing-down spectrum. High absorption in the thermal energy range is apparent in the radial flux profile of Fig. 7.3.

A GAMBLE two-dimensional calculation was also done for Experiment 8. A comparison to the GAZE results for total capture, fission, and leakage rates is given in Table 7.16. The good agreement supports the validity of using the one-dimensional technique.

Table 7. 16

## COMPARISON OF GAZE AND GAMBLE, EXPERIMENT 8

	<u>GAZE</u>	<u>GAMBLE</u>
Total Flux/Source Neutron	45.40	45.46
Total Captures/Source Neutron	.5052	.5044
Total Fissions/Source Neutron	.3988	.4023
Total Leakage/Source Neutron	.09619	.09336

## 7.3.9 EXPERIMENT 9

This assembly had two cylindrical tungsten inserts per tube. The analysis of Experiment 9 gave the following results:

Table 7. 17

## RESULTS FOR ZPR 9

<u>Method</u>	<u>k<sub>eff</sub></u>	<u>Radial Core Leakage</u>	<u>Axial Core Leakage</u>
GAZE Radial	0.978	0.1973	0.0656
GAPLSN Radial	0.997	0.1950	0.0656

## 7.3.10 EXPERIMENT 10

With one cylindrical tungsten insert per tube, and the same critical height as Experiments 8 and 9, the analysis of Experiment 10 gave the following results:

Table 7. 18

## RESULTS FOR ZPR 10

<u>Method</u>	<u>k<sub>eff</sub></u>	<u>Radial Core Leakage</u>	<u>Axial Core Leakage</u>
GAZE Radial	0.990	0.1903	0.0702
GAPLSN Radial	1.004	0.1853	0.0708

7.4 SUMMARY OF RESULTS

A summary tabulation of all the results for all the experiments is given in Table 7.19. Neutron balances are exhibited in Tables 7.20 through 7.23. The balance tables are grouped into sets according to the parameters varied, as indicated in Section 7.1. They illustrate the relative competition of capture, fission, and leakage in the neutron balance. All tables are normalized to one source neutron.

Table 7.19

SUMMARY OF RESULTS

<u>Expt. No.</u>	<u><math>N_H/N_{U-235}</math></u>	<u>Critical Ht., in.</u>	<u>Tubes</u>	<u>Division Calc. (GAZE)</u>	<u>Transport Calc. (GAPLSN)</u>
1	152.9	5.44	0	0.952	0.991 $P_1S_8$ 0.996 $P_3S_8$
2	995.0	10.76	0	0.972	0.993 $P_1S_8$
3	1650.0	29.95	0	0.988	0.991 $P_1S_4$
4	1240.0	29.69	19	1.016	1.029 <sup>a</sup> $P_1S_8$
5	865.0	29.66	37	1.024	1.041 <sup>a</sup> $P_1S_8$
6	634.0	20.25	37	1.024	1.042 $P_1S_8$
7	436.0	15.24	37	1.011	1.020 $P_1S_8$
8	436.0	29.74	37(3W) <sup>b</sup>	0.970	0.991 $P_1S_8$
9	509.0	29.60	37(2W) <sup>b</sup>	0.978	0.997 $P_1S_8$
10	634.0	30.28	37(1W) <sup>b</sup>	0.990	1.004 $P_1S_8$

<sup>a</sup>Extrapolated from nearly converged problems

<sup>b</sup>(3W) indicates three tungsten cylindrical inserts, etc.

Table 7.20  
NEUTRON BALANCE

Parameters Varied:  $N_H/N_{U-235}$ , Height

Parameters Fixed: No. of Tubes (None)

Nuclide	Experiment 1 Ht = 5.44 in.		Experiment 2 Ht = 10.76 in.		Experiment 3 Ht = 29.95 in.	
	Cap.	Fiss.	Cap.	Fiss.	Cap.	Fiss.
H	3.668-2 <sup>(1)</sup>		2.388-1		3.928-1	
O	2.235-3		2.745-3		3.045-3	
F	1.566-4		4.276-5		3.371-5	
Al	0.0		0.0		0.0	
U-234	1.855-3	3.848-5	1.059-3	7.170-6	9.778-4	4.708-6
U-235	8.876-2	4.075-1	7.503-2	4.085-1	7.383-2	4.065-1
U-236	9.606-5	2.826-6	2.860-5	5.255-7	2.251-5	3.472-7
U-238	2.608-3	5.155-5	7.196-4	9.674-6	5.360-4	6.377-6
Core Totals	1.324-1	4.076-1	3.184-1	4.085-1	4.712-1	4.065-1

Core Captures	1.324-1	3.184-1	4.712-1
Core Fissions	4.076-1	4.085-1	4.065-1
Core Rad. Lkg.	5.623-2	7.330-2	8.340-2
Core Ax. Lkg.	<u>4.033-1</u>	<u>1.992-1</u>	<u>3.582-2</u>
	0.9995 <sup>(2)</sup>	0.9994 <sup>(2)</sup>	0.9969

(1) Multiplicative powers of ten are denoted in this and subsequent tables by a sign and number; thus, 3.0-2 indicates  $3.0 \times 10^{-2}$ .

(2) These neutron balance tables were constructed from the final GAPLSN edit for the axial direction. Absorptions in the reflector are thus not explicitly represented.

Table 7.21  
NEUTRON BALANCE

Parameters Varied:  $N_H/N_{U-235}$ , Voided Tubes

Parameters Fixed: Height

Nuclide	Experiment 3 No Voids		Experiment 4 19 Void Tubes		Experiment 5 37 Void Tubes	
	Cap.	Fiss.	Cap.	Fiss.	Cap.	Fiss.
H	3.928-1		3.010-1		2.137-1	
O	3.045-3		2.772-3		2.352-3	
F	3.371-5		3.777-5		4.344-5	
Al	0.0		9.968-3		1.683-2	
U-234	9.778-4	4.708-6	1.033-3	5.786-6	1.107-3	7.569-6
U-235	7.383-2	4.065-1	7.519-2	4.133-1	7.750-2	4.205-1
U-236	2.251-5	3.472-7	2.582-5	4.252-7	3.109-5	5.512-7
U-238	5.360-4	6.377-6	6.309-4	7.790-6	7.842-4	1.001-5
Core Totals	<u>4.712-1</u>	<u>4.065-1</u>	<u>3.907-1</u>	<u>4.133-1</u>	<u>3.123-1</u>	<u>4.205-1</u>
Refl. H	7.390-2		1.022-1		1.387-1	
Refl. O	2.491-4		3.936-4		5.243-4	
Al Vessel	4.041-3		5.538-3		6.620-3	
Total Captures	5.494-1		4.988-1		4.582-1	
Total Fissions	4.065-1		4.133-1		4.205-1	
Tot. Rad. Lkg.	9.779-3		1.240-2		1.757-2	
Tot. Ax. Lkg.	<u>4.126-2</u>		<u>7.180-2</u>		<u>1.016-1</u>	
	1.0069		0.9963		0.9979	

Totals do not add to 1.0000 due to the approximate nature of the neutron current calculations in the GAZE diffusion code. This is reflected in a slight error in the radial leakage rates and hence the neutron balance.



Table 7.22  
NEUTRON BALANCE

Parameters Varied:  $N_H/N_{U-235}$ , Height

Parameters Fixed: No. of Voided Tubes (37)

Nuclide	Experiment 5 Ht = 29.66 in.		Experiment 6 Ht = 20.25 in.		Experiment 7 Ht = 15.24 in.	
	<u>Cap.</u>	<u>Fiss.</u>	<u>Cap.</u>	<u>Fiss.</u>	<u>Cap.</u>	<u>Fiss.</u>
H	2.137-1		1.562-1		1.038-1	
O	2.352-3		2.188-3		2.069-3	
F	4.344-5		5.078-5		6.266-5	
Al	1.683-2		1.178-2		7.338-3	
U-234	1.107-3	7.569-6	1.167-3	9.723-6	1.235-3	1.317-5
U-235	7.750-2	4.205-1	7.833-2	4.189-1	7.746-2	4.045-1
U-236	3.109-5	5.512-7	3.642-5	7.080-7	4.416-5	9.625-7
U-238	7.842-4	1.001-5	9.405-4	1.281-5	1.166-3	1.741-5
Core Totals	<u>3.123-1</u>	<u>4.205-1</u>	<u>2.507-1</u>	<u>4.189-1</u>	<u>1.932-1</u>	<u>4.045-1</u>
Refl. H	1.387-1		1.319-1		1.182-1	
Refl. O	5.243-4		5.169-4		5.256-4	
Al Vessel	6.620-3		5.712-3		4.642-3	
Total Captures	4.582-1		3.889-1		3.166-1	
Total Fissions	4.205-1		4.189-1		4.045-1	
Tot. Rad. Lkg.	1.757-2		1.698-2		1.576-2	
Tot. Ax. Lkg.	<u>1.016-1</u>		<u>1.781-1</u>		<u>2.593-1</u>	
	0.9979		1.0029		0.9962	

Table 7.23

## NEUTRON BALANCE

Nuclide	Experiment 8 3 Tungsten Inserts/Tube		Experiment 9 2 Tungsten Inserts/Tube		Experiment 10 1 Tungsten Inserts/Tube		Experiment 5 Voided Tubes	
	Cap.	Fiss.	Cap.	Fiss.	Cap.	Fiss.	Cap.	Fiss.
H	1.021-1		1.202-1		1.517-1		2.137-1	
O	2.185-3		2.272-3		2.284-3		2.352-3	
F1	6.550-5		5.977-5		5.183-5		4.344-5	
Al	4.111-3		5.872-3		9.119-3		1.683-2	
W-182	3.906-2		3.305-2		2.386-2		0.0	
W-183	2.097-2		1.644-2		1.103-2		0.0	
W-184	4.602-3		3.766-3		2.601-3		0.0	
W-186	7.583-2		6.496-2		4.706-2		0.0	
U-234	1.265-3	1.397-5	1.217-3	1.218-5	1.159-3	1.005-5	1.107-3	7.569-6
U-235	7.700-2	3.974-1	7.669-2	4.013-1	7.647-2	4.067-1	7.750-2	4.205-1
U-236	4.781-5	1.015-6	4.321-5	8.902-7	3.754-5	7.320-7	3.109-5	5.512-7
U-238	1.230-3	1.836-5	1.106-3	1.611-5	9.603-4	1.326-5	7.842-4	1.001-5
Core Totals	3.284-1	3.977-1	3.257-1	4.013-1	3.264-1	4.067-1	3.123-1	4.205-1
Ref. H	1.632-1		1.572-1		1.517-1		1.387-1	
Ref. O	6.742-4		6.489-4		5.914-4		5.243-4	
Al Vessel	512-3		6.627-3		6.786-3		6.620-3	
Total Captures	4.989-1		4.902-1		4.855-1		4.582-1	
Total Fission	3.977-1		4.013-1		4.067-1		4.205-1	
Total Rad. Lkg.	2.250-2		2.132-2		2.014-2		1.757-2	
Total Axial Lkg.	7.717-2		8.335-2		8.743-2		1.016-1	
	0.9953		0.9962		0.9997		0.9979	

Experiments 1, 2, and 3 show good agreement with experimental results and indicate that a leakage iteration technique gives good results even in very small cores. The eigenvalues for Experiments 3, 4, and 5 show a significant trend toward overestimation of the eigenvalue as the number of voided tubes increases. The eigenvalues for Experiments 5, 6, and 7 are high. The eigenvalues for Experiments 8, 9, and 10 show good agreement with experiment, indicating only a minor trend.

In all calculations, the atom densities for natural tungsten was assumed to be 0.0600 atom/b-cm, corresponding to a density of 95% that of theoretical. The density is inconsistent with the weights quoted in Table 7.3 for a 0.020 in. thick sleeve; the average atom density calculated from these weights is 0.0635 atom/b-cm.

The apparently higher density may be due to a slightly larger wall thickness in the tungsten tubes, or a higher density than 95% of theoretical. If it is consistent and real, the effect on the eigenvalue calculations would be not more than that shown in Table 7.24.

Table 7.24

**MAXIMUM ESTIMATED EFFECT ON EIGENVALUE OF USING  
A TUNGSTEN DENSITY OF 0.0635 ATOM/b-CM**

<u>Experiment</u>	<u><math>\Delta k/k</math></u>
8	- 0.012
9	- 0.010
10	- 0.007

**7.5 RECALCULATION OF EXPERIMENTS 5 AND 10**

The most striking comparison in the results summarized by Table 7.19 is that between Experiments 5 and 10. Differing in configuration only by the presence of a 20-mil ring of tungsten within the void in Experiment 10, the calculated multiplication factors are separated by approximately 4%. This apparent anomaly prompted a re-examination of these two experiments. The same method of analysis was used; however, the following changes were incorporated in the recalculation:

1. The final set of tables relating atom densities to solution densities released on 1/7/65(63) were used. The revised atom densities corrected for temperature are listed in Table 7.25.

Table 7.25

REVISED HOMOGENIZED ATOM DENSITIES FOR  
LEWIS CRITICAL EXPERIMENTS NOS. 5 AND 10  
(Atoms/b-cm Multiplied by  $10^4$ )

## REGION OF FULL DENSITY SOLUTION

<u>Nuclide</u>	<u>Experiment No. 5</u>	<u>Experiment No. 10</u>
H	664.9	663.9
$\phi$	334.1	334.2
F	1.622	2.203
$U^{234}$	0.00829	0.01124
$U^{235}$	0.7559	1.0265
$U^{236}$	0.00129	0.00177
$U^{238}$	0.0551	0.0747

## REGION OF VOIDED TUBES

<u>Nuclide</u>	<u>Experiment No. 5</u>	<u>Experiment No. 10</u>
H	285.3	284.9
$\phi$	143.35	143.4
F	0.6959	0.9452
Al	59.42	59.42
$W^{182}$	0.0	1.538
$W^{183}$	0.0	0.8391
$W^{184}$	0.0	1.783
$W^{186}$	0.0	1.655
$U^{234}$	0.00356	0.00482
$U^{235}$	0.3243	0.4404
$U^{236}$	0.000553	0.000759
$U^{238}$	0.02363	0.03205

2. The value of 0.0635 atom/b-cm, obtained from the measured tungsten ring weights, was used for the atom density of tungsten.
3. Revised values of the bucklings, obtained from the previous final diffusion calculations for each experiment, were used in the calculation of the spectrum. These bucklings are listed in Table 7.26.
4. The P-1 source terms to the GATHER code were previously incorrect due to an error in the GAM code. This error gave rise to fallacious thermal current spectra and thermal transport cross sections. In the present calculations source terms derived from a 1/E slowing-down flux were used.

The results of the calculations are given in Table 7.27. The multiplication constants and core leakages are tabulated for each experiment, comparing diffusion and transport calculations. The transport calculations were incompletely converged (hence leakage fractions are not given for the GAPLSN calculations); however, convergence was of sufficient uniformity to permit extrapolation to the converged eigenvalue with a high degree of confidence. Complete neutron balances from the GAZE diffusion calculations are given in Table 7.28.

Table 7.26

**BUCKLING USED IN SPECTRUM CALCULATIONS FOR  
LEWIS EXPERIMENTS NOS. 5 AND 10  
( $B^2$  in  $\text{cm}^{-2}$ )**

	<u>Inner Core</u>		<u>Outer Core</u>	
	<u>Fast</u>	<u>Thermal</u>	<u>Fast</u>	<u>Thermal</u>
Experiment 5	0.00226	0.00202	0.01762	0.0
Experiment 10	0.00163	0.00063	0.02303	0.0

Table 7.27  
 RESULTS OF RECALCULATION OF  
 EXPERIMENTS NOS. 5 AND 10

	$k_{\text{eff}}$	<u>Radial Core Leakage</u>		<u>Axial Core Leakage</u>	
		<u>Fast</u>	<u>Thermal</u>	<u>Fast</u>	<u>Thermal</u>
Experiment No. 5					
GAZE	1.015	0.175	- 0.002	0.0761	0.0138
GAPLSN	1.025	---	---	----	----
Experiment No. 10					
GAZE	0.955	0.203	- 0.0108	0.0641	0.0090
GAPLSN	0.971	---	---	----	----

## 7.6 DISCUSSION AND CONCLUSIONS

The small homogeneous Lewis cores of Experiments 1, 2, and 3 are predicted well by one-dimensional transport theory. Diffusion theory gives errors as high as 5% in multiplication. Special care is necessary in considering the effects of over-all core leakage on the cross sections. The results of Experiments 3, 4, and 5 indicate that the homogenization procedure is inadequate for treating the streaming problem associated with void introduction, with the results demonstrating a trend toward greater overestimation of the multiplication factor as the number of voids is increased. The application of Behrens and Benoist corrections for anisotropic streaming highly overestimates the magnitude of the axial leakage, and thus these methods appear to be inadequate for handling this problem. The results of Experiment 5 and 6 suggest that the error in the predicted multiplication factor is insensitive to the ratio of void radius to core height, although the result of Experiment 7 indicates an apparent inverse relationship. Although the results for Experiments 8, 9, and 10 demonstrate good agreement with experiment, the question arises as to why the presence of a thin tungsten ring inside the voids apparently eliminates the streaming problem associated with the purely voided tubes.

Table 7.28

## NEUTRON BALANCE FROM RECALCULATION

## LEWIS EXPERIMENT NO. 5

	<u>Nuclide</u>	<u>Capture</u>	<u>Fission</u>
H		2.159-1	
$\phi$		2.382-3	
F		4.308-5	
Al*		2.368-2	
U-234		1.097-3	7.431-6
U-235		7.692-2	4.177-1
U-236		3.043-5	5.397-7
U-238		<u>9.322-4</u>	<u>1.086-5</u>
Core Total		3.235-1	4.177-1
Reflector H		1.391-1	
Reflector O		5.397-4	
Total Capture		4.606-1	
Total Fission		4.177-1	
Fast Radial Leakage		8.518-3	
Thermal Radial Leakage		8.776-3	
Fast Axial Leakage		8.294-2	
Thermal Axial Leakage		<u>1.859-2</u>	
		0.9971	

## LEWIS EXPERIMENT NO. 10

	<u>Nuclide</u>	<u>Capture</u>	<u>Fission</u>
H		1.496-1	
$\phi$		2.299-3	
F		5.058-5	
Al*		1.632-2	
W <sup>182</sup>		2.733-2	
W <sup>183</sup>		1.162-2	
W <sup>184</sup>		2.999-3	
W <sup>186</sup>		5.512-2	
U <sup>234</sup>		1.121-3	9.753-6
U <sup>235</sup>		7.391-2	3.930-1
U <sup>236</sup>		3.655-5	7.156-7
U <sup>238</sup>		<u>1.124-3</u>	<u>1.421-5</u>
Core Total		3.415-1	3.930-1
Reflector H		1.559-1	
Reflector O		6.261-4	
Total Capture		4.980-1	
Total Fission		3.930-1	
Fast Radial Leakage		1.004-2	
Thermal Radial Leakage		1.013-2	
Fast Axial Leakage		7.190-2	
Thermal Axial Leakage		<u>1.395-2</u>	
		0.9970	

\* Including aluminum vessel.

The unusually large spread between transport and diffusion theory in the calculated values of the multiplication factors for Experiments 4 through 10 is due to the two-region nature of these cores. The material discontinuities, where diffusion theory breaks down, are in an exceptionally high worth region of the cores. The effect is demonstrated in Fig. 7.4, where the calculated radial fission source distribution is plotted. Both the GAZE and GAPLSN source densities are normalized to make the total absorptions plus leakage equal to unity, and, thus making the integral under each curve equal to the multiplication factor.

The most striking result of these calculations is the apparent elimination of neutron streaming by the introduction of thin tungsten rings into the voids. The best demonstration of this effect is afforded by a comparison between Experiments 5 and 10, which differ principally by the existence of a 20-mil tungsten ring in the voids of Experiment 10. The initial results, given in Table 7.19, indicate a spread in  $k_{\text{eff}}$  of approximately 4% between the two experiments. The results of recalculations, given in Table 7.27, indicate an even larger spread of approximately 5% and this difference is apparently caused by neutron streaming in Experiment 5.

The recalculations also indicate a general decrease in  $k_{\text{eff}}$  of 1.5 to 2% for both experiments. The principal reasons for this change are the increased tungsten atom densities and the decreased  $\text{U}^{235}$  densities in the solution. (The error in the previous diffusion coefficients is reflected principally by the diffusion theory results.) The recalculation of Experiment 10 suggests that the previous agreement with experiment for Experiments 8, 9, and 10 was fortuitous.

It is concluded that the present treatment of the voids by homogenization is inadequate. A more sophisticated treatment of the axial leakage, involving two-dimensional transport calculations of the voided cells, was initiated at General Atomic and is being pursued at the Lewis Research Center.



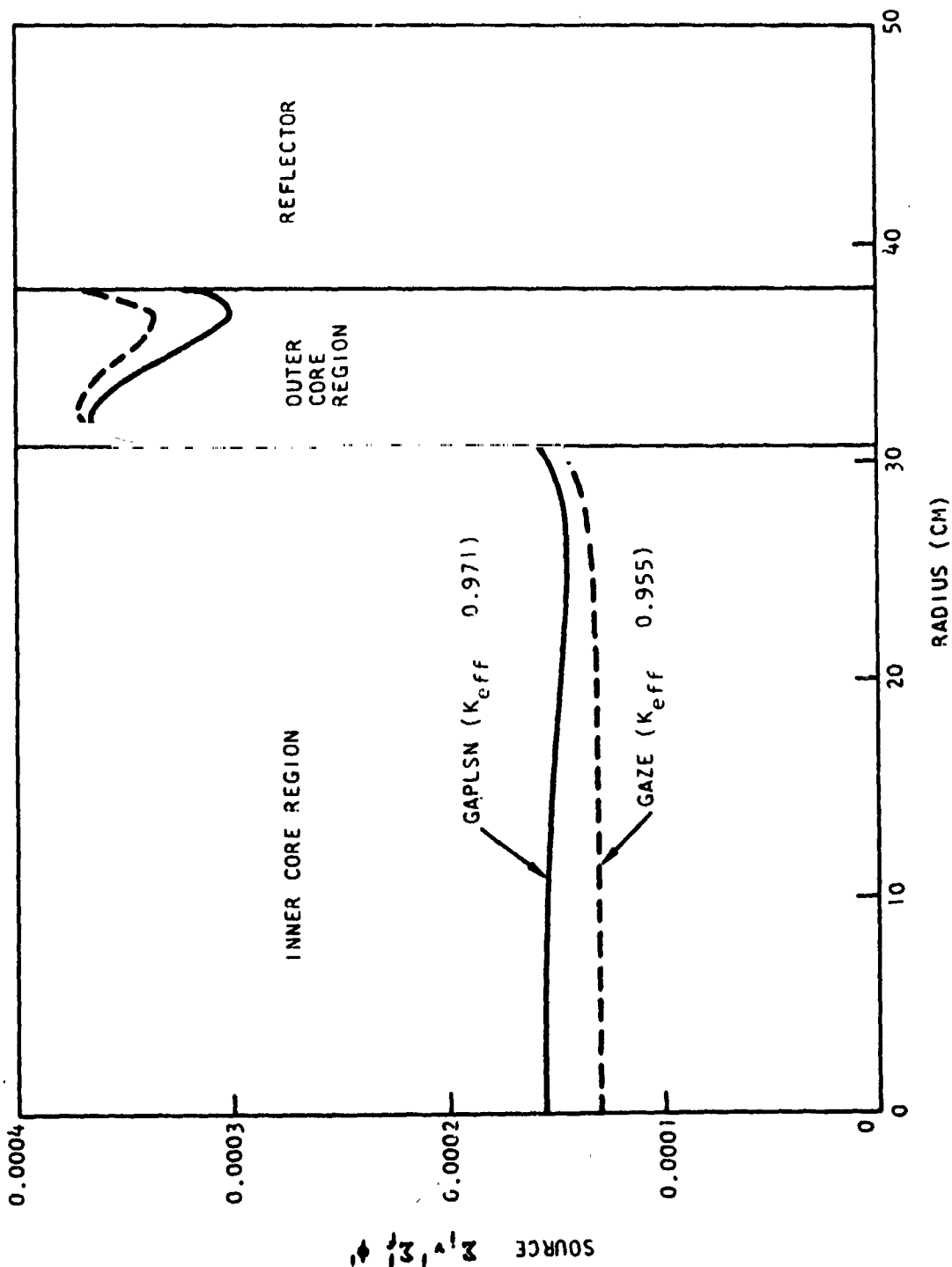


Fig. 7.4--Fission source vs radius. Lewis experiment No. 10  
(normalized to: absorptions plus leakage = 1.0)

## VIII. DISCUSSION OF RESULTS

### 8.1 REFINED CALCULATION OF CRITICALITY

As shown in Section 6.1, the refined calculation of the 3.0-in. water-reflected core gives an estimate for  $k_{\text{eff}}$  which is a considerable improvement above the estimate obtained from the precritical calculations. In this section the components of the refined calculation are discussed individually, with an estimate of the effect on reactivity of incorporating each component separately.\*

#### 8.1.1 TWO-DIMENSIONAL CALCULATION OF THE UNIT CELL THERMAL DISADVANTAGE FACTORS

A comparison of the thermal  $U^{235}$  disadvantage factors obtained in one-dimensional and two-dimensional calculations is shown in Table 8.1. In order to examine the gap effect, the two-dimensional calculation omitted the cadmium in the cell. It can be seen that neutron streaming into the 1/8 in. gap increases the average thermal flux in the fuel. Analysis of the results indicates that the largest flux increase occurs near the end of fuel ring D, as expected. It is estimated that the effect on reactivity of including the gap in the disadvantage factor calculation is approximately +0.7%.

---

\*It should be noted that in the complete calculation the effects of the individual components are not necessarily separable.

Table 8. 1

COMPARISON OF ONE- AND TWO-DIMENSIONAL  
DISADVANTAGE FACTOR CALCULATIONS  
(CADMIUM OMITTED)

<u>Thermal Group</u>	<u>U<sup>235</sup> Disadvantage Factors</u>	
	<u>1D</u>	<u>2D</u>
1	0. 9371	0. 9369
2	0. 7634	0. 7833
3	0. 6238	0. 6503
4	0. 5152	0. 5464
5	0. 3313	0. 3715

As discussed in Section 4. 10. 2, the cadmium was represented as a thin ring at the outer boundary of the cell in the two-dimensional calculations of the unit cell thermal disadvantage factors. The choice of this scheme for representing the cadmium was based upon the results of the two-dimensional cadmium disadvantage factor calculations discussed in Section 4. 10. 2. In these calculations, the outer fuel ring was represented explicitly, whereas the inner rings were homogenized along with the other cell constituents inside the outer ring. Although these calculations were not expected to yield accurate fuel disadvantage factors, the relative change in fuel disadvantage factors with cadmium density should be accurately predicted. The U<sup>235</sup> disadvantage factors for the five thermal group structure are shown in Fig. 8. 1 as a function of Cd<sup>113</sup> concentration.

The fuel disadvantage factors were computed with three different cadmium representations - the first with no cadmium, the second with cadmium homogenized uniformly throughout the moderator, and the third with cadmium represented as a thin ring at the cell outer boundary. The percentage changes in the calculated disadvantage factors from the case with no cadmium are given in Columns 2 and 3 of Table 8. 2.

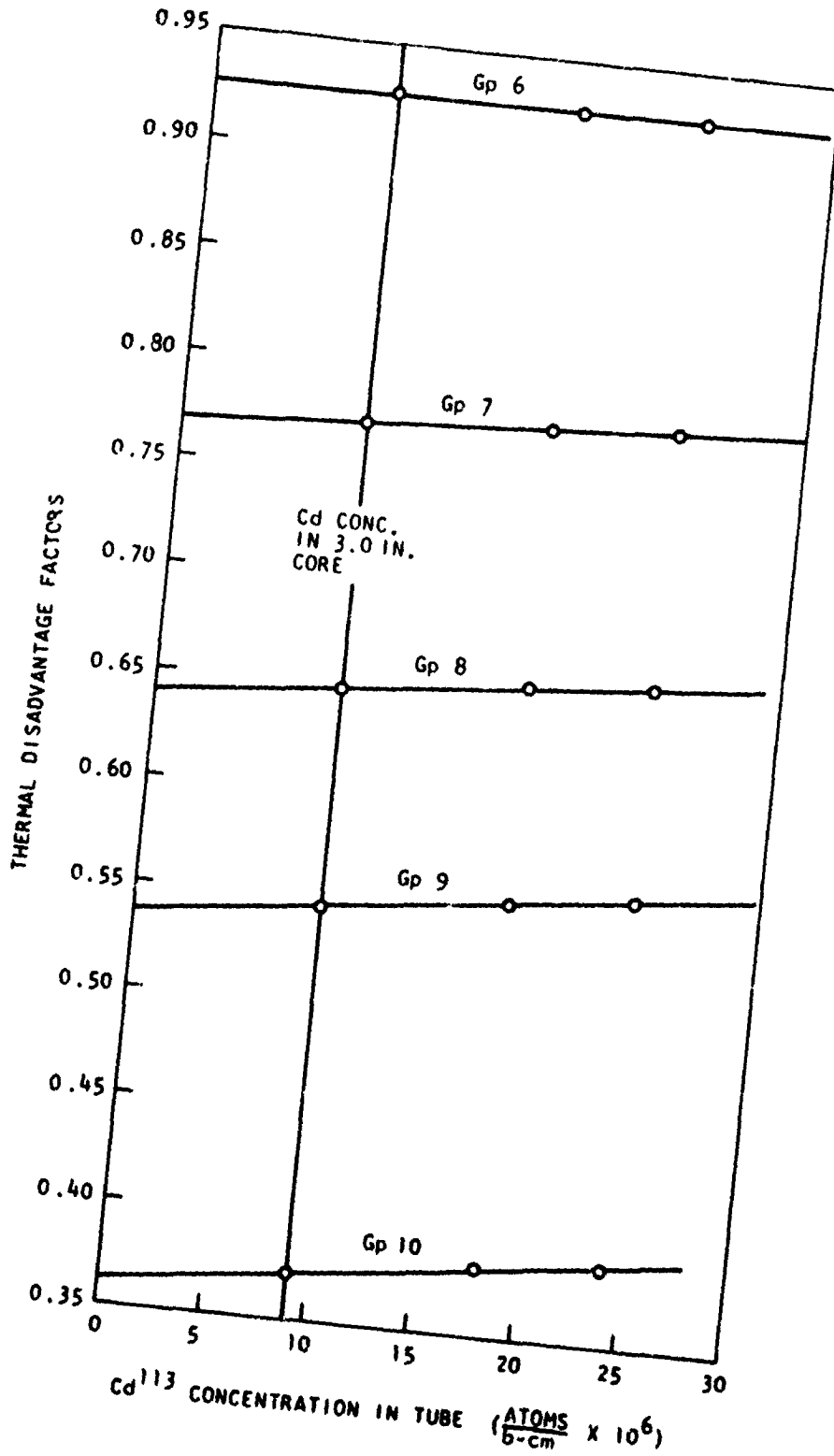


Fig. 8. 1--Effect of Cd concentration on U<sup>235</sup> disadvantage factors (2 DXY P<sub>0</sub> cell calculation)

These percentage changes are to be compared with the change given in Column 4, which was obtained by extrapolating the 2 DXY results to zero cadmium concentration.

It is apparent from Table 8.2 that the representation of the cadmium as a thin annular ring at the cell boundary gives more valid results than when the cadmium is homogenized in the moderator. It is estimated that the effect on reactivity of this cadmium representation in the calculation of unit cell thermal disadvantage factors is approximately +0.3%.

Table 8.2  
CHANGE IN  $U^{235}$  DISADVANTAGE FACTORS FOR  
THREE CADMIUM REPRESENTATIONS

Thermal Energy Gp.	Cd. Homog. in Mod. $\delta g_i$	Cd. in Thin Ring $\delta g_i$	2DXY $\delta g_i$
1	0.0%	0.0%	0.0%
2	-0.1%	+0.5%	+0.7%
3	-0.1%	+0.6%	+1.2%
4	-0.1%	+0.8%	+1.5%
5	-0.1%	+1.7%	+2.5%

#### 8.1.2 TWO-DIMENSIONAL CALCULATION OF THE CADMIUM THERMAL DISADVANTAGE FACTORS

A comparison of the cadmium thermal disadvantage factors obtained in the two-dimensional and one-dimensional, tube-centered cell, calculations is presented in Table 8.3. The results are shown for a cadmium concentration of  $9.0 \times 10^{-6}$  atom/b-cm, pertinent to the 3.0-in. pitch, water-reflected core. The one-dimensional results have been corrected for two-dimensional effects in the manner outlined in Section 4.10.1. It can be seen that the one-dimensional, tube-centered cell, calculation overestimates the effect of cadmium poison in the core. It is

estimated that the effect of replacing the one-dimensional cadmium disadvantage factors with those obtained in the two-dimensional calculation is +0.5% in reactivity.

Table 8.3  
COMPARISON OF ONE- AND TWO-DIMENSIONAL  
CADMIUM DISADVANTAGE FACTOR RESULTS

<u>Thermal Group</u>	<u>1D</u>	<u>2D</u>
1	1.193	1.143
2	1.377	1.328
3	1.710	1.603
4	1.973	1.820
5	2.392	2.142

### 8.1.3 TREATMENT OF THE INTERSTITIAL MATERIAL IN RESONANCE ABSORPTION CALCULATIONS

The effect of including interstitial aluminum in the resonance calculation on the effective absorption cross sections of the tungsten isotopes and  $U^{238}$  is shown in Table 8.4. The effect on reactivity is approximately -0.9%.

Table 8.4  
EFFECTIVE ABSORPTION CROSS SECTIONS  
IN THE 3.0-IN. PITCH CORE  
FROM 2.38 TO 61.4 eV

	$\bar{\sigma}_a$ (barns) Interstitial Aluminum Neglected	$\bar{\sigma}_a$ (barns) Interstitial Aluminum Considered
$W^{182}$	19.28	19.96
$W^{183}$	27.36	28.95
$W^{184}$	0.093	0.093
$W^{186}$	20.35	20.48
$U^{238}$	3.71	4.03

## 8.1.4 RESONANCE INTERFERENCE

The effect of tungsten resonance overlap on the effective absorption cross sections of  $W^{182}$ ,  $W^{183}$ , and  $W^{186}$  in the energy range from 2.38 to 61.4 eV is given in Table 8.5. For calculational simplicity, the cross sections have been averaged over  $1/E$  spectra. The magnitude of the effect should be diminished when the cross sections are averaged over realistic core spectra. The most significant overlap effect occurs between the 18.83 eV level of  $W^{186}$  and the 21.2 eV level of  $W^{182}$ , giving rise to a 9.3% decrease in  $\bar{\sigma}_a$  for  $W^{182}$ .

The effect of  $U^{238}$  overlap on the tungsten nuclides was calculated by homogenizing the  $U^{238}$  ring into the tungsten rings. The effective absorption cross sections of the tungsten isotopes with and without the  $U^{238}$  homogenized into the rings are compared in Table 8.6. It is seen that  $W^{182}$  is affected to the greatest extent by overlap from  $U^{238}$ . Comparison of the level structure of  $U^{238}$  with that of tungsten indicates the primary overlap is between the 21.0 eV level of  $U^{238}$  and the 21.2 eV level of  $W^{182}$ .

Table 8.5

EFFECTIVE ABSORPTION CROSS SECTIONS OF THE  
TUNGSTEN ISOTOPES WITH AND WITHOUT  
RESONANCE OVERLAP;  $1/E$  SPECTRUM

Nuclide	$\bar{\sigma}_a$ (barns)		% Dev.
	(no overlap)	(with overlap)	
$W^{182}$	22.89	21.41	-6.5%
$W^{183}$	26.27	25.96	-1.2%
$W^{186}$	22.02	19.97	-9.3%

Table 8.6

EFFECTIVE ABSORPTION CROSS SECTIONS OF  
THE TUNGSTEN ISOTOPES WITH AND WITHOUT  
OVERLAP FROM U<sup>238</sup>; 1/E SPECTRUM

Nuclide	$\bar{\sigma}_a$ (barns)		% Dev.
	Overlap Between Tungsten Isotopes Only	Overlap of U <sup>238</sup> on Tungsten Included	
W <sup>182</sup>	21.41	19.90	-7.1%
W <sup>183</sup>	25.96	25.35	-2.3%
W <sup>186</sup>	19.97	18.98	-5.0%

It is estimated that the effects of resonance overlap on the tungsten resonances accounts for +0.4% reactivity. The effects of tungsten resonance overlap on the U<sup>238</sup> resonances has been ignored because the relative spatial position of the U<sup>238</sup> ring and the tungsten rings suggests that this effect is insignificant.

#### 8.1.5 U<sup>235</sup> RESONANCE CALCULATION

The results of the resonance calculation for U<sup>235</sup> in the 3.0 in. pitch core indicate a significant degree of U<sup>235</sup> self-shielding within the fuel rings. The extent of the resonance self-shielding can be appreciated by referring to Table 8.7, where epithermal one-group averages of infinite dilution U<sup>235</sup> cross sections are compared with those obtained from the self-shielding calculation. The first section of Table 8.7 presents  $\sigma_c$ ,  $\sigma_f$ , and  $\alpha$  averaged over 1/E spectra from 2.38 eV to 14.9 MeV.

The actual effect of the U<sup>235</sup> resonance treatment on the characteristics of the 3.0-in. pitch, water-reflected core was obtained by performing a GAM calculation incorporating the U<sup>235</sup> self-shielded cross sections from 2.38 eV to 961 eV. In the second section of Table 8.7, the infinite dilution and self-shielded values of  $\sigma_c$ ,  $\sigma_f$ , and  $\alpha$  averaged over the actual core spectrum are compared.



Despite the significant depression in the epithermal capture cross section and the diminution of  $\bar{\alpha}$ , the effect of the  $U^{235}$  resonance calculation is negligible in terms of reactivity, which is decreased by -0.1%. Because of the large magnitude of nonfissile absorptions in the epithermal region of the spectrum, these cores are considerably more sensitive to the magnitude of the epithermal fission cross section itself than to  $\alpha$ . The calculated distribution of fissions, however, is altered significantly by the consideration of self-shielding in  $U^{235}$ . The ratio of total-to-thermal (0 to 2.38 eV) fissions, which is 1.30 when infinite dilution  $U^{235}$  cross sections are used, diminishes to a value of 1.23 when  $U^{235}$  self-shielding is included.

Table 8.7  
COMPARISON OF  $U^{235}$  INFINITE DILUTION  
CROSS SECTIONS WITH RESONANCE  
SELF-SHIELDED CROSS SECTIONS  
2.38 EV TO 14.9 MEV

	<u>Infinite Dilution</u>	<u>Resonance Self-Shielded</u>
	<u>Averaged Over 1/E Spectrum</u>	
$\sigma_c$ barns	8.48	5.81
$\sigma_f$ barns	12.22	9.20
$\alpha$	0.694	0.632
	<u>Averaged Over GAM 3.0 in. Core Spectrum</u>	
$\sigma_c$ barns	3.92	2.90
$\sigma_f$ barns	6.47	5.28
$\alpha$	0.607	0.549

## 8.1.6 TWO-REGION RESONANCE CALCULATION

A comparison of the results of a one- and two-region resonance calculation is given in Table 8.8 for the natural tungsten mixture in the 3.0-in. pitch core. The effect, as seen in the table, is substantial. The largest change occurs in  $W^{182}$ , where the two-region calculation gives a 32% increase in  $\bar{\sigma}_a$ . Most of this increase is derived from the 21.2 eV level, which is adjacent to the 18.8 eV level of  $W^{186}$ . Figure 8.2 illustrates the deviation from  $1/E$  of the moderator flux from 17.6 to 22.6 eV. Despite the significant deviation from  $1/E$  in the moderator, it is not the relaxation of the  $1/E$  approximation in the solution of Eqs. 4.18 and 4.19 that gives rise to the effect. This is verified in Fig. 8.3, where it is seen that the absorber flux is predicted quite well in the one-region calculation. It is the application of the two-region, flux-volume weighting to the cross section, given by Eq. 4.20, which causes the increase shown in Table 8.8.

Table 8.8  
EFFECTIVE ABSORPTION CROSS SECTIONS OF THE  
TUNGSTEN ISOTOPES FROM 2.38 TO 61.4 EV  
OBTAINED FROM ONE- AND TWO-REGION  
CALCULATIONS; 3.0-IN. PITCH CORE SPECTRUM

Nuclide	$\bar{\sigma}_a$ (barns)		% Dev.
	One-Region Calculation	Two-Region Calculation	
$W^{182}$	18.32	24.12	+31.7%
$W^{183}$	27.28	29.98	+ 9.9%
$W^{186}$	18.65	23.70	+27.1%

A rough estimate of the effect of the two-region resonance calculation on the reactivity of the 3.0-in. pitch, water-reflected core is -2.0%. However, as discussed in Section 4.11.5, consideration of the

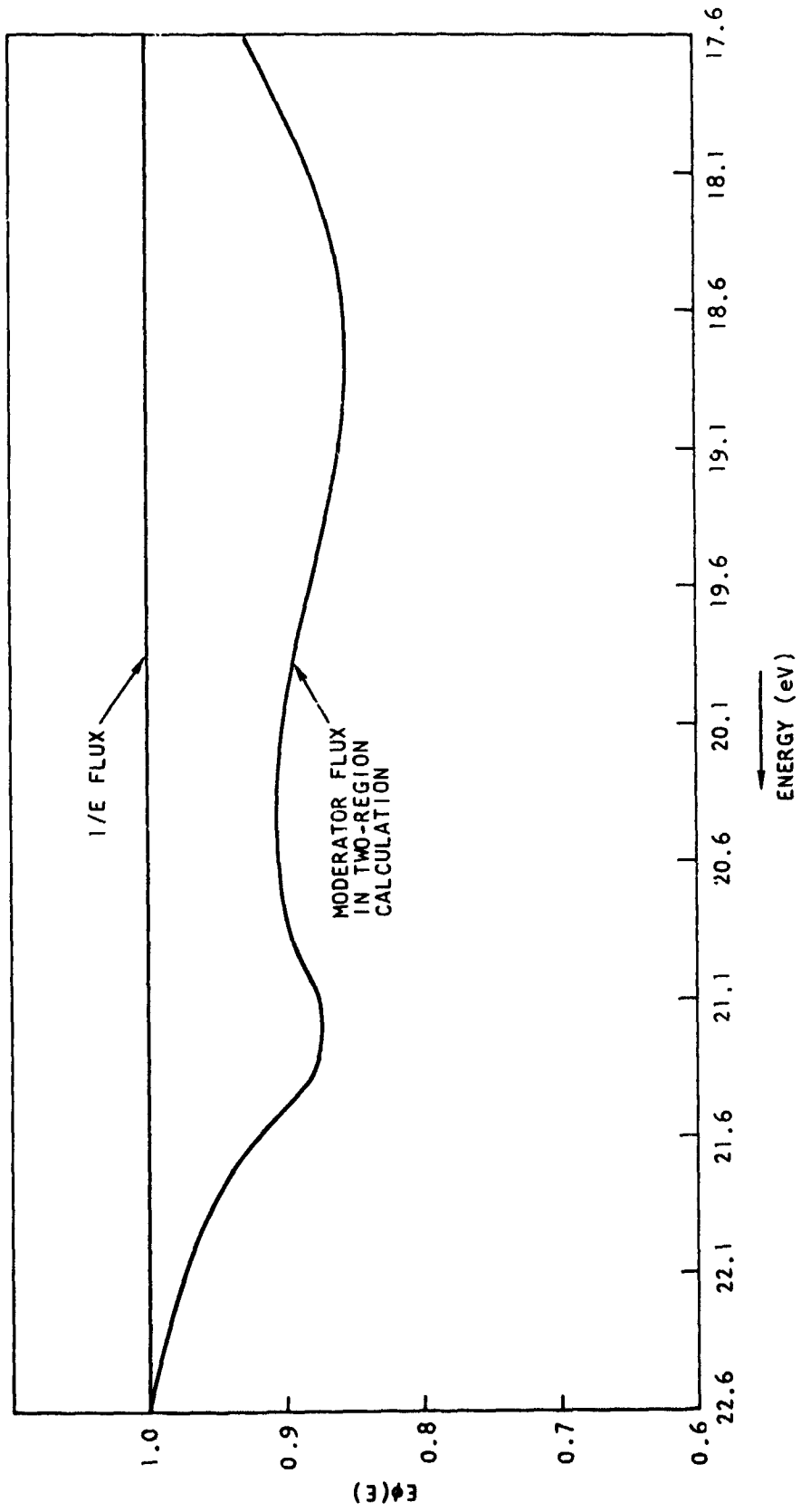


Fig. 8.2--Flux in moderator region; 17.6 to 22.6 eV

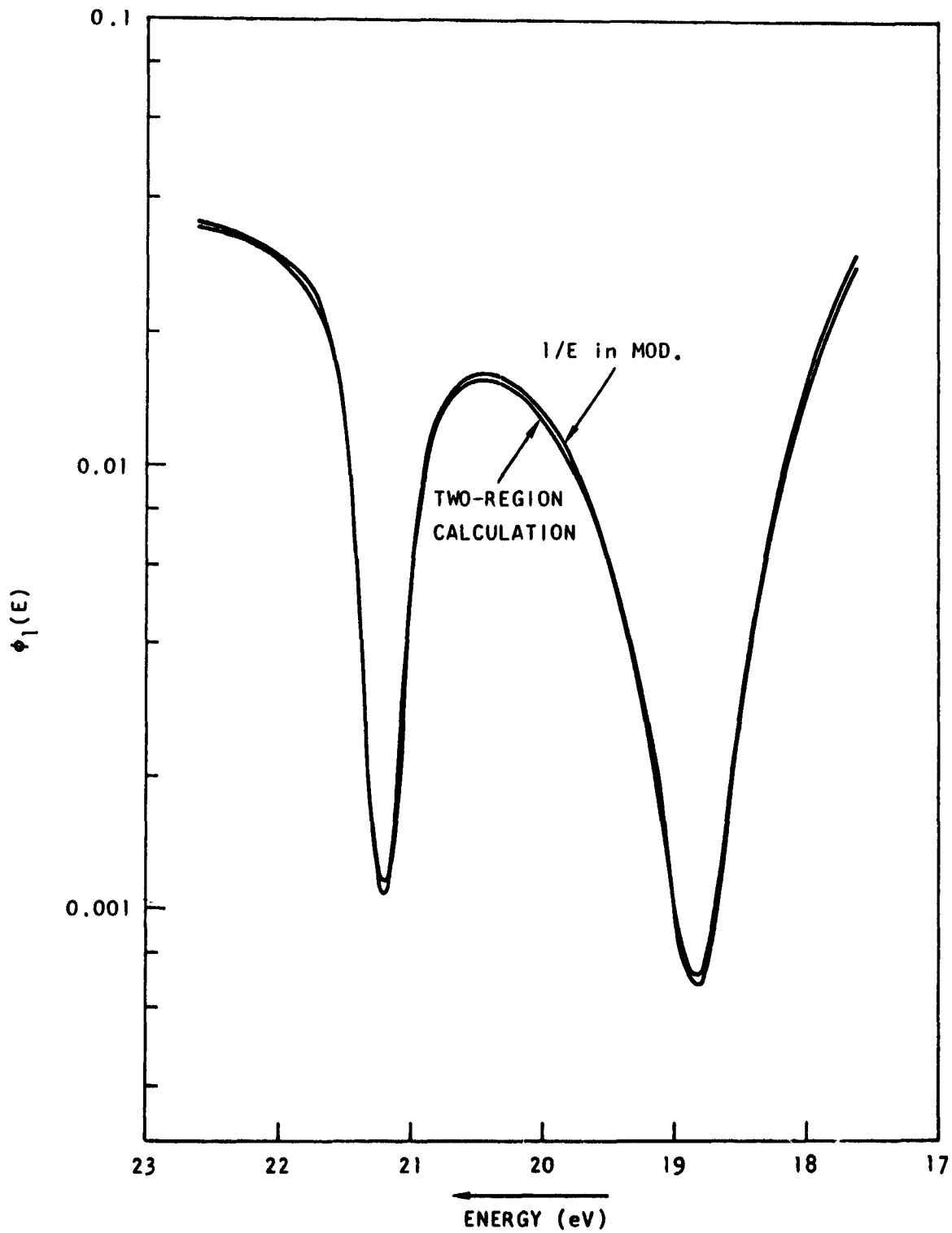


Fig. 8.3--Flux in absorber region; 17.6 to 22.6 eV

effect on  $\bar{\sigma}_a$  exclusively is inadequate. Moderator nuclides are also subject to cell flux fine-structure considerations in the resonance region of the spectrum. Epithermal advantage factors in the GAM fine groups for the tungsten resonance calculation discussed above are given in Table 8.9. These numbers are enhanced when all constituents of the absorber region are included in the calculation. The principal effect of these advantage factors is to increase the extent of elastic downscattering, which, for the 3.0-in. pitch core almost exactly compensates for the effect on  $\bar{\sigma}_a$

Table 8.9  
 EPITHERMAL ADVANTAGE FACTORS  
 FROM TUNGSTEN  
 TWO-REGION CALCULATION

<u>GAM Group</u>	<u>Energy Range (eV)</u>	<u>W<sub>i</sub></u>
80	61.4 to 47.8	1.016
81	47.8 to 37.3	1.048
82	37.3 to 29.0	1.005
83	29.0 to 22.6	1.076
84	22.6 to 17.6	1.451
85	17.6 to 13.7	1.034
86	13.7 to 10.7	1.013
87	10.7 to 8.3	1.010
88	8.3 to 6.5	1.073
89	6.5 to 5.0	1.012
90	5.0 to 3.9	1.187
91	3.9 to 3.1	1.043
92	3.1 to 2.38	1.012

#### 8.1.7 TWO-DIMENSIONAL DIFFUSION CALCULATION

A two-dimensional diffusion calculation, rather than the conventional one-dimensional buckling iteration procedure, as seen in Table 6.4, contributes approximately +0.7% in computed reactivity.

### 8. 1. 8 ESTIMATION OF THE EFFECT OF APPROXIMATIONS IN THE REFINED CALCULATION

There are several approximations which are still inherent in the refined calculation of the 3.0-in. pitch, water-reflected core. A cursory examination of several second order effects, which are discussed in this section, indicates that they are slightly on the positive side in reactivity. It is assumed that other approximations, which have not been investigated by virtue of time limitations or oversight, are also of second order and are compensatory.

The ten-group structure, described in Table 6.1, has been used for all criticality calculations. The group structure was chosen on the basis of the following considerations. The upper three groups encompass nearly all of the leakage. The fourth group includes absorptions in the unresolved resonance region and a portion of the resolved resonance region, and the fifth group encompasses most of the absorptions in the resolved resonance region. A thermal cutoff of 2.38 eV was chosen as the upper bound for significant upscattering in the moderator. The bottom four groups divide the thermal absorptions into roughly equal portions. Ten groups is the maximum number feasible in the two-dimensional calculations. The effect of a twenty-group structure, in which each of the former ten groups is split into two groups of equal lethargy width, was investigated for the 3.0 in. pitch, water-reflected core. The calculation indicated a +0.125% increase in computed reactivity.

The annular ring representation, as discussed in Section 8.1.1, is the most adequate R-Z representation of the effect of the cadmium on the disadvantage factors of the other constituents of the unit cell. However, as demonstrated in Table 8.2, this representation only accounts for approximately two-thirds of the entire effect. It is estimated that a correct representation would account for an additional +0.1% in reactivity.

The core disadvantage factors for cadmium have been used for the cadmium in the axial reflectors. This is a poor approximation, since there is no fuel influence on the thermal fine-structure in the axial reflector. The error associated with this approximation has been investigated by repeating the diffusion calculations of the 3.0 in. pitch, water-reflected core with the cadmium in the reflector omitted altogether. The results of this calculation indicate an increase in reactivity of +0.2%. Since it is estimated that the effect of omitting fuel in the calculation is to decrease the magnitude of the cadmium disadvantage factors by about 50%, the correct representation would be worth approximately +0.1% in reactivity.

The cylindrical equivalence principle, discussed in Section 4.11.1, is quite adequate for computing the collision probabilities in the flat source approximation of the annular ring absorbers in the fuel element. The single depleted uranium ring exhibits the only significant deviation between collision probabilities evaluated by transport calculations, as discussed in Section 4.4.5, and an evaluation by the equivalent cylinder method. The effect of this deviation has been evaluated and the results indicate that the more correct treatment would contribute +0.05% in reactivity.

The effect of resonance overlap of  $U^{238}$  on tungsten was taken into account by homogenizing the depleted uranium ring into the tungsten rings. This representation is a crude approximation, since there is considerable spatial separation between the tungsten and  $U^{238}$  in the fuel element, and it is expected that  $U^{238}$  homogenization underestimates the overlap effect because the  $U^{238}$  ring acts as a filter. In order to examine this approximation, a simulation of the three-region cell was accomplished by a synthesis of the  $U^{238}$  ring flux in the moderator region of a GAROL calculation (the GAROL code is restricted to a two-region treatment). The  $U^{238}$  ring flux was obtained first in a calculation in which the  $U^{238}$

ring is represented as the absorber region in a conventional two-region calculation. This flux is synthesized in the moderator region of a second two-region calculation, in which the tungsten nuclides are represented in the absorber region, by assuming the following cross section in a large moderator zone of mass unity:

$$\sigma_t(E) = \sigma_s(E) = \frac{1}{E\phi^{238}(E)}, \quad (8.1)$$

where  $\phi^{238}(E)$  is the  $U^{238}$  ring flux obtained in the first calculation.

The results of this calculation, which is expected to adequately represent the tungsten ring flux in a  $U^{238}$ -filtered spectrum, are given in Table 8.10. The effective absorption cross sections of the tungsten nuclides (2.38 to 61.4 eV), obtained with  $U^{238}$  overlap computed by the homogenization method (see Table 8.6) are compared with the results of the method described in this section. As expected, the homogenization procedure provides an underestimation of the overlap effect. It is estimated that the additional overlap computed by the  $U^{238}$ -filtered spectrum method is worth approximately +0.1% in reactivity.

Table 8.10

**EFFECTIVE ABSORPTION CROSS SECTIONS OF THE  
TUNGSTEN ISOTOPES WITH  $U^{238}$  OVERLAP; 1/E SPECTRUM**

<u>Nuclide</u>	<u>Homogenization Method</u>	<u><math>U^{238}</math>-Filtered Spectrum Method</u>	<u>% Dev.</u>
W <sup>182</sup>	19.90	19.06	-4.2%
W <sup>183</sup>	25.35	24.89	-1.8%
W <sup>184</sup>	18.95	18.50	-2.4%



It is assumed in the cell calculations that a repeating array of identical cells exists. This assumption clearly breaks down for the outer ring of fuel elements, where two or more of the six cells surrounding each element in a repeating hexagonal lattice are absent. A crude estimate of the effect of this approximation was obtained in the following manner. The white boundary condition, used in the conventional cell calculations, was replaced by five inches of water at the outer boundary of the 3.0-in. pitch unit cell. The cell disadvantage factors obtained in this configuration were used for the outer ring of cells in a complete one-dimensional analysis of the 3.0-in. pitch, water-reflected core.

High energy and thermal disadvantage factors for hydrogen and  $U^{235}$  obtained in this isolated cell treatment are compared with those obtained in the conventional one-dimensional repeating array treatment in Table 8.11. The result of the complete core calculation indicates a decrease in the computed value of  $k_{eff}$  of -0.48%. Most of the influence on  $k_{eff}$  arises from enhanced high energy leakage from the outer ring of fuel elements; this could be predicted by noting the significant change in the high energy disadvantage factors shown in Table 8.11. Since less than three, on the average, of the adjoining cells are absent at the outer ring of fuel elements, it is estimated from this calculation that an exact treatment of the boundary condition would lead to a calculated reactivity effect of approximately -0.2%.

It is felt that the thermal cross sections of the tungsten isotopes are adequately known. However, there may exist some uncertainties in the eipthermal region of the spectrum. Shook and Bogart<sup>(58)</sup> found good agreement between experiment and theory for the effective resonance integrals of all the tungsten isotopes except  $W^{186}$ . Assuming that the experimental results are correct, the calculated resonance integral for

$W^{186}$  at a value of  $\sqrt{S/M} \approx 1$  (corresponding to the tungsten in the fuel element) is approximately 20% high. Decreasing the epithermal captures in  $W^{186}$  by this amount gives rise to a +0.3% enhancement in the calculated reactivity.

Table 8.11

COMPARISON OF DISADVANTAGE FACTORS OBTAINED FOR  
ISOLATED CELL AND REPEATING ARRAY

Gp.	Energy Range	Hydrogen		$U^{235}$	
		Isolated Cell	Repeating Array	Isolated Cell	Repeating Array
1	14.9 to 2.73 MeV	0.622	0.904	1.331	1.087
2	2.73 to .50 MeV	0.638	0.896	1.303	1.086
3	.50 MeV to 67.4 keV	0.770	0.939	1.190	1.048
-----					
6	2.38 to .414 eV	1.077	1.074	0.936	0.938
7	.414 to .090 eV	1.332	1.312	0.756	0.757
8	.090 to .050 eV	1.539	1.500	0.617	0.626
9	.050 to .030 eV	1.704	1.654	0.508	0.521
10	.030 to 0.0 eV	1.998	1.936	0.322	0.339

A discussion of the infinite dilution  $U^{235}$  epithermal cross sections was given in Section 5.2. It was noted that normalization of the  $U^{235}$  epithermal cross sections<sup>(36)</sup> to recently measured integral values of  $I_f$  and  $\alpha$  leads to as much as +1.5% increase in calculated reactivity for the 3.0-in. pitch, water-reflected core. For the refined calculation, which incorporates resonance self-shielded epithermal  $U^{235}$  cross sections, an estimate for the effect of the normalization,  $I_f = 276$  barns and  $\alpha = 0.48$ , is +1.0% in reactivity. This effect will remain uncertain until the discrepancy between the integral and differential  $U^{235}$  epithermal cross section measurements is resolved.

Although a refined calculation has not been performed for the 2.9-in. pitch or beryllium-reflected cores, it is reasonable to conclude that the enhancement in  $k_\infty$  of the refined calculation for the 3.0-in. pitch,

water-reflected core would carry over to the other cores. This conclusion is based upon the fact that the leakage fractions from the one-dimensional diffusion calculations are nearly identical for the precritical and refined analyses. The enhancement in  $k_{\text{eff}}$  obtained in the two-dimensional diffusion calculation may not carry over to the other cores to the same extent, since the core leakages are involved.

The refined analysis involves arduous and time-consuming constituent calculations. This procedure is not recommended for routine survey calculations of tungsten water-moderated reactor cores. Depending upon the extent to which the refinements are incorporated into the model, predictions for  $k_{\text{eff}}$  may range from three percent low to one percent high. The complexity of these cores lies in their extreme heterogeneity combined with very heavy loadings.

## 8.2 REACTIVITY MEASUREMENTS AND ANALYSIS

### 8.2.1 AREAS OF AGREEMENT BETWEEN EXPERIMENT AND ANALYSIS

Most of the reactivity worths analyzed show good agreement with the measured results. This agreement corroborates both the experimental and analytical methods and no further discussion will be made of these measurements. The following measurements fall into this category:

- a. Safety and regulating rod worths
- b. Poison worth as a function of radius
- c. Poison worth as a function of concentration
- d. Top reflector worth.

Other measurements were made which were not analyzed in this phase of the contract. They may be analyzed in the future, if warranted. They include:

- a. Worth of boron poison substituted for cadmium
- b. Worth of boron-stainless steel substituted for tungsten
- c. Individual worth of fuel rings D and E.

### 8.2.2 PROMPT NEUTRON LIFETIME

The comparison of the measured and calculated values of the prompt neutron lifetime given in Table 6.11 shows the calculated values to be about 15% low in every case but that of the 85-element (no cadmium) core. The agreement in this case, however, may be fortuitous, since the calculation depended upon a buckling iteration technique in a high leakage core. Nevertheless, the agreement in this case suggests that the error might lie in either the treatment of leakage or in the cadmium cross sections. The latter possibility is very unlikely, since relatively large changes in the disadvantage factors for cadmium have resulted in virtually no change in the calculated lifetime. The first possibility suggests that the results may improve through the use of two-dimensional alpha calculations. This has not been attempted due to the high cost involved. The reason for the discrepancy is, at present, unknown.

### 8.2.3 EXCESS REACTIVITY

The measurement of excess reactivity by the mapping of the individual cadmium poison tubes has proven to be an effective and apparently accurate method. Comparison of the measured results to precritical calculations as given in Table 6.16 shows an error of about three dollars of reactivity in the calculated values. The calculated values were obtained in each case using the precritical methods, and thus are subject to the considerations presented for criticality calculations in Section 8.1. It is believed that the discrepancy between the measured and calculated values listed in Table 6.16 can be entirely ascribed to the causes discussed in Section 8.1, and that the error can be virtually eliminated by refined eigenvalue calculations.

#### 8.2.4 FUEL ELEMENT COMPONENT WORTHS

The results shown in Tables 6.19 and 6.20 illustrate that central fuel element component worths can be reasonably well predicted by perturbation analysis if the worths are small (less than say \$0.40). Larger changes, however, require consideration of local flux perturbations caused by removal of the component. These larger changes can be treated, for the central fuel element at least, by means of one-dimensional eigenvalue calculations in which the central cell can be explicitly represented. The worths of the components as calculated by the eigenvalue method are in fair agreement with the measurements.

Calculation of the removal worth of fuel element components in the outer locations B-6 and A-5 gave results of lower accuracy even for small worths. These discrepancies may be attributed to the local heterogeneities at the core edge which are largely lost in a one-dimensional diffusion calculation.

It is believed that the data of Tables 6.19 and 6.20 show reasonable agreement within the limitations of one-dimensional diffusion calculations and perturbation analysis.

#### 8.2.5 SIMULATION EXPERIMENT

The Simulation Experiment led to the specification of an enriched tungsten cell configuration which was an almost exact match in reactivity worth to the mockup cell. Because only five stages of the central fuel element were replaced, possible differences in leakage between a complete assembly of mockup elements and a complete assembly of pseudo-reference elements were not necessarily shown. These differences should be of second order, however, since the two cells are identical in fuel and H<sub>2</sub>O content.

Analysis of the experiment did demonstrate a close match in the infinite medium value of  $k_{\infty}$ , the pseudo-reference configuration having a value only .005  $\Delta k/k$  higher than the mockup. This close match lends strong support to the methods of analysis, especially those concerned with resonance absorption. As may be seen in Table 6.22, the pseudo-reference element has more resonance absorption in tungsten which is matched in the mockup element by resonance absorption in  $U^{238}$ . This match was one of the original intentions in the design of the mockup fuel element.

Table 6.23, which illustrates the structure of the reactivity worths of the two fuel sections, is more illustrative of the actual experiment. These calculations, which are normalized to the average axial worth, illustrate again that the reactivity match is achieved by trading tungsten absorptions in the pseudo-reference elements for  $U^{238}$  absorptions in the mockup element, and that the mockup element is a close simulation in all other respects.

### 8.3 FLUX AND POWER DISTRIBUTIONS

The general agreement between calculated and measured foil activation data was good in the water-reflected cores. The power density within a fuel element, the radial power traverse, and the axial copper activation data all compared well with the results of the corresponding calculation. Significant discrepancies occurred only at the core-reflector interface in the radial power traverse. The two high points near the interface in Fig. 6.11 are both measurements made on the outermost edge of an outer fuel ring; they directly face the reflector and consequently are in a higher thermal flux than that calculated for the same radius in a homogenized diffusion calculation. This discrepancy is thus qualitatively understood.

The calculated gold cadmium ratios gave close agreement to the measured values for two different pitches and at several locations in the core. The agreement of these data also tends to corroborate the experimental and analytical methods used.

The comparison of the experimental and calculated axial power profiles in Fig. 6.12 for the beryllium reflected core showed a significant deviation near the bottom beryllium reflector. The discrepancy may be caused in part by streaming of thermal neutrons up from the solid reflector. However, there is little evidence of this effect in the axial flux traverse of the water-reflected core, shown in Fig. 6.10. At present this discrepancy is unexplained.

#### 8.4 TEMPERATURE COEFFICIENTS

The complexity of the structure of the temperature coefficient in terms of its component parts is demonstrated in Tables 6.34 and 6.35. Each component, except  $\eta$ , is greater than or approximately equal to the net effect. The fast components,  $\epsilon$  and  $p$ , are particularly large for these cores, which could be anticipated from the large fraction of epithermal fissions. The large positive effect associated with the thermal utilization, and to a certain extent with  $\epsilon$ , is derived primarily from the density reduction of the cadmium solution. The behavior of the temperature coefficient in these cores, therefore, is quite sensitive to the cadmium concentration in the poison tubes.

It is seen in Table 6.33 that the effect of the change in thermal disadvantage factors with temperature, which has not been considered in the results presented in Tables 6.31 and 6.32, is significant. The effect, which can be attributed to an increase in the magnitude of the positive component associated with the thermal utilization, is a 25% increase in the predicted reactivity at 100°C for the water-reflected core. With the change in disadvantage factors taken into account, the calculated

over-all temperature coefficient ( $27^{\circ}\text{C}$  to  $100^{\circ}\text{C}$ ) of the water-reflected core is brought into good agreement with experiment. (Some reservation should be exercised here, as the  $100^{\circ}\text{C}$  measured value is based upon a linear extrapolation.) On the other hand, the  $50^{\circ}\text{C}$  and  $70^{\circ}\text{C}$  points for the water-reflected core are anomalously high, and the effect of considering the change in thermal disadvantage factors would be to further increase the deviation from experiment. Although the water-reflected curve exhibits a positive region, the positive peak occurs at  $35^{\circ}\text{C}$ , and crosses the axis at approximately  $43^{\circ}\text{C}$ . The calculated positive reactivity at  $50^{\circ}\text{C}$  remains unexplained.

The deviation from experiment of the  $50^{\circ}\text{C}$  and  $100^{\circ}\text{C}$  points for the beryllium-reflected core would be expected to diminish with the incorporation of temperature dependent thermal disadvantage factors in the analysis. This consideration suggests that the agreement at  $70^{\circ}\text{C}$  is misleading, and that with the incorporation of temperature dependent thermal disadvantage factors, this point would be high by approximately 20%. The behavior of the leakage component between  $50^{\circ}\text{C}$  and  $70^{\circ}\text{C}$ , shown in Table 6.35, lends additional credence to this conjecture. The magnitude of this component is anomalously low, suggesting that  $P_{NL}$  at  $70^{\circ}\text{C}$  is high by approximately 0.15%, but the reason for this is unknown.

Comparison between Tables 6.34 and 6.35 indicates a significant difference between the construction of the temperature coefficient of the water-reflected core and the beryllium-reflected core. The higher combined positive effect associated with  $f$  and  $\epsilon$  for the beryllium-reflected core is largely due to the increased cadmium loading. The slight decrease in the positive effect associated with  $f$  (the thermal utilization itself is lower because of the competition with cadmium for thermal captures) is more than compensated by the large positive effect associated with  $\epsilon$ , which is higher itself because of an increase in the mean fission energy. These positive contributions, however, are offset by



the large, and unexpected, increase in the component associated with  $p$ . No positive portion of the reactivity curve was observed in the water-reflected core. It is felt that the positive portion observed in the water-reflected core is eliminated by the increased negative component of the nonleakage probability,  $P_{NL}$ , between 27°C and 50°C for the beryllium-reflected core. The difference between the calculated reflecting properties of water and beryllium arises primarily from the large difference in the coefficients of expansion of the two materials (see Table 6.28).

Several sources of error are implicit in the calculations. The effect of temperature dependent thermal disadvantage factors has already been discussed. The effect of density changes on the high energy disadvantage factors and the small change in buckling due to increased leakage has been neglected, but a single calculation of these effects at 100°C indicates only a 6% error associated with their omission. The metal expansion has been neglected in the calculation of the 100°C thermal disadvantage factors. The magnitude of this effect is unknown, but assumed to be insignificant. The error associated with the termination of the buckling iterations after the second radial calculation is estimated to be less than 0.2¢ in reactivity. Finally, a free linear expansion of the grid plate and of the axial core support members has been assumed, since the degree of restraint in the thermal expansion of the assembly is unknown. A rough estimate of the contribution to the calculated reactivity from a free radial expansion of the grid plate is approximately - 2.0¢ in reactivity.

It is concluded that the temperature behavior of the 3.0-in. pitch cores is reasonably well understood. The gas and crystal kernels for beryllium yield nearly identical results for the reactivity of the beryllium-reflected core. The structure of the temperature coefficient from its components is exceedingly complex, thus rendering predictions of the temperature behavior of TWMR cores inadvisable without a thorough and careful analysis.

## 8.5 MEASUREMENT OF THE ASYMPTOTIC DECAY CONSTANT

The deviation between the measured and calculated values of  $\alpha$ , the asymptotic prompt neutron decay constant, may be seen in Table 6.36. The reason for the - \$1.44 discrepancy in the just critical 0.1255 molar case is primarily the one-dimensional method used in the calculations. As discussed in Section 8.1.7, a difference of approximately \$1.00 has been found between one- and two-dimensional calculations for this core. Thus the discrepancy for this case amounts to approximately - \$0.44 from unknown causes. However, in the more heavily loaded subcritical cases, the error from unknown causes increases to - \$1.58 in the 0.1677 molar case and to - \$2.35 in the 0.2899 molar case.

The reactivity of these cases was also obtained by mapping of the cadmium worth. The results, given in Table 3.6, are in reasonable agreement with the results found by the pulsed neutron method, the mapped values being about - \$0.35 more subcritical in each case. Thus the two different experimental determinations tend to confirm one another.

The calculated values of the prompt neutron lifetime demonstrate the same type of discrepancy. In the lifetime measurement,  $\alpha$  is found in a core with a known reactivity. Thus in these measurements the absolute value of  $\alpha$  found by experiment is again smaller than that found by calculation.

It is possible, as discussed in Section 7.2, that a two-dimensional calculation of  $\alpha$  may eliminate the discrepancy. Other potential sources of error which remain to be investigated are the change in the average inverse velocity in the outermost row of fuel elements and the possible interference, in the more heavily loaded cores, of higher modes.

At present, these differences between the measured and calculated values of  $\alpha$  are the outstanding discrepancy in the calculation of unzoned cores.

## IX. CONCLUSIONS AND SUGGESTIONS FOR FUTURE WORK

### 9.1 REVIEW AND MEASUREMENT OF CROSS SECTIONS

The compilation and review of nuclear data for the isotopes of tungsten, and for beryllium, aluminum, cadmium,  $U^{235}$  and  $U^{238}$  have been published in various topical reports listed in Section I. Furthermore, the neutron capture cross section from 0.01 to 10 eV for the isotopes  $W^{182}$ ,  $W^{183}$ ,  $W^{184}$  and  $W^{186}$  have been measured and analyzed in Section 5.3 of this report. These cross section data are believed to be of sufficient accuracy and detail for nearly all design purposes for the tungsten, water-moderated reactor concept. Further work is required, however, in two areas. The importance of  $W^{183}$  in the determination of the Doppler coefficient of the enriched tungsten suggests that the resonance parameters of this isotope should be measured up to at least 1.0 keV. The same techniques as used for the 0.01 to 10 eV range should be used to obtain a consistent set of nuclear data. The second area which requires more work is the well known problem of the  $U^{235}$  epithermal cross sections. This problem was discussed in Section 5.2 where it was shown that integral measurements of the values of  $\alpha$ , the ratio of the infinite dilute epithermal capture integral to the fission integral, favor a value about 10% lower than that found by analysis of the differential data. The discrepancy is under investigation at several laboratories: as the results become available, further analysis will be required to understand and resolve the potential error which may now lie in the epithermal  $U^{235}$  cross section data.

## 9.2 ANALYSIS OF CRITICAL EXPERIMENTS AT THE LEWIS RESEARCH CENTER

The analysis of the ten Lewis critical experiments presented in Section VII proved that the small unvoided cores could be well predicted using one-dimensional transport theory. It was also demonstrated that homogenization techniques were inadequate to treat the neutron streaming in cores containing large voids; the use of Behrens and Benoist corrections for anisotropic diffusion overestimated the streaming. Finally, the analysis indicated that the presence of a thin tungsten tube inside the voided tube apparently eliminated neutron streaming.

It is concluded that homogenization methods are inadequate to treat neutron streaming in these cores; a more sophisticated treatment of the axial leakage involving two-dimensional transport calculations of the voided cells remains to be tried.

## 9.3 CRITICALITY MEASUREMENTS AND ANALYSIS

The agreement between criticality measurements and analysis has been found to be good. The methods of calculation for the unzoned critical assemblies have been extensively investigated and found to be adequate for all criticality design purposes.

The precritical analyses gave eigenvalues within 2% of the measurements, yet were based on relatively inexpensive methods. The errors associated with these survey methods are known and can be virtually eliminated by using more sophisticated calculational techniques. These refined methods are arduous and time consuming, however, and should be used primarily as a check of the accuracy of the survey calculations.

#### 9.4 REACTIVITY MEASUREMENTS AND ANALYSIS

The good agreement between analysis and experiment has shown that the calculational methods are quite adequate for the prediction of control rod worth, poison tube worth, fuel element component worths, and to top reflector worth in these cores. Furthermore, the measurement of the excess reactivity by the mapping of individual poison tube worths has given accurate estimates of the excess reactivity available in these cores.

A 15% discrepancy exists between calculated and measured values of the prompt neutron lifetime; the cause is at present unknown and should be further investigated, possibly by means of two-dimensional diffusion calculations.

The simulation experiment proved that experimentally matched mockup and pseudo reference elements had nearly identical calculated values of  $k_{\infty}$ . This agreement tends to confirm the methods of analysis.

#### 9.5 FLUX AND POWER DISTRIBUTIONS

The agreement between calculated and measured foil activations was good in the water-reflected cores, the only significant deviation occurring at the core reflector interface. The problem of accurately predicting power densities at the radial interface is well known; the rapidly changing thermal neutron spectrum and the local heterogeneities contribute to make an exact solution difficult. However, because the outer row of fuel elements comprises nearly 25% of the core, it is important to find better methods to predict power densities in these outermost elements.

The measured axial power distribution in the beryllium-reflected core showed a significant deviation from calculated values near the bottom beryllium reflector. The cause of this discrepancy is not understood. Further investigation is warranted, due to the importance of correctly predicting axial power distributions in zoned cores.

## 9.6 TEMPERATURE COEFFICIENTS

An extensive analysis of the temperature coefficient in the water-reflected and beryllium-reflected cores has led to a reasonable understanding of the temperature behavior of these assemblies. A strong negative temperature coefficient of  $-1.0\%$ / $^{\circ}\text{C}$  is available in the beryllium-reflected core, and calculational methods exist to determine the temperature coefficient in differing geometries. However, construction of the temperature coefficient from its components has proven to be quite complex, and predictions of the temperature behavior of these cores is inadvisable without a thorough and careful analysis.

## 9.7 ASYMPTOTIC DECAY CONSTANT

A persistent discrepancy has been found between the measured and calculated values of  $\alpha$ , the asymptotic prompt neutron decay constant. The cause of this discrepancy, which also is noted in the prompt neutron lifetime, is unknown, and further investigation of it is warranted. At present, these differences between the measured and calculated values of  $\alpha$  are the outstanding discrepancy in the calculation of unzoned cores.

## 9.8 CALCULATION OF ZONED CORES

It is believed that the analytical methods used for the unzoned cores can be extended in general, to the analysis of zoned cores. The use of one-dimensional leakage synthesis calculations will probably not be possible; however, either two-dimensional diffusion calculations or flux-synthesis techniques may be required instead to calculate power density profiles and eigenvalues.

There are several possible ways to flatten or shape the power distribution in these cores. They include pitch variation, fuel distribution, and poison distribution. These methods should all be carefully analyzed and experiments conducted on the optimum designs.

## REFERENCES

1. Project Staff, "Tungsten Nuclear Rocket Critical Facility, Description and Hazards Analysis, " General Atomic Report GA-5846 Rev., Feb. 18, 1965.
2. R. G. Bardes and J. C. Peak, "Technical Specification for the General Atomic Nuclear Rocket Critical Facility, " General Atomic Report GA-6315, Apr. 15, 1965.
3. Physical Aspects of Irradiation, N. B. S. Handbook, 85, March 31, 1964, p. 2.
4. G. J. Hine and G. L. Brownell, Radiation Dosimetry, Academic Press, Inc., New York (1956), p. 160.
5. J. W. T. Spinks and R. J. Woods, An Introduction to Radiation Chemistry, John Wiley and Sons, Inc., New York (1964), p. 88.
6. C. R. Hatcher and C. P. Jupiter, "Measurements of High-Intensity Gamma Radiation, " USAEC Report UCRL-7223, University of California Radiation Laboratory, Jan. 31, 1963.
7. C. P. Jupiter and J. Parez, "A Study of the Scintillation Properties of Various Hydrogenous and Non-Hydrogenous Solutes Dissolved in Hexafluorobenzene" - to be published in IEEE Transactions on Nuclear Science, February, 1966.
8. D. L. Williams, "HFB Liquid Scintillators, " USAEC Report TID 7612 (1960).
9. J. B. Birks, The Theory and Practice of Scintillation Counting, Pergamon Press/MacMillan Company, 1964, p. 270.
10. A. W. Boyd, H. W. J. Connor, and J. J. Pieroni, "Methods of Dosimetry and Flux Measurements and Their Application in the NRX Reactor, " Atomic Energy of Canada Ltd. Report AECL-2203 (CRC-1210), January 1965.



11. G. D. Joanou, C. V. Smith, and H. A. Vieweg, "GATHER-II, An IBM-7090 FORTRAN-II Program for the Computation of Thermal Neutron Spectra in Associated Multigroup Cross Sections," General Atomic Report GA-4132, July 8, 1963.
12. G. D. Joanou and J. S. Dudek, "GAM-II, A B<sub>3</sub> Code for the Calculation of Fast Neutron Spectra and Associated Multigroup Constants," General Atomic Report GA-4265, Sept. 16, 1963.
13. A. M. Weinberg and E. P. Wigner, The Physical Theory of Neutron Chain Reactors, The University of Chicago Press, Chicago, 1958, p. 619.
14. B. Carlson, "Numerical Solution of Neutron Transport Problems," Proceedings of the Symposia in Applied Mathematics, Vol. 11, American Mathematical Society, Providence, (1961), pp. 219-232.
15. J. H. Alexander, G. W. Hinman, and J. R. Triplett, "GAPLSN, A Modified DSN Program for the Solution of the One-Dimensional Anisotropic Transport Equation," General Atomic Report GA-4972, March 16, 1964.
16. J. Hardy and D. Klein, Trans. Am. Nucl. Soc. 8, 446 (1965).
17. J. A. Thie, Nucl. Sci. Eng. 9, 286 (1961).
18. W. W. Clendenin, Nucl. Sci. Eng. 14, 103 (1962).
19. H. C. Honeck, Trans. Am. Nucl. Soc. 5, 350 (1962).
20. G. C. Pomraning, Nucl. Sci. Eng. 17, 311 (1963).
21. Z. Weiss and R. J. J. Stamm'ler, Nucl. Sci. Eng. 19, 374 (1964).
22. Project Staff, "Tungsten Nuclear Rocket Final Report," NASA Report NASA CR-54909, Part 2, General Atomic Division General Dynamics Corporation (1966) Confidential.
23. L. W. Nordheim, "A Program of Research and Calculation of Resonance Absorption," USAEC Report GA-2527, General Atomic Division General Dynamics Corporation, Aug. 28, 1961.
24. G. C. Pomraning, Nucl. Sci. Eng. 19, 250 (1964).

25. G. C. Pomraning, USAEC Report APED-4343, General Electric Co., Sept. 1963.
26. G. Rakavy and Y. Yeivin, Nucl. Sci. Eng. 15, 158 (1963).
27. S. R. Lenihan, "GAZE-2, A One-Dimensional, Multigroup, Neutron Diffusion Theory Code for the IBM-7090, " General Atomic Report GA-3152, Aug. 3, 1962.
28. J. P. Dorsey, "GAMBLE-4, A Program for the Solution of the Multigroup Neutron-Diffusion Equations in Two Dimensions, with Arbitrary Group Scattering, for the IBM-7044 FORTRAN IV System, " General Atomic Report GA-6540, Jul. 1, 1965.
29. J. J. Loechler and J. E. MacDonald, "Flexible Monte Carlo Programs FMC-N and FMG-G, " USAEC Report APEX-706, General Electric Co., Apr. 28, 1961.
30. J. Bengton, et al., "2 DXY, Two-Dimensional, Cartesian Coordinate  $S_n$  Transport Calculation, " USAEC Report AGN TM-392, Aerojet-General Nucleonics, June 1961.
31. K. M. Case, F. de Hoffmann, and G. Placzek, "Introduction to the Theory of Neutron Diffusion, " Vol. 1, Los Alamos Scientific Laboratory, June 1953, p. 21.
32. S. M. Dancoff and M. Ginsburg, "Surface Resonance Absorption in a Close Packed Lattice, " Manhattan Engineering District Report CP-2157, University of Chicago Met. Lab., Oct. 1944.
33. Lattice Constants for Thermal Heterogeneous Systems, Sect. 4, p. 280, Reactor Physics Constants, USAEC Report ANL-5800, Argonne National Laboratory, July 1963.
34. C. A. Stevens and C. V. Smith, "GAROL, A Computer Program for Evaluating Resonance Absorption Including Resonance Overlap, " General Atomic Report GA-6637, Aug. 24, 1965.
35. C. A. Stevens and G. D. Joanou, Trans. Am. Nucl. Soc. 8, 287, June 1965.
36. G. D. Joanou and M. K. Drake, "Neutron Cross Sections for  $U^{235}$ , " NASA Report NASA CR-54263, General Atomic Division General Dynamics Corporation, Dec. 10, 1964.

37. A. F. Henry and S. Kaplan, "An Experiment to Measure Effective Delayed Neutron Fraction, " USAEC Report WAPD-TM-290, Westinghouse Electric Corp. Atomic Power Div., (1960).
38. G. R. Keepin, "Basic Kinetics Data and Neutron Effectiveness Calculations, " Proceedings of Symposium on Reactor Kinetics and Control, University of Arizona, p. 334, Mar. 1964.
39. G. de Saussure, et al., Nucl. Sci. Eng. 23, 45 (1965).
40. C. R. Lubitz, " $^{235}\text{U}$  Cross Sections, " KAPL Cross Section Newsletter, MUFT Deck 018A, pp. 15-64, Nov. 1964.
41. D. J. Hughes, Pile Neutron Research, Addison-Wesley Publishing Co., Cambridge, Mass. (1953), p. 201.
42. W. S. Lyon, Nucl. Sci. and Eng. 8, 378 (1960).
43. R. E. Schmunk, P. D. Randolph, and R. M. Brugger, Nucl. Sci. and Eng. 7, 193 (1960).
44. R. S. Carter, H. Palevsky, V. W. Myers, and D. J. Hughes, Phys. Rev., 92, 716 (1953).
45. E. Haddad, R. B. Walton, S. J. Friesenhahn, and W. M. Lopez, Nucl. Sci. and Methods, 31, 125 (1964).
46. L. V. Groshev, A. M. Demidov, V. N. Lutsenko, and V. I. Pelekhov, Atlas of Gamma Ray Spectra from Radiative Capture of Thermal Neutrons, Pergamon Press, New York, (1959), pp. 160-174.
47. Nuclear Data Sheets, National Academy of Sciences - National Research Council.
48. R. C. Barrall and W. M. McElroy, "Neutron Flux Spectra Determination by Foil Activation, " AFWL-TR-65-34, Vol. II.
49. J. Julien, et al., "Détermination du Spin et des Paramètres des Résonances pour  $^{197}\text{Au} + n$  de 10 eV à 1000 eV, " Saclay, France (to be published).
50. J. D. Garrison and B. W. Roos, Nucl. Sci. and Eng. 12, 115 (1962).

51. D. J. Seth, B. L. Zimmerman, and R. C. Garth, Phys. Rev., 110, 692 (1958).
52. F. H. Fröhner and E. Haddad, Nucl. Phys. 31, 129 (1965).
53. Brother Austin Bernabie, F. S. C., "The Effects of Crystalline Binding on the Doppler Broadening of a Neutron Resonance," USAEC Report BNL 860 (T-344), Brookhaven National Laboratory, Apr. 1, 1964.
54. D. J. Hughes and B. B. Schwartz, USAEC Report BNL 325, 2nd Ed. Brookhaven National Laboratory (1958), p. 61.
55. G. D. Joanou and C. A. Stevens, "Neutron Cross Sections for Tungsten Isotopes," NASA Report NASA CR-54261, General Atomic Division General Dynamics Corporation, Nov. 1964.
56. D. J. Hughes, B. A. Magurno, and M. K. Brussel, USAEC Report BNL 325, Supp. No. 1, 2nd Ed., Brookhaven National Laboratory, p. 36.
57. J. E. Russell, B. W. Hockenbury, and B. C. Block, "Neutron Capture Measurements on the Isotopes of Tungsten," USAEC Report WASH 1046, p. 104.
58. D. Shook and D. Bogart, Trans. Am. Nucl. Soc. 8, (1965), p. 284.
59. G. R. Keepin, et al., Phys. Rev. 107, 1044 (1957).
60. G. F. Kuncir, "GANIT, A Program for the Calculation of Resonance Integrals," General Atomic Report GA-2525, Aug. 1961.
61. D. J. Behrens, Proc. of Phys. Soc. (London), 62A, 607, (1949).
62. P. Benoist, "Formulation Générale. . . du Coefficient de Diffusion," Report CEA-1354, Commissariat de l'Energie Atomique, Saclay (1959).
63. Personal Communication, P. Klann to J. C. Peak, General Atomic, Jan. 7, 1965.